ORBIT MAINTENANCE STRATEGIES FOR SUN-EARTH/MOON

LIBRATION POINT MISSIONS: PARAMETER SELECTION FOR

TARGET POINT AND CAUCHY-GREEN TENSOR APPROACHES

A Thesis

Submitted to the Faculty

of

Purdue University

by

Vivek Muralidharan

In Partial Fulfillment of the

Requirements for the Degree

of

Master of Science in Aeronautics and Astronautics

December 2017

Purdue University

West Lafayette, Indiana

THE PURDUE UNIVERSITY GRADUATE SCHOOL
STATEMENT OF THESIS APPROVAL

Professor Kathleen C. Howell, Chair

    School of Aeronautics and Astronautics

Professor David A. Spencer

    School of Aeronautics and Astronautics

Professor Carolin E. Frueh

    School of Aeronautics and Astronautics

Approved by:

    Professor Weinong Wayne Chen

        Aeronautics and Astronautics Associate Head for Graduate Education

ACKNOWLEDGMENTS

Firstly, I would like to express my profound gratitude to my adviser and mentor, Professor Kathleen Howell, for providing me the opportunity to learn and evolve. It is both challenging and satisfying to do research under her supervision. I greatly appreciate her constant guidance and feedback on my research as well as her patient effort in editing my writings. Her thoughts and advice have always been invaluable, both personally and professionally.

Sincere thanks to my committee members, Professor David A. Spencer and Professor Carolin Frueh, for critiquing my thesis as well as providing me advice and feedback. During the course, I had the privilege to meet Dr. R.V. Ramanan, scientist and professor at the Indian Institute of Space Science and Technology. I thank him for sharing his expertise and elaborating me on Indian space missions.

All the members of my research group, both, past, and present have been excellent technical support and great friends. Special thanks to Dr. Davide Guzzetti for being an approachable instructor and a great motivator. Had he not taught the course on Advanced Orbital Dynamics, maybe I wouldn't have been pursuing research in the same area.

I am grateful to the Minority Engineering Program (MEP) for providing me with a Graduate Assistantship to overcome financial obligations at Purdue. Ms. Virginia Booth Womack, director, and Dr. Darryl Dickerson, associate director of the MEP have really been humble and approachable. Sincere thanks to the School of Aeronautics and Astronautics at Purdue University, and the staffs. I appreciate the facility

at the Rune and Barbara Eliasen Visualization Laboratory.

My parents made me recognize the importance of education early in my life. Without their unconditional support, I wouldn't have been able to pursue my graduate studies in the United States. With their love and blessings, I shall continue to chase my dreams. As always, I am overwhelmed by the belief my brother, Varun shows in me. The encouragement shown by Anjaly has always alleviated me during the challenging times at Purdue. Finally, I extend my thanks to all friends and well-wishers.

TABLE OF CONTENTS

LIST OF TABLES

LIST OF FIGURES

Figure $\qquad$ Page

ABSTRACT

Muralidharan, Vivek. M.S.A.A, Purdue University, December 2017. Orbit Maintenance Strategies for Sun-Earth/Moon Libration Point Missions: Parameter Selection for Target Point and Cauchy-Green Tensor Approaches. Major Professor: Kathleen C. Howell.

The libration point orbits in the Sun-Earth/Moon system are formed by concurrent gravitational influences by various celestial bodies, originating in a nonlinear dynamical regime. Coupled with the unstable nature of the orbit, the impact of any perturbations are expected to increase rapidly. The feasibility of a flow-based, Cauchy-Green tensor control strategy for station-keeping is examined. An orbit consistent with the mission objectives is selected for examination. The station-keeping process is stochastic, thus Gaussian random errors are introduced for simulation. The evolution of a velocity perturbation over time is monitored, beyond which the attainable state in the accessible region nearest to the target state is employed as a feedback to compute the necessary full, three-component corrective maneuver. The application and appropriateness of single axis control maneuvers for orbit maintenance are also evaluated. The selection procedure for certain parameters such as tolerances and weighting values are developed to incorporate the available dynamical information, yielding a versatile and straightforward strategy. Weighting matrices within the target point approach are effective in influencing the station-keeping costs as well as size and direction of maneuvers. Moreover, selection of appropriate tolerance values in the application of the Cauchy-Green tensor exploits the dominant stretching direction of the perturbation magnitude to inform the maneuver construction process. The work is demonstrated in the context of the upcoming Aditya-1 mission to a Sun-Earth/Moon L_1 halo orbit for solar observations and the James Webb Telescope to a Sun-Earth/Moon L_2 halo orbit for astronomy.

1. INTRODUCTION

The quest for scientific discovery throughout the universe has long been of focus of human interest. It is only recently that humans gained the capability to venture into the space with both crewed and robotic vehicles. One of the main challenges in deploying a spacecraft for scientific exploration is delivering the vehicle to a wide variety of destinations in support of ever-expanding and increasingly complex goals. Leveraging multi-body dynamical environments has produced a much wider array of options for space exploration. In particular, trajectories associated with the Lagrange points or libration points in a wide range of systems are very beneficial for scientific discovery.

Ever since the successful launch of the International Sun Earth Explorer-3 (ISEE-3) mission in 1978 to the Sun-Earth L_1 Lagrange point, interest has grown in missions to the Sun-Earth libration points, especially L_1 and L_2, i.e., the libration points closest to Earth. While ISEE-1 and ISEE-2 [1] were deployed to examine the dynamical behavior within the Earth's magnetosphere, ISEE-3 investigated the cosmic rays and solar wind patterns. The launch of the WIND mission in 1994, the Solar Heliospheric Observatory (SOHO) in 1995 and the Advanced Composition Explorer (ACE) in 1997 [2] followed ISEE-3 to support helio-physics research while positioned at the Sun-Earth L_1 halo orbits. The Genesis spacecraft [3] collected samples of solar wind maintaining itself along a halo orbit at the Sun-Earth L_1 libration point while the Wilkinson Microwave Anisotropy Probe (WMAP) [4] spacecraft hovering in an orbit about the Sun-Earth L_2 Lagrange point investigated the cosmic waves from the big bang. Many such spacecraft have explored such areas and more missions have been planned to utilize this location for scientific studies. Such investigations would not be possible unless the spacecraft is maintained in a predefined orbit near the Lagrange points. Orbits in the proximity of these libration points are highly unstable, therefore

robust low-cost station-keeping techniques are required to maintain the spacecrafts in its predetermined orbit to enable scientific investigations.

The libration point orbits with potential benefits do pose a few challenges. The libration points L_1 and L_2 in the Sun-Earth system are about 1.5 million km from the Earth. The circular restricted three body problem (CR3BP) does not take into consideration the eccentricity of the Earth's orbit around the Sun, therefore, it neglects the oscillatory behavior of the L_1 and L_2 distances. The Moon's orbit is also at a fairly close distance to these equilibrium points; as a result the Moon's gravity acts as a strong perturbing force, consequently, neither the uniform predictable behavior of the orbits in CR3BP is preserved nor the existence of any equilibrium points are guaranteed. Furthermore, the large distance from the Earth to the spacecraft in the vicinity of such equilibrium points presents navigational challenges. The orbit maintenance strategies developed must be effective in maintaining the spacecraft close to the baseline path by overcoming such challenges. The station-keeping algorithm must be able to compute an effective maneuver despite the navigational limitations. The algorithm must be able to incorporate the gravitational forces of other perturbing bodies to simulate a real mission scenario.

1.1   Problem Definition

The scientific advantages of the two Sun-Earth collinear equilibrium points in the vicinity of the Earth has motivated more missions in their vicinity. Scheduled to launch in 2019-20, the goals for the Aditya-1 mission [4] to the vicinity of the Sun-Earth L_1 Lagrange point includes examination of the Sun's corona and the particle flux emissions while the James Webb Telescope [5] to a Sun-Earth L_2 Lagrange point orbit is expected to be launched in October 2018 to observe distant events in the Universe including formation of stars, galaxies etc. The potential orbits for these missions to the vicinity of L_1 and L_2 libration points are highly unstable, therefore, an efficient

station-keeping algorithm is sought to successfully maintain the spacecraft close to the reference orbits for the mission duration. Since the Aditya-1 mission is relatively new, the exact orbit for this mission is not yet available, however, the overall mission objectives are similar to that of ISEE-3 and SOHO mission, thus the orbit is assumed similar to that used for these previous missions. Moreover, values from the literature are used to analyze the results. Based on these factors, an orbit similar to ISEE-3 mission is used extensively throughout this work.

Station-keeping simulations are accomplished to estimate the orbit maintenance cost of the Aditya-1 mission, using three different approaches, the target point, the Floquet mode and the Cauchy-Green tensor approach. The aim of conducting station-keeping using these approaches are not to distinguish these methods based on their advantages and disadvantages, rather to understand their functioning and explore the possibilities from modifying certain parameters based on dynamical information rather than an arbitrary or heuristic selection. The focus of this research has been to answer the following questions. The target point approach is a simple and robust method but depends greatly on the weighting matrices to compute a low cost maneuver. The Floquet mode approach on the contrary, uses qualitative information from the eigenstructure of the monodromy matrix to compute a maneuver. Can the qualitative information available from the Floquet Mode approach be leveraged to find the right weighting matrices in the target point approach? Also, can the target point approached be further tuned to obtain even lower costs? Moreover, instead of selecting the weights by trial and error method, can range of probable weights be analyzed to identify any orderly behavior, in terms of cost minimization and maneuver direction.

The Cauchy-Green tensor approach is analyzed in the Sun-Earth/Moon system as a potential station-keeping strategy for libration point orbits for the first time. The feasibility of the CGT approach for such a highly unstable orbit in the Sun-

Earth/Moon system is worth examining. Would the CGT method yield station-keeping costs of the same order of magnitude as that estimated using the target point and the Floquet mode approach? Since the CGT approach is driven by design variables such as horizon time, minimum executable maneuver size and target tolerance, their effect on the overall station-keeping costs and computational expense are worth investigating. Further, can information based decision be made rather than a heuristic based decision on the value of target tolerance, that affects the station-keeping costs and computational expense? Finally, are there certain trends in the location of the maneuvers? Are certain regions more prone to maneuvers than the others?

1.2   Previous Contributions

1.2.1   Multibody Dynamics

During the early seventeenth century, Johannes Kepler (1571 - 1630) postulated his three laws, that govern a two body motion based on the heliocentric theory given by Nicolaus Copernicus [6,7]. The work was only corroborated in 1687 after Sir Isaac Newton (1642 - 1727) formulated the Universal Laws of Gravitation in *Philosophiæ-Naturalis Principia Mathematica* [8] that explained Kepler's laws. Although a very simplified model, the two body problem, in general, offered a good approximation of the planetary motion around the Sun. Since each body in space applies a gravitational force on the other, a model with a central gravitational body is not sufficient to explain the complex nature of space. Despite the benefits of a two body problem, a more comprehensive model was sought until Leonhard Euler (1707 - 1783) in 1767 formulated a simple restricted three body problem [9]. Joseph-Louis Lagrange (1736 - 1813) in 1772 computed the existence of equilibrium points based on the Euler's three body problem [10]. During the same time a lot of other astronomers and mathematicians offered in their theories and improvised the existing models. Carl Gustav Jacob Jacobi (1804 - 1851) came up with the concept of energy-like constant that exists in CR3BP, that is now known as Jacobi Constant or Jacobi integrals [11]. Jules

Henri Poincaré (1854 - 1912) investigated the nature of various trajectories and came up with a visualization technique using maps in 1899 [12], now denoted as Poincaré Maps, to represent different dynamical behavior of the trajectories as noted by saddle, focus, center or nodes. In 1967, Victor Szebehely's *Theory of Orbits* [13] summarizes the improvements done in the circular restricted three body problem till then and substantiates theories with appropriate numerical results.

With the ability to venture into space, the mathematical solutions of the three body problem became an interest for practical applications. The launch of ISEE-3 mission in 1978 to the Sun-Earth L_1 Lagrange point, marked the new beginning in the area of multi-body dynamics. With confidence in operating space missions and the quest for scientific experiments that are otherwise not possible on the Earth has boosted the research in the area of multi-body dynamics. A lot of research has been done to explore different dynamical structures in the multi-body systems suitable for space missions. Farquhar in 1968, describes a 3 dimensional halo orbit that exists close to the collinear equilibrium points in his PhD thesis [14]. He endorsed it for a communications station along the L_2 halo orbit for its locational benefits. The orbit is suitable for continuous communication with the Earth and the far side of the Moon without being blocked by the Moon shadow. Later in 1973, Farquhar and Kamel, produced analytical solutions to represent quasi-periodic orbit using Lindstedt-Poincaré approach [15]. In 1980, Richardson came up with an analytical solution to represent halo orbits for ISEE-3 mission [16]. Howell in 1984 developed a numerical computation technique for precise halo orbit construction [17]. Howell and Pernicka extended the research to determine Lissajous trajectory in CR3BP [18]. Recent work by Nath and Ramanan also focuses on precise halo orbit design [19]. The close proximity of the Sun-Earth L_1 and L_2 halo orbits to the Earth and continuous communication possibilities makes it a favorable choice for a lot of space missions. The launch of the WIND mission in 1994, the Solar Heliospheric Observatory (SOHO) in 1995 and the Advanced Composition Explorer (ACE) in 1997 [2], the Genesis mission [3] and

the Wilkinson Microwave Anisotropy Probe [20] in 2001 have successfully followed ISEE-3 to their respective libration point orbits.

1.2.2 Orbit Maintenance Strategies

The orbits close to the collinear equilibrium points are unstable in general, requiring regular orbit maintenance maneuvers to keep the spacecraft in close vicinity to the ideal path. Early orbit maintenance research was done by Farquhar et al. [1, 21] over the ISEE-3 mission during 1970-80s. Other prevalent research over station-keeping of the ISEE-3 missions had been done by Heuberger [22] as well as Erickson and Glass [23] during the same time. Other studies on ISEE-3 are found in [24–26]. With more missions that followed ISEE-3, more researchers have worked on orbit maintenance strategies. Rodriguez and Hechler [27] studies aspects of SOHO mission design while Sharer et al. examined the WIND Trajectory design and control [28]. Few other station-keeping studies in the Sun-Earth system is found in [29–31]. Some of the early works in the Earth-Moon system is found in the studies done by Breakwell et al. [32, 33], Colombo [34], Euler and Yu [35]. Recent studies on orbit maintenance for ARTEMIS mission were conducted by Folta et al [36–38] as well as Howell and Pavlak [39].

Howell and Pernicka [24, 25] incorporate statistical errors into the computation of station-keeping costs in a numerical simulation. Their work is highly utilized to generate large number of simulations especially with advancements in computational technology. Their work also illustrates a new maneuver computation technique using the target point approach. Later improvements to this method were made by Howell and Gordon [40, 41] as well as Howell and Keeter [42, 43]. Williams et al. [30] used a simplified version of the target point approach with single future position targeting for orbit maintenance of the Genesis spacecraft. Another noted station-keeping technique using the Floquet mode was first seen in the works of Gomez et al [44, 45]

in 1985, that deals with removing the unstable component of the eigenvectors of the monodromy matrix to maintain the spacecraft close to the nominal trajectory. The method has been used successively by Simo et al. [46, 47], Howell and Keeter [42, 43] Howell and Pavlak [39] and Meng et al. [48]. In 2017, Guzzetti et al. formulated a method to perform station-keeping for missions along the Earth-Moon near rectilinear halo orbits using the Cauchy-Green tensor method [49]. Many more research using impulsive control methods for station-keeping has been seen in the works of Ghorbani and Assadian [50], Howell and Barden [51], Lu et al. [52]. A summary of few orbit maintenance techniques for libration point orbits has been provided by Shirobokov et al. [53].

1.3   Present Work

In this research, well established station-keeping techniques like the target point approach has been analyzed with the Floquet mode approach for performance tuning. Besides, for the first time, application of a recently developed method using the Cauchy-Green tensor has been analyzed in the Sun-Earth system.

The target point approach although being a simple and robust method, uses different weighting matrices in the cost function. It may become challenging to find appropriate weights that produce a low-cost maneuver with minimal deviation from the nominal orbit. The Floquet mode approach on the other hand uses rich information about the flow, but is computationally intensive. In this work, the qualitative information provided by the Floquet mode is utilized to find the corresponding weights that gives a similar, cost-effective station-keeping budget. Further efforts have been put to tune the target point approach to give lower station-keeping costs than the Floquet mode approach.

The Cauchy-Green tensor method was previously analyzed in the Earth-Moon near rectilinear halo orbit that has a very low stability index. The method for the very first time has been analyzed in the Sun-Earth/Moon L_1 halo orbit that has significantly larger stability index and larger stretching. The effects of other parameters such as target tolerance and horizon time on orbit maintenance costs and computational time has been analyzed.

The applications of this research are not limited to the Aditya-1 or the James Webb Telescope mission to the Sun-Earth Lagrange points, but applicable to many other missions in future.

The study is summarized as follows.

- Chapter 2

  The equations of motions in the circular restricted three body problem are modeled based on a few fundamental assumptions. The equilibrium solutions are calculated. Energy-like constant is defined, thus determining the accessible regions. Behavior in close vicinity to a reference solution is examined using linearization. A higher fidelity model using n-gravitational bodies is formulated. Further, ways to transform different coordinate systems are derived in this chapter.

- Chapter 3

  The CR3BP is a nonlinear dynamical system; consequently, determining an initial condition that would drive to a desired final state is non-intuitive. Dynamical systems theory provides tools to resolve this challenge using linear state transition matrix (STM) over a chosen reference solution. Differential correction techniques use the STM information for trajectory design as well as station-keeping techniques investigated in this chapter. Likewise, single shoot-

ing and multiple shooting techniques for complex trajectory corrections are derived. Application of this tool in a higher fidelity model is also discussed.

- Chapter 4

  Setup of a station-keeping algorithm is addressed in this chapter. Steps to select a baseline solution and converting into a higher fidelity model are shown. Ways to introduce stochastic errors for simulating an actual orbit maintenance scenario is introduced. Insight into Monte Carlo simulations is provided with explanation on impact of number of runs on confidence levels.

- Chapter 5

  Detailed explanation on the target point and the Floquet mode approach for station-keeping has been included in this chapter. The two approaches are correlated to explore the impact of weighting matrix in the target point approach on station-keeping costs and amount of drift from baseline solution. Also, trends in maneuver direction is studied. Feasibility of corrective maneuvers in a fixed direction, for simplicity, is inspected.

- Chapter 6

  The concept of the Cauchy-Green tensor(CGT) and its application in orbit maintenance is presented. Different parameters that could potentially affect the station-keeping costs and computational time such as target tolerance and horizon time are investigated. Dynamical information based selection of target tolerance is proposed. Preliminary results are documented in this chapter. Feasibility of x-direction controlled maneuver is surveyed. Magnitudes of maneuver computed using the CGT approach are compared with those produces using a single shooting differential correction process.

- Chapter 7

  The station-keeping budget computed using the Cauchy-Green Tensor is compared with the other two well established methods to check for costs. Effort

has been put to analyze the distribution of maneuver locations along the orbit. Survey of libration point missions in the Sun-Earth/Moon system are provided.

- Chapter 8

  The research developments on orbit maintenance strategies using the three methods are summarized. Some peculiar observations are highlighted. Recommendations for future work are offered.

2. SYSTEM MODELS

The "two body problem" represents the behavior of two particles under their mutual gravitational attraction. The two body problem is expressed mathematically with relatively straight forward simple differential equations and an analytical solution is available. With additional gravitational bodies, the complexity increases and an analytical solution ceases to exist. Some characteristics of the system behavior are exposed by numerical propagation of the governing differential equations. Adding only one additional gravitational source the three body problem is formulated and serves well as a foundation for more complex motion.

2.1 Circular Restricted Three Body Problem (CR3BP)

Infinitely many gravitational bodies can influence the motion of every other body in the solar system. The motion of one body influenced by '$n-1$' other bodies in the solar system is modeled as 'the n-body problem.' To formulate the n body problem define each of 'n' bodies as P_i with mass m_i where $i = 1, 2, ..., n$. Assuming all the n bodies to be spherically symmetric, Newton's Law of motion is applied to compute the force acting on the particle of interest. Let orthonormal unit vectors $\hat{X}, \hat{Y}, \hat{Z}$ represent the coordinates of the inertially fixed frame, I, with O as the inertially fixed base point or the origin. The vector $\bar{r}_i$ describes the position of body P_i with respect to the base point O while the vector $\bar{r}_{qi}$ describes the position of body P_i with respect to the body P_q as shown in Figure 2.1. Therefore, as expressed in [54], the total force acting on body P_i as a result of all other bodies is

$$\bar{F}_i = -\tilde{G} \sum_{j=1,\ j\neq i}^{n} \frac{m_i m_j}{r_{ji}^3}\, \bar{r}_{ji} \qquad (2.1)$$

such that, $\tilde{G}$ is the dimensional scalar gravitational constant given by 6.67408 x 10^{-11} $m^3kg^{-1}s^{-2}$ [55] and $\bar{F}_i$ is the force vector acting on body P_i.
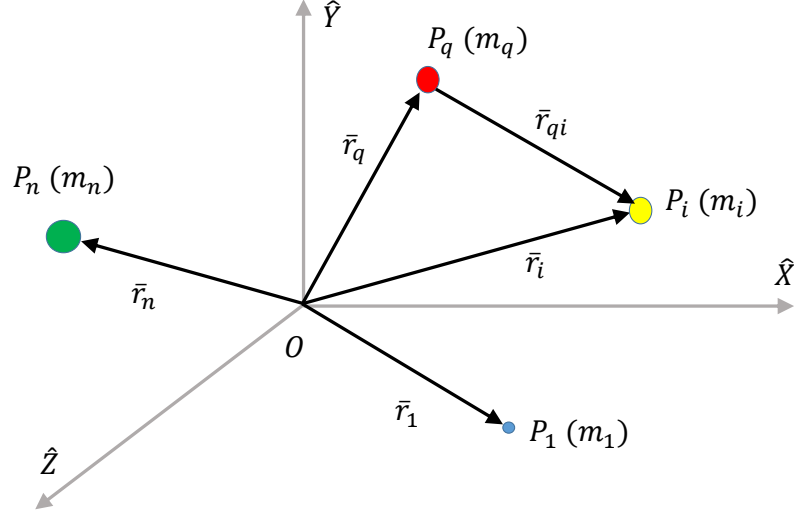
Figure 2.1. Gravitational interactions between n bodies in space.

The motion of a body is well expressed in terms of kinematic quantities. Using Newton's second law of motion, equation (2.1) is expressed in terms of acceleration of body P_i in the inertial frame, I, as

$$\bar{F}_i = m_i\ddot{\bar{r}}_i = -\tilde{G}\sum_{\substack{j=1\\j\neq i}}^{n} \frac{m_i m_j}{r_{ji}^3}\, \bar{r}_{ji} \tag{2.2}$$

such that,

$$\ddot{\bar{r}}_i = -\tilde{G}\sum_{\substack{j=1\\j\neq i}}^{n} \frac{m_j}{r_{ji}^3}\, \bar{r}_{ji} \tag{2.3}$$

where $\ddot{\bar{r}}_i$ represents the acceleration of body P_i due to gravitational forces due to all other particles in the n-body system. It is the double derivative of the position vector with respect to the dimensional time as observed in the inertial frame.

For a system with more than two gravitational bodies, an analytical solution does not exist. Hence, gaining some insight into the system behavior is a challenge but the highest priority. For the n-body system, each of the bodies are sensitive to changes in position, velocity and acceleration due to the influence of all other bodies in the solar system hence a generic equation of motion cannot be formulated that is independent of time. A multi-body problem can be analyzed with selected number of bodies about a fixed epoch date and real time data describing the states, called the ephemeres model. A less complex, time invariant mathematical model with three gravitational bodies is formulated with certain assumptions making a reliable framework to understand the characteristic behavior of the system. The Circular Restricted Three Body Problem, CR3BP, is the most commonly used method of formulating the equations of motion of one body influenced by two other bodies, independent of time, with some assumptions stated in section 2.1.1. The solution obtained using the CR3BP model can be used as an initial guess for the higher fidelity model.

2.1.1 Assumptions

The Circular Restricted Three Body Problem is a specific case of the n-body problem where the total number of bodies are three. Equation (2.3) delivers the expression of a n-body system, so for $n = 3$

$$\ddot{\bar{r}}_3 = -\tilde{G} \left[\frac{m_1}{r_{13}^3} \, \bar{r}_{13} + \frac{m_2}{r_{23}^3} \bar{r}_{23} \right] \tag{2.4}$$

where the position vectors $\bar{r}_{13}$ and $\bar{r}_{23}$ are given as

$$\bar{r}_{13} = \bar{r}_3 - \bar{r}_1 \tag{2.5}$$

$$\bar{r}_{23} = \bar{r}_3 - \bar{r}_2 \tag{2.6}$$

such that, $\bar{r}_i$ is the position vector of body i with respect to the origin. To solve for the differential equation, time history of $\bar{r}_1$ and $\bar{r}_2$ are to be known, but such information is not available as states of P_1 and P_2 are themselves influenced by $\bar{r}_3(t)$. Hence to

solve for the three body problem 18 integrals of motion are to be solved i.e. 6 states (3 position and 3 velocity states) for each of the 3 bodies, but only 10 integrals are known. A two body problem has a closed form solution but with addition of one more gravitational body i.e. $n = 3$, a closed form solution ceases to exist. With certain additional assumptions, a refined model is described that quite accurately illustrates the behavior of a number of systems.

- $m_3 << m_1, m_2$

  Let the three bodies P_1, P_2 and P_3 be point mass bodies with masses m_1, m_2 and m_3, such that $m_3 << m_1, m_2$. The two bodies P_1 and P_2 are considered as primaries that are massive in comparison to the third body, P_3, that is modeled as infinitesimally small body like a spacecraft, a comet etc. The assumption is further extended to $m_1 < m_2$ to represent a larger primary body and a smaller primary body.

- m_3 does not influence the motion of m_1 and m_2

  When m_3 is modeled as infinitesimally small body in comparison to the primaries it is assumed that the gravitational force due to m_3 does not influence the motion of m_1 and m_2. This results in an isolated two body system with primary body m_1 and secondary body m_2, for which solution is known to be a conic. m_3 is known to coexist within the stable system of m_1 and m_2.

- m_1 and m_2 move on circular orbits about its barycenter

  Further it is assumed that the primaries move in a circular orbit about its barycenter. This assumption is not necessary but simplifies the model from an elliptic restricted three body problem. As a result, the barycenter is regarded as inertially fixed and treated as the origin for developing the equations of motion in the circular restricted three body problem.

Now that the circular restricted three body problem is defined, let the bodies be oriented in as shown in Figure 2.2. Let orthonormal unit vectors $\hat{X}, \hat{Y}, \hat{Z}$ represent

the coordinates of the inertially fixed frame, I, with origin at the barycenter (B) of the primaries. Since P_1 and P_2 have a conic solution, the motion of the primaries are fixed in $\hat{X}\hat{Y}$ plane. The angular momentum vector of the motion of the primaries is along the positive $\hat{Z}$ direction.
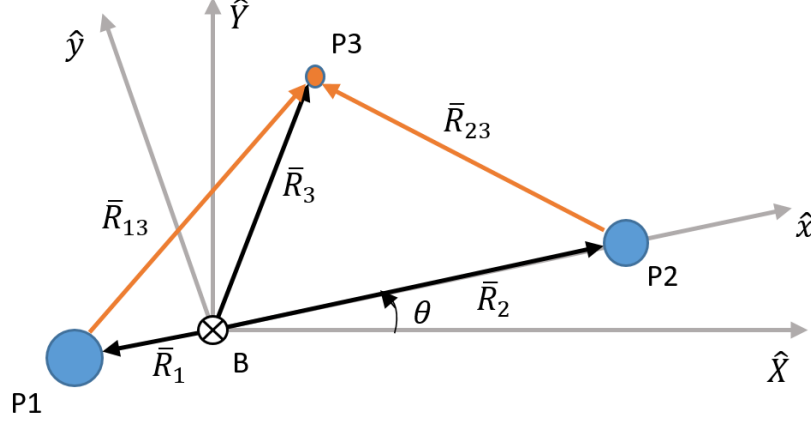
Figure 2.2. Three-body orientation in space.

2.1.2 Equations of Motion

Since the primaries move in a circular orbit about the barycenter observed in the inertial frame, the angular velocity of its motion is fixed. Let $\dot{\theta}$ represent the angular velocity or the mean motion. The motion of the primaries is defined in the inertial fixed frame as a function of time, t, as

$$\bar{R}_1 = R_1 \left[-cos(\dot{\theta}t)\hat{X} - sin(\dot{\theta}t)\hat{Y} \right] \tag{2.7}$$

$$\bar{R}_2 = R_2 \left[cos(\dot{\theta}t)\hat{X} + sin(\dot{\theta}t)\hat{Y} \right] \tag{2.8}$$

where $\bar{R}_1$ an $\bar{R}_2$ are the position vectors from the barycenter towards primaries P_1 and P_2 respectively. The magnitude of each of the vectors $\bar{R}_1$ and $\bar{R}_2$ are displayed as R_1 and R_2 respectively. In this investigation, non bold italicized letters represents the scalar magnitude of a quantity while the non bold italicized letters with a bar

sign on top represents the vector quantity. The position vector of the third body P_3 denoted by $\bar{R}_3$ is free to change in all three spatial directions. Computing the states $\bar{R}_3$ and $\dot{\bar{R}}_3$ in the inertial frame requires computation of the position and velocity states of the primaries at all times. A rotating coordinate frame, R, that moves along the primaries removes the necessity to evaluate the states of the primaries that are explicit functions of time. The energy of the system in the rotating frame, R, remains conserved as in the inertial frame, I. Define $\hat{x}, \hat{y}, \hat{z}$ as the unit vectors that define the rotational frame of reference, such that $\hat{x}$ gives the direction from Primary P_1 to P_2. $\hat{z}$ gives the direction of the angular momentum of the primaries aligned along the positive $\hat{Z}$ axis. $\hat{y}$ completes the right hand coordinate system.

To further generalize the equations for different three body systems and minimize the chances of round-off errors during numerical integration, all terms of the equations of motion are non-dimensionalized by corresponding characteristic quantities. All quantities of distance is reduced by characteristics length, all quantities of mass is reduced using characteristics mass and quantities of time with characteristic time. The characteristic length, l^*, is defined as the constant distance between the two primaries such as

$$l^* = R_1 + R_2, \tag{2.9}$$

the characteristic mass, m^*, is the total mass of the system given as

$$m^* = m_1 + m_2 \tag{2.10}$$

and the characteristic time is defined as the reciprocal of the mean motion,

$$t^* = 1/\dot{\theta} = \sqrt{l^{*3}/\tilde{G}m^*} \tag{2.11}$$

where the subscript 1 denotes the characteristic properties of primary P_1 while subscript 2 denotes properties of primary P_2. Let the system mass ratio, μ, be another defining quantity, given as,

$$\mu = \frac{m_2}{m_1 + m_2} = \frac{m_2}{m^*} \tag{2.12}$$

hence, $m_2 = \mu m^*$ and $m_1 = (1 - \mu)m^*$. The characteristic quantities and the system mass ratio are sufficient to portray the nature of a system. The circular restricted three body is therefore formulated in the non-dimensional units. The differential equation that governs the motion of body P_3 as given by equation (2.4), is non-dimensionalized as

$$\ddot{\bar{r}}_3 = \frac{1 - \mu}{r_{13}^3}\, \bar{r}_{13} + \frac{\mu}{r_{23}^3}\bar{r}_{23} \tag{2.13}$$

where $\bar{r}_3$ is now expressed in the rotational frame as $\bar{r}_3 = x\hat{x} + y\hat{y} + z\hat{z}$. The vectors $\bar{r}_{13}$ and $\bar{r}_{23}$ given as

$$\bar{r}_{13} = \bar{r}_3 - \bar{r}_1 = (x - \mu)\hat{x} + y\hat{y} + z\hat{z} \tag{2.14}$$

$$\bar{r}_{23} = \bar{r}_3 - \bar{r}_2 = (x - 1 + \mu)\hat{x} + y\hat{y} + z\hat{z} \tag{2.15}$$

depends on the location of the primaries along the $\hat{x}$ axis i.e. $\bar{r}_1 = -\mu\hat{x}$ and $\bar{r}_2 = (1 - \mu)\hat{x}$. The derivatives i.e. $\dot{\bar{r}}_3$ and $\ddot{\bar{r}}_3$ are with respect to non-dimensional time τ where $\tau = t/t^*$.

To formulate the equations of motion in the rotational frame, the derivative is taken in the rotational frame, R, with respect to an inertial frame, I. The Basic Kinematic equation (BKE) relates derivatives in the rotational frame to the inertial frame as

$$\frac{^I d\bar{r}_3}{d\tau} = \frac{^R d\bar{r}_3}{d\tau} + {}^I\omega^R \times \bar{r}_3 \tag{2.16}$$

where ${}^I\omega^R = \dot{\theta}\hat{z}$ gives the angular velocity of the rotational frame about $\hat{z}$ axis. The velocity of the body P_3 therefore becomes

$$\begin{aligned}
{}^I\dot{\bar{r}}_3 &= \dot{x}\hat{x} + \dot{y}\hat{y} + \dot{z}\hat{z} + [\dot{\theta}\hat{z}] \times [x\hat{x} + y\hat{y} + z\hat{z}] \\
&= (\dot{x} - \dot{\theta}y)\hat{x} + (\dot{y} + \dot{\theta}x)\hat{y} + \dot{z}\hat{z}
\end{aligned} \tag{2.17}$$

in the rotational frame, R. The second derivative of the position vector $\bar{r}_3$, yields

$$^I\ddot{\bar{r}}_3 = (\ddot{x} - 2\dot{\theta}\dot{y} - \dot{\theta}^2 x)\hat{x} + (\ddot{y} + 2\dot{\theta}\dot{x} - \dot{\theta}^2 y)\hat{y} + \ddot{z}\hat{z} \tag{2.18}$$

where $^I\ddot{r}_3$ is the instantaneous acceleration in the rotating frame. Substituting the equations, (2.14), (2.15) and (2.18) into equation (2.13) along with non-dimensional value of $\dot{\theta}$, that is 1 for CR3BP, yields three scalar equations of motion of P_3 purely in the rotational frame, R, given by

$$\ddot{x} - 2\dot{y} - x = -\frac{1-\mu}{d^3}(x + \mu) - \frac{\mu}{r^3}(x - 1 + \mu) \tag{2.19}$$

$$\ddot{y} + 2\dot{x} - y = -\frac{1-\mu}{d^3}y - \frac{\mu}{r^3}y \tag{2.20}$$

$$\ddot{z} = -\frac{1-\mu}{d^3}z - \frac{\mu}{r^3}z \tag{2.21}$$

such that,

$$d = r_{13} = \sqrt{(x + \mu)^2 + (y)^2 + (z)^2} \tag{2.22}$$

$$r = r_{23} = \sqrt{(x - 1 + \mu)^2 + (y)^2 + (z)^2} \tag{2.23}$$

where d represents the non-dimensional distance from P_3 to primary body P_1 and r represents the non-dimensional distance from P_3 to smaller primary body P_2.

2.1.3 Jacobi Constant

The conservation of energy does not hold true for a non inertial system. A similar quantity that is conserved in the rotational frame is of high significance. A *potential function (U)* represents the work done to displace a unit mass from infinity to that particular point. For CR3BP, this is given by,

$$U = \frac{1-\mu}{d} + \frac{\mu}{r} \tag{2.24}$$

such that, $\bar{\nabla}U_i = m_i\ddot{r}_i$ for a unit mass m_i. Similarly a *pseudo-potential function (U*)* is defined such that,

$$U^* = U + \frac{1}{2}\left(x^2 + y^2\right) = \frac{1-\mu}{d} + \frac{\mu}{r} + \frac{1}{2}\left(x^2 + y^2\right) \tag{2.25}$$

where U and U^* are both functions of only positions and give useful insights about the motion of the spacecrafts. The scalar equations of motion in equations (2.19), (2.20) and (2.21) when rendered as a function of pseudo-potential function, given by

$$\ddot{x} - 2\dot{y} = \frac{\partial U^*}{\partial x} \tag{2.26}$$

$$\ddot{y} + 2\dot{x} = \frac{\partial U^*}{\partial y} \tag{2.27}$$

$$\ddot{z} = \frac{\partial U^*}{\partial z} \tag{2.28}$$

indicates that the acceleration in the x and y directions as in equations (2.26) and (2.27) are decoupled from any out of plane components in the z direction. This implies that the xy planar motion evolves independently of the out of plane motion and vice-versa. Any motion in the orbit plane of primaries will remain in the same plane unless any out of plane maneuver is applied. Both U and U^* do not remain conserved in the rotational frame.

An energy integral is computed by integrating the dot product of the velocity and the acceleration components of the third body in motion due to the gravitational forces exerted on it by the two primaries. In the rotational frame, this is given by

$$\begin{aligned}
\dot{\vec{r}}_3 \cdot \ddot{\vec{r}}_3 &= [\dot{x}\hat{x} + \dot{y}\hat{y} + \dot{z}\hat{z}] \cdot [\ddot{x}\hat{x} + \ddot{y}\hat{y} + \ddot{z}\hat{z}] \\
&= \dot{x}\ddot{x} + \dot{y}\ddot{y} + \dot{z}\ddot{z} \\
&= \frac{\partial U^*}{\partial x}\dot{x} + \frac{\partial U^*}{\partial y}\dot{y} + \frac{\partial U^*}{\partial z}\dot{z} \\
&= \frac{\partial U^*}{\partial t}
\end{aligned} \tag{2.29}$$

which is the time derivative of the pseudo-potential function. The integration of the partials in equation (2.29) yields,

$$\dot{r}_3^2 = v^2 = 2U^* - C \qquad \rightarrow \qquad C = 2U^* - v^2 \tag{2.30}$$

here C is the constant of integration and v is the velocity of the third body P_3 in the rotating frame. The constant C, known as *Jacobi Constant* represents a conserved

energy-like quantity in the rotational frame. An increase in energy of the system relative to the rotating frame represents a decrease in the Jacobi constant and vice-versa. Jacobi constant has various uses in the circular restricted three body problem. It is used to determine accuracy of numerical integration by monitoring the change in the value of C, to manipulate change in energy required for transfers, to understand the energy limits of families of orbits and many more.

2.1.4 Equilibrium Solutions

Determining equilibrium solutions helps gain further insight into the CR3BP. The equilibrium solutions correspond to the positions where the third body, free from any initial acceleration or velocity remains stationary in the rotating frame for an indefinite period of time. This implies that all time derivatives are zero i.e. $\dot{x} = \dot{y} = \dot{z} = \ddot{x} = \ddot{y} = \ddot{z} = 0$. Substituting this relation into the equations (2.26)-(2.28) indicates that the gradient of pseudo-potential function is zero i.e. $\nabla U^* = 0$. Therefore, the equilibrium solutions are computed by solving the following factored equations

$$\frac{\partial U^*}{\partial x} = \frac{\partial U^*}{\partial y} = \frac{\partial U^*}{\partial z} = 0 \tag{2.31}$$

using numerical schemes. The equilibrium points are also commonly described as *Lagrange points* or *Libration points* (L_i). Each Libration point L_i is found by numerically solving the equation (2.31) that yields,

$$\frac{\partial U^*}{\partial x} = -\frac{1-\mu}{d_{L_i}^3}(x_{L_i} + \mu) - \frac{\mu}{r_{L_i}^3}(x_{L_i} - 1 + \mu) + x_{L_i} = 0 \tag{2.32}$$

$$\frac{\partial U^*}{\partial y} = -\frac{1-\mu}{d_{L_i}^3}y_{L_i} - \frac{\mu}{r_{L_i}^3}y_{L_i} + y_{L_i} = 0 \tag{2.33}$$

$$\frac{\partial U^*}{\partial z} = -\frac{1-\mu}{d_{L_i}^3}z_{L_i} - \frac{\mu}{r_{L_i}^3}z_{L_i} = 0 \tag{2.34}$$

where $d_{L_i}^3$ and $r_{L_i}^3$ are the distances from the libration point L_i to each of the two primaries while the coordinates of the equilibrium points are $(x_{L_i}, y_{L_i}, z_{L_i})$.

Each combination of $(x_{L_i}, y_{L_i}, z_{L_i})$ corresponds to one libration point. Equation (2.34) is satisfied with $z_{L_i} = 0$, thus all libration points lie in the orbit plane of the primaries. Similarly, $y_{L_i} = 0$, is a solution of equation (2.33), hence one or more equilibrium solutions exists on the x-axis given by $(x_{L_i}, 0, 0)$ that satisfies equation (2.32) as

$$-\frac{1-\mu}{|x_{L_i} + \mu|^3}(x_{L_i} + \mu) - \frac{\mu}{|x_{L_i} - 1 + \mu|^3}(x_{L_i} - 1 + \mu) + x_{L_i} = 0 \qquad (2.35)$$

but equation (2.35) has no closed form solution therefore roots are computed numerically that yields three real solutions. Imaginary solutions are neglected as physical locations cannot be represented by imaginary numbers. The three possible solutions of equation (2.35) are represented in terms of the displacement from the nearest primary using γ_i. Coordinates of the three collinear libration points are given as $(x_{L_i}, y_{L_i}, z_{L_i})$, such that,

$$L_1: \qquad (1 - \mu - \gamma_1, \quad 0, \quad 0) \qquad (2.36)$$

$$L_2: \qquad (1 - \mu + \gamma_2, \quad 0, \quad 0) \qquad (2.37)$$

$$L_3: \qquad (\quad -\mu - \gamma_3, \quad 0, \quad 0) \qquad (2.38)$$

where γ_i indirectly depends on the value of μ i.e. different values of γ_i for different three body systems. The values of γ_i is solved by iterating the equation (2.35) at each collinear L_i, specifically

$$-\frac{1-\mu}{(1-\gamma_1)^2} + \frac{\mu}{\gamma_1^2} + 1 - \mu - \gamma_1 = 0 \qquad (2.39)$$

$$-\frac{1-\mu}{(1+\gamma_2)^2} - \frac{\mu}{\gamma_2^2} + 1 - \mu + \gamma_2 = 0 \qquad (2.40)$$

$$\frac{1-\mu}{\gamma_3^2} + \frac{\mu}{(1+\gamma_3)^2} - \mu + \gamma_3 = 0 \qquad (2.41)$$

for different system mass ratio μ. Libration point L_1 lies between the two primaries, L_2 lies to the right of smaller primary while L_3 lies to the left of larger primary as shown in Figure 2.3. Each of the libration points are numbered congruent to the convention followed in most of the recent papers.

Besides the three collinear solution, two other equilibrium solutions exists in the CR3BP. Equations (2.32) and (2.33) are also satisfied simultaneously for $d = r = 1$ that completes the equilateral triangle with the distance between the primaries as the side of the equilateral triangle. This results in two equilibrium points on either side of the $x - z$ plane equidistant from both the primaries as shown in Figure 2.3. By virtue of their location, these points are denoted as triangular or equilateral Libration points. As per convention coordinates of the triangular libration points are

$$L_4: \qquad \left(\frac{1}{2} - \mu, \quad \frac{\sqrt{3}}{2}, \quad 0 \right) \qquad\qquad (2.42)$$

$$L_5: \qquad \left(\frac{1}{2} - \mu, \quad -\frac{\sqrt{3}}{2}, \quad 0 \right) \qquad\qquad (2.43)$$

where L_4 is located in the positive $\hat{y}$ region while L_5 is located in the negative $\hat{y}$ region.

2.1.5   Zero Velocity Curves

Within the CR3BP, the motion of P_3, under the influence of the two primary bodies, is bounded by the total energy it possesses. The value of the Jacobi Constant along with the equilibrium solutions renders the boundaries of motion. Equation (2.30), $v^2 = 2U^* - C$, leads to the conclusion that the velocity of P_3 will become imaginary if $C > 2U^*$ which is mathematically possible but physically absurd. The region where the velocity becomes imaginary is physically inaccessible hence it is termed as the forbidden region. The motion of the third body P_3 is confined within
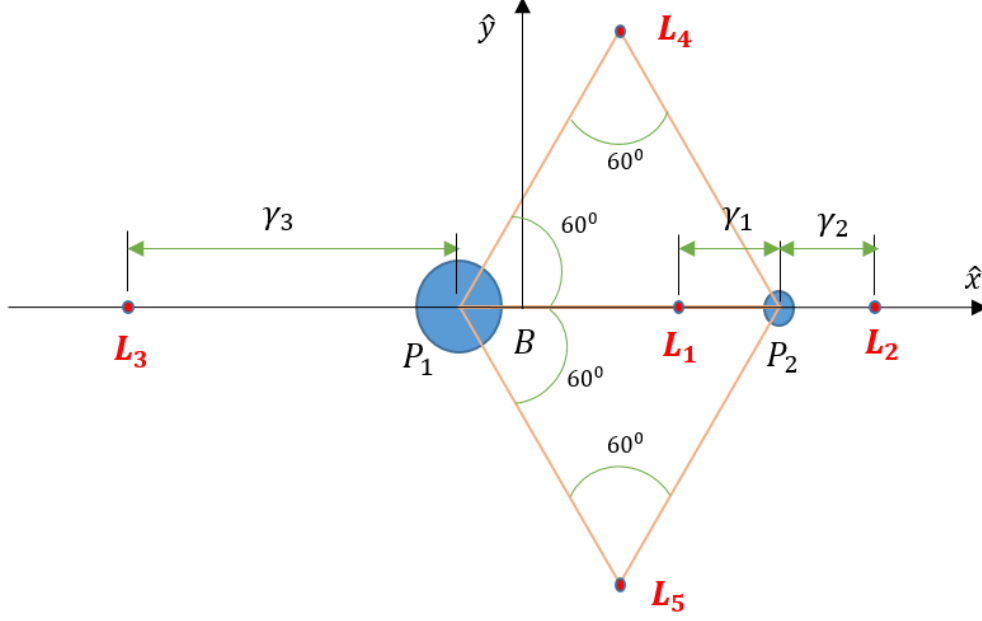
Figure 2.3. Equilibrium solutions in CR3BP.

the region where $C \leq 2U^*$. The boundary occurs where P_3 is theoretically stationary with zero velocity or

$$C = 2U^* = \frac{2(1-\mu)}{d} + \frac{2\mu}{r} + \left(x^2 + y^2\right) \tag{2.44}$$

where an infinitely many combinations of (x, y, z) satisfy the equation (2.44) generating a three-dimensional surface called the *Zero Velocity Surface (ZVS)*. An example of a ZVS in the Earth-Moon system is illustrated in Figure 2.4.

A two-dimensional curve formed out of cross section of the ZVS is called the *Zero Velocity Curves (ZVC)*. To examine a planar motion, a cross section of the Zero Velocity Surface is considered along the $x - y$ plane forming a Zero Velocity Curve representing the boundary for the planar motion.
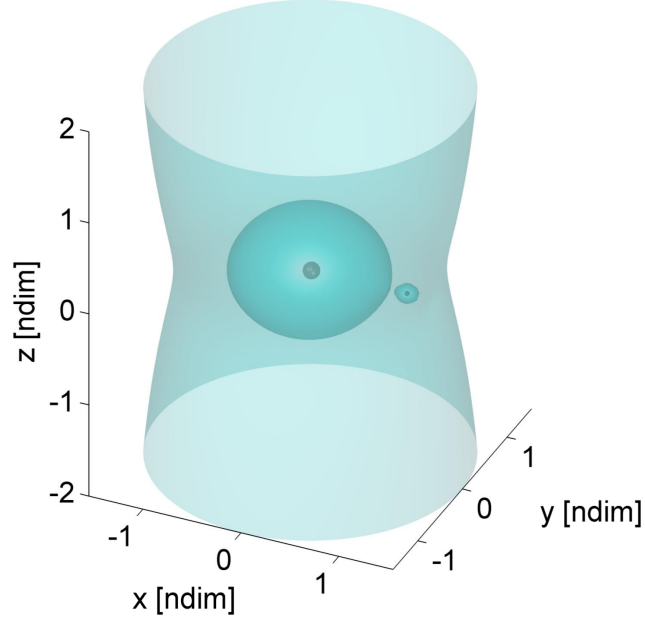
Figure 2.4. Zero Velocity Surface in the Earth-Moon system for $C = 3.2$. (Earth and Moon not to scale)

The Zero Velocity Curves for different energy levels (or different Jacobi values) decides the range P_3 can travel in the plane. Each equilibrium point corresponds to a Jacobi Value (C_{L_i}). As the ZVCs evolve for different Jacobi values, it becomes important to monitor the changes in the ZVCs as it crosses each C_{L_i}. Figure 2.5 illustrates the evolution of ZVCs for different Jacobi values in comparison to the Jacobi values at the Lagrange points mentioned as C_{L_i} for the Earth Moon (EM) system, and its impact on the accessible regions in space.

The Jacobi values at the Lagrange points, C_{L_i}, are critical factors that decide the shape of the ZVCs. The traits of the changing geometry is as explained

- $C_{L_1} < C$

  For an energy level less than at L_1 i.e. $C_{L_1} < C$, the third body P_3 is trapped in the vicinity of either one of the primary as indicated in Figure 2.5(a). If initially

(a) $C_{L_1} < C$

(b) $C_{L_2} < C < C_{L_1}$

(c) $C_{L_3} < C < C_{L_2}$

(d) $C_{L_{4,5}} < C < C_{L_3}$
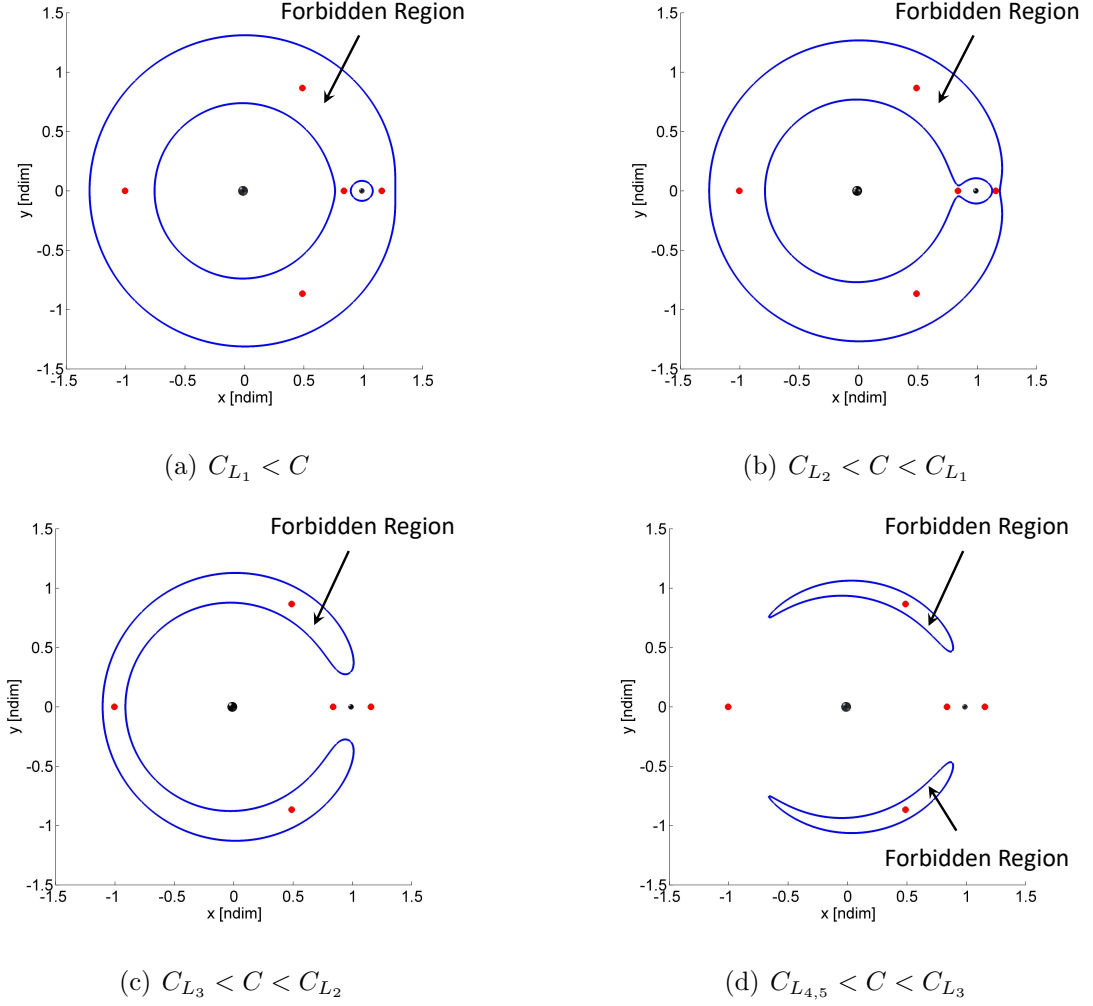
Figure 2.5. Zero Velocity Curves in the $x-y$ plane for different Jacobi values in the Earth-Moon (EM) system.

present near main primary then it continues to remain in the vicinity of the main primary. Similarly, if present near the second primary then it remains bounded near the second primary. The energy level is not enough to cross the forbidden region near the Lagrange point L_1 to travel from one primary body to the other.

- $C_{L_2} < C < C_{L_1}$

  For ZVCs with Jacobi values intermediate of the Jacobi at L_1 and L_2 it can be seen from Figure 2.5(b) that, a gateway opens up near L_1 connecting regions

near the two primaries. In this range of C, P_3 can pass from one primary to another, however, P_3 still does not possess enough energy to escape into outer space.

- $C_{L_3} < C < C_{L_2}$

  With increase in energy level more than L_2, gateway opens up near L_2 allowing P_3 to escape into outer space near the second primary. Forbidden region still persists towards the left of the main primary, thus access to outer space is possible only along the positive x direction.

- $C_{L_{4,5}} < C < C_{L_3}$

  The ZVC splits near L_3 at Jacobi level C_{L_3} opening gateway to outer space near L_3 as well. In this range of Jacobi values, P_3 has enough energy to move out of vicinity of both the primaries in either direction. The forbidden regions eventually contracts towards $L_{4,5}$.

- $C < C_{L_{4,5}}$

  For lower Jacobi values less than at $L_{4,5}$, the ZVC ceases to exist in the $x - y$ plane. This does not imply that P_3 is now free to move anywhere, it just means that it is free to move anywhere in the planar space and there are still out of plane regions that are inaccessible. It is important to note that at this range of Jacobi values the Zero Velocity Surface has split into two distinct surfaces at L_4 and L_5 and is now no longer single surface, unlike at lower energy levels. The two distinct Zero Velocity Surfaces continues to shrink with decrease in C values in the direction away from the principal plane of motion i.e. $x - y$ plane.

The Zero Velocity Surfaces provides practicable information especially for mission design. A maneuver is performed to increase the energy level to reach from one primary to another by opening a gateway near L_1, similarly a energy reducing maneuver can capture the spacecraft in the vicinity of the primaries by closing the gateways near L_1 and L_2.

2.2 Linearized Model

Any nonlinear system is difficult to analyze directly. A linearized model thus assists in understanding the behavior of the system in the local vicinity of equilibrium solutions. The behavior of certain states in the nonlinear system close to an already known solution is predicted using the linearized model without actually requiring to propagate the selected states. With the same intention the equations of motion of CR3BP is linearized about its equilibria.

2.2.1 Linearized Variational Equations of Motion

The motion in circular restricted three body problem is governed by coupled, second order non linear differential equations that does not have closed form analytical solution. Linearized solutions is generated near the equilibrium points to realize the local behavior. All the six states are perturbed about the equilibrium points to develop the linearized equations of motion. Let (x_{eq}, y_{eq}, z_{eq}) represent the position of the equilibrium points and (ξ, η, ζ) be the perturbations in $(\hat{x}, \hat{y}, \hat{z})$ directions respectively such that,

$$x = x_{eq} + \xi \tag{2.45}$$

$$y = y_{eq} + \eta \tag{2.46}$$

$$z = z_{eq} + \zeta \tag{2.47}$$

where (x, y, z) are the new states in the vicinity of the equilibrium points. For any state q, such that $q = q_{eq} + \delta q$, where δq is a small deviation from reference solution q_{eq}, the derivative is expressed as

$$\dot{q} = f(q, t) \tag{2.48}$$

which is approximated to the first order derivative term using Taylor Series. As a result, equation (2.48) becomes,

$$\dot{q}_{eq} + \dot{\delta q} \approx f(q_{eq} + \delta q, t) = f(q_{eq}, t) + \left. \frac{\partial f}{\partial q} \right|_{q_{eq}} dq + H.O.T.s \tag{2.49}$$

where, $H.O.T.s$ represents the higher order terms that are neglected here for approximating the integration to first order, assuming perturbations are very small. The first order approximation yields

$$\delta \dot{q} = \frac{\partial f}{\partial q}\bigg|_{q_{eq}} \delta q = A(t)\delta q \tag{2.50}$$

where $A(t)$ is known as the Jacobian Matrix and contains the partials of f with respect to state q. Using equation (2.50), the time derivatives of the position and velocity states near equilibrium points in CR3BP is also written in the same form,

$$\dot{x} = \dot{x}_{eq} + \dot{\xi} = \dot{\xi} \tag{2.51}$$

$$\dot{y} = \dot{y}_{eq} + \dot{\eta} = \dot{\eta} \tag{2.52}$$

$$\dot{z} = \dot{z}_{eq} + \dot{\zeta} = \dot{\zeta} \tag{2.53}$$

$$\ddot{x} = \ddot{x}_{eq} + \ddot{\xi} = \ddot{\xi} \tag{2.54}$$

$$\ddot{y} = \ddot{y}_{eq} + \ddot{\eta} = \ddot{\eta} \tag{2.55}$$

$$\ddot{z} = \ddot{z}_{eq} + \ddot{\zeta} = \ddot{\zeta} \tag{2.56}$$

since $[\dot{x}_{eq}, \dot{y}_{eq}, \dot{z}_{eq}, \ddot{x}_{eq}, \ddot{y}_{eq}, \ddot{y}_{eq}]^T = \bar{0}$, as the equilibrium points are stationary in CR3BP. The variational equations are developed by taking the derivatives of the equations (2.26), (2.27) and (2.28) and expressed in terms of pseudo potential function, U^*, as

$$\ddot{\xi} - 2\dot{\eta} = U_{xx}^*\xi + U_{xy}^*\eta + U_{xz}^*\zeta \tag{2.57}$$

$$\ddot{\eta} + 2\dot{\xi} = U_{yx}^*\xi + U_{yy}^*\eta + U_{yz}^*\zeta \tag{2.58}$$

$$\ddot{\zeta} = U_{zx}^*\xi + U_{zy}^*\eta + U_{zz}^*\zeta \tag{2.59}$$

where each $U_{ij}^* = \dfrac{\partial^2 U^*}{\partial i \partial j}$ are the second order partials of U^* with respect to the directions expressed as the subscripts. For each $i, j \in \{x, y, z\}$, the partials are expanded as

$$U_{xx}^* = 1 - \frac{1-\mu}{d^3} - \frac{\mu}{r^3} + \frac{3(1-\mu)(x+\mu)^2}{d^5} + \frac{3\mu(x-1+\mu)^2}{r^5} \tag{2.60}$$

$$U_{yy}^* = 1 - \frac{1-\mu}{d^3} - \frac{\mu}{r^3} + \frac{3(1-\mu)y^2}{d^5} + \frac{3\mu y^2}{r^5} \tag{2.61}$$

$$U_{zz}^* = -\frac{1-\mu}{d^3} - \frac{\mu}{r^3} + \frac{3(1-\mu)z^2}{d^5} + \frac{3\mu z^2}{r^5} \tag{2.62}$$

$$U_{xy}^* = \frac{3(1-\mu)(x+\mu)y}{d^5} + \frac{3\mu(x-1+\mu)y}{r^5} = U_{yx}^* \tag{2.63}$$

$$U_{xz}^* = \frac{3(1-\mu)(x+\mu)z}{d^5} + \frac{3\mu(x-1+\mu)z}{r^5} = U_{zx}^* \tag{2.64}$$

$$U_{yz}^* = \frac{3(1-\mu)yz}{d^5} + \frac{3\mu yz}{r^5} = U_{zy}^* \tag{2.65}$$

where d, r and μ retain their original definitions.

In CR3BP, the natural motion is represented by 6 state variables, $[\xi, \eta, \zeta, \dot{\xi}, \dot{\eta}, \dot{\zeta}]^T$. The linearized variational equations of motion are expressed in first order state space form as

$$\begin{pmatrix} \dot{\xi} \\ \dot{\eta} \\ \dot{\zeta} \\ \ddot{\xi} \\ \ddot{\eta} \\ \ddot{\zeta} \end{pmatrix} = \begin{bmatrix} 0 & 0 & 0 & 1 & 0 & 0 \\ 0 & 0 & 0 & 0 & 1 & 0 \\ 0 & 0 & 0 & 0 & 0 & 1 \\ U_{xx}^* & U_{xy}^* & U_{xz}^* & 0 & 2 & 0 \\ U_{yx}^* & U_{yy}^* & U_{yz}^* & -2 & 0 & 0 \\ U_{zx}^* & U_{zy}^* & U_{zz}^* & 0 & 0 & 0 \end{bmatrix} \begin{pmatrix} \xi \\ \eta \\ \zeta \\ \dot{\xi} \\ \dot{\eta} \\ \dot{\zeta} \end{pmatrix} \tag{2.66}$$

that is numerically integrated to determine the 6 states required to express the motion of a spacecraft uniquely. For ease of representation, if $\delta\bar{q}$ denotes the states $[\xi, \eta, \zeta, \dot{\xi}, \dot{\eta}, \dot{\zeta}]^T$, then $\delta\dot{\bar{q}} = A(t)\delta\bar{q}$ portrays equation (2.66), such that $A(t)$ is the 6x6 Jacobian matrix that is reduced to smaller 3x3 submatrices as,

$$A(t) = \begin{bmatrix} O_{3\times3} & I_{3\times3} \\ U_{XX} & \Omega_{3\times3} \end{bmatrix} \tag{2.67}$$

where O, I, U_{XX} and Ω are 3x3 submatrices of 6x6 Jacobian matrix in equation (2.66). Always, O denotes a zero matrix while I indicates an identity matrix.

2.2.2 Stability of the Equilibrium Points

The motion of the spacecraft in the vicinity of the equilibrium solutions can not be analyzed using linearized equations of motion unless the stability is properly defined. There are multiple ways to define the stability of a solution, of which the most suitable choice is made depending on the objective of the given problem. An equilibrium point is considered stable if, the motion of a particle that is subjected to any small perturbations remains bounded in the near neighborhood of the equilibrium point. The definition of the stability in this case is in lieu with Lyapunov Stability Criteria. Mathematically, an equilibrium point ψ_e is Lyapunov Stable if for all $\epsilon > 0$ there exists $\delta > 0$, such that if at time, $t = 0$, $||\psi(0) - \psi_e|| < \delta$, then for $t \geq 0$, $||\psi(t) - \psi_e|| < \epsilon$. Alternatively, if an initial perturbation δ is given about the equilibrium point then subsequent motion should remain bounded within a defined ϵ. Furthermore, the solution is said to be asymptotically stable if, the solution satisfies the Lyapunov Stability and, for an initial perturbation within some $\delta > 0$, i.e. at $t = 0$, $||\psi(0) - \psi_e|| < \delta$, there exists,

$$\lim_{t \to \infty} ||\psi(0) - \psi_e|| = 0 \tag{2.68}$$

indicating the convergent behavior.

The Lyapunov stability of a linearized system defined as, $\delta \dot{q} = A \delta \bar{q}$, is computed by inspecting the eigenvalues of the Jacobian Matrix A (assuming A constant). The eigenvalues λ_i are the roots of the characteristics equation of A for which the determinant $||\lambda I - A|| = 0$ is evaluated. A system is classified as unstable, marginally stable or asymptotically stable based on the eigenvalues. The criteria are

- **Unstable**: If at-least one of the eigenvalues have a positive real part i.e. $R(\lambda_i) > 0$, then the linearized system is unstable. The corresponding nonlinear system is also unstable.

- **Marginally Stable**: If all of the eigenvalues are purely imaginary i.e. $R(\lambda_i) = 0$, then the linearized system is marginally stable. A marginally stable linearized

system is bounded but not asymptotically stable. No conclusions can be made about the stability of the corresponding nonlinear system.

- **Asymptotically Stable**: If all of the eigenvalues have negative real part i.e. $R(\lambda_i) < 0$, then the linearized system is marginally stable. The corresponding nonlinear system is stable in the local vicinity.

The linearized equations of motion are computed about the equilibrium points to assess the stability. The equilibrium points computed in section 2.1.4 indicates that all of them lie in the plane of the primaries i.e. $z = 0$. Therefore, partials given in equations (2.64) and (2.65) becomes $U_{xz}^* = U_{yz}^* = U_{zx}^* = U_{zy}^* = 0$. The linearized equations in (2.57) - (2.59) are simplified to three equations

$$\ddot{\xi} - 2\dot{\eta} = U_{xx}^* \xi + U_{xy}^* \eta \tag{2.69}$$

$$\ddot{\eta} + 2\dot{\xi} = U_{yx}^* \xi + U_{yy}^* \eta \tag{2.70}$$

$$\ddot{\zeta} = U_{zz}^* \zeta \tag{2.71}$$

with fewer number of partials. The linearized equations of motion about the equilibrium solutions expressed in equations (2.69) - (2.71) indicates that the motion of spacecraft in the out of plane direction i.e. z direction given in (2.71) is decoupled from equations (2.69) and (2.70) that relate the inplane motion. Subsequently implying that the motion in the out of plane direction evolves independent of the motion in the plane of primaries.

The fact that equation (2.71) is decoupled from equations (2.69) and (2.70), the out of plane motion and the inplane motion are analyzed independently. For all equilibrium points, $U_{zz}^* < 0$, hence out of plane motion in the vicinity of all equilibrium points undergo simple harmonic motion like a spring mass system. Moreover, the eigenvalues $\lambda_z = \pm i\omega_z = \pm i\sqrt{|U_{zz}^*|}$, implying marginal stability with the frequency of out of plane motion given by $\omega_z = \sqrt{|U_{zz}^*|}$. For Lagrange points L_4 and L_5, the value

of $|U_{zz}^*| = 1$, i.e. $\omega_z = 1$, hence the period of out of plane motion $\mathbb{P} = 2\pi/\omega_z = 2\pi$ (in non-dimensional unit) which is same as the period of the primaries. For variational inplane motion about the equilibrium points the states are given by $\delta\bar{q} = [\xi, \eta, \dot{\xi}, \dot{\eta}]^T$ such that,

$$\delta\dot{\bar{q}} = A_{xy}\delta\bar{q} \tag{2.72}$$

$$A_{xy} = \begin{bmatrix} O_{2\times2} & I_{2\times2} \\ U_{XX,2\times2} & \Omega_{2\times2} \end{bmatrix} \tag{2.73}$$

where A_{xy} denotes the Jacobian matrix of the inplane motion, with submatrices as

$$U_{XX,2\times2} = \begin{bmatrix} U_{xx}^* & U_{xy}^* \\ U_{yx}^* & U_{yy}^* \end{bmatrix} \tag{2.74}$$

$$\Omega_{2\times2} = \begin{bmatrix} 0 & 2 \\ -2 & 0 \end{bmatrix} \tag{2.75}$$

while $O_{2\times2}$ is a 2×2 zero matrix and $I_{2\times2}$ is a 2×2 identity matrix. The eigenvalues of the inplane system near the equilibrium points are the roots of the characteristic equations given by determinant $||\lambda I - A_{xy}|| = 0$ i.e.

$$\lambda^4 + (4 - U_{xx}^* - U_{yy}^*)\lambda^2 + (-2U_{xy}^* + 2U_{yx}^*)\lambda + (U_{xx}^*U_{yy}^* - U_{xy}^*U_{yx}^*) = 0 \tag{2.76}$$

where the values U_{xx}^*, U_{xy}^* and U_{yx}^* are different for different equilibrium points. Consequently, each equilibrium point has different stability properties that are analyzed separately.

2.2.3 Motion near the Collinear Equilibrium Points

The collinear equilibrium points L_1, L_2 and L_3 lie along the x-axis, which simplifies the solution of the linearized model in their vicinity. Since $y_{L_i} = z_{L_i} = 0$, some of the terms in the linear variational equations of motion is nullified in the vicinity of the collinear Lagrange points i.e. $U_{xy}^* = U_{yx}^* = 0$. Thus, the characteristic equation for the inplane motion as in equation (2.76) simplifies to

$$\lambda^4 + (4 - U_{xx}^* - U_{yy}^*)\lambda^2 + (U_{xx}^* U_{yy}^*) = 0 \tag{2.77}$$

with fewer variable. The eigenvalues corresponding to the system are the roots of the characteristic equations that are given by,

$$\lambda_{1,2} = \pm\sqrt{-\beta_1 + (\beta_1^2 + \beta_2^2)^{1/2}} \tag{2.78}$$

$$\lambda_{3,4} = \pm\sqrt{-\beta_1 - (\beta_1^2 + \beta_2^2)^{1/2}} \tag{2.79}$$

where, for simplicity β_1 and β_2 are defined as

$$\beta_1 = 2 - \frac{U_{xx}^* + U_{yy}^*}{2} \tag{2.80}$$

$$\beta_2^2 = -U_{xx}^* U_{yy}^* \tag{2.81}$$

that are functions of pseudo-potential evaluated at corresponding equilibrium point L_i. Further, for additional simplicity, define

$$s = \sqrt{\beta_1 + (\beta_1^2 + \beta_2^2)^{1/2}} \tag{2.82}$$

$$\beta_3 = \frac{s^2 + U_{xx}^*}{2s} \tag{2.83}$$

as constants for representation. The analytical solution of variational equations in terms of position along x and y directions near the equilibrium points are expressed as

$$\xi = \sum_{i=1}^{4} A_i e^{\lambda_i t} \tag{2.84}$$

$$\eta = \sum_{i=1}^{4} B_i e^{\lambda_i t} \tag{2.85}$$

where A_i and B_i are coefficients corresponding to stimulated eigenvector with λ_i as the corresponding eigenvalue. Here, A_i and B_i are related to each other as

$$B_i = \alpha_i A_i \tag{2.86}$$

$$\alpha_i = \frac{\lambda_i^2 - U_{xx}^*}{2\lambda_i} \tag{2.87}$$

because of coupled xy motion. To expose the motion along a particular direction, the linearized variational model is excited along the corresponding eigenvector direction. It is important to note here that $\lambda_{3,4} = \pm is$ where s is as defined in equation (2.82) implying that $\lambda_{3,4}$ are purely imaginary indicating marginal stability, while $\lambda_{1,2}$ exists as positive and negative real pair. A periodic solution in the linearized system may exists only along the eigenvalues $\lambda_{3,4}$, demanding a suppression of eigenvalues $\lambda_{1,2}$ that can potentially destabilize the system due to its unstable component. Henceforth, conditions such that, $A_1 = A_2 = 0$ are set to modify equations (2.84) and (2.85) to

$$\xi = A_3 e^{\lambda_3 t} + A_4 e^{\lambda_4 t} \tag{2.88}$$

$$\eta = B_3 e^{\lambda_3 t} + B_4 e^{\lambda_4 t} = \alpha_3 A_3 e^{\lambda_3 t} + \alpha_4 A_4 e^{\lambda_4 t} \tag{2.89}$$

resulting in a solution may potentially be periodic in the vicinity of the collinear libration points. On evaluating, A_3 and A_4 in terms of $s, \alpha_3, \xi_0, \eta_0$, the analytical representation of the periodic behavior of the motion of the spacecraft in the vicinity of the collinear equilibrium points are given by

$$\xi = \xi_0 \cos(s(\tau - \tau_0)) + \frac{\eta_0}{\beta_3} \sin(s(\tau - \tau_0)) \tag{2.90}$$

$$\eta = \eta_0 \cos(s(\tau - \tau_0)) - \xi_0 \beta_3 \sin(s(\tau - \tau_0)) \tag{2.91}$$

$$\dot{\xi} = -\xi_0 s \sin(s(\tau - \tau_0)) + \frac{\eta_0}{\beta_3} s \cos(s(\tau - \tau_0)) \tag{2.92}$$

$$\dot{\eta} = -\eta_0 s \sin(s(\tau - \tau_0)) - \xi_0 \beta_3 s \sin(s(\tau - \tau_0)) \tag{2.93}$$

where, τ represents the non-dimensional time. The linearized variational equations of motion are developed given the initial positions (ξ_0, η_0) and velocity $(\dot{\xi}_0, \dot{\eta}_0)$ in the x and y directions respectively at initial non-dimensional time τ_0. The periodicity of formed orbit is given by

$$\mathbb{P} = \frac{2\pi}{s} \tag{2.94}$$

where, orbit time period $\mathbb{P}$ is expressed in non-dimensional time.

2.2.4 Motion near the Triangular Equilibrium Points

Similar to collinear equilibrium points, analytical linearized variational equations of motion are used to leverage the dynamics is close vicinity to the triangular equilibrium points. The out of plane motion is decoupled from the inplane motion and hence it evolves independently. As discussed in section 2.2.2, the period of out of plane motion is same as the period of the primaries about the barycenter. While, the inplane motion is represented by the characteristic equation given in equation (2.76). For equilibrium points L_4 and L_5, the partials of the pseudo-potential functions are evaluated as

$$U_{xx}^* = \frac{3}{4} \tag{2.95}$$

$$U_{yy}^* = \frac{9}{4} \tag{2.96}$$

$$U_{xy}^* = U_{yx}^* = \pm\frac{3\sqrt{3}}{2}\left(\mu - \frac{1}{2}\right) \tag{2.97}$$

where U_{xy}^* and U_{yx}^* is positive for L_4 and negative for L_5. On substituting these in equation (2.76), the characteristic equations for the inplane motion becomes,

$$\lambda^4 + \lambda^2 + \frac{27}{4}\mu\left(1 - \mu\right) = 0 \tag{2.98}$$

which is purely a function of the system mass ratio, μ. The roots of the characteristic equation are computed to be

$$\lambda_{1,2} = \pm\sqrt{\frac{1}{2}\left(-1 + \sqrt{g}\right)} \tag{2.99}$$

$$\lambda_{3,4} = \pm\sqrt{\frac{1}{2}\left(-1 - \sqrt{g}\right)} \tag{2.100}$$

such that,

$$g = 1 - 27\mu\left(1 - \mu\right) \tag{2.101}$$

is a constant value defined for simplicity.

The eigenvalues that determine the stability of the system depends on the value of g which is a function of mass ratio μ, hence stability characteristics of triangular libration points in different three body systems is different. The stability characteristics change at certain critical system mass ratios as explained.

- $0 < g < 1$ or $0 < \mu < 0.03852$

  On careful inspection, it is seen that for all values of $0 < \mu < 0.03852$, $\lambda_{1,2}$ and $\lambda_{3,4}$ are purely imaginary hence the motion of the third body about the triangular equilibrium points is periodic in linear sense. The eigenvalues are represented in terms of their frequencies i.e. $\lambda_{1,2} = \pm i\omega_1$ and $\lambda_{3,4} = \pm i\omega_2$, where ω_1 is the smaller frequency that corresponds to long period motion ($\mathbb{P} = 2\pi/\omega_1$) and ω_2 is the larger frequency that corresponds to short period motion ($\mathbb{P} = 2\pi/\omega_2$). The motion near the Lagrange points L_4 and L_5 are a linear combination of short period motion and long period motion. Stability in the nonlinear system is however not determined. This case is same as $0.96148 < \mu < 1$ except that the positions of the primaries bodies are interchanged.

- $g = 0$ or $\mu = 0.03852$

  At this critical mass ratio, $\lambda_{1,2} = \lambda_{3,4} = \pm \left(1/\sqrt{2}\right) i$, which means that one of the short period or long period motion is eliminated. Additionally in the linear model, repeated imaginary eigenvalues results in an unstable system.

- $g < 0$ or $0.03852 < \mu$

  For any three body system with mass ratio μ such that, $0.03852 < \mu$ (or $\mu < 1 - 0.03852 = 0.96148$), the eigenvalues exists in the form

$$\lambda_{1,2} = \pm\sqrt{\frac{1}{2}\left(-1 + \sqrt{g}\right)} = \pm\sqrt{\frac{1}{2}\left(-1 \pm i\delta\right)} \tag{2.102}$$

$$\lambda_{3,4} = \pm\sqrt{\frac{1}{2}\left(-1 - \sqrt{g}\right)} = \pm\sqrt{\frac{1}{2}\left(-1 \mp i\delta\right)} \tag{2.103}$$

where $\sqrt{g} = \pm i\delta$. The eigenvalues for this system exist in the form $\lambda_i = p + iq$, with two positive real and two negative real part, making the system unstable. Still, initial conditions can be wisely selected in the direction of eigenvectors corresponding to negative real eigenvalues to generate a linear model which would result in an asymptotically stable linear system in the local vicinity. This will result in the body undergoing a spiral motion eventually approaching the triangular equilibrium point.

- $g \geq 1$ or $\mu \leq 0$, $1 \leq \mu$

  Such mass ratio indicates negative mass for either of the primary body. Such system cannot exist physically.

2.3 Higher Fidelity Ephemeris Model

The circular restricted three body problem fundamentally captures details of the motion of the spacecraft due to gravitational interaction with two main primary bodies. The presence of other non finite gravitational bodies could substantially alter the motion of the spacecraft. The higher fidelity model is a more accurate representation of this complex dynamical regime, used to represent accurate trajectory designs and compute orbit maintenance costs with reduced errors. DE405 planetary ephemerides from NASA Jet Propulsion Laboratory (JPL) is used to identify the position and velocity of different celestial bodies used in simulating in the higher fidelity model. The inclusion of precise orbit eccentricities and inclination in the ephemeris model improves the authenticity of the solutions unlike in the lower fidelity CR3BP model where such parameters are either ignored or assumed constant.

2.3.1 n-body Dynamical Model

For improved accuracy, the governing equations of motion of the object of interest is derived in this n-body dynamical regime. The additional higher fidelity force terms enhances the solution over a restricted three body problem. The objective of this model is to study the motion of a body P_i in an n-body gravitational model. In section 2.1, the differential equations of motion of a n-body model were written with respect to an inertially fixed base point. Since the DE405 planetary ephemerides data provides relative location of a celestial body with respect to another, it is practically convenient to formulate the equations of motion with respect to a central body P_q as portrayed in Figure 2.6. The central body is denoted by subscript q, the object of interest or the spacecraft as i, while the remaining of the n bodies are labeled as j. $\bar{r}_{qi}$ represents the relative position of spacecraft with respect to the central body.
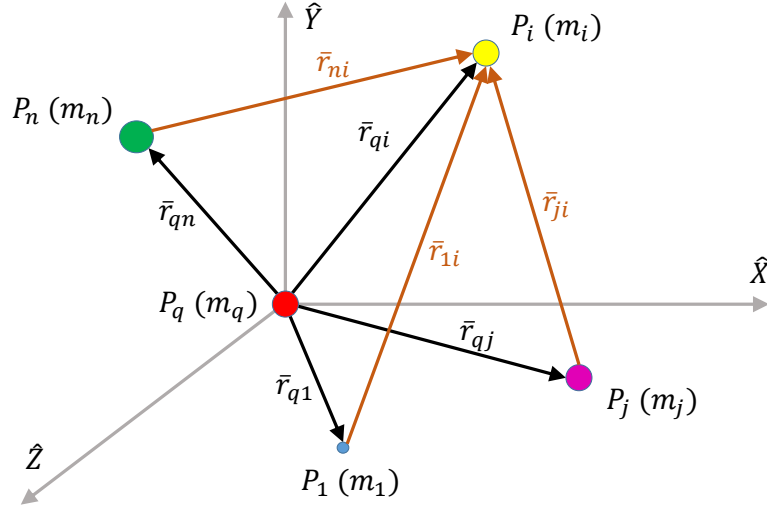
Figure 2.6. Geometry of the n-body problem.

The second order vector differential equation that governs the motion of the spacecraft with respect to the central body is derived upon the instantaneous position vectors $\bar{r}_{ij}$ and $\bar{r}_{qj}$, as demonstrated using the geometry in Figure 2.6, as

$$\ddot{\bar{r}}_{qi} = -\frac{\tilde{G}(m_i + m_q)}{r_{qi}^3}\bar{r}_{qi} - \tilde{G}\sum_{\substack{j=1 \\ j\neq i,q}}^{n} m_j \left(\frac{\bar{r}_{ij}}{r_{ij}^3} - \frac{\bar{r}_{qj}}{r_{qj}^3}\right) \tag{2.104}$$

where the vector $\bar{r}_{qj}$ is directly obtained from DE405 ephemerides data while the vector $\bar{r}_{ij}$ is obtained by vector operation i.e.

$$\bar{r}_{ij} = \bar{r}_{qj} - \bar{r}_{qi} \tag{2.105}$$

where the vector $\bar{r}_{qi}$ is the continuously monitored position of the spacecraft relative to the central body. Additionally, $\bar{r}_{ij} = -\bar{r}_{ji}$ denotes the relative location of the perturbing body P_j with respect to the body of interest P_i.

The n-body equation of motion as given in equation (2.104) is expressed in dimensional units, however for practical use and computational ease for numerical integration, the terms are non-dimensionalized using corresponding characteristic quantities of the most relevant CR3BP system. The accuracy of this model can be further improved by additional force models such as Solar Radiation Pressure, J2 perturbation etc. but it is beyond the scope of this work.

2.4 Coordinate Frame Transformations

The circular restricted three body problem is formulated in the coordinate frame that rotates along with the primaries. With respect to the inertial frame this frame appears to be rotating at the rate equal to the angular velocity of the primaries about its barycenter, hence, commonly denoted as rotating frame. The trajectory of the spacecraft with respect to the primaries may not be evident in the inertial frame, on contrary the ephemeris data is given in the inertial coordinate frame. From the designer's perspective it becomes necessary to transform from one coordinate frame to another to get useful information. The apparent motion in one frame may not reveal its behavior in the other frame, therefore, regardless of the frame in which the

trajectory is computed, for visual understanding coordinate transformation of the states becomes necessary.

2.4.1 Correlating the Inertial and Rotating Coordinate Frames

The most straight forward way of correlating states in one frame to another is using a transformation matrix that can be multiplied directly with the states in one frame to get the states in other frame. Figure 2.2 indicates the relation between the rotating frame and the inertial frame. The rotating coordinate frame, R, is indicated using unit vectors $\hat{x}, \hat{y}, \hat{z}$ (small letters) while the inertial coordinate frame, I, is indicated using unit vectors $\hat{X}, \hat{Y}, \hat{Z}$ (capital letters). The angle that relates frame R to frame I given by θ that is a function of non-dimensional time such that, $\theta = \dot{\theta}\tau = \tau$, as $\dot{\theta} = 1$ for CR3BP in non-dimensional units. The Direction Cosine Matrix (DCM) defined as $^IC^R$,

$$^IC^R = \begin{bmatrix} cos(\theta) & -sin(\theta) & 0 \\ sin(\theta) & cos(\theta) & 0 \\ 0 & 0 & 1 \end{bmatrix} \tag{2.106}$$

transforms the position states in the rotational frame to the inertial frame as

$$\begin{bmatrix} r_X \\ r_Y \\ r_Z \end{bmatrix} = {}^IC^R \begin{bmatrix} r_x \\ r_y \\ r_z \end{bmatrix} \tag{2.107}$$

where the superscript R on the right of $^IC^R$ indicates that the column vector of the states in rotating frame is multiplied to the DCM. Similarly, a direction cosine matrix $^RC^I$ is used to convert the states in inertial frame to rotating frame where $^RC^I = \left[{}^IC^R\right]^{-1}$.

Since velocity components are derivatives of position with respect to time the conversion from inertial frame to rotational frame requires an additional consideration. Either using the equation (2.16) or by taking the derivative of equation (2.107) with respect to non-dimensional time, the velocity between the two frames is related as

$$
\begin{bmatrix} v_X \\ v_Y \\ v_Z \end{bmatrix} = {}^I\dot{C}^R \begin{bmatrix} r_x \\ r_y \\ r_z \end{bmatrix} + {}^I C^R \begin{bmatrix} v_x \\ v_y \\ v_z \end{bmatrix} \tag{2.108}
$$

where ${}^I\dot{C}^R$ indicates derivative of each element of ${}^I C^R$ with respect to non-dimensional time. A combined, total transformation matrix is established that converts both the position and velocity states from the rotational frame to the inertial frame.

$$
\begin{bmatrix} r_X \\ r_Y \\ r_Z \\ x_X \\ x_Y \\ x_Z \end{bmatrix} = \begin{bmatrix} {}^I C^R & O_{3x3} \\ {}^I\dot{C}^R & {}^I C^R \end{bmatrix} \begin{bmatrix} r_x \\ r_y \\ r_z \\ v_x \\ v_y \\ v_z \end{bmatrix} \tag{2.109}
$$

where O_{3x3} is a 3×3 zero matrix. Similarly, full states from inertial frame can be converted to rotational frame using the inverse of 6×6 DCM used in equation (2.109).

2.4.2   Correlating the Inertial J2000 and Rotating Coordinate Frames

Transitioning from an Inertial J2000 frame to a rotating frame is comparable to the transformation in section 2.4.1 except that planetary ephemerides information is also incorporated while performing the transformation. Since the barycenter of the two main primary bodies P_1 and P_2 is not inertially fixed, it is not possible to introduce the rotation matrix with respect to the barycenter. Instead, it is convenient to convert to primary centered rotational frame about the main primary body P_1. The

instantaneous position and velocity of the smaller primary with respect to the main primary obtained from DE405 ephemerides data is used to convert the frame.

The rotating frame is derived from the available relative positions of primaries from the ephemerides data. Let the vector

$$\bar{R} = \bar{r}_{12} = \begin{bmatrix} r_X \\ r_Y \\ r_Z \end{bmatrix} \tag{2.110}$$

be the instantaneous position of smaller primary with respect to the main primary obtained from DE405 in the primary centered inertial frame. In a rotating frame the smaller primary is always directed to the positive x-axis of the rotating frame while z-axis corresponds to the direction of angular momentum and y-axis completes the dextral coordinate system. Using the same principle, the instantaneous rotating frame is defined as

$$\hat{x} = \frac{\bar{R}}{||\bar{R}||} \tag{2.111}$$

$$\hat{z} = \frac{\bar{R} \times \bar{V}}{||\bar{R} \times \bar{V}||} \tag{2.112}$$

$$\hat{y} = \hat{z} \times \hat{x} \tag{2.113}$$

where $\bar{R}$ and $\bar{V}$ are the instantaneous position and velocity vectors of smaller primary body P_2 with respect to the main primary P_1 expressed in the primary centered inertial J2000 frame. The instantaneous transformation matrix to convert position in primary centered rotational frame to inertial J2000 frame is given by

$$^{I}C^{R} = \begin{bmatrix} \hat{x} & \hat{y} & \hat{z} \end{bmatrix} = \begin{bmatrix} C_{11} & C_{12} & C_{13} \\ C_{21} & C_{22} & C_{23} \\ C_{31} & C_{32} & C_{33} \end{bmatrix} \tag{2.114}$$

where each C_{ij} represents the (i, j) term of the transformation matrix $^IC^R$. $^IC^R$ transforms the position of a body represented in the primary centered rotational frame to primary centered inertial J2000 frame as

$$
\begin{bmatrix} X_{PC} \\ Y_{PC} \\ Z_{PC} \end{bmatrix} = {}^IC^R \begin{bmatrix} x_{PC} \\ y_{PC} \\ z_{PC} \end{bmatrix}
\tag{2.115}
$$

such that, the subscript PC denotes that the vectors in rotational and inertial frame of reference are with respect to primary center.

Contradictory to the circular restricted three body problem, the angular velocity in an ephemeris model is not constant, instead, it is a time variant function. The instantaneous angular velocity defined as

$$
\dot{\theta} = \frac{h}{||\bar{R}||^2} = \frac{\bar{R} \times \bar{V}}{||\bar{R}||^2}
\tag{2.116}
$$

is used to relate the velocity of the object of interest in the primary centered rotating frame to primary centered inertial J2000 frame.

The Basic kinematic equation (BKE) is used to relate the velocity of the body of interest P_3 in the primary centered rotational frame to the velocity in the primary centered inertial frame. It is mathematically expressed as

$$
\frac{^Id\bar{r}_{13}}{d\tau} = \frac{^Rd\bar{r}_{13}}{d\tau} + {}^I\omega^R \times \bar{r}_{13}
\tag{2.117}
$$

where subscript 1 denotes the primary body. For simplicity, this is denoted as primary centered system where all measurements of the spacecraft are taken with respect to this primary body, hence, $\bar{r}_{PC} = \bar{r}_{13}$. Therefore, the Basic Kinematic equation is expressed alternatively as

$$
\frac{^Id\bar{r}_{PC}}{d\tau} = \frac{^Rd\bar{r}_{PC}}{d\tau} + {}^I\omega^R \times \bar{r}_{PC}
\tag{2.118}
$$

$$\frac{^{I}d\bar{r}_{PC}}{d\tau} = (\dot{x}_{PC} - \dot{\theta}y_{PC})\hat{x} + (\dot{y}_{PC} + \dot{\theta}x_{PC})\hat{y} + \dot{z}_{PC}\hat{z} \qquad (2.119)$$

where $^{I}\omega^{R} = \dot{\theta}\hat{z}$ represents the angular velocity of the instantaneous primary centered rotating frame to the primary centered inertial J2000 frame. Equation (2.119) is used to correlate velocity in the inertial frame to the position and velocity states in the primary centered rotational frame. When expressed in the matrix form equation (2.119) becomes

$$\begin{bmatrix} \dot{X}_{PC} \\ \dot{Y}_{PC} \\ \dot{Z}_{PC} \end{bmatrix} = \begin{bmatrix} \dot{\theta}C_{12} & -\dot{\theta}C_{11} & 0 & C_{11} & C_{12} & C_{13} \\ \dot{\theta}C_{22} & -\dot{\theta}C_{21} & 0 & C_{12} & C_{22} & C_{23} \\ \dot{\theta}C_{32} & -\dot{\theta}C_{31} & 0 & C_{13} & C_{32} & C_{33} \end{bmatrix} \begin{bmatrix} x_{PC} \\ y_{PC} \\ z_{PC} \\ \dot{x}_{PC} \\ \dot{y}_{PC} \\ \dot{z}_{PC} \end{bmatrix} \qquad (2.120)$$

where velocity states in inertial frame are now a function of both position and velocity states in the rotating frame. Combining equations (2.115) and (2.120) provides a 6×6 transformation matrix that converts the three position and three velocity states of the body of interest in primary centered rotational frame to primary centered inertial J2000 frame in one step i.e.

$$\begin{bmatrix} X_{PC} \\ Y_{PC} \\ Z_{PC} \\ \dot{X}_{PC} \\ \dot{Y}_{PC} \\ \dot{Z}_{PC} \end{bmatrix} = \begin{bmatrix} C_{11} & C_{12} & C_{13} & 0 & 0 & 0 \\ C_{12} & C_{22} & C_{23} & 0 & 0 & 0 \\ C_{13} & C_{32} & C_{33} & 0 & 0 & 0 \\ \dot{\theta}C_{12} & -\dot{\theta}C_{11} & 0 & C_{11} & C_{12} & C_{13} \\ \dot{\theta}C_{22} & -\dot{\theta}C_{21} & 0 & C_{12} & C_{22} & C_{23} \\ \dot{\theta}C_{32} & -\dot{\theta}C_{31} & 0 & C_{13} & C_{32} & C_{33} \end{bmatrix} \begin{bmatrix} x_{PC} \\ y_{PC} \\ z_{PC} \\ \dot{x}_{PC} \\ \dot{y}_{PC} \\ \dot{z}_{PC} \end{bmatrix} \qquad (2.121)$$

where the transformation matrix is a function of C_{ij} obtained from equation (2.114) and $\dot{\theta}$ obtained from equation (2.116). Since the bottom left 3×3 matrix is dimensional due to the presence of $\dot{\theta}$ that is measured in rad/s, the entire transformation is done

in the dimensional units. Once transformed, the vectors is non-dimensionalized for convenience. Similar to the transformation procedure in the circular restricted model, the states in primary centered J2000 inertial frame can be converted to primary centered rotational frame by taking the inverse of the transformation matrix.

3. DYNAMICAL SYSTEMS THEORY

From the mission perspective, it is vital to deduce an initial condition that drives the spacecraft to the desired final states. The nonlinear equations of motion of the Circular Restricted Three Body Problem does not provide the observability to estimate the initial state to reach a particular target. The desired final state may be close to observed final state along any baseline trajectory. The initial conditions can be modified in infinite ways out of which only one true initial condition would drive to the target, thus it is highly unlikely that a chosen starting condition drives to the desired end. The Dynamical Systems theory provides intuitive schemes to predict the right conditions that leads to the desired final states.

3.1   State Transition Matrix

The *State Transition Matrix (STM)* is a linear operator that correlates the initial variation about the baseline solution to the variation at the end. It is a fundamental tool that predicts the changes in states at the final time due to certain minute changes in initial condition contemplated in the linear sense. Similar to linearizing the nonlinear equations of motions of CR3BP about its equilibria, linearization is exercised along a fixed baseline/reference trajectory using Taylor series expansion to develop the State Transition Matrix.

The State Transition Matrix is formulated by considering the flow of a trajectory nearby a reference trajectory. Let the reference trajectory be represented by the asterisks(*) symbol, the initial initial state vector $\bar{x}_0^*$ is propagated for time, t, to a final state $\bar{x}^*(t)$. Let a nearby varied trajectory, with isochronous correspondence, be obtained by perturbing the initial states of the reference trajectory and propagating

for the same time, t, as demonstrated in Figure 3.1. Let the initial condition of the perturbed solution be denoted by

$$\bar{x}_0 = \bar{x}_0^* + \delta\bar{x}_0 \tag{3.1}$$

where $\delta\bar{x}_0$ is the small perturbation applied at the initial time. The new initial condition drives the solution to a new final state $\bar{x}(\bar{x}_0, t)$ such that,

$$\bar{x}(\bar{x}_0, t) = \bar{x}^*(\bar{x}_0^*, t) + \delta\bar{x}(t) \tag{3.2}$$

where $\delta\bar{x}(t)$ is the small variation about the reference solution at time, t, while the elements within the brackets, $(\bar{x}_0, t)$ and $(\bar{x}_0^*, t)$ are the initial state vector they were propagated from, and the time of propagation. Since $\bar{x}_0 = \bar{x}_0^* + \delta\bar{x}_0$, equation (3.2) becomes,

$$\bar{x}(\bar{x}_0^* + \delta\bar{x}_0, t) = \bar{x}^*(\bar{x}_0^*, t) + \delta\bar{x}(t) \tag{3.3}$$

where all the vectors are presented purely in terms of states of the nearby reference solution and the corresponding perturbation at anytime t. First order Taylor expansion applied to equation (3.3) as

$$\bar{x}^*(\bar{x}_0^*, t) + \frac{\partial\bar{x}}{\partial\bar{x}_0}\delta\bar{x}_0 + H.O.T.s = \bar{x}^*(\bar{x}_0^*, t) + \delta\bar{x}(t) \tag{3.4}$$

to compute the linear State transition Matrix. Since approximation only up to first oder is required, the higher order terms $H.O.T.s$ are neglected to yield

$$\frac{\partial\bar{x}}{\partial\bar{x}_0}\delta\bar{x}_0 \approx \delta\bar{x}(t) \tag{3.5}$$

where the partial $\frac{\partial\bar{x}}{\partial\bar{x}_0}$ is the $n \times n$ sensitivity matrix or the State Transition Matrix which is a linear correlation between the initial variation to the variation at the final time computed along some baseline trajectory. The perturbation vectors $\delta\bar{x}_0$ and $\delta\bar{x}(t)$ are $n \times 1$ matrices that relates to the variation in the n states measured along the reference trajectory at initial time t_0 and final time t respectively.
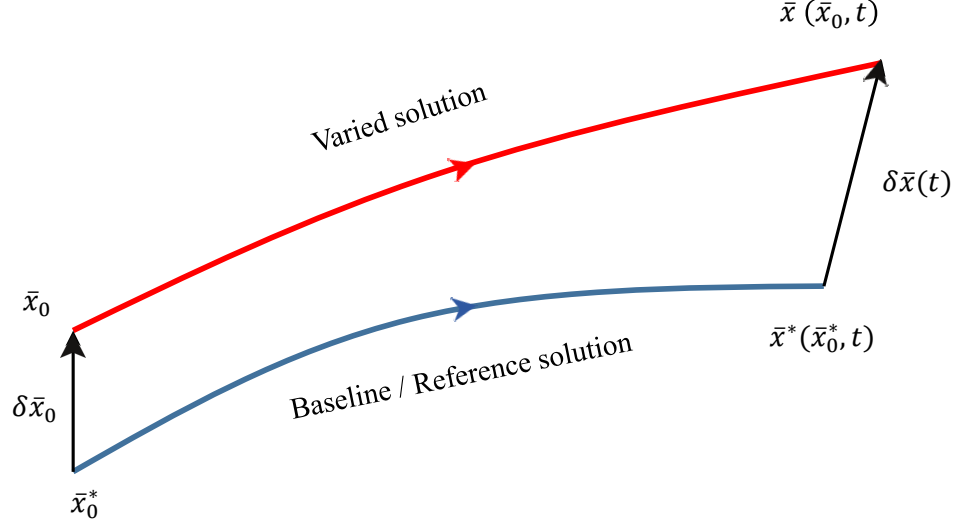
Figure 3.1. Baseline/Reference solution and isochronous variation.

Specifically for the circular restricted three body problem where there are 6 states inclusive of 3 position and 3 velocity states, the State Transition Matrix is of the size 6×6. The partials in the STM is calculated by propagating the states along the reference orbit for time, t, as

$$\phi(t, t_0) = \frac{\partial \bar{x}(t)}{\partial \bar{x}_0} = \begin{bmatrix} \frac{\partial x}{\partial x_0} & \frac{\partial x}{\partial y_0} & \frac{\partial x}{\partial z_0} & \frac{\partial x}{\partial \dot{x}_0} & \frac{\partial x}{\partial \dot{y}_0} & \frac{\partial x}{\partial \dot{z}_0} \\ \frac{\partial y}{\partial x_0} & \frac{\partial y}{\partial y_0} & \frac{\partial y}{\partial z_0} & \frac{\partial y}{\partial \dot{x}_0} & \frac{\partial y}{\partial \dot{y}_0} & \frac{\partial y}{\partial \dot{z}_0} \\ \frac{\partial z}{\partial x_0} & \frac{\partial z}{\partial y_0} & \frac{\partial z}{\partial z_0} & \frac{\partial z}{\partial \dot{x}_0} & \frac{\partial z}{\partial \dot{y}_0} & \frac{\partial z}{\partial \dot{z}_0} \\ \frac{\partial \dot{x}}{\partial x_0} & \frac{\partial \dot{x}}{\partial y_0} & \frac{\partial \dot{x}}{\partial z_0} & \frac{\partial \dot{x}}{\partial \dot{x}_0} & \frac{\partial \dot{x}}{\partial \dot{y}_0} & \frac{\partial \dot{x}}{\partial \dot{z}_0} \\ \frac{\partial \dot{y}}{\partial x_0} & \frac{\partial \dot{y}}{\partial y_0} & \frac{\partial \dot{y}}{\partial z_0} & \frac{\partial \dot{y}}{\partial \dot{x}_0} & \frac{\partial \dot{y}}{\partial \dot{y}_0} & \frac{\partial \dot{y}}{\partial \dot{z}_0} \\ \frac{\partial \dot{z}}{\partial x_0} & \frac{\partial \dot{z}}{\partial y_0} & \frac{\partial \dot{z}}{\partial z_0} & \frac{\partial \dot{z}}{\partial \dot{x}_0} & \frac{\partial \dot{z}}{\partial \dot{y}_0} & \frac{\partial \dot{z}}{\partial \dot{z}_0} \end{bmatrix} \tag{3.6}$$

where $[x, y, z, \dot{x}, \dot{y}, \dot{z}]^T$ are the final states along the reference orbit propagated from $[x_0, y_0, z_0, \dot{x}_0, \dot{y}_0, \dot{z}_0]^T$. At time $t = t_0$, since the initial and final states along the reference trajectory is the same, the STM $\phi(t_0, t_0) = I_{6 \times 6}$, a six-dimensional identity matrix, mathematically this describes the derivative of the initial states with respect

to itself. The 6×6 STM can be written in a more compact form, by collectively representing the position states r and velocity states v as

$$\phi(t, t_0) = \begin{bmatrix} \phi_{rr} & \phi_{rv} \\ \phi_{vr} & \phi_{vv} \end{bmatrix} \tag{3.7}$$

where ϕ_{rr} is the partial of final position states to initial position states, ϕ_{rv} relates final velocity states to initial position states, ϕ_{vr} relates final position states to initial velocity states and finally ϕ_{vv} is the partial of final velocity states to initial velocity states.

To perform certain conditions, state correction process is performed with the help of STM information. The partials of the state transition matrix is also integrated numerically along with the equations of motion in the CR3BP model, and in higher fidelity model. The differential equations that govern the partials of the STM are

$$\dot{\phi}(t, t_0) = \frac{d}{dt} \frac{\partial \bar{x}}{\partial \bar{x}_0} = \frac{\partial \dot{\bar{x}}}{\partial \bar{x}_0} \tag{3.8}$$

that is essentially the partials of the derivative of the final states with respect to the initial states. From equation (2.50), $\dot{\bar{x}} = A(t)\bar{x}$, hence equation (3.8) is reduced to

$$\dot{\phi}(t, t_0) = \frac{\partial A(t)\bar{x}}{\partial \bar{x}_0} = A(t) \frac{\partial \bar{x}}{\partial \bar{x}_0} \tag{3.9}$$

$$\dot{\phi}(t, t_0) = A(t)\phi(t, t_0) \tag{3.10}$$

that produces a 6×6 matrix $\dot{\phi}(t, t_0)$, producing 36 scalar partial differential equations. Combined with the 6 equations of motion, a total of 42 partial differential equations are numerically propagated to get the time history of the actual states and the partials of the final states with respect to the initial states.

The State Transition matrix being a linear operator, the accuracy substantially depends on the initial variation, that is expected to be small. A large initial variation may amplify the error in the final solution as the linear STM may no longer be capable

of accurately predicting the flow. In general, when predicting the desired initial or final states, the baseline trajectory is updated continuously to minimize variation every successive step. The accuracy of the STM increases as variation diminishes. The same principal concept is applied in the Differential Correction process

3.2 Differential Correction Process

Targeting a desired state is one of the most sought after tasks especially for trajectory design and optimization. Differential correction process is a scheme that facilitates targeting certain final conditions. Since STM is a linear operator that estimates the final variation due to some initial variation about a baseline solution, Differential Correction process involving the State Transition Matrix is exploited to target the required end conditions for trajectory design in the CR3BP. Finally, an iterative process is applied till demanded tolerance is reached.

Several schemes are available for implementing the Differential Correction Process. Throughout this work, the method of free variables and constraints as carried out by many other researchers have been used [56], [57], [58]. This method employs the Newton-Raphson approximation technique which uses the truncated Taylor expansion to the first order [59]. The method is formulated by considering a design variable vector $\bar{X}$ with n free variables which are subjected to updates. Vector $\bar{X}$ is defined as a column vector

$$\bar{X} = \begin{bmatrix} X_1 \\ X_2 \\ \vdots \\ X_n \end{bmatrix} \tag{3.11}$$

where X_1, X_2, ... , X_n may be position states, velocity states, time and/or any other relevant design variables. The constraint vector $\bar{F}(\bar{X})$ defined as a column vector

$$\bar{F}(\bar{X}) = \begin{bmatrix} F_1(\bar{X}) \\ F_2(\bar{X}) \\ \vdots \\ F_m(\bar{X}) \end{bmatrix} \tag{3.12}$$

is subjected to m different constraints $F_1(\bar{X})$, $F_2(\bar{X})$ through $F_m(\bar{X})$ which may be combination of continuity constraints, altitude constraints, energy constraint or any other user defined constraint that are a function of the defined state variables $\bar{X}$. Taylor series expansion of $\bar{F}(\bar{X})$ with free variable at initial time $\bar{X}_0$ results in

$$\bar{F}(\bar{X}) = \bar{F}(\bar{X}_0) + D\bar{F}(\bar{X}_0)\left(\bar{X} - \bar{X}_0\right) + H.O.T.s \tag{3.13}$$

where the higher order terms, $H.O.T.s$, are neglected as Newton-Raphson method truncates the Taylor series expansion to only the first order term. Additionally, the aim of this method is to update the free design variable till $\bar{X}$ drives the constraint vector $\bar{F}(\bar{X}) = 0$. Hence equation (3.13) reduces to

$$\bar{0} \approx \bar{F}(\bar{X}_0) + D\bar{F}(\bar{X}_0)\left(\bar{X} - \bar{X}_0\right) \tag{3.14}$$

where $D\bar{F}(\bar{X}_0)$ is the Jacobian matrix of size $m \times n$ as

$$D\bar{F}(\bar{X}_0) = \frac{\partial \bar{F}(\bar{X}_0)}{\partial \bar{X}_0)} = \begin{bmatrix} \frac{\partial F_1}{\partial X_1} & \cdots & \frac{\partial F_1}{\partial X_n} \\ \vdots & \ddots & \vdots \\ \frac{\partial F_m}{\partial X_1} & \cdots & \frac{\partial F_m}{\partial X_n} \end{bmatrix} \tag{3.15}$$

that consists of the first order partials of each of the constraint vector F_i with respect to each of the state variables X_j, such that $i \in \{1, ..., m\}$ and $j \in \{1, ..., n\}$.

For a linear problem a single step would have been suffice for Differential correction process to update the free design vector that would drive the constraint vector to zero, however, for a nonlinear problem, iterative approach is applied to drive the constraint vector below the specified tolerance level. The updated design variable after every

successive iteration is used as the new initial condition for the baseline solution upon which the Newton's method is applied again. To incorporate the iterative strategy equation (3.14) is modified to

$$\bar{F}(\bar{X}_j) + D\bar{F}(\bar{X}_j)\left(\bar{X}_{j+1} - \bar{X}_j\right) = \bar{0} \tag{3.16}$$

where j is the number of iterations performed and $\bar{X}_{j+1}$ is the updated free variable after jth iteration that serves as the initial condition for the updated baseline solution. If the number of design variables n and number of constraints m are equal i.e $n = m$, then a unique solution exists for $\bar{X}_{j+1}$,

$$\bar{X}_{j+1} = \bar{X}_j - \left[D\bar{F}(\bar{X}_j)\right]^{-1}\bar{F}(\bar{X}_j) \tag{3.17}$$

such that, $\left[D\bar{F}(\bar{X}_j)\right]^{-1}$ is perfectly invertible. If there are more design variables than the number of constraints i.e. $n > m$ the system is under-determined, infinitely many solutions exits. A potential solution,

$$\bar{X}_{j+1} = \bar{X}_j - D\bar{F}(\bar{X}_j)^T\left[D\bar{F}(\bar{X}_j)\ D\bar{F}(\bar{X}_j)^T\right]^{-1}\bar{F}(\bar{X}_j) \tag{3.18}$$

is computed using minimum norm solution. On the contrary, if there are less design variables than the number of constraints i.e. $n < m$ the system is over-determined, no solutions exits. Using the least squares approach, a conceivable solution is computed as

$$\bar{X}_{j+1} = \bar{X}_j - \left[D\bar{F}(\bar{X}_j)^T\ D\bar{F}(\bar{X}_j)\right]^{-1}D\bar{F}(\bar{X}_j)^T\bar{F}(\bar{X}_j) \tag{3.19}$$

that produces the minimum error. Least squares approach is used in several other places such as curve fitting and optimization where errors are to be minimized. Using the Newton's method, the solutions are likely to converge every successive iteration and is continued till required tolerance is achieved.

3.3 Single Shooting

The State Transition Matrix is utilized to achieve various end conditions in the CR3BP. As its name suggests, Single shooting technique implies correcting a single

reference transfer arc to target a predefined end condition. Since the STM is not self-starting, a baseline solution is generated upon some initial conditions over which the STM is computed and single shooting algorithm is applied. The technique is illustrated in detail involving a fixed time target and a variable time target scheme.

3.3.1 Fixed Time Position Target

The most common application of Single shooting technique involving the STM in CR3BP is to target a desired position from an initial location. As in Figure 3.2, let the initial position be defined as $\bar{r}_0$ and the predefined target position be $\bar{r}_d$. The initial velocity $\bar{v}_{old}$ drives the reference trajectory to final position $\bar{x}$ at time T. Since this is a fixed time position target, the desired trajectory should take exactly 'T' time to travel from $\bar{r}_0$ to $\bar{r}_d$ with no constraint on the arrival velocity at the target location. The initial position $\bar{r}_0$ being fixed, the aim is to determine the required change in velocity components i.e. Δv maneuver required to achieve $\bar{r}_d$ at time T.

To apply the Differential Correction scheme, free variables and constraints have to be defined distinctly. Let the free design variables be expressed as the three initial velocity components i.e.

$$\bar{X} = \begin{bmatrix} \dot{x}_0 \\ \dot{y}_0 \\ \dot{z}_0 \end{bmatrix} \tag{3.20}$$

that will change over every iteration till it drives to desired state $\bar{r}_d$ at time T with some tolerance. Here, $\bar{r}_d = [x_d, y_d, z_d]^T$. Similarly, the constraint vector $\bar{F}(\bar{X})$,

$$\bar{F}(\bar{X}) = \begin{bmatrix} x(T) - x_d \\ y(T) - y_d \\ z(T) - z_d \end{bmatrix} \tag{3.21}$$

is defined as the difference between the positions at the end of the reference trajectory
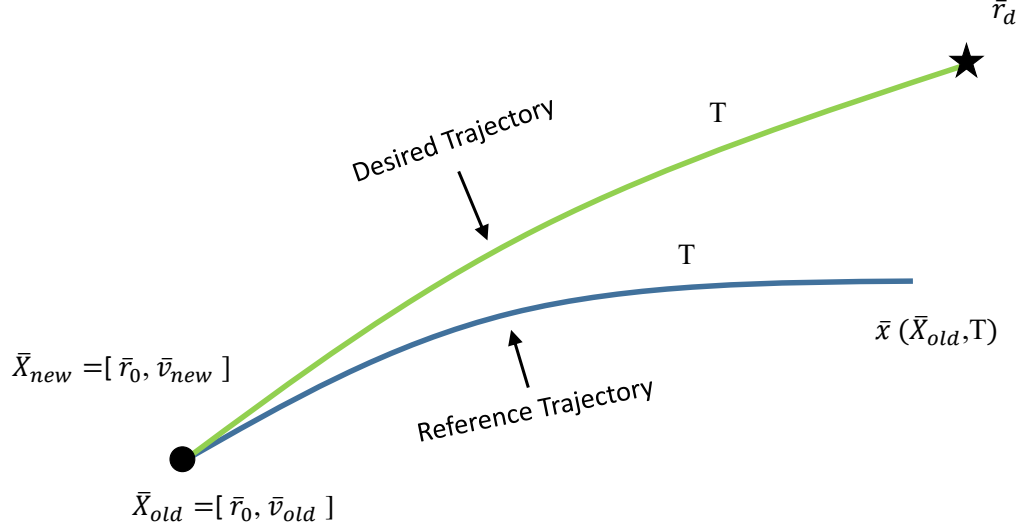
Figure 3.2. Single shooting technique with fixed time position target.

and the desired state. As the solution approaches the desired solution, $\bar{F}(\bar{X})$ tends to zero. The corresponding Jacobian matrix for the fixed time position target is

$$
D\bar{F}(\bar{X}) = \begin{bmatrix} \frac{\partial F_1}{\partial X_1} & \frac{\partial F_1}{\partial X_2} & \frac{\partial F_1}{\partial X_3} \\ \frac{\partial F_2}{\partial X_1} & \frac{\partial F_2}{\partial X_2} & \frac{\partial F_2}{\partial X_3} \\ \frac{\partial F_3}{\partial X_1} & \frac{\partial F_3}{\partial X_2} & \frac{\partial F_3}{\partial X_3} \end{bmatrix} = \begin{bmatrix} \frac{\partial x(T)}{\partial \dot{x}_0} & \frac{\partial x(T)}{\partial \dot{y}_0} & \frac{\partial x(T)}{\partial \dot{z}_0} \\ \frac{\partial y(T)}{\partial \dot{x}_0} & \frac{\partial y(T)}{\partial \dot{y}_0} & \frac{\partial y(T)}{\partial \dot{z}_0} \\ \frac{\partial z(T)}{\partial \dot{x}_0} & \frac{\partial z(T)}{\partial \dot{y}_0} & \frac{\partial z(T)}{\partial \dot{z}_0} \end{bmatrix} \tag{3.22}
$$

where the partials for $D\bar{F}(\bar{X})$ constitute the STM defined in equation (3.6), therefore

$$
D\bar{F}(\bar{X}) = \begin{bmatrix} \phi_{14} & \phi_{15} & \phi_{16} \\ \phi_{24} & \phi_{25} & \phi_{26} \\ \phi_{34} & \phi_{26} & \phi_{36} \end{bmatrix} \tag{3.23}
$$

where each ϕ_{ij} corresponds to the element in the ith row and jth column of the 6×6 STM. Here, $D\bar{F}(\bar{X})$ is same as the ϕ_{vr} matrix defined in equation (3.7). Once the free design vector $\bar{X}$, constraint vector $\bar{F}(\bar{X})$ and the Jacobian matrix $D\bar{F}(\bar{X})$ is defined,

the Newton's equation is applied to find the required update. In this case, the number of variables and the number of constraints are equal hence a unique solution exists. The appropriate update to the reference solution is computed as $\delta\bar{X}$,

$$\delta\bar{X} = -[D\bar{F}(\bar{X})]^{-1}\bar{F}(\bar{X}) \tag{3.24}$$

from equation (3.17). After every successive iteration, the reference solution is updated as

$$\bar{X}_{j+1} = \bar{X}_j + \delta\bar{X} \tag{3.25}$$

till the desired tolerance level is attained. The Differential Correction process computes variation using linear approximation while CR3BP is a nonlinear problem, therefore no matter how many iterations are performed, the reference trajectory will never be exactly equal to the desired solution. With every successful iteration, constraint vector $\bar{F}(\bar{X})$ diminishes hence the numerical process can be terminated once the norm $||\bar{F}(\bar{X})||$ is within the permissible tolerance.

3.3.2   Variable Time Position Target

Unlike for fixed time position target, as shown in Figure 3.3, the time of flight from the initial position to the desired position is not constrained to be the same as the time of flight of the reference trajectory, hence this is a variable time position target problem. The method only tries to find one possible trajectory that satisfies both the initial and final position states.

For any targeting scheme, free variables and constraints are to be defined appropriately. The time of flight T becomes an additional design variable hence,

$$\bar{X} = \begin{bmatrix} \dot{x}_0 \\ \dot{y}_0 \\ \dot{z}_0 \\ T \end{bmatrix} \tag{3.26}$$
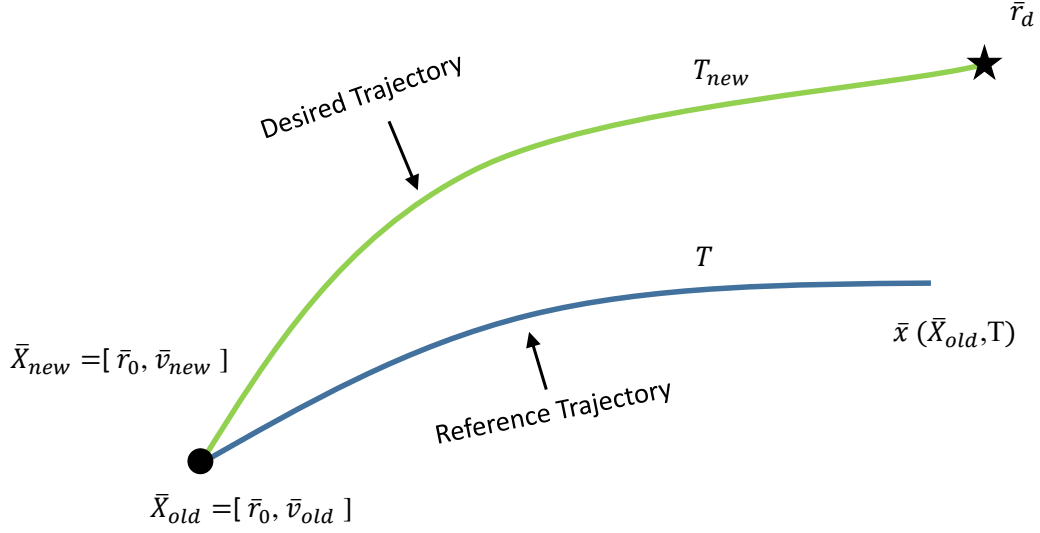
Figure 3.3. Single shooting technique with variable time position target.

is defined as the new free variable vector. The goal is only to achieve the predefined position states at the end hence the end conditions still remains the same. As a result there is no modifications to the constraint vector $\bar{F}(\bar{X})$. Nonetheless, $D\bar{F}(\bar{X})$ is altered due to a different design vector $\bar{X}$, thus

$$D\bar{F}(\bar{X}) = \begin{bmatrix} \frac{\partial x(T)}{\partial \dot{x}_0} & \frac{\partial x(T)}{\partial \dot{y}_0} & \frac{\partial x(T)}{\partial \dot{z}_0} & \frac{\partial x(T)}{\partial T} \\ \frac{\partial y(T)}{\partial \dot{x}_0} & \frac{\partial y(T)}{\partial \dot{y}_0} & \frac{\partial y(T)}{\partial \dot{z}_0} & \frac{\partial y(T)}{\partial T} \\ \frac{\partial z(T)}{\partial \dot{x}_0} & \frac{\partial z(T)}{\partial \dot{y}_0} & \frac{\partial z(T)}{\partial \dot{z}_0} & \frac{\partial z(T)}{\partial T} \end{bmatrix} = \begin{bmatrix} \phi_{14} & \phi_{15} & \phi_{16} & \dot{x}(T) \\ \phi_{24} & \phi_{25} & \phi_{26} & \dot{y}(T) \\ \phi_{34} & \phi_{26} & \phi_{36} & \dot{z}(T) \end{bmatrix} \quad (3.27)$$

where an additional column of the derivative of the position states with respect to time are also included. $D\bar{F}(\bar{X})$ is no longer a square matrix. There are more design variables than the number of constraints, hence, infinitely many solutions exists. One

such solution can be found using the minimum norm approach. The update to the reference can be computed to be,

$$\delta \bar{X} = -D\bar{F}(\bar{X})^T \left[D\bar{F}(\bar{X}) \ D\bar{F}(\bar{X})^T \right]^{-1} \bar{F}(\bar{X}) \tag{3.28}$$

as mentioned in equation (3.18). The iterative process is continued till acceptable tolerance is reached.

The single shooting technique is illustrated using position target scheme. The application is not limited to just position target. The design vector, the constraint vector and the corresponding Jacobian matrix can be modified to target any combinations of position, velocity and/or any other relevant quantity. The technique is although restricted to only single target vector. To target multiple conditions, more robust methods like multiple shooting technique is applied.

3.4 Multiple Shooting

A single shooting technique has vast applications, however, when the trajectory passes through regions of higher sensitivities, this technique struggles to converge. In such cases, few intermediate patch points are incorporated through which the trajectories should traverse before reaching the desired end condition. Multiple shooting is a strategy to cumulatively use single shooting technique to target two adjacent patch points forming a sub-arc as described in Figure 3.4. The process is continued till a transfer trajectory is created from the initial location to the final state that is continuous in position and velocity at each of the updated patch points within some acceptable tolerance. The patch points are free to move around in any directions in the phase space. Similar to single shooting technique, the final state can be achieved either through a fixed time target strategy or a variable time target strategy.
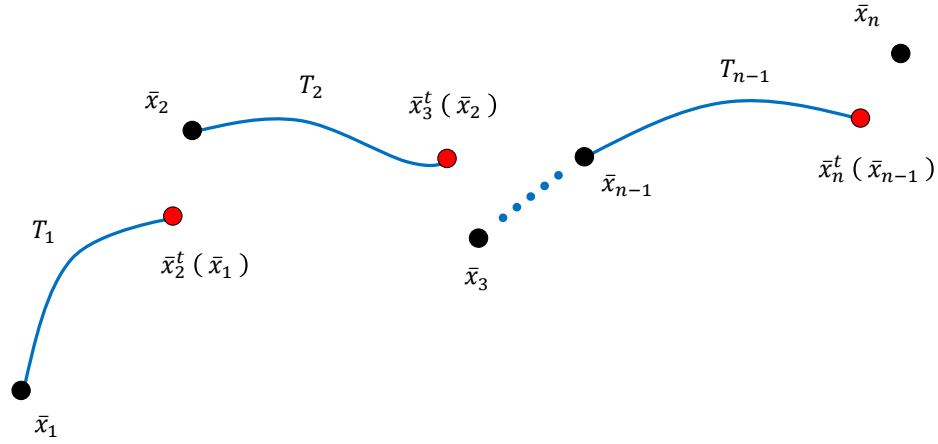
(a) Intermediate Sub-arcs
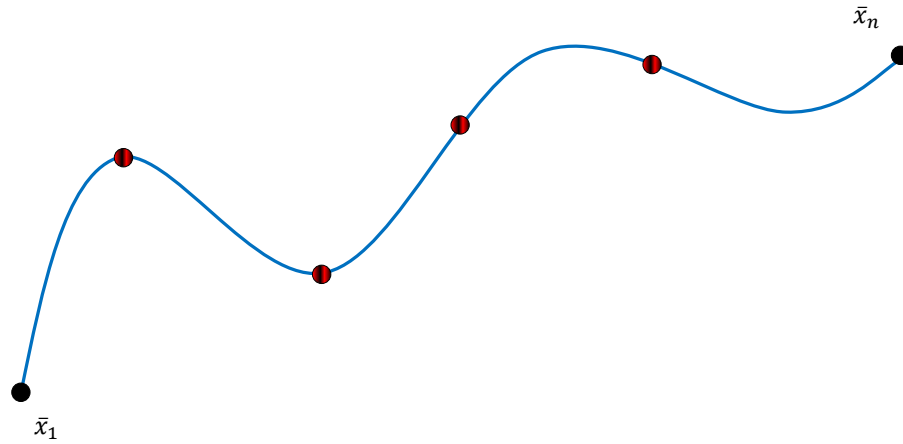
(b) Final Converged Trajectory

Figure 3.4. Concept of multiple shooting target algorithm.

3.4.1   Fixed Time Multiple Shooting

Similar to a fixed time single shooting process where the time between the starting point and the end point is fixed, in fixed time multiple shooting the time of flight between any two successive patch points is fixed. Identical to formulating the single shooting technique, free design variables and constraints are to be defined for the multiple shooting target algorithm. The free design variables at all the defined patch

points are accumulated into one stacked vector. It is considered that the states at each of the patch points are free to be updated every iteration i.e. $\bar{x}_i$ according to Figure 3.4(a). The design variable $\bar{X}$ is therefore a $6n$ sized vector,

$$\bar{X} = \begin{bmatrix} \bar{x}_1 \\ \bar{x}_2 \\ \vdots \\ \bar{x}_n \end{bmatrix} \tag{3.29}$$

where each $\bar{x}_i$ is a column vector with position and velocity states at that patch point. The sub-arcs have to be continuous in position and time at the intermediate patch points in order to achieve a smooth trajectory between the initial and final point as the solution converges. Hence the constraint vector $\bar{F}(\bar{X})$ is defined as

$$\bar{F}(\bar{X}) = \begin{bmatrix} \bar{x}_2^t(\bar{x}_1) - \bar{x}_2 \\ \bar{x}_3^t(\bar{x}_2) - \bar{x}_3 \\ \vdots \\ \bar{x}_n^t(\bar{x}_{n-1}) - \bar{x}_n \end{bmatrix} \tag{3.30}$$

where each $\bar{x}_{j+1}^t(\bar{x}_j)$ are the states achieved by propagating state vector $\bar{x}_j$ as the initial condition for fixed predefined time. Since the trajectory originates at the initial point there is no constraint at $\bar{x}_1$, so the length of the constraint vector is $6(n-1)$. The corresponding Jacobian Matrix becomes

$$D\bar{F}(\bar{X}) = \begin{bmatrix} \left(\frac{\partial \bar{x}_2^t}{\partial \bar{x}_1} - \frac{\partial \bar{x}_2^t}{\partial \bar{x}_1}\right) & \left(\frac{\partial \bar{x}_2^t}{\partial \bar{x}_2} - \frac{\partial \bar{x}_2^t}{\partial \bar{x}_2}\right) & & \\ & \ddots & \ddots & \\ & & \left(\frac{\partial \bar{x}_n^t}{\partial \bar{x}_{n-1}} - \frac{\partial \bar{x}_n^t}{\partial \bar{x}_{n-1}}\right) & \left(\frac{\partial \bar{x}_n^t}{\partial \bar{x}_n} - \frac{\partial \bar{x}_n^t}{\partial \bar{x}_n}\right) \end{bmatrix} \tag{3.31}$$

that is reduced to more revealing form by correlating the partials to the STM, as

$$D\bar{F}(\bar{X}) = \begin{bmatrix} \phi_{2,1} & -I_{6\times6} & & \\ & \ddots & \ddots & \\ & & \phi_{n,n-1} & -I_{6\times6} \end{bmatrix} \tag{3.32}$$

where each $\phi_{i+1,i}$, is the 6×6 State transition Matrix computed between ith patch point to $(i+1)$th patch point. Newton's method is used to update position and velocity states the patch points and iterated till acceptable level of accuracy is obtained.

3.4.2 Variable Time Multiple Shooting with Additional Constraints

Alike variable time single shooting process, where the time between initial time and the desired final state is not constrained, in variable time multiple shooting, the time of flight between two successive patch points is not constrained. To consider a time variable multiple shooting technique, let the time of flight between each patch points be T_i as in Figure 3.4(a), that can be considered as a design variable additional to its position and velocity states. Hence a total of $7n - 1$ design variable exists for this case i.e.

$$\bar{X} = \begin{bmatrix} \bar{x}_1 \\ \bar{x}_2 \\ \vdots \\ \bar{x}_n \\ T_1 \\ \vdots \\ T_{n-1} \end{bmatrix} \tag{3.33}$$

where each T_i represents the time of flight between ith patch point and $(i + 1)$th patch point. To represent a more specific problem, like a trajectory with predefined Jacobi constant, or trajectory with fixed starting point and/or fixed end point or any other criterion, Multiple shooting technique provides the leverage to add additional constraints to represent the same. Let '$\mathcal{C}$' denote any additional constraint besides

the ones defined for fixed time multiple shooting, such that upon convergence $\mathcal{C} = 0$. Hence, the constraint vector $\bar{F}(\bar{X})$ becomes

$$\bar{F}(\bar{X}) = \begin{bmatrix} \bar{x}_2^t(\bar{x}_1) - \bar{x}_2 \\ \bar{x}_3^t(\bar{x}_2) - \bar{x}_3 \\ \vdots \\ \bar{x}_n^t(\bar{x}_{n-1}) - \bar{x}_n \\ \mathcal{C} \end{bmatrix} \tag{3.34}$$

where $\mathcal{C}$ is an added constraint that is a function of the state variables at any one or more patch points. The Jacobian matrix in this variable time multiple shooting method with added constraints defined as $D\bar{F}(\bar{X})$,

$$D\bar{F}(\bar{X}) = \left[\begin{array}{cccc|ccc} \phi_{1,2} & -I_{6\times6} & & & \dot{\bar{x}}_2^t & & \\ & \ddots & \ddots & & & \ddots & \\ & & \phi_{n-1,n} & -I_{6\times6} & & & \dot{\bar{x}}_n^t \\ \hline \frac{\partial \mathcal{C}}{\partial \bar{x}_1} & \cdots & \cdots & \frac{\partial \mathcal{C}}{\partial \bar{x}_n} & \frac{\partial \mathcal{C}}{\partial T_1} & \cdots & \frac{\partial \mathcal{C}}{\partial T_{n-1}} \end{array} \right] \tag{3.35}$$

contains additional partials that represents time derivatives with respect to free variables as well as partials of '$\mathcal{C}$' with the states at all patch points and corresponding time of flights. The additional partials that $\dot{\bar{x}}_i^t$ represents the time derivative of $\bar{x}_i$ with respect to the time of flight from $(i-1)$th to ith patch point i.e. $\dot{\bar{x}}_i^t = \partial \bar{x}_i / \partial T_{i-1}$. For every iteration, the update can be computed by taking direct inverse or minimum norm depending on the dimensions of the Jacobian Matrix.

4. ORBIT MAINTENANCE OPERATIONS

The principal step of a mission design process is to determine a nominal orbit. The actual spacecraft is expected to move along this reference path. Due to unmodeled perturbations the spacecraft tends to drift away from the reference path, and the unstable nature of most of the libration point orbits will amplify the deviation in both position and velocity states. A station-keeping strategy is introduced to compute timely maneuvers that can secure the spacecraft within an acceptable region defined as a torus centered about the reference path. The algorithm computes impulsive maneuver (both magnitude and direction) that potentially sustains the spacecraft through the mission duration. Decreasing the maneuver magnitude for increased life of the spacecraft is a principal part of the program.

4.1   Representation of Reference Orbit

To perform orbit maintenance, a precise nominal path must be known. Previous studies have shown ways to compute precise halo orbits in the Circular Restricted Three Body Problem [16–19,60]. The orbits are determined by propagating the non-linear equations of motion and corrected using differential correction schemes [17]. Computing Lissajous orbits and quasi-halo orbits in the vicinity of the libration points can be challenging as they are non-periodic. Howell and Pernicka [18] use a two-level patching algorithm to join trajectories of arbitrary duration to form a continuous trajectory. This technique can be used to patch trajectories other than the halo and Lissajous orbits. The application is extended in higher fidelity model as well.

For a real mission scenario, the trajectory of choice may not be exactly periodic, like a halo orbit in CR3BP, primarily due to other perturbing bodies in space that has

non-periodic behavior. Considering a periodic halo orbit as the reference trajectory for the station-keeping process may therefore not be the right choice if simulated in the ephemeris model. A more accurate trajectory is generated by numerically converging a continuous trajectory in the higher fidelity ephemeris model that acts as a baseline trajectory.

In this work, India's upcoming Aditya-1 mission to Sun-Earth L_1 libration point is considered while designing the nominal trajectory and performing station-keeping maneuvers. The scientific goal of this mission includes studying the solar corona, solar flares and energy distribution. The reasons to choose this orbit as the reference are due to its similarity with the ISEE-3 and the SOHO mission in its scientific objectives [1] and that the orbit avoids the solar exclusion zone. As explained by Howell and Pernicka [25], the solar exclusion zone is the region where the spacecraft appears right in front of the solar disk as viewed from the Earth, causing radio interferences that can potentially result in loss of communication link. Besides, a lot of literature sources are available on the ISEE-3 and SOHO mission [24, 25, 40–43], therefore, considering an orbit similar to ISEE-3 for the Aditya-1 mission would offer an opportunity to compare results. Consequently, a halo orbit, similar to ISEE-3, in the vicinity of the libration point L_1 of the Sun-Earth/Moon barycenter CR3BP system is selected that is later corrected in the ephemeris model. A L_1 southern halo orbit with approximate y-amplitude $A_y = 668700$ km and out of plane amplitude $A_z = 124680$ km is chosen in the CR3BP. The orbit corresponds to a Jacobi constant of 3.000826905620419 and an orbit period of 177.86 days. The chosen orbit is in close proximity to L_1 libration point in comparison to other orbits in the same family as indicated in Figure 4.1. Typically the orbits in close proximity to the L_1 libration points are highly unstable, analogous to the unstable nature of the L_1 libration point. The unstable nature of the orbit can be mathematically represented as

$$\tilde{\nu} = \frac{1}{2}\left(|\lambda_{max}| + \frac{1}{|\lambda_{max}|}\right) \tag{4.1}$$

where $\tilde{\nu}$ is called the *stability index* and λ_{max} is the largest eigenvalue (by magnitude) of the monodromy matrix computed for the particular orbit. In the linear terms, a marginally stable orbit will have $\tilde{\nu} = 1$ and as the value of $\tilde{\nu} > 1$, the unstable nature of the orbit becomes increasingly dominant. The orbit in consideration here has a stability index, $\tilde{\nu} = 866.98$, exhibiting very high unstable nature.

The dimensions of the chosen orbit is evident from the Figure 4.2, as it displays the three planar projections and an isometric view of the reference halo orbit in the Sun-Earth/Moon barycenter CR3BP. The x-axis is along the line joining the primaries from the Sun to the Earth/Moon barycenter. The z-axis is along the angular momentum vector and y-axis completes the dextral coordinate system. The origin is shifted to the L_1 libration point.

The orbit's initial conditions from the CR3BP when propagated in the higher fidelity model will not result in a closed orbit, due to perturbations caused by un-modeled forces including gravitational force of other celestial bodies. In fact, it is likely that the trajectory will escape the halo orbit region and never return. To obtain a near halo trajectory in the ephemeris model that better approximates a real mission scenario, 20 patch points per orbit equally spaced in time from the CR3BP solution is selected and a multiple shooting technique is incorporated to converge a solution continuous in states and time. To model with improved accuracy, ephemeris data of more planetary bodies can be added, but with more number of bodies added, increases the computational challenges. It becomes important to select the right number of bodies, such that accuracy of the solution is not compromised at the expense of computational time. Besides the forces due to other celestial bodies, the solar radiation pressure (SRP) may also induce perturbations to the spacecraft. Figure 4.3 demonstrates the magnitude of net perturbing acceleration due to different celestial bodies in the solar system as well as the solar radiation pressure acting at the Sun-Earth/Moon libration point L_1 over the duration of 2 years with starting epoch
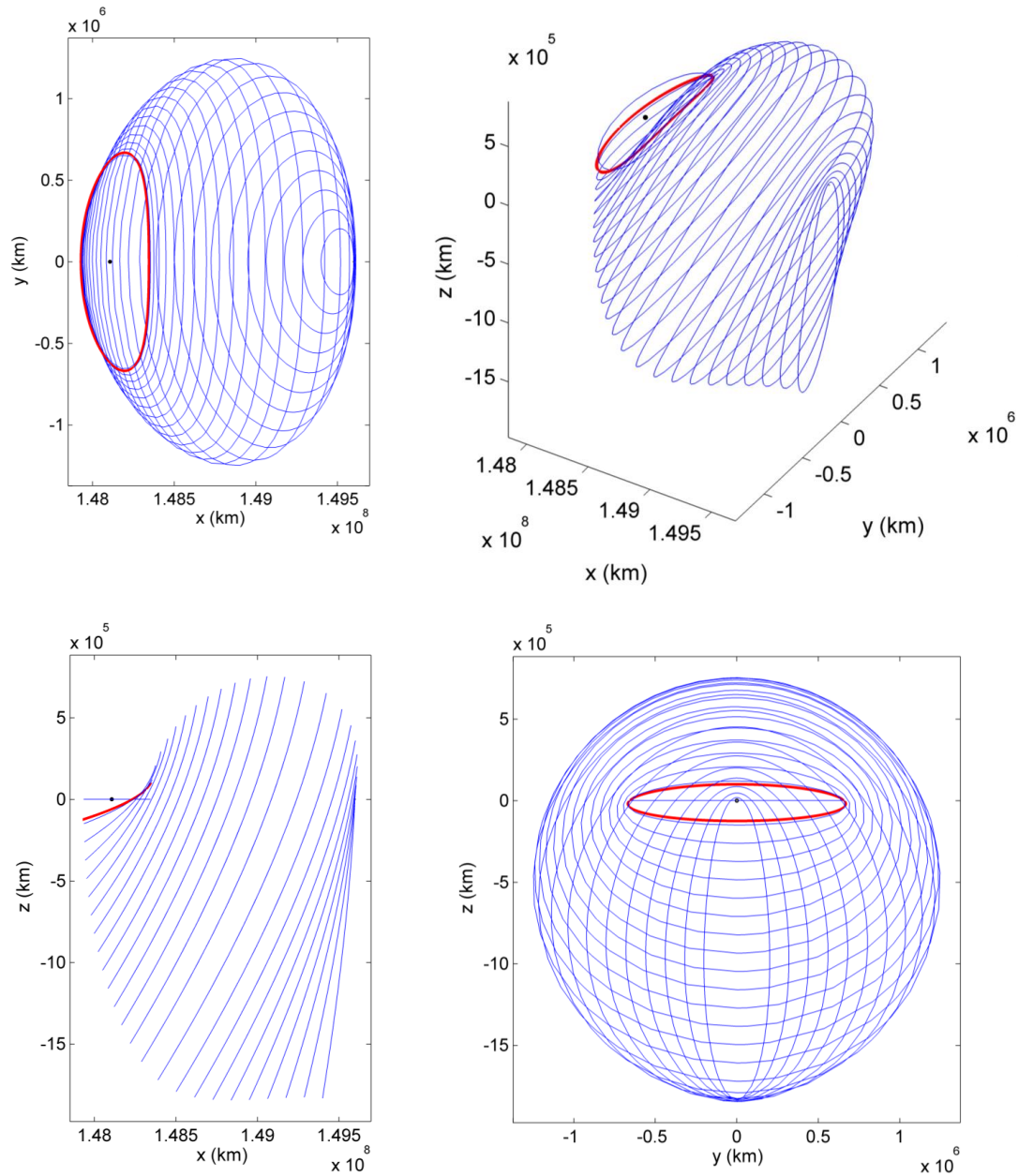
Figure 4.1. Location of the nominal orbit in the family of southern L_1 halo orbit of the Sun-Earth/Moon barycenter system.

date chosen as January 13, 2020. Clearly the Sun, the Earth and the Moon are the three dominant influencing bodies at the L_1 libration point. Therefore, gravitational forces of the Sun, the Earth and the Moon are selected to model the higher fidelity
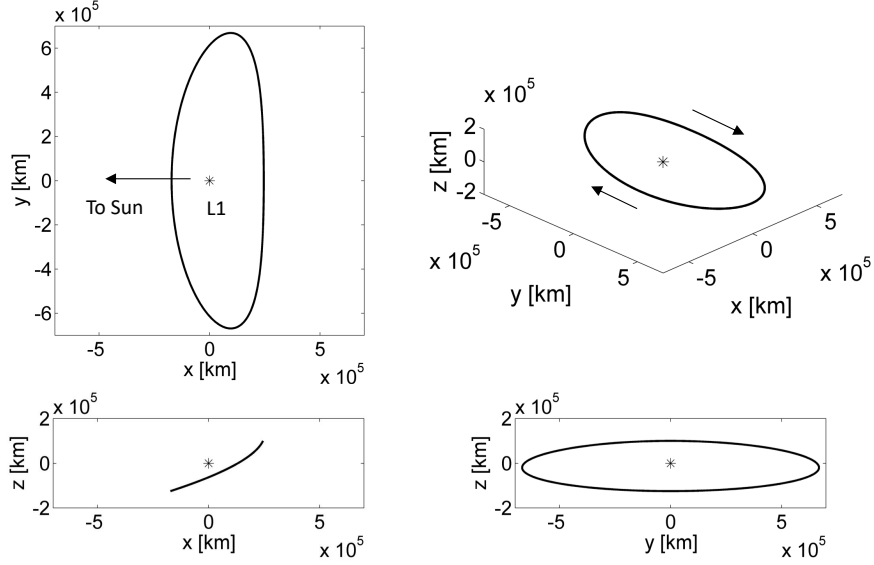
Figure 4.2. Planar projections of the nominal orbit modeled in the CR3BP.

solution. This model is identified as the SEM model, similar nomenclature used by other researchers [24, 25, 40–43]. All other forces are neglected for the sole purpose of computational speed; however, Jupiter and Venus may be added as other perturbing bodies if increased accuracy is demanded. Similarly, based on the knowledge about the actual spacecraft the impact of solar radiation pressure can also be taken into consideration.

4.1.1 Effect of Solar Radiation Pressure on the Aditya-1 Mission

The Aditya-1 spacecraft as planned has an aluminum honeycomb structure of dimensions 89 cm x 89 cm x 61.5 cm. In addition to the payload, the spacecraft features two solar cell electric panels of dimensions 120 cm x 81 cm each. Overall the spacecraft is expected to weigh about 400 kg [61]. Considering the dimensions of the Aditya-1 spacecraft, the maximum surface area that is exposed to the Sun at any time would be 2.7361 m^2. Consequently, the area to mass ratio (AMR) is 0.00684025 m^2/kg or the mass to area ratio (σ_{MAR}) is 146.1935 kg/m^2. The additional perturbing

force due to solar radiation pressure (SRP) acts on the spacecraft due to its surface, that is otherwise trivial if modeled as a point mass. For a perfectly reflective surface, the mass to area ratio, $\sigma_{MAR}^* = 1.53 \times 10^{-3}$ kg/m^2 is the critical value at which the solar radiation pressure acting on the spacecraft is exactly equal to the gravitational force acting due to the Sun. A dimensionless sail lightness parameter β_{sail} (or sail loading parameter) is defined as

$$\beta_{sail} = \frac{\sigma_{MAR}^*}{\sigma_{MAR}} \tag{4.2}$$

that is effectively the ratio between the solar radiation pressure acting on the spacecraft to the gravitational force due to the Sun [62,63]. The value of $\beta_{sail} = 0$, represent a point mass object. For the Aditya-1 spacecraft, the value of β_{sail} is computed to be 1.0466×10^{-5}. The acceleration due to the solar radiation pressure acting on the spacecraft is given as

$$\ddot{\vec{r}}_{SRP} = \beta_{sail} \left(\frac{\tilde{k}}{2} \right) \frac{\tilde{G} M_S}{R_{S-s/c}^2} cos^2(\alpha) \, \hat{n}_{sail} \tag{4.3}$$

where, α is the angle between the direction of incident photons and the normal to the surface of the spacecraft, $\hat{n}_{sail}$ is the direction normal to the surface of the spacecraft, $\tilde{G}$ is the universal gravitational constant, M_S is the mass of the Sun, $R_{S-s/c}$ is the distance from the Sun to the spacecraft while $\tilde{k}$ is a material parameter such that $0 \leq \tilde{k} \leq 2$ where $\tilde{k} = 2$ indicates perfectly reflective surface while $\tilde{k} = 0$ indicates perfectly light absorbing surface [62, 63]. The net perturbing acceleration due to multiple celestial bodies is compared with the solar radiation pressure for the mission duration of two years in Figure 4.3. It is assumed that the surface of the spacecraft is perfectly reflective i.e. $\tilde{k} = 2$, and the maximum area of the spacecraft is projected towards the Sun at all times i.e. $\alpha = 0^o$, to incorporate the maximum impact of the solar radiation pressure. The net acceleration due to the SRP is of the order of the net perturbing acceleration due to Venus and Jupiter. For spacecraft, such as the

Aditya-1 with a very low value of β_{sail}, the behavior as expected is similar to a point mass object. The acceleration due to the SRP is extremely small in comparison to the dominant acceleration due to the Sun, the Earth and the Moon; therefore, as discussed, the gravitational forces due to the Sun, the Earth and the Moon are the only forces incorporated for calculation in this work to save computational expense, however for higher precision other forces can be incorporated. If the mass to area ratio (σ_{MAR}) of the spacecraft is small, then the effect of the SRP is more prominent.
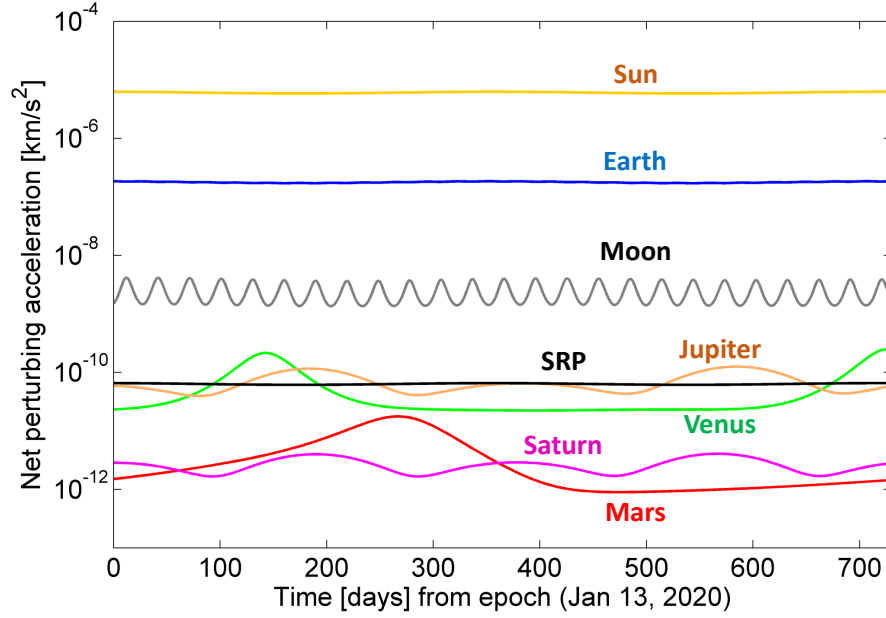
Figure 4.3. Net perturbing acceleration due to various celestial bodies acting at the Sun-Earth/Moon L_1 Lagrange point.

Considering that the impact of the solar radiation pressure is to be incorporated while modeling the motion of the spacecraft and selecting an orbit that satisfies the mission objectives, the acceleration due to the SRP is incorporated into the CR3BP equations of motion making it the solar sail - circular restricted three body problem (SS-CR3BP). Due to the change in dynamics due to additional acceleration components, the equilibrium solutions of the equation of motions in the SS-CR3BP are

different than the standard CR3BP, that are a function of sail lightness parameter and orientation of the spacecraft. For the Aditya-1 spacecraft, with a solar lightness parameter $\beta_{sail} = 1.0466 \times 10^{-5}$ and the spacecraft assumed to be projecting maximum surface area to the Sun i.e. $\alpha = 0^o$ with 100% reflecting surface ($\tilde{k} = 2$), the L_1 libration point shifts 175 km towards the Sun. For the ISEE-3 mission with $\tilde{k}\beta_{sail} = 7.65 \times 10^{-6}$ as derived from Bell [64], the L_1 libration point moves 127 km towards the Sun. Accordingly, considering a more practical value of $\tilde{k}$, for the Aditya-1 mission, the libration point is expected to move much less than 175 km towards the Sun. New periodic orbit families can be generated about the SS-CR3BP libration point L_1 for different combinations of $\tilde{k}\beta_{sail}$. Analytical solutions from the linearized model in the vicinity of the equilibrium solutions are used as initial guess, that is converged using differential correction scheme with the modified state transition matrix that incorporates additional SRP terms to generate periodic orbits. The additional variables in the SS-CR3BP presents a wider range of solutions than the standard CR3BP, however the desired halo orbit generated in the SS-CR3BP model maintains approximately the same geometry as the CR3BP halo orbit, except that the position and velocity states are marginally shifted. The new reference orbit in the SS-CR3BP model is further converged in the ephemeris model to simulate with increased fidelity based on real time. The deviation due to solar radiation pressure for the Aditya-1 spacecraft is negligible, considering the characteristics distance in the Sun-Earth/Moon system, to cause any significant change to the position and velocity states of the spacecraft, however for future missions with effective solar sails, a periodic halo orbit converged in the SS-CR3BP would serve as the baseline solution. For this research, the SEM model is used wherever higher fidelity is addressed.

Using the SEM model, the patch points from the CR3BP halo orbit is converged into a continuous trajectory for mission duration of 2 years which roughly corresponds to 4 orbit periods. The epoch date at the halo orbit injection (HOI) is assumed to be January 13, 2020 UT1: 00:00:00.0 (Julian Date: 2458861.5) which is comparable

to the planned mission schedule for the Aditya-1 mission. The Figure 4.4 displays the nominal trajectory converged in the SEM model for 2 years viewed in the Sun-Earth/Moon L_1 rotating frame. The L_1 equilibrium point may not exist in the SEM model because of non-periodicity of the acting gravitational bodies, however for representation, location of L_1 obtained from the circular restricted model can be used. Additionally, the orbits no more possess periodic behavior, but they still retain quasi-halo like behavior as observed in the CR3BP.
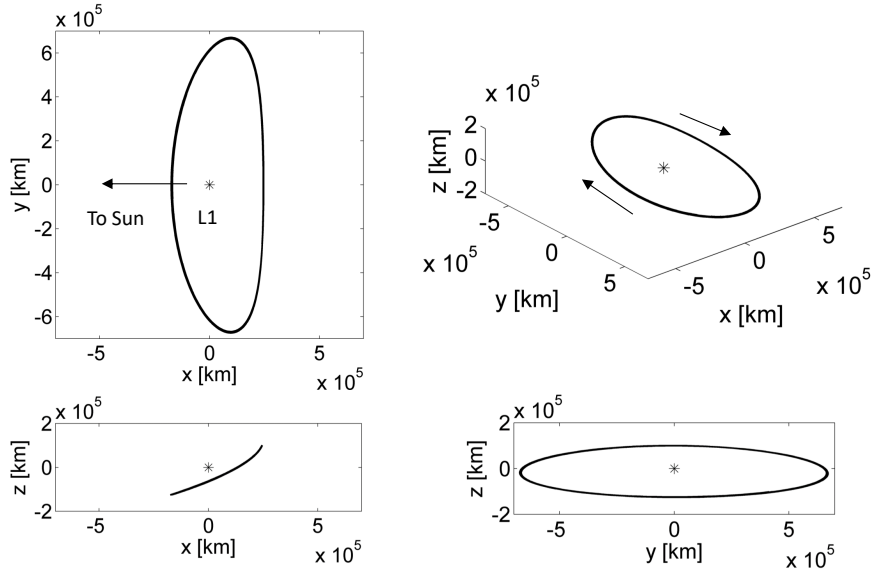
Figure 4.4. Planar projections of the nominal orbit converged in the SEM Model.

As per the mission plan the spacecraft is expected to sail along the nominal orbit converged in the SEM model, nevertheless, it may drift away from the nominal path due to unmodeled error and the unstable nature of the orbit. It is crucial to continuously track the spacecraft against this reference orbit, which is obtained from converging in the higher fidelity system, in form of tabular listings of time, position and velocity states. It is computationally expensive to store large data sets as well retrieve the large data every time to compare the true spacecraft states to the reference. Howell and Pernicka [24, 25] concluded that, data points spaced within 1.1 days pro-

vides fairly accurate representation of the nominal path. When the data points were spaced more than 1.1 days apart, the station-keeping costs seem to have risen drastically. Since the computational ability at present is more advanced, it was therefore decided to store data points at 2.5 hour spacing, so that accuracy is not compromised.

There has been substantial literature on the type of curve that could be used to retrieve interpolated data accurately. Richardson [16] uses a complete 13th order analytical Fourier series representation of the halo orbit. Howell and Pernicka [24, 25] use Akima cubic spline interpolation while Gordon in his dissertation [41] and Howell and Gordon [40] analyzed different interpolating schemes and concluded that cubic splines especially Akima cubic splines gave smoother representation. For estimating intermediate states and times from the available data points placed interval of 2.5 hours, different methods such as linear interpolation, quadratic polynomial fit, cubic spline and Akima cubic spline are investigated for their accuracies. Since the data points were placed in a mere 2.5 hours interval, linear interpolation could present fairly accurate results with errors well within 0.1 km and 1 mm/s, but it was still inferior in comparison to other methods. The accuracies of other three methods were comparable. Nevertheless, to not compromise on accuracy in any extreme case, Akima cubic spline is selected as the primary interpolating technique throughout this work.

4.2   Assumptions

A spacecraft experiences perturbations ever since its launch, due to several factors like atmospheric drag, limitations of the measuring apparatus, additional gravitational bodies, magnetic field of earth, charged particles, solar radiation pressure etc. Besides, modeling errors can also result in the spacecraft's true path being different from the reference path. Despite all these potential challenges, the primary focus of a station-keeping process is restricted to sustaining the spacecraft to unmodeled

errors post the orbit injection phase, which essentially depends on orbit injection error, tracking error and maneuver execution error. These errors are inevitable due to limitations of the orbit determination apparatus and the engine thrusting abilities. The magnitude of these errors can although be decreased by using better quality and sophisticated instruments, but cannot be overcome perfectly. Some other errors including the solar radiation pressure and gravitational effects of the unaccounted bodies can be overcome by adding their effects into the model, however, for this research, solar radiation pressure and gravity due to bodies other than the Sun, the Earth and the Moon are not taken into consideration. These can be added in future depending on mission demands.

Station-keeping maneuvers can be executed either as an impulsive maneuver or a continuous thrust. Since the main aim of this research is to compare different strategies and use the station-keeping process as a tool to sustain the spacecraft in a desired orbit and not to focus on the abilities of different thrusters, no attempt has been made to perform station-keeping using continuous thrusters. All maneuvers executed are single impulse maneuvers.

For consistency throughout this work, the constants retrieved from Adaptive Trajectory Design (ATD) software is used wherever Circular Restricted Three Body is mentioned. Since the orbits are sensitive to the characteristic values they are represented in, even the minutest change in any of the constants can change the entire course of the trajectory. The values are therefore summarized in table 4.1.

4.3   Unmodeled Orbit Determination Errors

Any uncertainty in the measurement of the position and the velocity states of the spacecraft is called orbit determination errors. The station-keeping phase begins post the injection of the spacecraft into its desired orbit. Therefore, the different

Table 4.1. Constants used throughout CR3BP applications.

Standard Gravitational Parameter	
$\tilde{\mu} = \tilde{G}M, \ km^3/s^2$	
Sun	132712197035.766
Earth	398600.432896939280908555
Moon	4902.800582147764544061

Characteristic quantities	
Sun-Earth/Moon system	
$\mu \ [ndim]$	$3.040428955805986 \times 10^{-6}$
$l^* \ [km]$	149597886
$t^* \ [s]$	5022640.66103807

types of orbit determination errors that can influence the motion of the spacecraft are the orbit injection error, tracking or navigational errors and maneuver execution errors. These errors are stochastic in nature, thus cannot be modeled into the system. If not addressed, these errors can potentially destabilize the motion of a spacecraft. From the simulation point of view, it is necessary to understand the evolution of these errors and how can these stochastic errors be incorporated to estimate the maneuvers required to maintain the spacecraft in the appropriate region. The orbit determination errors are broadly classified into the three types.

4.3.1   Orbit Injection Errors

The orbit injection marks the beginning of the station-keeping process. At the end of the transfer trajectory an orbit injection maneuver is applied to inject the spacecraft into its orbit at the desired position with a desired velocity. Undoubtedly, the injection would not be perfect due to limitations in the engine performance and

tracking apparatus which measures the spacecraft location. Therefore, the resulting position and velocity states immediately after the orbit injection would be different from the reference states.

To incorporate this error, in the simulation, each component of the reference position and velocity states are perturbed independently. A Gaussian random number generator is used to perturb each of the states. The mean of the perturbation is zero while the standard deviation is chosen based on the knowledge of the existing hardware. The perturbed states are propagated in the SEM model to obtain the actual trajectory or the true path of the spacecraft.

4.3.2   Tracking Errors

As the spacecraft traverses along the orbit about the libration point, the earth based tracking stations determine the position and velocity states of the spacecraft at discrete intervals, better known as tracking intervals. Due to limitations in the orbit determination equipment, the states are never known to complete accuracy. A station-keeping strategy should successfully compute a reasonable maneuver to maintain the spacecraft close to the reference solution despite of this tracking errors.

To simulate the tracking error, each component of the position and velocity states determined at each tracking interval is purposefully perturbed with a Gaussian error similar to orbit injection error. Again, the mean is set to zero and the standard deviation is chosen depending on knowledge about the tracking instrument. Each component is perturbed independently. The perturbed states are propagated in the SEM model as usual.

4.3.3 Maneuver Execution Errors

As the spacecraft deviates away from the reference solution, the station-keeping algorithm computes a corrective maneuver to maintain the spacecraft back in a close torus about the reference solution. But the computed maneuver and the implemented maneuver is never exact, typically due to engine thrusting limitations. To incorporate this inaccuracy, each of the components of the computed maneuver is perturbed using Gaussian distribution, again with mean zero and some standard deviation known from engine capabilities.

4.4 Station-keeping Algorithm

To replicate a real mission station-keeping scenario, different errors are introduced on purpose. As soon as the spacecraft is injected in to the desired orbit the process of station-keeping commences. The halo orbit injection (HOI) is assumed to be the starting point of this process. Based on the knowledge of the thrusters, standard deviation for the orbit injection error is introduced. The three position and the three velocity states are perturbed with a random number generated using Gaussian probability distribution corresponding to standard deviation of orbit injection error. The spacecraft will naturally deviate from the desired orbit due to the errors in the states, hence station-keeping algorithm should be performed to keep the spacecraft within a specified torus about the nominal path. The exact states of the spacecraft is never exactly known due to tracking errors, hence at every tracking interval the states are intentionally perturbed corresponding to the tracking errors. From literature studies, it was concluded that, for an SEM system tracking intervals of 2 days is typical. The unmodeled errors and the unstable mature of the orbit may result in the spacecraft drifting away from the nominal path. A corrective maneuver is calculated to ensure the spacecraft is in close vicinity to the nominal path. As summarized in Figure 4.5, certain constraints are taken into consideration to compute and implement the maneuver, which includes
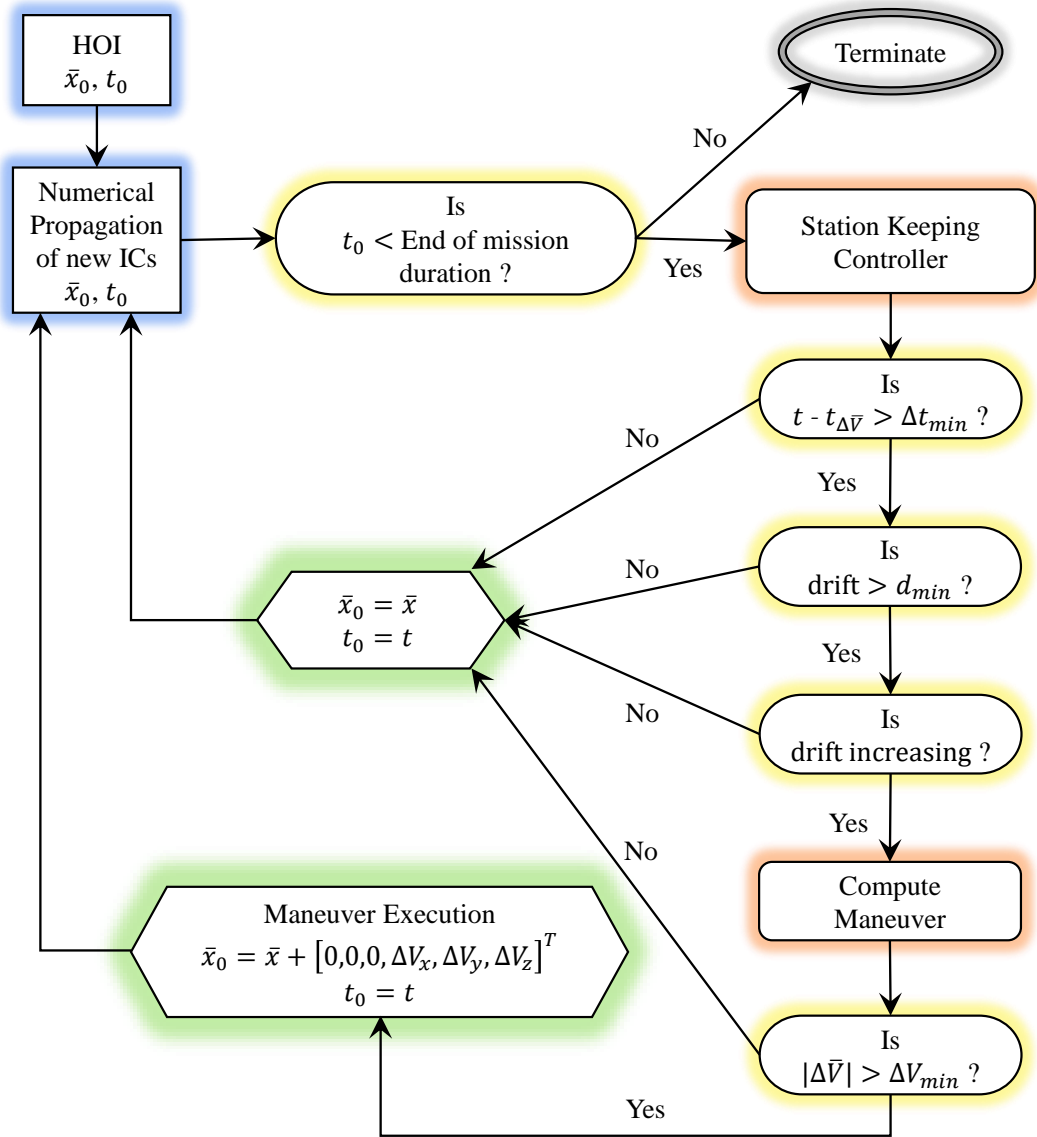
HOI : Halo Orbit Injection

$\bar{x}_0, t_0$: Initial condition (IC) for numerical propagation

$\bar{x}, t$: Current state and time

$t_{\Delta\bar{V}}$: Time at previously executed maneuver

Δt_{min} : Minimum time of separation between successive maneuvers

d_{min} : Minimum magnitude of deviation from nominal path

ΔV_{min} : Minimum maneuver magnitude that can be executed

$\Delta\bar{V} = \begin{bmatrix} \Delta V_x, \Delta V_y, \Delta V_z \end{bmatrix}^T$

Figure 4.5. Station-keeping decision making process.

1. A minimum length of time Δt_{min} must elapse between two successive maneuvers to provide ample time for orbit estimation, undergo attitude change and/or payload constraints. A maneuver at current time, t, will be computed and/or implemented only if $t - t_{\Delta \bar{V}} > \Delta t_{min}$, where $t_{\Delta \bar{V}}$ is the time at the last implemented maneuver.

2. The spacecraft must deviate more than the minimum specified drift from the nominal orbit, d_{min}, to consider a requirement for a corrective maneuver. A maneuver is not calculated or executed if $\underline{d} < d_{min}$, where $\underline{d}$ is the current deviation of the spacecraft from the nominal path.

3. The spacecraft deviation from the nominal path must be increasing for a maneuver to be computed and/or executed. Mathematically, $\underline{d}_{i+1} > \underline{d}_i$, where i and $i+1$ are the measurements at two successive tracking intervals. In a continuous system a positive rate of deviation is equivalent to $d(\underline{d})/dt > 0$.

4. Only if steps 1-3 are satisfied, a maneuver is computed. Concerning the engine limitations, a maneuver will be implemented only if the computed maneuver is larger than minimum executable maneuver defined as ΔV_{min} i.e. $\Delta V \geq \Delta V_{min}$.

Due to inaccuracy in attitude change or due to engine performance limitations the implemented maneuver cannot be exactly equal to the computed maneuver hence the maneuver executed is altered based on the ciphered standard deviation of the maneuver execution error. The current states are updated to get the new initial conditions which is propagated further. After simulating till the end of mission duration, the magnitude of all implemented maneuvers within the mission duration are considered to estimate the station-keeping costs. For a stochastic process, multiple simulations are conducted to estimate the mean and standard deviation.

For station-keeping algorithm used throughout this research, in addition to the minimum drift condition, a maximum drift case is also considered. In case the space-

craft drifts unacceptably far from the reference, the simulation is ceased immediately and the computed costs for that particular iteration is ignored. The termination distance is capped at 50000 km for this work. This value seems to be an appropriate choice in the Sun-Earth/Moon system for many other researchers as well [24, 25, 40–43]. A new set of random numbers are generated and the simulation is continued.

Throughout this work, two different sets of orbit determination errors have been used, Type A and Type B, the details of which are enumerated in Table 4.2. Type A has low orbit injection, tracking and maneuver execution error sigma limits. While Type B has comparatively larger error variance. Using two different but extreme values, one low and another higher level of error would provide more dynamic range to compare the performance of the station-keeping algorithms. Finally, comparison is made with sources from literature with similar orbit determination errors.

4.5   Monte Carlo Simulation

Station-keeping algorithm uses random sampling errors to represents uncertainties in orbit determination and maneuver execution which is then propagated using a nonlinear regime. Computing the mean maneuver cost is not possible using an analytical approach. Due to its stochastic nature, it is convenient to use Monte Carlo simulation to determine the probabilistic mean. The quality of the solution obtained using the Monte Carlo process can be considered high only if the computed solution is close to the true solution. Hence sufficiently large sample size is required.

For problems, whose true solution is known, the sample size can be adjusted based on the how close solution is required. But in the case of station-keeping, the true solution itself is unknown. Hence, it is challenging to decide the sample size required to estimate the mean value close to the true value. A sample size about 20 or 30 is

Table 4.2. Selected orbit determination error and input parameters for station-keeping simulation, Type A and Type B.

Type	A	B
Minimum time between maneuvers, Δt_{min} [days]	30	30
Minimum drift from the nominal path for a corrective maneuver, d_{min} [km]	0	0
Maximum drift from the nominal path for termination, d_{max} [km]	50000	50000
Minimum magnitude of executable maneuvers, ΔV_{min} [cm/s]	Variable 5, 10, 20, 50, 100	Variable 5, 10, 20, 50, 100
Tracking interval [days]	2	2
Orbit injection & tracking Error (1σ) • Position [km] • Velocity [mm/s]	1.5, 2.5, 15 1, 1, 3	3, 30, 30 15, 15, 30
Maneuver execution error (1σ)	2.5% of planned maneuver magnitude in each direction	5% of planned maneuver magnitude in each direction
Halo orbit injection epoch	January 13, 2020	January 13, 2020

generally too small to get a solution with high confidence level required for comparison. On the other hand, having too many simulations, adds very little information at high computational expense, which is ineffective. An appropriate sample size is

desired that provides substantially high confidence level making comparison effective.

Many researchers in the past have used about 50, 100, 300, 500 or even 1000 Monte Carlo runs without providing remarks on their confidence level. Few researchers have used some approaches to compute the either the appropriate number of Monte Carlo runs or specified the standard deviation at the end of the simulation [40–43, 65]. Sample size determination can be vital for Monte Carlo simulations. Muralidharan [66] elaborates the process of determining the right sample size based on the accepted confidence intervals. The strategy had been adopted by Gordon [41] for his station-keeping application. For a trial that produces observations $\varkappa_1$, $\varkappa_2$, ..., $\varkappa_n$, the mean, $\bar{\varkappa}$ and the standard deviation, $S_\varkappa$, of the samples can be computed by

$$\bar{\varkappa} = \frac{1}{n} \sum_{i=1}^{n} \varkappa_i \tag{4.4}$$

$$S_\varkappa^2 = \frac{1}{n-1} \sum_{i=1}^{n} (\varkappa_i - \bar{\varkappa})^2 \tag{4.5}$$

where n is the sample size. The mean computed from the samples may not be exactly equal to the true mean, therefore, the variance of the computed mean, $\sigma_{\bar{\varkappa}}^2$, is defined as

$$\sigma_{\bar{\varkappa}}^2 = \frac{S_\varkappa^2}{n} \tag{4.6}$$

that is a function of the variance of the samples $S_\varkappa^2$. A superior quality Monte Carlo simulation will estimate the computed mean, $\bar{\varkappa}$, close to the true mean, $\mu_\varkappa$. The confidence level of the computed mean determines if the true mean lies within a certain bounded region about the computed mean. As demonstrated in Figure 4.6, let the *lower control limit* and the *upper control limit* of the bounded region be denoted as LCL and UCL respectively. Mathematically, LCL and UCL can be defined as

$$[LCL, \ UCL] = \bar{\varkappa} \pm z_c \sigma_{\bar{\varkappa}} = \bar{\varkappa} \pm z_c \frac{S_\varkappa}{\sqrt{n}} \tag{4.7}$$

where z_c defines the percentage confidence level in terms of sigma limits that signifies how confident should the user be that the true mean lies within LCL and UCL.

The relation between percentage confidence level and the corresponding sigma limit is provided in table 4.3 [66]. As the sample size increases, the gap between LCL and UCL becomes narrower. consequently, the true mean and the computed mean gets closer. The half width, h, also referred to as 'precision' by some researchers, between LCL and UCL can be a deciding factor on the number on Monte Carlo runs. The precision or half width is defined as

$$h = \frac{UCL - LCL}{2} = z_c \frac{S_\varkappa}{\sqrt{n}} \qquad (4.8)$$

that inversely depends on the number of iterations. Large number of iterations will produce a more precise result at the cost of immense computational time. The number of simulations actually required is in fact a function of the preferred precision level. The precision or the half width, h, desired may be an absolute parameter or a relative parameter in comparison to the mean. The number of Monte Carlo runs can be estimated in either case.

- Absolute Precision

  Assuming that the precision of the required solution is given in terms of the permissible absolute error, α. In other words, for the chosen confidence level, true mean should be within $\bar{\varkappa} \pm \alpha$, thus

$$h = \alpha = z_c \frac{S_\varkappa}{\sqrt{n}} \quad \rightarrow \quad n = \left(\frac{z_c S_\varkappa}{\alpha} \right)^2 \qquad (4.9)$$

- Relative Precision

  If the precision of the required solution is given in terms of the permissible relative error ($\alpha\%$). In other words, for the chosen confidence level, true mean should be within $\bar{\varkappa} \pm (\alpha/100)\bar{\varkappa}$, thus

$$h = \frac{\alpha}{100} \bar{\varkappa} = z_c \frac{S_\varkappa}{\sqrt{n}} \quad \rightarrow \quad n = \left(100 \frac{z_c S_\varkappa}{\alpha \bar{\varkappa}} \right)^2 \qquad (4.10)$$

Either of equations (4.9) or (4.10) can be used to compute the required number of Monte Carlo simulations that yields computed mean that would be close to the

true mean within the accepted confidence level. The sample size, n, depends on the accepted sigma limit, z_c, the permissible absolute or relative error, α, the present computed mean, $\bar{\varkappa}$ and standard deviation of the samples tested, $S_\varkappa$.
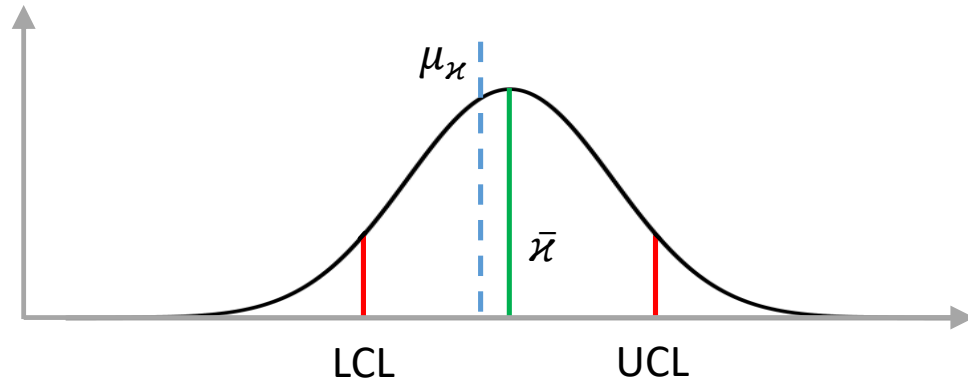
Figure 4.6. Precision in a stochastic process.

Table 4.3. Percentage confidence level and corresponding sigma limits.

Confidence Level (%)	Sigma Limit (z_c)
68.26	1
95	1.96
95.45	2
99	2.58
99.73	3
99.99	3.89

It was observed that few authors have used the estimate value of $S_\varkappa$ to predict the desired number of runs. Making the right estimate of $S_\varkappa$ without any prior Monte Carlo runs is however not possible, hence, the reason for their choice is uncertain. A better method is sought to overcome this challenge. It was observed from different Monte Carlo runs that at least 30 runs are required to stabilize the variance. It

is proposed in this research that the value of $S_\varkappa$ after first 30 runs can be used to substituted in equation (4.9) or (4.10) to compute the number of Monte Carlo runs required. Besides continuous computation of required sample size using the value of $S_\varkappa$ calculated every run beyond 30 is an effective method. The following scheme can be adopted to compute the right number of Monte Carlo runs.

1. Perform 'i' number of trials such that, $i \geq 30$.

2. Compute statistical information available from conducted trials. Mean $\bar{\varkappa}$ and Standard deviation $S_\varkappa$.

3. Compute required number of trials/Sample size 'n'. Use equation (4.9) or (4.10) based on desired absolute precision or relative precision.

4. If required number of trials are more than the performed number of trials i.e. $n \geq i$ go to step 5 else go to step 6.

5. $i = i + 1$, perform additional trial. Go to step 1.

6. More trials have been performed than the required. Simulation is terminated. Computed mean is $\bar{\varkappa}_i$.
   Standard deviation of the mean is $S_{\varkappa_i}/\sqrt{i}$.

Monte Carlo method is a probabilistic mean computation technique based on stochastic sampling hence no fixed number of runs or value of precision is defined. The termination of a Monte Carlo process is based on the precision demanded by the user to evaluate the data appropriately. Either based on predefined precision level, the sample size can be estimated using the procedures discussed, or, the standard deviation of the total number of runs must be specified along with the computed mean to provide the essence of the actual distribution.

5. CORRELATING TARGET POINT APPROACH WITH FLOQUET MODE APPROACH

The target point and the Floquet mode approaches are two of the most popular methods of station-keeping for libration point orbits in the Sun-Earth/Moon system. The early use of the Floquet mode method for station-keeping are found in the work by Gomez et al. [44,45] in 1985, and ever since, there has been substantial research on the application of the Floquet mode approach for orbit maintenance of different missions. The target point approach known for its simplicity was illustrated for station-keeping along the libration point orbits for the first time by Howell and Pernicka [24, 25] in 1990. Since then many studies have been conducted on various parameters within the method to improvise. Keeter [42,43] analyzed the weighting matrices used in the cost function of the target point approach to automate the selection process but observed that the automation process although decreased manual effort, increased the station-keeping costs. The effect of certain free parameters are analyzed to understand how each parameter potentially alters the orbit maintenance costs. The concept of the Floquet mode approach is used to evaluate the dimensions of the right weighting matrix that should provide sufficiently low costs using the target point approach.

5.1 Target Point Approach

The fundamental principle of the target point approach (TPA) is minimizing the predefined cost function, that is a combination of the applied maneuver and the deviation in position and velocity states at all the targeted future times. Introduced by Dwivedi [67] the approach is used to maintain spacecraft close to the nominal path in interplanetary missions, by targeting future position states. Howell and Pernicka [24,25] modified the algorithm to incorporate the strategy for libration point missions

by introducing additional future velocity target conditions. Howell and Gordon [40,41] and Keeter [42,43] get credits for enhancing the strategy to include more conditions. In general, the target point approach tries to compute a maneuver at present time t_0 that minimizes the cost function J defined as

$$J(\bar{p}_0, \bar{e}_0, \Delta\bar{V}) = \Delta\bar{V}^T Q \Delta\bar{V} + \sum_{i=1}^{n} \left\{ \bar{m}_i^T \mathbb{R}_i \bar{m}_i + \bar{v}_i^T \mathbb{R}_{V_i} \bar{v}_i \right\} \tag{5.1}$$

where $\Delta\bar{V}$ is the maneuver computed, $\bar{p}_0$ and $\bar{e}_0$ are the position and velocity deviation from the nominal path measured at the present time. Here, n is the total number of future target points while $\bar{m}_i$ and $\bar{v}_i$ are position and velocity deviation that would result at the ith target point if the maneuver $\Delta\bar{V}$ is implemented. The value of $\bar{m}_i$ and $\bar{v}_i$ are retrieved using the state transition matrix as

$$\begin{bmatrix} \bar{m}_i \\ \bar{v}_i \end{bmatrix} = \phi(t_i, t_0) \begin{bmatrix} \bar{p}_0 \\ \bar{e}_0 + \Delta\bar{V} \end{bmatrix} \tag{5.2}$$

$$\phi(t_i, t_0) = \begin{bmatrix} A_{i0} & B_{i0} \\ C_{i0} & D_{i0} \end{bmatrix} \tag{5.3}$$

where A_{i0}, B_{i0}, C_{i0} and D_{i0} are the 3×3 submatrices of the STM, $\phi(t_i, t_0)$. The weighting matrix Q is positive definite while $\mathbb{R}_i$ and $\mathbb{R}_{v_i}$ are positive semidefinite weighting matrix corresponding to the position and velocity deviations at ith future target point respectively. The equation (5.1) indicates an exact n combination of position and velocity deviation for future target, however, only position deviation or velocity deviation or any combination of the two can be considered as future targets. To not consider a particular state as future target, either the term is ignored or the corresponding weighting matrix is set to $\bar{0}$. The goal of TPA method is to compute a maneuver that minimizes the cost function defined in equation (5.1) that is equivalent of determining the root of the equation

$$\frac{\partial}{\partial t} J(\bar{p}_0, \bar{e}_0, \Delta\bar{V}) = 0 \tag{5.4}$$

that correspond to the minima of the cost function, J. The maneuver computed is therefore a function of the number and types of future target conditions selected.

Besides computing a low cost maneuver, one of the primary goals of a station-keeping technique is to compute a maneuver that essentially secures the spacecraft near the reference trajectory by performing maneuvers at regular intervals. Howell and Pernicka [24, 25] use two future position targets in equation (5.4) to predict the maneuver as

$$
\begin{aligned}
\Delta \bar{V} = - & \left[Q + B_{10}^T \mathbb{R}_1 B_{10} + B_{20}^T \mathbb{R}_2 B_{20} \right]^{-1} \\
& \left[\left(B_{10}^T \mathbb{R}_1 B_{10} + B_{20}^T \mathbb{R}_2 B_{20} \right) \bar{e}_0 + \left(B_{10}^T \mathbb{R}_1 A_{10} + B_{20}^T \mathbb{R}_2 A_{20} \right) \bar{p}_0 \right]
\end{aligned}
\tag{5.5}
$$

where, each A_{i0} and B_{i0} are the corresponding submatrices of STMs $\phi(t_i, t_0)$, as in equation (5.3), computed to first target point and second target points. As usual, Q is the wighting matrix corresponding to the maneuver while $\mathbb{R}_1$ and $\mathbb{R}_2$ matrices weigh the first position and second position targets respectively. Howell and Gordon [40, 41] and Keeter [42, 43] include more target points and weigh velocity states in addition to position states as additional station-keeping constraints.

The target point approach is very robust and hence used for station-keeping for orbits with wide range of stability properties. Computation of minimum maneuver does not require any advanced mathematical operators making this method not computationally expensive, however, the TPA approach uses a lot of weighting matrices Q, $\mathbb{R}_i$ and $\mathbb{R}_{V_i}$. As more future target points are considered more weighting matrices are included (each for position and velocity). Since there is no established way of selecting the weighting matrix, trial and error approach is used to identify the coefficients of each weighting matrix, to compute a low cost maneuver. As a result, the process can become tedious as more future targets are taken into consideration. Serious examination is required to understand the effects of different free parameters on the orbit maintenance costs and explore the range of appropriate weights.

5.2   Floquet Mode Approach

The Floquet mode approach (FMA) utilizes the qualitative information about the dynamical flow of the phase space along the periodic orbit, using the Invariant Manifold Theorem [68], to compute a corrective maneuver. The state deviation vectors are decomposed into its constituent linear combination of the Floquet modes utilizing the eigenstructure of the monodromy matrix i.e. the state transition matrix over one orbit period. The controller then computes an impulsive maneuver that cancels the unstable component of the state deviation vector to maintain the spacecraft close to the nominal path.

5.2.1   Floquet Theory

The state transition matrix provides a linear correlation of the flow of a deviation vector at two different times. The direction of flow of a nearby trajectory is determined by the linear combination of the Floquet modes that constitutes its states, evaluated using properties of the state transition matrix computed upon the reference path. Consider the differential equation that drives the STM,

$$\dot{\phi} = A(t)\phi \tag{5.6}$$

that is governed by a linear periodic Jacobian matrix $A(t)$ as introduced in equation (2.50). For a periodic coefficient linear system expressed as equation (5.6), the Floquet mode, $F(t)$, provides a time variant solution of ϕ as

$$\phi(t,0) = F(t)e^{\mathcal{J}t}F^{-1}(0) \tag{5.7}$$

where $\mathcal{J}$ is a constant matrix that contains the Poincaré exponents of the monodromy matrix along its diagonals. As the Jacobian matrix $A(t)$ is periodic, so is the STM and the Floquet mode $F(t)$ periodic with periodicity $T = \mathbb{P}$, where $\mathbb{P}$ is the time period of the chosen orbit. The monodromy matrix is thus expressed as

$$\phi(T,0) = F(T)e^{\mathcal{J}T}F^{-1}(0) \tag{5.8}$$

such that, $F(t)$ is periodic with $F(T) = F(0)$. Consequently, the eigenstructure at the same location on the periodic orbit is the same. The columns of matrix $F(0)$ are the eigenvectors of the monodromy matrix and columns of matrix $e^{\mathcal{J}T}$ are the corresponding eigenvalues. Let ϖ_i be the Poincaré exponent along the diagonals of matrix $\mathcal{J}$. Therefore each

$$\lambda_i = e^{\varpi_i T} \tag{5.9}$$

defines the eigenvalues of the state transition matrix. Using equation (5.9), each Poincaré exponent is computed as

$$\varpi_i = \frac{1}{T} ln(\lambda_i) \tag{5.10}$$

that are time invariant constants that represents the flow unlike the STM. The time invariance of ϖ_i provides better understanding of the flow and produces a superior behavior in numerical propagation of the states unlike the STM. The six eigenvalues of STM occurs in pairs of unstable-stable, two ones, and two complex conjugate pairs, so the Poincaré exponents are also retrieved in similar pairs.

- Unstable and Stable eigenvalues

  For unstable and stable eigenvalues, λ_i takes a value greater than 1 and smaller than 1 respectively. The Poincaré exponents are computed from equation (5.9) in the same form as

  $$\varpi_i = \frac{1}{T} ln(\lambda_i) \tag{5.11}$$

  where the unstable eigenvalue corresponds to a positive Poincaré exponent while a stable eigenvalue is denoted by a negative Poincaré exponent.

- Unit eigenvalues

  For eigenvalues that are 1, the Poincaré exponents computed from equation (5.9) by substituting $\lambda_i = 1$ yields,

  $$\varpi_i = 0 \tag{5.12}$$

- Complex conjugate pairs of eigenvalues

  The complex conjugate eigenvalues exists as $\lambda_i = a \pm ib = \mathcal{R}e^{\pm i\vartheta}$, the Poincaré exponents computed from equation (5.9) is in the form,

  $$\varpi_i = \frac{1}{T}ln\left(\mathcal{R}e^{\pm i\vartheta}\right) = \frac{1}{T}\left\{ln(\mathcal{R}) \pm i\vartheta\right\} \tag{5.13}$$

  where, $\mathcal{R} = \sqrt{a^2 + b^2}$ and $\vartheta = tan^{-1}(b/a)$.

The time invariant $\mathcal{J}$ matrix is used as a basis to describe the direction of flow at any time using the Floquet modes. From equation (5.7), the Floquet modes at any time, t, is represented as

$$F(t) = \phi(t,0)F(0)e^{-\mathcal{J}t} \tag{5.14}$$

where $t = 0$ corresponds to any chosen initial condition along the periodic orbit. The Floquet modes $F(t)$ exists as a six-dimensional column vectors, $\bar{\mathcal{F}}_i(t)$, with non orthogonal basis as

$$F(t) = \left[\bar{\mathcal{F}}_1(t), \bar{\mathcal{F}}_2(t), \bar{\mathcal{F}}_3(t), \bar{\mathcal{F}}_4(t), \bar{\mathcal{F}}_5(t), \bar{\mathcal{F}}_6(t)\right] \tag{5.15}$$

that are computed using equations (5.11), (5.12), (5.13) and (5.14) as

$$\bar{\mathcal{F}}_1(t) = \phi(t,0)\bar{\mathcal{F}}_1(0)\exp\left(-\frac{t}{T}ln(\lambda_1)\right) \tag{5.16}$$

$$\bar{\mathcal{F}}_2(t) = \phi(t,0)\bar{\mathcal{F}}_2(0)\exp\left(-\frac{t}{T}ln(\lambda_2)\right) \tag{5.17}$$

$$\bar{\mathcal{F}}_3(t) = \phi(t,0)\bar{\mathcal{F}}_3(0) \tag{5.18}$$

$$\bar{\mathcal{F}}_4(t) = \phi(t,0)\bar{\mathcal{F}}_4(0) \tag{5.19}$$

$$\bar{\mathcal{F}}_5(t) = \phi(t,0)\bar{\mathcal{F}}_5(0)\mathcal{R}^{-t/T}\left\{\cos\left(\vartheta\frac{t}{T}\right) - i\,sin\left(\vartheta\frac{t}{T}\right)\right\} \tag{5.20}$$

$$\bar{\mathcal{F}}_6(t) = \phi(t,0)\bar{\mathcal{F}}_6(0)\mathcal{R}^{-t/T}\left\{\cos\left(\vartheta\frac{t}{T}\right) + i\,sin\left(\vartheta\frac{t}{T}\right)\right\} \tag{5.21}$$

such that, $\bar{\mathcal{F}}_i(0)$ are the eigenvectors of the corresponding monodromy matrix. The Floquet modes provide the flow dynamics of the spacecraft along the periodic orbit. Any state in the vicinity of the periodic orbit can be modeled as a linear combinations of the Floquet modes. The same principle is applied for orbit maintenance by filtering out the unstable mode.

5.2.2 Floquet Controller

The ability to filter a given state as a linear combination of its different constituent Floquet modes are exercised to compute a station-keeping maneuver. The aim is to calculate a maneuver that will cancel any component in the direction of the unstable Floquet mode to prevent the spacecraft from deviating. Since the L_1 libration point orbit in the Sun-Earth/Moon system chosen for the mission is highly unstable, the spacecraft will deviate from the nominal orbit due to perturbations along the way. Any perturbation in position and velocity at any time, t, is modeled as a linear combination of the six Floquet modes as

$$\delta \bar{x}(t) = \sum_{i=1}^{6} c_i \bar{\mathcal{F}}_i(t) \tag{5.22}$$

where c_i are some coefficients and $\bar{\mathcal{F}}_i$ are the corresponding Floquet mode vectors. Since the Floquet modes are modeled upon the eigenvalues, they too exists as unstable, stable and oscillatory modes. Rather, if equation (5.22) is represented as

$$\delta \bar{x}(t) = \delta \bar{x}_1(t) + \delta \bar{x}_2(t) + \delta \bar{x}_3(t) + \delta \bar{x}_4(t) + \delta \bar{x}_5(t) + \delta \bar{x}_6(t) \tag{5.23}$$

then, $\delta \bar{x}_1(t)$ represents the unstable component of the perturbation, $\delta \bar{x}_2(t)$ is the stable component while components $\delta \bar{x}_{3-6}(t)$ are oriented along the oscillatory Floquet modes. Let vector $\bar{\mathcal{F}}_1(t)$ represent the unstable mode, so the component of perturbation, $\delta \bar{x}_1(t)$, in this direction will amplify over time. The controller in the Floquet mode station-keeping method estimates a corrective maneuver $\Delta \bar{V}$ that cancels the component of perturbation oriented along the unstable Floquet mode. Mathematically, addition of a maneuver $\Delta \bar{V}$ amends the equation (5.22) to

$$\delta \bar{x}(t) + \Delta \bar{V} = \sum_{i=2}^{6} \alpha_i \bar{\mathcal{F}}_i(t) \tag{5.24}$$

that is void of any component along the unstable Floquet mode direction.

The addition of a maneuver $\Delta \bar{V}$ alters only the components along the three velocity states but equation (5.24) can be potentially satisfied by modification of linear

combination of the five Floquet modes $\bar{\mathcal{F}}_2(t)$ through $\bar{\mathcal{F}}_6(t)$ by their coefficients α_2 through α_6, hence there are infinitely many solutions possible. A possible solution is the minimum norm solution, but several other possible solutions are considered based on mission requirements. For a perturbation $\bar{p}_0$ in position and $\bar{e}_0$ in velocity at time, $t = 0$, the corrective maneuver computed satisfies

$$\begin{bmatrix} \bar{p}_0 \\ \bar{e}_0 \end{bmatrix} + \begin{bmatrix} \bar{0} \\ \Delta \bar{V} \end{bmatrix} = \begin{bmatrix} \bar{\mathcal{F}}_2(0) & \bar{\mathcal{F}}_3(0) & \bar{\mathcal{F}}_4(0) & \bar{\mathcal{F}}_5(0) & \bar{\mathcal{F}}_6(0) \end{bmatrix} \begin{pmatrix} \alpha_2 \\ \alpha_3 \\ \alpha_4 \\ \alpha_5 \\ \alpha_6 \end{pmatrix} = F(0) \begin{pmatrix} 0 \\ \alpha_2 \\ \alpha_3 \\ \alpha_4 \\ \alpha_5 \\ \alpha_6 \end{pmatrix} \quad (5.25)$$

where α_2 through α_6 are 5 free variables while $\Delta\bar{V}$ can be up to 3 free variables. Each $\bar{\mathcal{F}}_i(0)$ is a 6×1 column vector. The value of $\Delta\bar{V}$ can be computed as per the mission requirement. Few potential constraints are as discussed.

- Single Axis Control

  A maneuver $\Delta\bar{V}$ is computed, such that it is aligned along one of the axis either x, y or z. For example, consider maneuver along x-axis, therefore equation (5.25) becomes

$$\begin{bmatrix} \bar{p}_0 \\ \bar{e}_0 \end{bmatrix} = \begin{bmatrix} \bar{\mathcal{F}}_2(0) & \bar{\mathcal{F}}_3(0) & \bar{\mathcal{F}}_4(0) & \bar{\mathcal{F}}_5(0) & \bar{\mathcal{F}}_6(0) & \begin{matrix} 0 \\ 0 \\ 0 \\ -1 \\ 0 \\ 0 \end{matrix} \end{bmatrix} \begin{pmatrix} \alpha_2 \\ \alpha_3 \\ \alpha_4 \\ \alpha_5 \\ \alpha_6 \\ \Delta V_x \end{pmatrix} \quad (5.26)$$

  where $[\alpha_2, \alpha_3, \alpha_4, \alpha_5, \alpha_6, \Delta V_x]^T$ are the 6 unknowns. There are 6 equations and 6 unknowns, hence a perfect solution can be computed. A unique maneuver exists in a single axis controller.

- Three Axis Control

  A maneuver $\Delta \bar{V}$ that is free to align itself along any 3D orientation can be computed from

$$
\begin{bmatrix} \bar{p}_0 \\ \bar{e}_0 \end{bmatrix} = \begin{bmatrix} \bar{\mathcal{F}}_2(0) & \bar{\mathcal{F}}_3(0) & \bar{\mathcal{F}}_4(0) & \bar{\mathcal{F}}_5(0) & \bar{\mathcal{F}}_6(0) & \begin{matrix} 0 & 0 & 0 \\ 0 & 0 & 0 \\ 0 & 0 & 0 \\ -1 & 0 & 0 \\ 0 & -1 & 0 \\ 0 & 0 & -1 \end{matrix} \end{bmatrix} \begin{pmatrix} \alpha_2 \\ \alpha_3 \\ \alpha_4 \\ \alpha_5 \\ \alpha_6 \\ \Delta V_x \\ \Delta V_y \\ \Delta V_z \end{pmatrix} \tag{5.27}
$$

  where $[\alpha_2, \alpha_3, \alpha_4, \alpha_5, \alpha_6, \Delta V_x, \Delta V_y, \Delta V_z]^T$ are the 8 unknowns. There are 6 equations and 8 unknowns, hence infinitely many solutions are possible, one such solution is the minimum norm solution.

Similarly, a two axis maneuver, a planar maneuver or any other mission design constraints can be incorporated into computing a corrective station-keeping maneuver. Maneuvers are computed and executed at regular intervals to maintain the spacecraft within a close distance to the nominal orbit.

5.3 Correlation between Target Point and Floquet mode Approaches

The target point approach uses a cost function that is minimized to compute a maneuver while the Floquet mode approach uses the qualitative information of the flow of the reference trajectory using the eigenstructure to predict a maneuver that cancels any unstable component at that location. To correlate the target point approach to the Floquet mode approach, it must be expressed in a similar way as the mode of operation of the later. The eigenvectors used in the Floquet mode approach are the property of the monodromy matrix, the state transition matrix computed over one time period. In the TPA method, targeting a base-point one time period

beyond essentially provides similar information as that of the Floquet mode approach. Additionally, let the computed maneuver result in a position deviation of $\bar{m}_1$ and a velocity deviation of $\bar{v}_1$ at the end of future target time of one time period, $\mathbb{P}$. The monodromy matrix relates the value $\bar{m}_1$ and $\bar{v}_1$ due to current position deviation $\bar{p}_0$, velocity deviation $\bar{e}_0$ and proposed maneuver $\Delta\bar{V}$ as

$$
\begin{bmatrix} \bar{m}_1 \\ \bar{v}_1 \end{bmatrix} = \phi(T,0) \begin{bmatrix} \bar{p}_0 \\ \bar{e}_0 + \Delta\bar{V} \end{bmatrix} = \begin{bmatrix} A_{10} & B_{10} \\ C_{10} & D_{10} \end{bmatrix} \begin{bmatrix} \bar{p}_0 \\ \bar{e}_0 + \Delta\bar{V} \end{bmatrix} \tag{5.28}
$$

where time $T = \mathbb{P}$ while A_{10}, B_{10}, C_{10} and D_{10} are 3×3 submatrices of $\phi(T,0)$. The equation (5.28) is expressed in the same form as Delta V Controller type 1 by Gordon [41] with one future position state and one future velocity state target. Using a combination of one position state and one velocity state targeting at a target time of one time period, the effective mode of operation of the target point approach should be similar to the Floquet mode approach. The similarity property is used to explore behavior of certain weighting matrices used in the target point approach.

The cost function J in the target point approach for Delta V Controller type 1 that could potentially replicate the behavior of the Floquet mode approach is modeled as

$$
J(\bar{p}_0, \bar{e}_0, \Delta\bar{V}) = \Delta\bar{V}^T Q \Delta\bar{V} + \bar{m}_1^T \mathbb{R} \bar{m}_1 + \bar{v}_1^T \mathbb{R}_V \bar{v}_1 \tag{5.29}
$$

where Q, $\mathbb{R}$ and $\mathbb{R}_V$ are weighting matrices. The positive definite matrix Q directly controls the size of the maneuver $\Delta\bar{V}$ while matrices $\mathbb{R}$ and $\mathbb{R}_V$ weighs the position and velocity deviation after one time period respectively. The maneuver that minimizes the cost function J essentially satisfies the relation

$$
\frac{\partial}{\partial\Delta\bar{V}} J(\bar{p}_0, \bar{e}_0, \Delta\bar{V}) = 0 \tag{5.30}
$$

$$
\begin{aligned}
Q\Delta\bar{V} = &- \left[B_{10}^T \mathbb{R} B_{10} + D_{10}^T \mathbb{R}_V D_{10} \right] \left(\bar{e}_0 + \Delta\bar{V} \right) \\
&- \left[B_{10}^T \mathbb{R} A_{10} + D_{10}^T \mathbb{R}_V C_{10} \right] \bar{p}_0
\end{aligned} \tag{5.31}
$$

resulting in an implicit relation. To compute the positive definite diagonal matrix Q, the values of $\Delta \bar{V}$ obtained from each of the Floquet mode maneuver are substituted into the equation (5.31) along with values of $\mathbb{R}$ and $\mathbb{R}_V$ that are taken as identity I, as the Floquet mode approach is not biased to any position or velocity states, however, $\mathbb{R}$ and $\mathbb{R}_V$ may be tuned if there seems to be a possibility of decreasing the maneuver magnitude once the matrix Q is tuned, but in general matrix Q seems to affect overall costs the most.

One of the most applicable information procured by correlating the target point approach with the Floquet mode approach is the dimensions of the Q matrix. Since the target point approach and the Floquet mode approach do not have one to one correspondence, the elements of the matrix Q calculated using equation (5.31) may be negative for some maneuvers computed by the Floquet mode approach. The equation (5.30) satisfies both the maxima and minima, but to minimize the cost function the value of Q computed in equation (5.31) should necessarily represent the local minima. The additional constraint to ensure a minima in equation (5.30) is

$$\frac{\partial^2}{\partial \Delta \bar{V}^2} J(\bar{p}_0, \bar{e}_0, \Delta \bar{V}) = Q > 0 \tag{5.32}$$

hence any solution for Q computed from equation (5.31) that results in negative value represents the local maxima, as a result they are disregarded. Only positive values of Q that represent the local minima are used for tuning the matrix Q. The purpose of a positive definite matrix Q used in the target point approach is thus justified.

5.4 Preliminary Results

5.4.1 Effect of Weighting Matrices on Station-keeping costs in the Target Point Approach

The target point station-keeping approach computes corrective maneuvers that corresponds to the local minima of the cost function. The weighting matrices govern

the magnitude and the direction of the computed maneuver. The primary challenge using TPA is that, as the number of future target points increases the number of weighting matrices to be used. Since there is no specific method to select the weights, applying trial and error to get the optimal solution from significantly large combinations of weights is implausible. Furthermore, addition of many future targets does not necessarily improve the solution. One of the aim of this research is to select relevant number of future target conditions and explore effect of the weighting matrices on the maneuver cost. It is studied in section 5.3 to establish a correlation between the Floquet mode and the target point approach. Although the Floquet mode provides explanatory solution it is computationally expensive. Tuning the target point approach with the right weights could make it more reliable.

The formulation of the cost function by itself reveals the effect of weighting matrices on the corresponding free variables. The Floquet mode method closely matches with Gordon's Delta V Controller type 1 [41] with future velocity and position target scheme at one time period downstream, for which, the cost function J is defined as

$$J = \Delta \bar{V}^T Q \Delta \bar{V} + \bar{m}_1^T \mathbb{R} \bar{m}_1 + \bar{v}_1^T \mathbb{R}_V \bar{v}_1 \tag{5.33}$$

where the matrix Q directly controls the maneuver $\Delta \bar{V}$ while $\mathbb{R}$ and $\mathbb{R}_V$ controls the deviation in position and velocity at the future target point that is one period downstream in this case. Here, subscripts of $\mathbb{R}$ and $\mathbb{R}_V$ are ignored as only one position and one velocity targets are considered. Since matrix Q has direct and maximum influence on the magnitude of the maneuver, it becomes the primary choice of improvement. If the system is assumed to be one-dimensional then a large value of Q would diminish the $\Delta \bar{V}$ magnitude and vice-versa, however, for a three-dimensional system making a direct conclusion is not definite. A component wise analysis is mandatory to describe the trend.

For consistency in analysis, the weighting matrices must be expressed in the right units. If the cost function J is expressed in the non-dimensional units with matrix

Q, $\mathbb{R}$ and $\mathbb{R}_V$ defined as identity, for simplicity, then the matrix Q in the dimensional units would be scaled by the order of magnitude of t^{*2} to obtain $\Delta\bar{V}$ in in terms of km/s. In the Sun-Earth/Moon barycenter system t^{*2} is approximately equal to 2.52×10^{13} s^2. Such large value of Q is comparable to the ones used by Howell and Pernicka [24,25], Howell and Gordon [40,41] and Howell and Keeter [42,43]. Since Q is a 3×3 positive definite diagonal matrix, let it be represented as

$$Q = \begin{bmatrix} q_1 & & \\ & q_2 & \\ & & q_3 \end{bmatrix} \qquad (5.34)$$

such that, $q_1, q_2, q_3 > 0$. Each of q_1, q_2 and q_3 weighs individual components of the $\Delta\bar{V}$ vector along x, y and z-direction respectively. At every location near the reference orbit where a maneuver of size ΔV_{min} is detected by Floquet mode approach, an alternative maneuver is computed using TPA to explore the influence of each of the q_i components within the TPA. The magnitude of $\Delta\bar{V}$ is computed by varying each of q_i from 10^{10} to 10^{18} in dimensional units, equivalent to approximately 10^{-4} to 10^4 in the non-dimensional case. As a result, a four-dimensional array of various combinations of q_1, q_2, q_3 and corresponding value of $\Delta\bar{V}$ are obtained, that is analyzed to understand the effect of the weighting matrix Q on the cost of each individual maneuver.

It was expected that a large value of q_i would decrease the maneuver along the corresponding direction, and vice-versa, but such a trend was found to be true only for the cases where minimum possible $\Delta\bar{V}$ was set to zero. The case suggests that no matter how small the computed maneuver is, it will be executed (Even of the order of mm/s or lesser). In no event, such small maneuver can be executed due to engine limitations. Besides, the maneuver computed is smaller than the orbit determination error making it impossible to even detect such small maneuvers. When the minimum executable $\Delta\bar{V}$ magnitude was altered to more practically feasible values

like 5 cm/s, 10 cm/s, 20 cm/s, 50 cm/s or 100 cm/s, the trend was unlike the previous case. To be certain about the trend, the four-dimensional array of combinations of q_i and $\Delta \bar{V}$ were computed at different maneuver locations, and for different ΔV_{min} conditions. For representation of this four-dimensional array, q_1, q_2 and q_3 are modeled as the three axis while the fourth dimension, ΔV magnitude, is indicated with a color scheme as demonstrated in Figure 5.1. An enlarged plot for an arbitrary maneuver for $\Delta V_{min} = 10$ cm/s is shown in Figure 5.2. The plots in Figures 5.1 and 5.2 are in fact a solid block with varying color scheme that represent the magnitude of computed maneuver in a three-dimensional grid. For visual inspection, a solid block is not a smart choice as it is not possible to examine the values not along the outside surface, hence for better visual representation, parallel planes with fixed q_3 values are chosen. The specific reason why q_3 was fixed instead of q_1 or q_2 is explained further. The plots in Figure 5.1 only showcase patterns observed at majority of the maneuver locations, without making a claim that all maneuvers exists in the same way. In fact at few maneuver locations the trend was not similar especially for low ΔV_{min} values such as 5 cm/s and 10 cm/s. Moreover, it was observed that with increase in ΔV_{min}, the trend became more ordered.

The magnitude of maneuver computed at a particular location depends greatly on the Q matrix and it is certain from the color distribution indicated in Figure 5.2. Based on knowledge about a one-dimensional cost function, it is expected that a large weight diminishes the value of the corresponding free variable and vice versa. Using the same intuition, it was expected that the lowest magnitude of computed velocity would appear at higher values of q_1, q_2 and q_3 while the highest value of maneuver magnitude would appear diagonally opposite to the lowest velocity case on the 3D grid map i.e. at low values of q_1, q_2 and q_3, but the actual trend observed contradicts this intuition. Indeed, the variations along the three axes q_1, q_2 and q_3 are not similar. Firstly, in most maneuver locations, fixing q_1 and q_2 and moving only along the q_3 axis does not make any significant changes in the magnitude of maneuver computed.
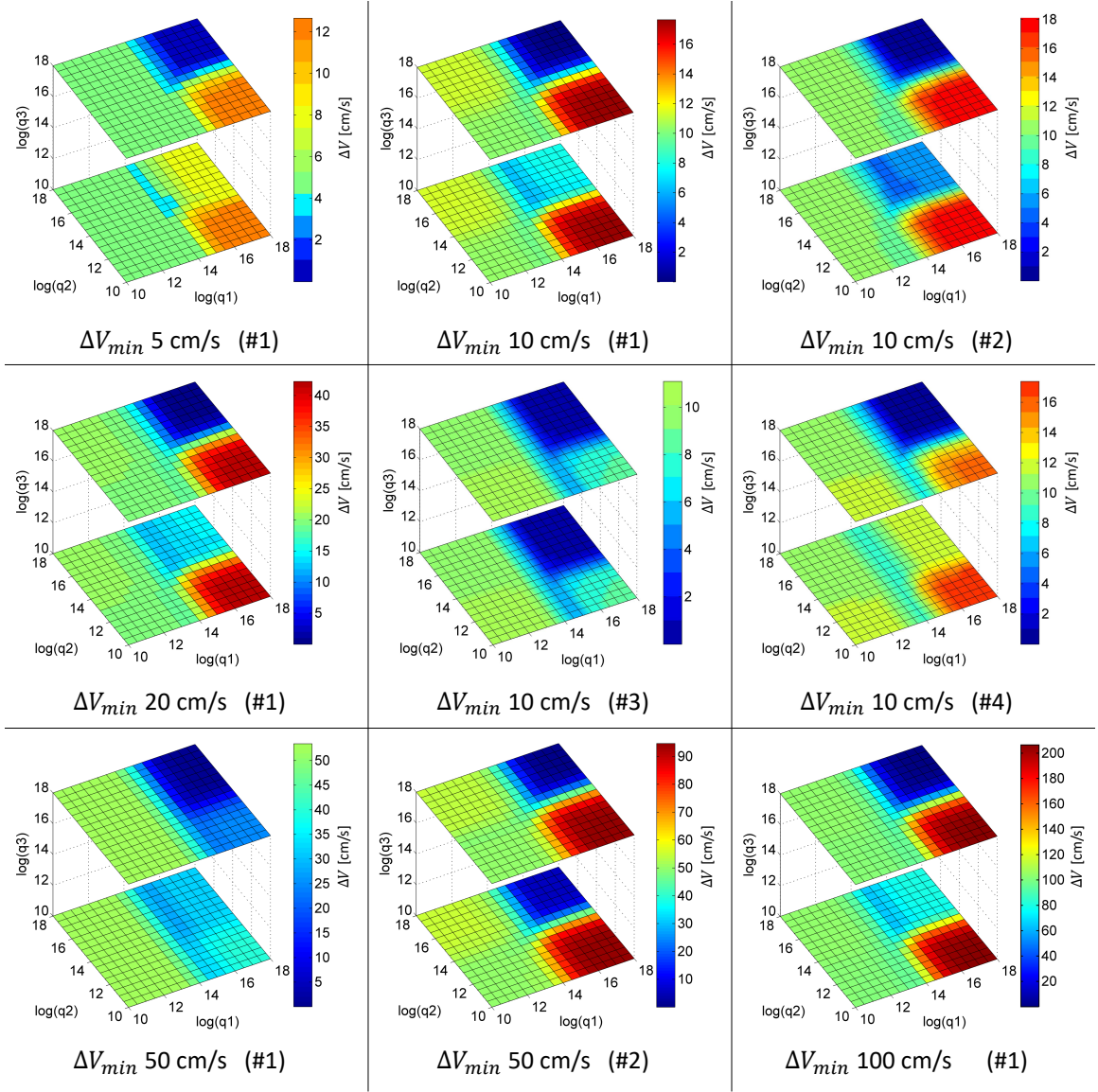
Figure 5.1. Variation in maneuver magnitude for different Q matrix combinations for different ΔV_{min} cases. Each individual plot corresponds to an arbitrary maneuver location. The symbol '#' indicates sequential numbering for a particular ΔV_{min} case. For consistency, color scheme is skewed to match ΔV_{min} with green color in all plots.
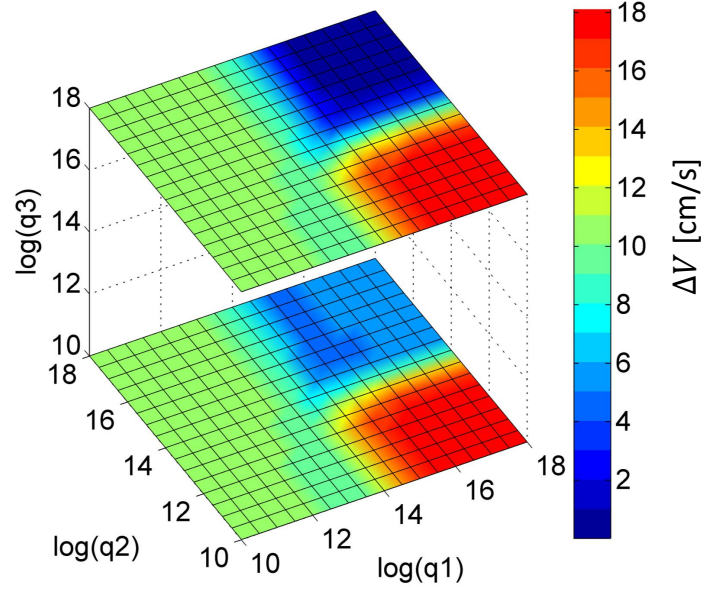
Figure 5.2. Variation in maneuver magnitude for different Q matrix combinations for $\Delta V_{min} = 10$ cm/s case at an arbitrary maneuver location. For consistency, color scheme is skewed to match ΔV_{min} with green color.

This is precisely the reason why the four-dimensional solid block is displayed as a combination of two parallel planes along the q_3 direction. The trend indicates that perturbations along the z-direction does not grow rapidly. thus, the necessity for a maneuver aligned along the z-direction is non trivial for the obit selected for the mission. The asymmetric distribution of computed maneuver along the three-dimensional grid implies maneuvers are not equal in all the three direction. Certain directions are more sensitive that the others. For low values of q_1 in Figure 5.2, moving parallel to q_2 axis for fixed q_1 and q_3 show no notable change in maneuver magnitude. The behavior implies that the change in y-velocity does not cause any substantial change in the overall maneuver magnitude especially when x-maneuver is not constrained. Only for large q_1 value (i.e. x-maneuver is forcefully restricted), change in y-velocity affects the maneuver magnitude. Evidently, the maneuvers are dominant along the

x-direction.

The algorithm when free to compute a maneuver in any spatial direction without any constraint i.e. using low values of dimensional matrices q_1, q_2 and q_3 ($q_1 = q_2 = q_3 = 10^{10}$), the magnitude of maneuver computed is same as computed for low value of q_1 with high values of q_2 and q_3 ($q_1 = 10^{10}$, $q_2 = q_3 = 10^{18}$). The maneuver is inclined almost along the x-direction, hence change in y and z-maneuvers makes almost no significant impact on the overall maneuver cost. The behavior is pictorially represented in Figure 5.3 as a plane with fixed low q_1 value indicating the different combination of weights that has the same maneuver magnitudes. The arrow represents directions of completely unrestricted maneuver (low values of q_i) and the direction of pure x-direction maneuver (low q_1 but high q_2, q_3). For the Sun-Earth/Moon L_1 Halo orbit chosen for the mission, the dominance of x-velocity is highlighted. The behavior can equated to the presence of strong gravitational force along the line joining the primaries that is along the rotational x-axis.

The trends observed were based on individual maneuver locations, however, the general behavior remained same across all the maneuver locations. It can therefore be concluded that, to purely capitalize the fixed x-direction maneuvers low value of q_1 with high values of q_2 and q_3 must be selected when performing station-keeping using the target point approach. Ability to perform only x-direction maneuvers holds beneficial from the mission attitude control perspective, as the orientation of the engine thrusters need not be altered to any spatial directions every time a maneuver needs to be executed.

5.4.2 Direction of Computed Maneuvers

The combinations of the weighting matrix Q in the target point approach supports the dominance of maneuvers along the x-direction, but needs to be measured in terms
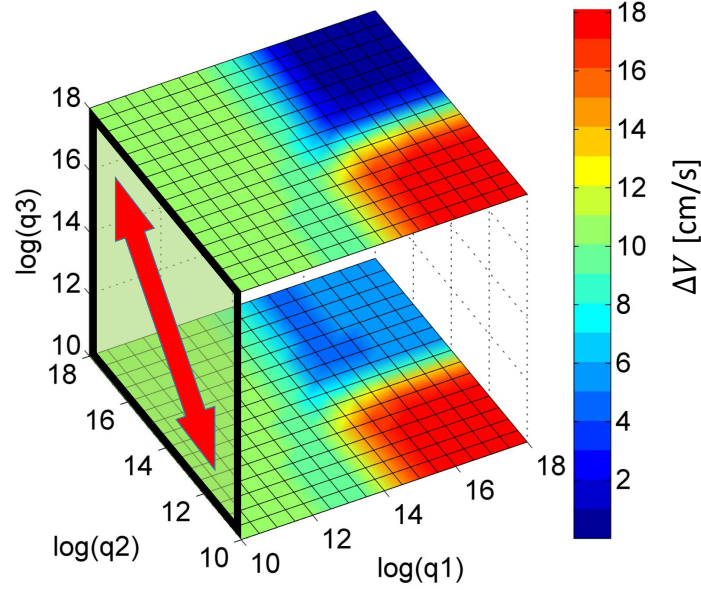
Figure 5.3. Almost constant maneuver magnitude for different $q_2 - q_3$ combinations for low q_1 values, reflective of dominance of x-direction maneuvers computed using the target point approach.

of some explicit quantity to make reasonable comparisons. Let a quantity v_x be defined as

$$v_x = \frac{\Delta V_x}{||\Delta \bar{V}||} \times 100\% \tag{5.35}$$

such that, ΔV_x is the component along the x-direction while $||\Delta \bar{V}||$ is the magnitude of the computed corrective maneuver. For simplicity $||\Delta \bar{V}||$ can also be represented as ΔV, i.e. without a vector symbol. At every maneuver location, the value of v_x is computed to quantify the x-dominance. For a maneuver perfectly aligned along the x-direction will have $v_x = 100\%$ while a maneuver with no component along the x-direction will have $v_x = 0\%$.

A station-keeping scenario is simulated for a mission duration of 2 years with parameters specified in Table 5.1. Both Type A and Type B orbit determination errors

Table 5.1. Input parameters for Station-Keeping simulation to detect direction of maneuvers.

Model	SEM Ephemeris
Station-keeping algorithm	Target point approach
Mission duration	2 Years
ΔV_{min} [cm/s]	Variable 5, 10, 20, 50, 100
Δt_{min} [days]	30
Tracking interval [days]	2
Orbit determination errors	Type A, Type B
Halo orbit injection epoch	January 13, 2020
Q [dimensional]	• Diag(10^{10}, 10^{10}, 10^{10}) • Diag(10^{10}, 10^{18}, 10^{18})
$\mathbb{R}$	$I_{3\times3}$
$\mathbb{R}_V$	$I_{3\times3}$

are used for simulation with two combination of Q matrix, one for unrestricted spatial maneuver and another for restricted x-direction maneuvers to make a reasonable comparison on the dominance of maneuvers along the x-direction. At each maneuver location v_x is calculated and displayed as color gradient as demonstrated in Figure 5.4 and Figure 5.5 for Type A and Type B ODEs respectively. Both Figure 5.4 and Figure 5.5 are records for 10 Monte Carlo iterations. For all plots on the left in Figure 5.4 and Figure 5.5, where $q_1 = q_2 = q_3 = 10^{10}$ i.e. algorithm is free to compute a maneuver is any spatial direction, but most maneuvers seem to be inclined towards x-direction except in a very few cases where the ΔV_{min} are small and for larger orbit determination error as in Type B. Besides as ΔV_{min} increases from 5 cm/s to 100 cm/s, the maneuvers become more aligned towards x-axis. The number of blue and yellow dots as in case of ΔV_{min}=5 cm/s reduces as ΔV_{min} increases for both Type

A and Type B ODEs. As the major gravitational bodies are along the rotational x-axis, perturbations are more likely to amplify along the x-direction, hence x-control maneuvers should be suffice for station-keeping. This is achieved by suppressing maneuvers along y and z-direction to get pure x-control maneuvers. The weights chosen as $q_1 = 10^{10}$ and $q_2 = q_3 = 10^{18}$ satisfy the criterion. All the maneuvers thus computed are essentially in the rotational x-direction. As indicated in the plots on the right hand side in Figure 5.4 and Figure 5.5, the v_x value computed for each maneuvers for different ΔV_{min} cases are all almost 100%.

5.4.3 Search for Low Cost x-direction Control Maneuvers

The unconstrained spatial maneuver obtained through $q_1 = q_2 = q_3 = 10^{10}$ in the target point approach being closely aligned in the x-direction indicates that constrained x-axis maneuver could be leveraged for the entire station-keeping process. Constraining a maneuver in a particular direction using the target point approach is done by providing corresponding asymmetric weights. Since maneuver is aimed only in the x-direction, the corresponding coefficient q_1 is chosen small to vary between 10^{10} and 10^{18} in the dimensional units. Besides, no component of maneuver in the y and z-direction is achieved by biasing q_2 and q_3 to be extremely high. Ideally $q_2 = q_3 = \infty$ for a perfect x-direction maneuver, however, for computational purposes $q_2, q_3 \geq 10^{18}$. Increasing q_2, q_3 much beyond 10^{18} have practically insignificant change in maneuver cost. Figure 5.6 indicates that the possible combinations of Q matrix required for a x-control maneuver that is procured by moving along the marked edge. The edge corresponds to varying q_1 value with a fixed large value of q_2 and q_3. As discussed, changing $q_2, q_3 \geq 10^{18}$ causes almost no meaningful change to maneuver cost. For convenience $q_2, q_3 = 10^{25}$ is used for this work.

The possible domain of Q matrix is essentially reduced to one dimension by varying only q_1 component and fixing $q_2, q_3 = 10^{25}$ but the suitable range of values are
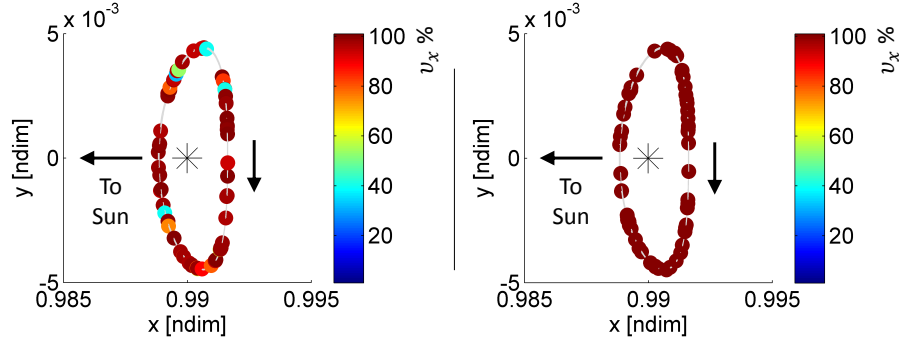
(a) $\Delta V_{min} = 5$ cm/s. Type A ODE. Left $q_1 = q_2 = q_3 = 10^{10}$. Right $q_1 = 10^{10}$, $q_2 = q_3 = 10^{18}$.
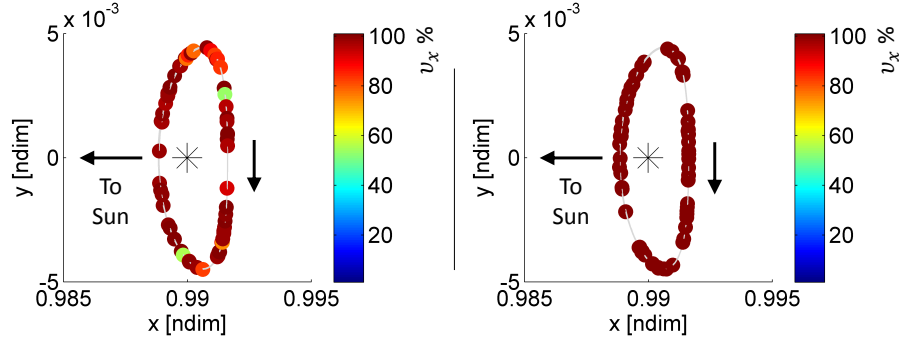
(b) $\Delta V_{min} = 10$ cm/s. Type A ODE. Left $q_1 = q_2 = q_3 = 10^{10}$. Right $q_1 = 10^{10}$, $q_2 = q_3 = 10^{18}$.
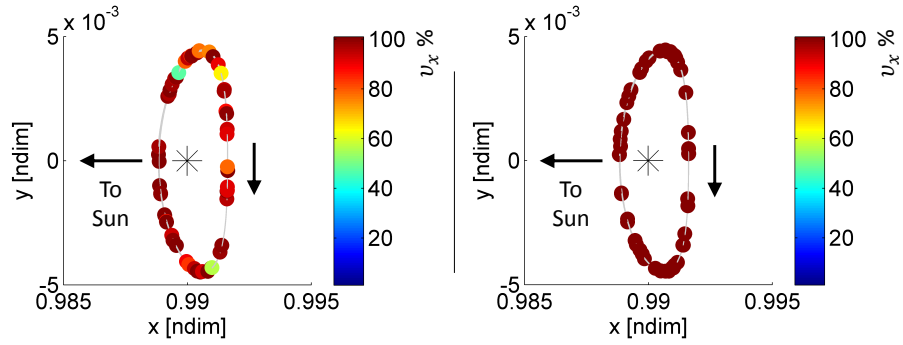
(c) $\Delta V_{min} = 20$ cm/s. Type A ODE. Left $q_1 = q_2 = q_3 = 10^{10}$. Right $q_1 = 10^{10}$, $q_2 = q_3 = 10^{18}$.
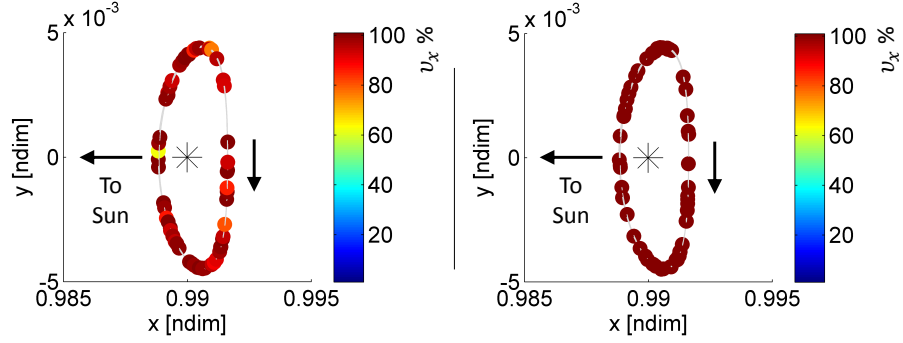
(d) $\Delta V_{min} = 50$ cm/s. Type A ODE. Left $q_1 = q_2 = q_3 = 10^{10}$. Right $q_1 = 10^{10}$, $q_2 = q_3 = 10^{18}$.
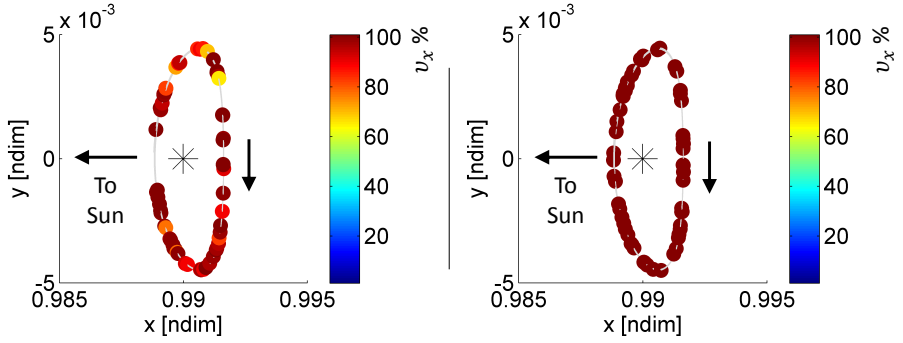
(e) $\Delta V_{min} = 100$ cm/s. Type A ODE. Left $q_1 = q_2 = q_3 = 10^{10}$. Right $q_1 = 10^{10}$, $q_2 = q_3 = 10^{18}$.

Figure 5.4. Alignment of maneuvers with x-direction measured as $v_x\%$ for different ΔV_{min} cases computed using the target point approach. Plot on left side within each sub figure corresponds to $q_1 = q_2 = q_3 = 10^{10}$ while plot on right side within each sub figure corresponds to $q_1 = 10^{10}$, $q_2 = q_3 = 10^{18}$. All figures correspond to Type A orbit determination error.
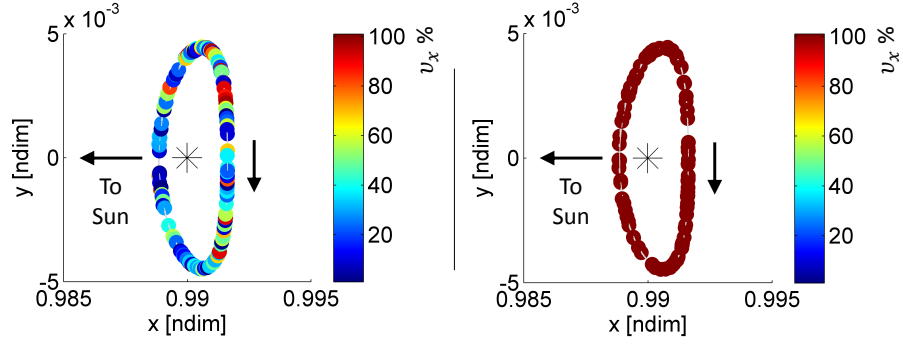
(a) $\Delta V_{min} = 5$ cm/s. Type B ODE. Left $q_1 = q_2 = q_3 = 10^{10}$. Right $q_1 = 10^{10}$, $q_2 = q_3 = 10^{18}$.
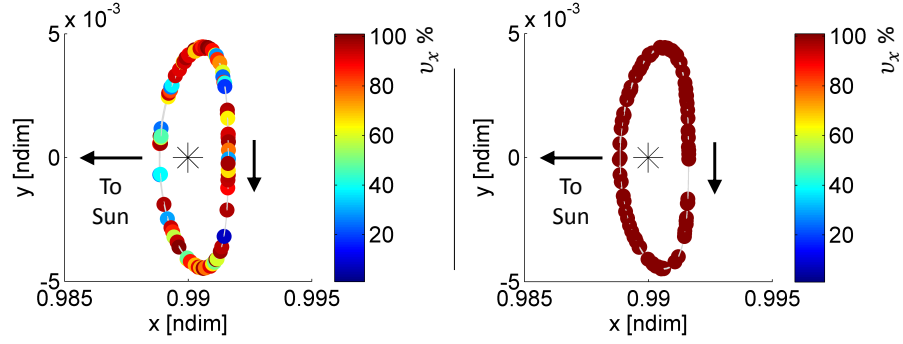
(b) $\Delta V_{min} = 10$ cm/s. Type B ODE. Left $q_1 = q_2 = q_3 = 10^{10}$. Right $q_1 = 10^{10}$, $q_2 = q_3 = 10^{18}$.
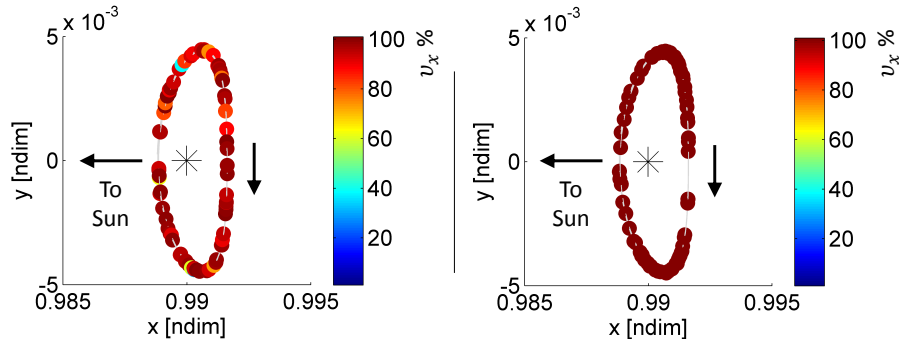
(c) $\Delta V_{min} = 20$ cm/s. Type B ODE. Left $q_1 = q_2 = q_3 = 10^{10}$. Right $q_1 = 10^{10}$, $q_2 = q_3 = 10^{18}$.
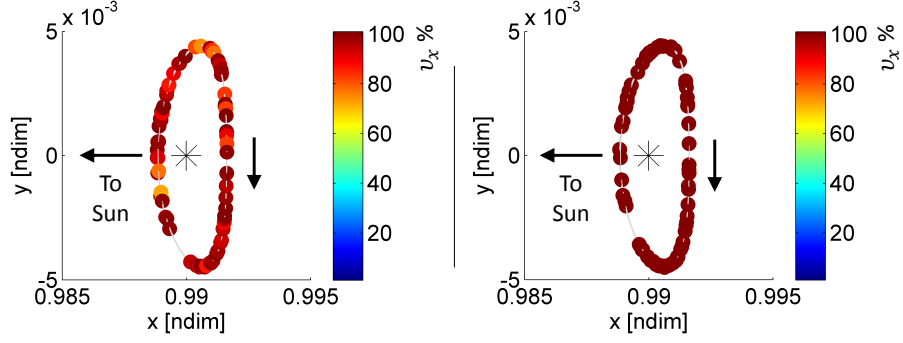
(d) $\Delta V_{min} = 50$ cm/s. Type B ODE. Left $q_1 = q_2 = q_3 = 10^{10}$. Right $q_1 = 10^{10}$, $q_2 = q_3 = 10^{18}$.
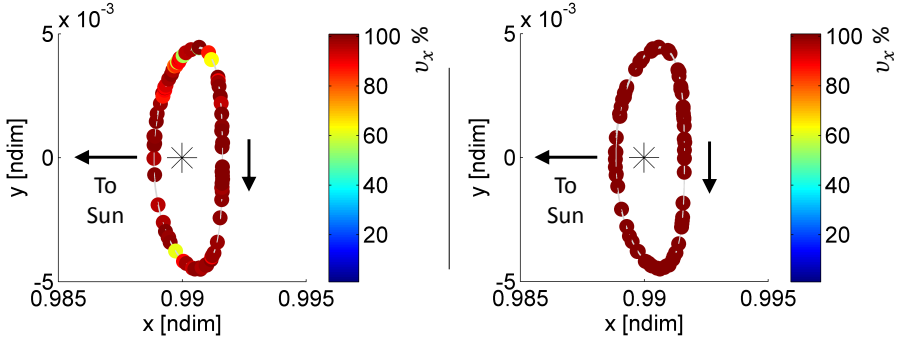
(e) $\Delta V_{min} = 100$ cm/s. Type B ODE. Left $q_1 = q_2 = q_3 = 10^{10}$. Right $q_1 = 10^{10}$, $q_2 = q_3 = 10^{18}$.

Figure 5.5. Alignment of maneuvers with x-direction measured as $v_x\%$ for different ΔV_{min} cases computed using the target point approach. Plot on left side within each sub figure corresponds to $q_1 = q_2 = q_3 = 10^{10}$ while plot on right side within each sub figure corresponds to $q_1 = 10^{10}$, $q_2 = q_3 = 10^{18}$. All figures correspond to Type B orbit determination error.
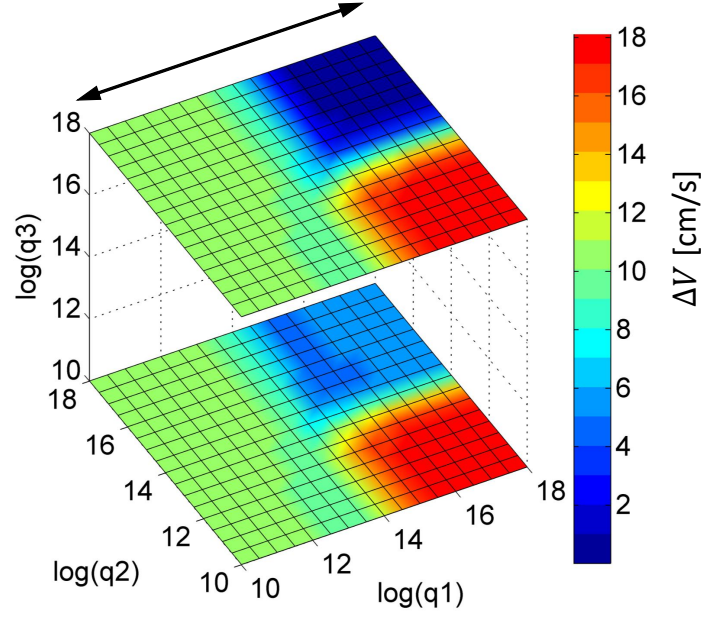
Figure 5.6. Potential domain of Q matrix for x-axis control maneuvers using the target point approach. The arrow represents possible combinations of q_1, q_2, q_3 that form diagonal elements of matrix Q.

however unknown to begin exploring for the minimal station-keeping cost. The Floquet mode approach has the capability to find x-control maneuvers required for the station-keeping process. The maneuvers from the Floquet mode approach are used to make a selection of a range of possible weights to explore the target point approach. Using the scheme discussed in section 5.3, each maneuver computed in the Floquet mode approach can be equivalently produced by the target point approach using a particular combination of Q matrix. Therefore, a station-keeping process is simulated using the Floquet mode approach and at every maneuver computed, an alternative but correlating value of q_1 that essentially produces the same maneuver if used in the target point approach, is recorded. Five different and practically likely cases of applicable ΔV_{min} with two different sets of orbit determination and maneuver execution

errors, Type A and Type B, are explored to find the correlating weighting matrix Q.

Table 5.2. Input parameters for station-keeping simulation using the Floquet mode approach to estimate total maneuver costs and predict equivalent q_1 value in the target point approach that would estimate the same maneuver.

Model	SEM Ephemeris
Station-keeping algorithm	Floquet mode approach
Mission duration	2 Years
ΔV_{min} [cm/s]	Variable
	5, 10, 20, 50, 100
Δt_{min} [days]	30
d_{min} [km]	0
Terminating distance, d_{max} [km]	50000
Tracking interval [days]	2
Orbit determination errors	Type A, Type B
Halo orbit injection Epoch	January 13, 2020

At all locations where the maneuver is computed using the Floquet mode approach, an equivalent minimizing positive definite Q matrix is sought for. Since $q_2, q_3 = 10^{25}$ is assumed for precise x-control maneuver the output obtained is just the values of q_1. Since the target point and the Floquet mode approach is mathematically different, same values of q_1 are not predicted throughout, instead it is spread over a range of values as described in Figure 5.7 and Figure 5.8. The obtained range of values marks the region to search for cost minimizing Q matrix. Figure 5.7 and Figure 5.8 show the distribution of q_1 over 10 Monte Carlo simulations for different ΔV_{min} cases. Clearly the distribution is spread across values between 10^{12} and 10^{20}

with more concentration between 10^{14} and 10^{18}. Mean of the distribution can be used as satisfying value of q_1 but it has no physical significance. Moreover, the mean obtained for different ΔV_{min} condition is also different, hence, finding particular q_1 that reduces the station-keeping costs for all the cases is hard to determine. Also, it need not guarantee the best result. Instead the range of values obtained is used as a test spectrum to explore for the q_1 that minimizes the station-keeping budget.

Station-keeping simulations conducted using different values of q_1 obtained from the distribution in Figure 5.7 and Figure 5.8, requires a baseline solution to determine whether the orbit maintenance costs produced by different q_1 values are comparable. A baseline solution is determined by performing station-keeping simulation purely using the Floquet mode approach. The results produced by different q_1 values is compared with the Floquet mode solutions to make a conclusion.
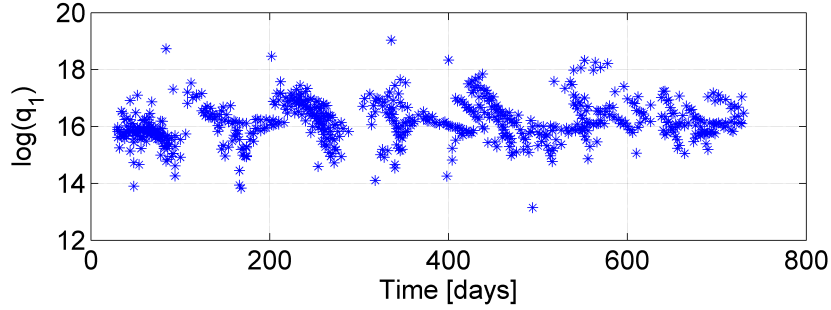
(a) $\Delta V_{min} = 5$ cm/s.
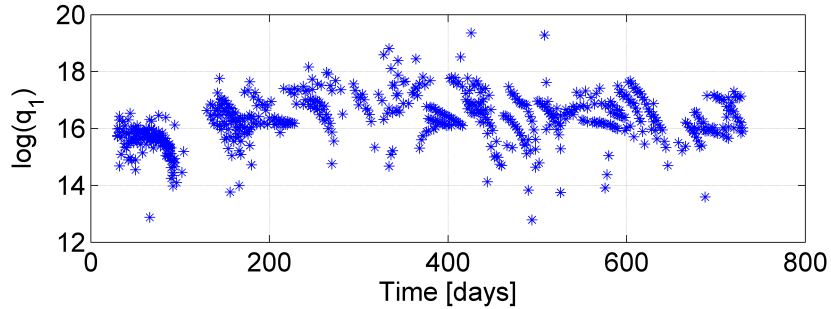
(b) $\Delta V_{min} = 10$ cm/s.
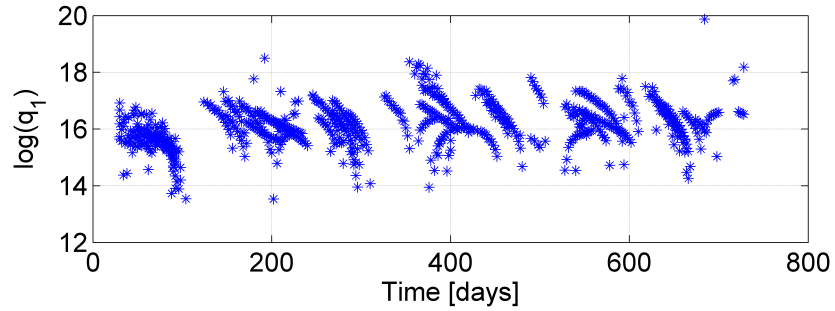
(c) $\Delta V_{min} = 20$ cm/s.
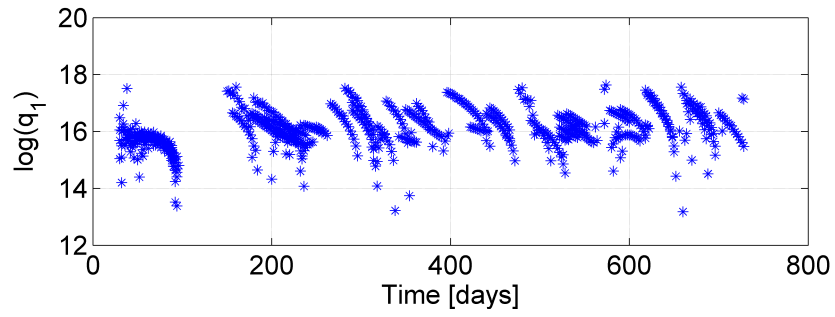
(d) $\Delta V_{min} = 50$ cm/s.
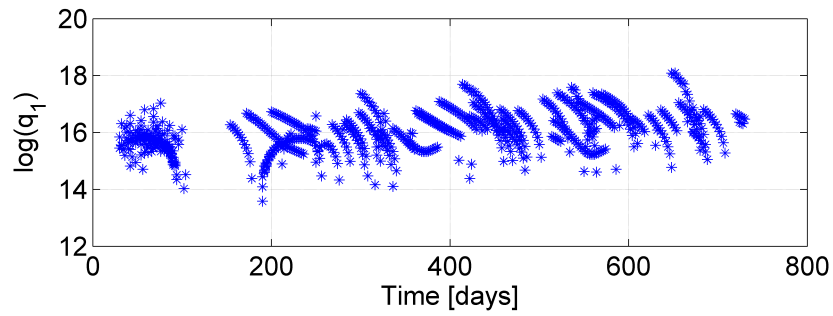
(e) $\Delta V_{min} = 100$ cm/s.

Figure 5.7. Potential range of q_1 values for the target point approach estimated from every corrective maneuvers computed using the Floquet mode approach. For all cases, Type A orbit determination error is incorporated.
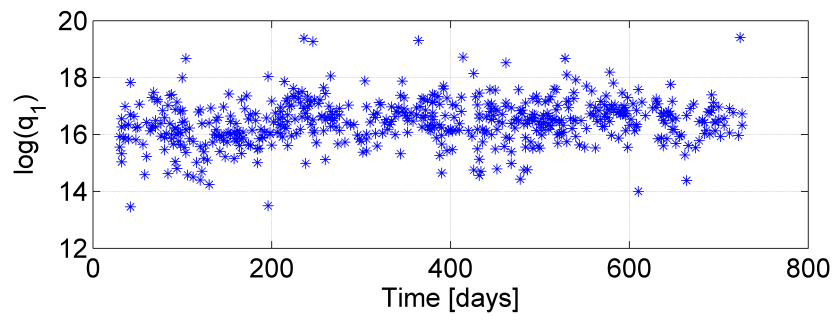
(a) $\Delta V_{min} = 5$ cm/s.
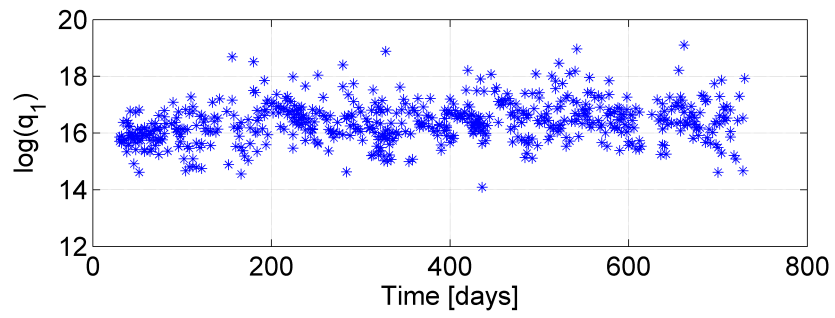
(b) $\Delta V_{min} = 10$ cm/s.
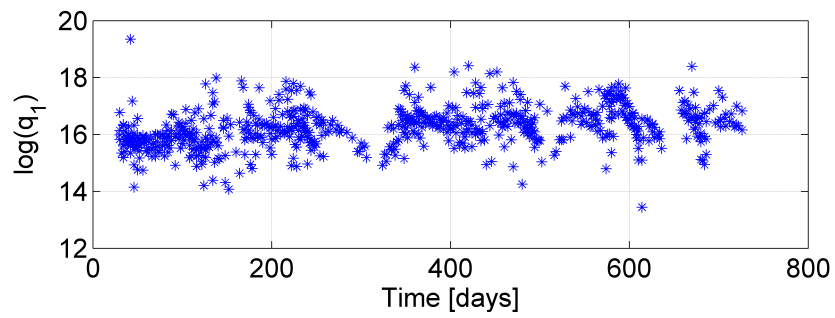
(c) $\Delta V_{min} = 20$ cm/s.
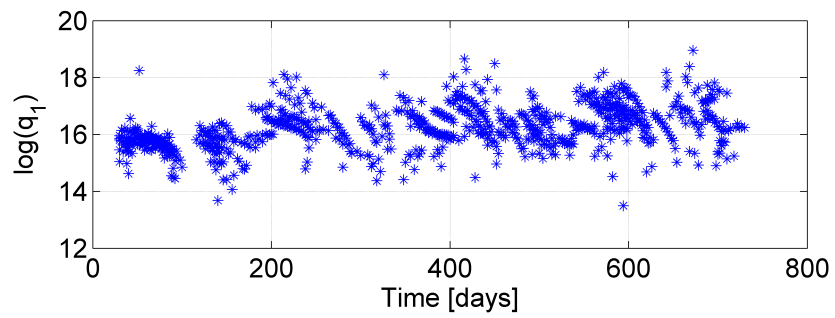
(d) $\Delta V_{min} = 50$ cm/s.
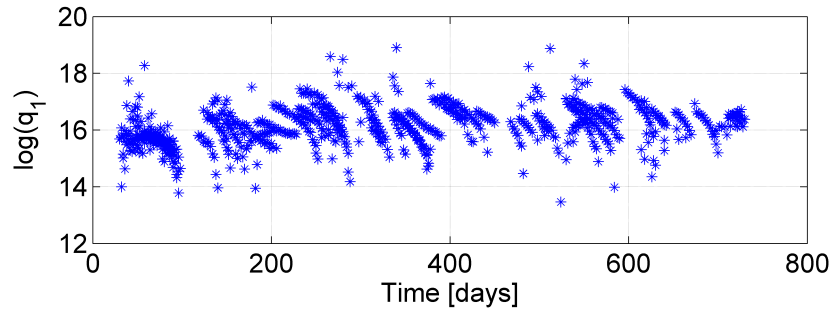
(e) $\Delta V_{min} = 100$ cm/s.

Figure 5.8. Potential range of q_1 values for the target point approach estimated from every corrective maneuvers computed using the Floquet mode approach. For all cases, Type B orbit determination error is incorporated.

Floquet Mode Station-keeping Budget

The Floquet mode leverages the natural dynamics of the flow in the libration point orbits. The method computes a maneuver that cancels the unstable Floquet mode thus driving the system along stable and oscillatory modes. The Floquet mode approach is used to estimate the station-keeping budget of the spacecraft in the desired orbit for a span of two years. The mission duration selected is equivalent to about 4 complete revolutions. The annual cost can serve as a baseline if the mission duration were to be scaled.

Since Monte Carlo technique is based on stochastic process, the number of iterations required to have an appropriate solution is very vital. More the number of iterations, better is the accuracy of the solution but performing too many iterations adds very little information, hence, it is important to terminate the total number of runs once the desired level of accuracy is obtained. Howell and Pernicka [24, 25] and Howell and Keeter [42, 43] use 100 simulation for their station-keeping process. Gordon concludes that, 30 iterations are sufficient to get a result with 10 % relative tolerance [40, 41]. Pavlak [39] uses about 500 simulations in search of more precise

results. In this work, choices of iterations are made depending on the required precision for each individual problem. The level of convergence is either mentioned in terms of targeted value of relative precision or converged value of standard deviation of the computed mean. For estimating the station-keeping cost using the Floquet mode approach, 3500 iterations have been used. The cited works indicates that less than 2% tolerance in the station-keeping costs is a good level of accuracy required for comparing different cases. Equation (4.10) is used to calculate the required number of iterations to have relative tolerance within 1%. Confidence level of 95% i.e. 1.96 sigma limit is assumed for the station-keeping problem.

A station-keeping simulation is performed using the Floquet mode approach using parameters specified in Table 5.2 to estimate the total orbit maintenance costs for 2 year mission duration. A total of 3500 Monte Carlo simulations are performed for estimating the cost and to study the convergence behavior. The mean station-keeping cost is estimated by taking the average of all the simulations performed. It may not always be feasible to compute 3500 Monte Carlo simulations due to computational limitations, therefore a continuous estimation of the mean is desirable. A moving mean is thus defined as the mean of all the previous simulations performed till that iteration number. Figure 5.9 displays the actual observations (2 year total maneuver cost) obtained for each of the 3500 Monte Carlo runs along with the moving mean. It is apparent that the moving mean stabilizes after the first 50 to 100 iterations, beyond which, it changes only marginally. The number of iterations used by the cited researchers, would therefore provide similar values, but with a comparatively lower confidence level. The mean station-keeping cost estimated for 2 year mission duration for Type A ODE obtained after 3500 iterations for $\Delta V_{min} =10$ cm/s case is 74.1 cm/s, as demonstrated in Figure 5.9.

The authenticity of the computed mean in a stochastic process depends on how close it is to the true mean. Unfortunately, for a station-keeping problem, the knowl-
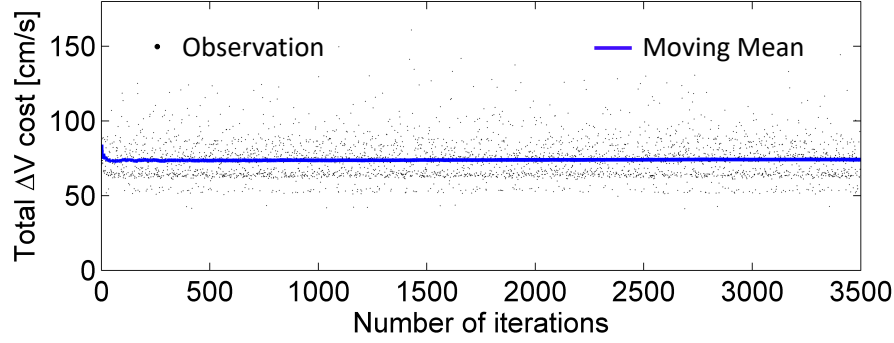
Figure 5.9. Mean station-keeping cost estimated from Monte Carlo runs. Example shown for $\Delta V_{min} = 10$ cm/s case with Type A orbit determination error computed using the Floquet mode approach (FMA).

edge about the true mean itself is unavailable. The standard deviation of the mean is evaluated to measure the convergence, that is a function of the standard deviation of the observations, produced in a Monte Carlo run. The dispersion of each observations about the mean, are indicated in Figure 5.10 in terms of standard deviation of the observations. After 3500 iterations, the standard deviation of the observations is 13.0 cm/s, indicating that if the station-keeping problem is assumed as a Gaussian distribution, 68% (1σ) of the observations lie within 74.1 ± 13.0 cm/s i.e. within 61.1 cm/s and 84.0 cm/s. The standard deviation of the observations obtained from Figure 5.10 is used to calculate the relative precision (or the half width) of the computed mean using equation (4.10). With each additional iteration the mean becomes more precise as the relative precision reduces as described in Figure 5.11. Clearly, there is a sharp drop in the precision value in the first 50 iterations, beyond which the rate of decrease is gradual. The abrupt change in precision level justifies the claim made by Gordon [41] that at least 30 iterations are required to get a result with less than 10% relative tolerance. For 95% confidence or 1.96 limits, the half width or precision as expressed in equation (4.10) would decrease gradually, rendering more proximity between true mean and computed mean. If the desired precision (half width) is 1%, then the number of iterations required is the abscissa corresponding to 1%.
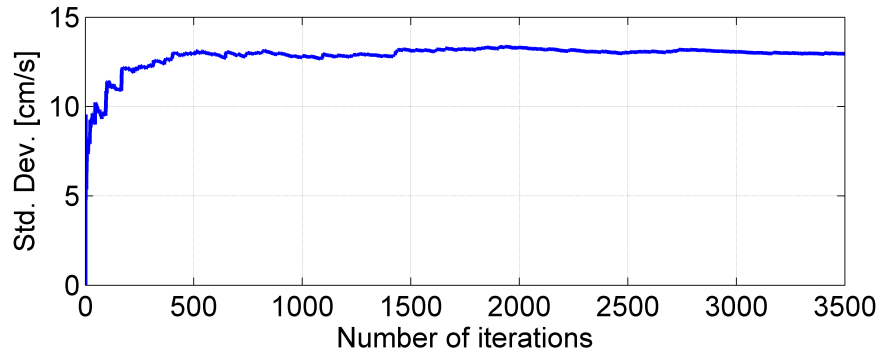
Figure 5.10. Variation in standard deviation of observations with increase in the number of Monte Carlo iterations. Example shown for $\Delta V_{min} = 10$ cm/s case with Type A orbit determination error computed using the Floquet mode Approach (FMA).
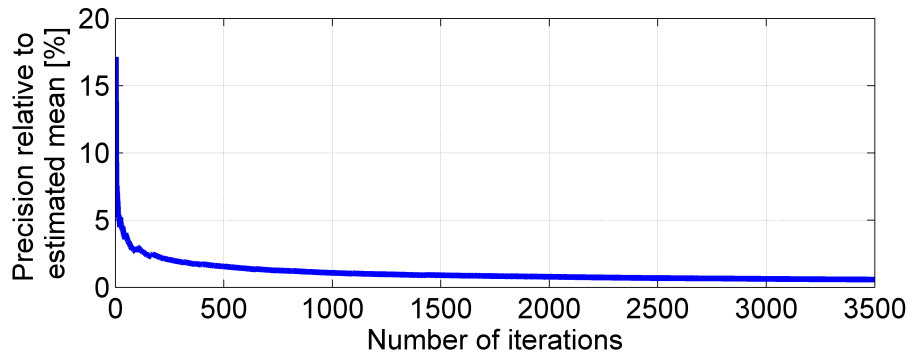
Figure 5.11. Effect of the number of Monte Carlo iterations on relative precision (or half width) of estimated mean. Example shown for $\Delta V_{min} = 10$ cm/s case with Type A orbit determination error computed using the Floquet mode approach (FMA).

In most station-keeping cases, where the simulation is computationally expensive, performing 3500 iterations to estimate the level of convergence may not be a wise option. A continuous estimation of the required number of Monte Carlo runs is preferable. Figure 5.12 illustrates the continuous prediction of required sample size (number of Monte Carlo iterations) as explained in section 4.5. The three lines in the Figure 5.12 denotes trials required for 1%, 0.75% and 0.6% relative precision. The desired precision is achieved if the actual number of trials performed exceeds the

predicted number of trials. For a precision of 1%, the number of Monte Carlo runs required is 1170, for which, the true mean is expected to be within 73.7 ± 0.7 i.e. within 73.0 cm/s and 74.4 cm/s. Similarly, 2171 trials to achieve precision of 0.75%; true mean is likely to be within 73.4 cm/s and 74.5 cm/s. Monte Carlo trials of 3270 yields 0.6% precision; true mean is likely between 73.8 cm/s and 74.6 cm/s. When a computed mean of a Monte Carlo simulations is required to be expressed in terms of a fixed relative or absolute precision, the method of predicting the desirable number of iterations is useful. Alternatively, specifying the standard deviation of the mean provides sufficient knowledge about the achieved convergence.
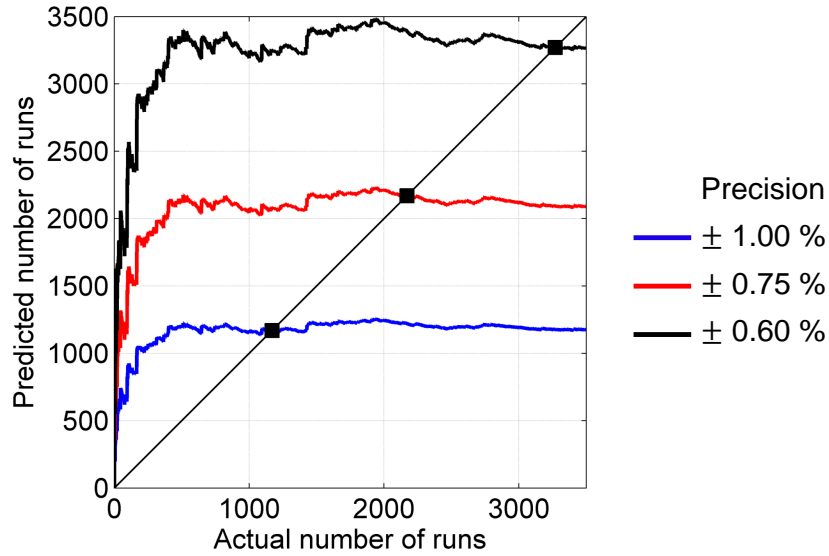
Figure 5.12. Number of Monte Carlo iterations required for predefined precision level. Example shown for $\Delta V_{min} = 10$ cm/s case with Type A orbit determination error computed using the Floquet mode approach (FMA). Precision is defined as a relative quantity with respect to the estimated mean.

The station-keeping costs estimated with the Floquet mode approach serves as a baseline solution for comparing with the target point approach with different weighting matrix Q, therefore precise estimation of the costs are desired. For computational convenience, a standard 3500 Monte Carlo iterations have been used for all cases, re-

sulting in precision within 0.75% for most cases (within 0.60% for some cases). For comparative purposes, this is a suitable level of precision. The station-keeping costs for 2 year mission are computed for different ΔV_{min} cases for both Type A and B orbit determination errors and summarized in Table 5.3 and Table 5.4 respectively.

Table 5.3. Outcome of station-keeping simulation using the Floquet mode approach for 2 year mission duration with Type A orbit determination error.

ΔV_{min} [cm/s]	Total ΔV cost, $\{\bar{\varkappa}\}$ [cm/s]	Std. dev. of observations, $\{S_{\varkappa}\}$ [cm/s]	Precision $(h/\bar{\varkappa}) \times 100$ [%]	Convergence [%]
5	37.2	5.3	0.47	100
10	74.1	13.0	0.58	99.97
20	146.2	27.8	0.63	99.97
50	355.5	72.7	0.68	99.94
100	685.5	134.9	0.65	99.71

The station-keeping cost is one of the most vital data to analyze the mission. The orbit maintenance costs increases with increase in the minimum applicable maneuver, ΔV_{min}. The orbit determination errors have significant impact on the orbit maintenance costs. As the ODE increases, as in Type B in comparison with Type A, the station-keeping costs rises for all ΔV_{min} cases. For 3500 Monte Carlo iterations to simulate the station-keeping process, relative precision for the results obtained is lower than 0.7% for all cases providing very precise value of computed mean. For almost 100% of the simulations, the spacecraft has successfully cruised through the mission duration without deviating uncontrollably far from the reference orbit for both the chosen orbit determination errors. The Floquet mode approach acts as an effective algorithm for station-keeping.

Table 5.4. Outcome of station-keeping simulation using the Floquet mode approach for 2 year mission duration with Type B orbit determination error.

ΔV_{min} [cm/s]	Total ΔV cost, $\{\bar{\varkappa}\}$ [cm/s]	Std. dev. of observations, $\{S_\varkappa\}$ [cm/s]	Precision $(h/\bar{\varkappa}) \times 100$ [%]	Convergence [%]
5	65.37	9.04	0.46	100.00
10	102.76	13.52	0.44	99.97
20	188.76	24.56	0.43	99.94
50	454.53	72.91	0.53	100.00
100	893.47	159.77	0.59	99.94

Target Point Approach

The search span of the weighting matrix Q that would reduce the station-keeping cost using the target point approach has been streamlined based on potential q_1 values obtained at each maneuver location computed using the Floquet mode approach. Since the maneuver is planned only along the x-direction, the search region is reduced to one dimension. The component of the weighting matrix that affects the maneuver in the y and z-direction has been effectively chosen to be $q_2 = q_3 = 10^{25}$, to effectively suppress any component of maneuver not directed along the line joining the primaries. Furthermore, the value of q_1 is further curtailed from the range of possible q_1 values obtained from the Floquet mode maneuver computation shown in Figure 5.7 and Figure 5.8 for different ΔV_{min} cases. Different values of q_1 between 10^{10} and 10^{18} are chosen and the station-keeping algorithm is performed using the target point approach to estimate the total cost after 2 year mission duration. Parameters specified in Table 5.5 are used for the simulation.

Table 5.5. Input specifications for station-keeping simulation using the target point approach.

Model	SEM Ephemeris
Station-keeping algorithm	Target point approach
Mission duration	2 Years
ΔV_{min} [cm/s]	Variable 5, 10, 20, 50, 100
Δt_{min} [days]	30
d_{min} [km]	0
Terminating distance, d_{max} [km]	50000
Tracking interval [days]	2
Future position targets	1
Future velocity targets	1
Duration to future target point [days]	177.8645 (1$\mathbb{P}$)
Orbit determination errors	Type A, Type B
Halo orbit injection epoch	January 13, 2020
Q [dimensional]	Diag (q_1, q_2, q_3) • $10^{10} \leq q_1 \leq 10^{18}$ • $q_2, q_3 = 10^{25}$
$\mathbb{R}$	$I_{3\times3}$
$\mathbb{R}_V$	$I_{3\times3}$

Precise station-keeping costs are sought for comparing the impact of each chosen value of q_1. As used for the Floquet mode approach, 3500 Monte Carlo runs are used for the target point approach as well, to ensure that the precision in the costs obtained are within 0.75%. For each value of q_1, total costs for different ΔV_{min} conditions are

computed for 3500 independent Monte Carlo iterations. The values obtained for each combination of q_1 and ΔV_{min} are given in Table 5.6 and Table 5.7 for Type A and Type B orbit determination errors respectively. A comparison of the values obtained using the Floquet mode approach and each q_1 using the target point approach are conducted and the results are displayed for Type A and Type B ODEs in Figure 5.13 and Figure 5.14 respectively.

An orderliness between q_1 component of the weighting matrix Q and the total station-keeping cost is observed. When q_1 is between 10^{10} and 10^{16}, the cost computed using the target point approach matches closely with the values computed using the Floquet mode approach for all the ΔV_{min} cases indicative of the efficiency of the target point approach. The TPA method uses only simple computations yet finds a value close to the one predicted by FMA method that utilizes the rich dynamics of the system. For q_1 between 10^{16} and 10^{18}, the TPA method computes a station-keeping cost lower than the FMA method initially and then increases rapidly. The setup of the cost function signifies that a larger weight should effectively decrease the individual maneuver cost, that is being applied in the case of TPA as well, as q_1 varies between 10^{10} and $10^{17.5}$, the cost is being reduced consistent with the weights and a decrease in the overall cost is observed. For Type A ODE, q_1 beyond $10^{17.5}$, the algorithm does compute an extremely low maneuver at each individual location, however, the maneuver executed is minuscule that the spacecraft it is not able to fully recover from its deviated state, hence with time, the deviation increases exponentially along the unstable orbit. With the rapid increase in the deviation, the corresponding maneuvers computed also grows. Therefore, an overall growth in the total station-keeping cost is observed for very large q_1.

Figure 5.13 and Figure 5.14 suggests that q_1 between 10^{16} and 10^{18} is a potential region to identify the weighting matrix that may provide an efficient low cost maneuver for the two types of ODE chosen for the simulation. The value of q_1 is
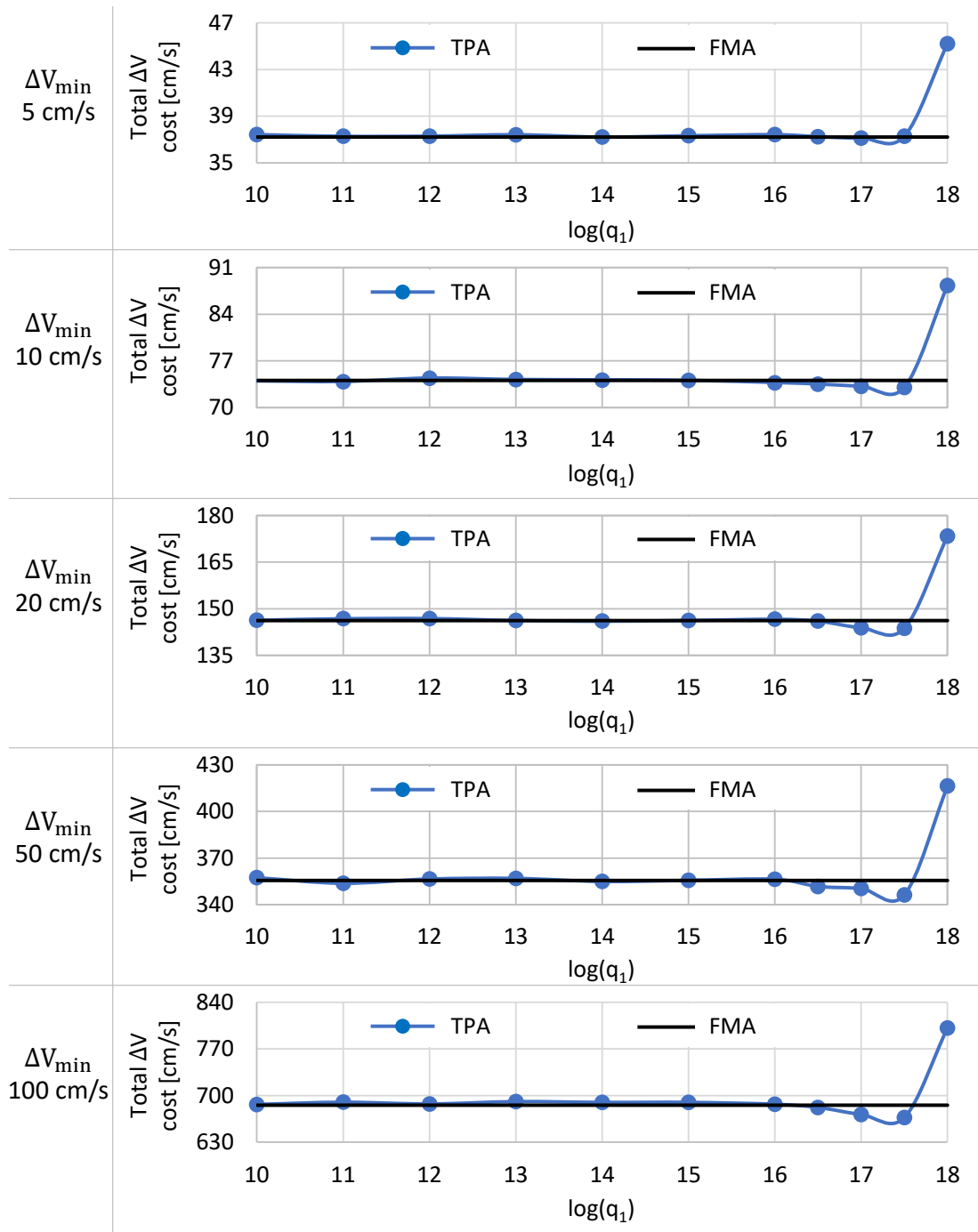
Figure 5.13. Comparison of station-keeping cost estimated using the Floquet mode approach (FMA) and different values of q_1 in the target point approach (TPA) for different ΔV_{min} cases and Type A orbit determination error.
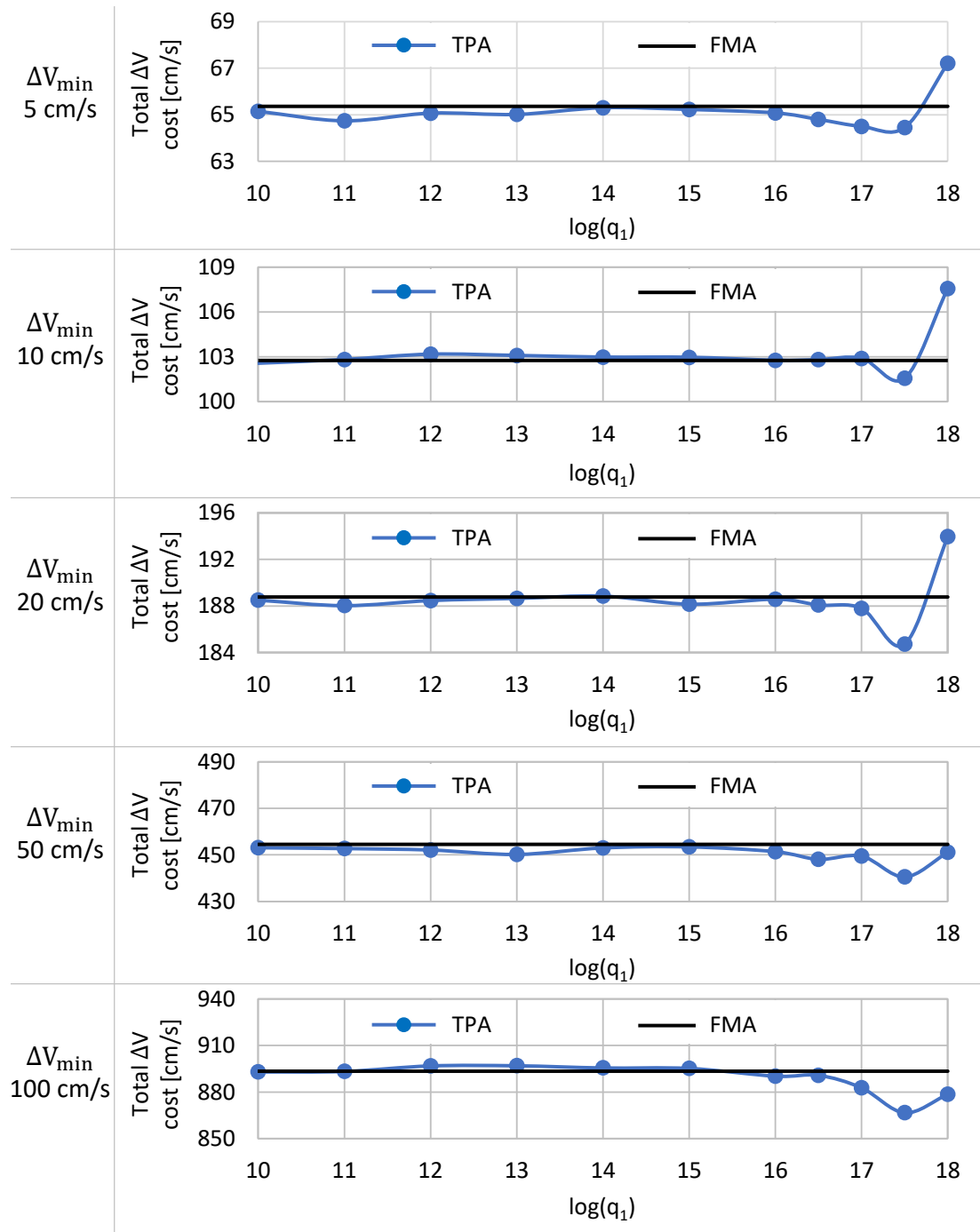
Figure 5.14. Comparison of station-keeping cost estimated using the Floquet mode approach (FMA) and different values of q_1 in the target point approach (TPA) for different ΔV_{min} cases and Type B orbit determination error.

Table 5.6. Station-keeping costs in cm/s estimated by the target point approach for 2 year mission duration with Type A orbit determination error and q_1 between 10^{10} and 10^{18}.

$log(q_1)$	ΔV_{min} [cm/s]				
	5	10	20	50	100
10	37.4	74.0	146.3	357.4	686.7
11	37.3	73.9	146.8	353.8	690.0
12	37.3	74.4	146.9	356.5	687.4
13	37.4	74.2	146.3	356.9	691.0
14	37.2	74.2	146.0	354.9	689.8
15	37.3	74.1	146.3	355.7	689.8
16	37.4	73.7	146.7	356.4	687.0
16.5	37.3	73.5	146.1	351.7	682.2
17	37.1	73.2	143.9	350.4	671.7
17.5	37.3	73.0	143.8	346.3	667.1
18	45.2	88.3	173.4	416.4	801.6

varied in multiples of $10^{0.1}$ to form 20 different intervals between 10^{16} and 10^{18} i.e. $10^{16.1}$, $10^{16.2}$, $\cdots$, $10^{17.9}$, $10^{18.0}$. Whether the step size should be further reduced to have more conditions is determined based on the performance of multiples of $10^{0.1}$. Again, station-keeping simulations are conducted by performing 3500 Monte Carlo simulations and the costs are estimated for different ΔV_{min} cases for both Type A and Type B ODE and the results are presented in Table 5.8 and Table 5.9 respectively. The lowest recorded station-keeping cost for each ΔV_{min} case is underlined.

Investigation of Table 5.8 and Table 5.9 yields that the minimal value of station-keeping costs for each ΔV_{min} case exists at distinct values of q_1. No particular value of

Table 5.7. Station-keeping costs in cm/s estimated by the target point approach for 2 year mission duration with Type B orbit determination error and q_1 between 10^{10} and 10^{18}.

$log(q_1)$	ΔV_{min} [cm/s]				
	5	10	20	50	100
10	65.2	102.6	188.5	453.1	893.0
11	64.7	102.8	188.0	452.7	893.3
12	65.1	103.2	188.5	452.1	896.9
13	65.0	103.1	188.7	450.2	897.0
14	65.3	103.0	188.8	453.0	895.6
15	65.2	103.0	188.2	453.4	895.2
16	65.1	102.8	188.6	451.4	890.3
16.5	64.8	102.8	188.1	448.1	890.8
17	64.5	102.9	187.8	449.5	882.7
17.5	64.5	101.6	184.7	440.5	866.6
18	67.2	107.6	194.0	451.1	878.5

q_1, results in the minimal solution that satisfies all cases tested. Different curve fitting methods are tested but none of them yields the same q_1 that satisfies the minimal ΔV_{min} for all cases. The lowest case for each ΔV_{min} is underlined in Table 5.8 and Table 5.9. Some better approach needs to be applied to select a right q_1 that would deliver the lowest station-keeping costs for majority number of cases. The fundamental aim is to determine a q_1 that provides the least cost for the most number of cases. Furthermore, an absolute decrease in the total cost is also as crucial as a relative decrease in maneuver cost. The change in the total cost computed for most of the values of q_1 vary not more than 1-2%. For example, consider case 1 where ΔV_{min}=5 cm/s for Type A, the lowest maneuver cost of 36.9 cm/s is predicted for $q_1 = 10^{17.1}$.

Table 5.8. Station-keeping costs in cm/s estimated by the target point approach for 2 year mission duration with Type A orbit determination error for refined values of $10^{16} \leq q_1 \leq 10^{18}$.

| $log(q_1)$ | ΔV_{min} [cm/s] | | | | | Sum |
	5	10	20	50	100	[cm/s]
16.1	37.2	73.7	146.3	350.5	684.5	1292.3
16.2	37.1	73.3	146.6	351.8	687.3	1296.1
16.3	37.3	74.1	144.8	355.3	685.9	1297.4
16.4	37.2	74.2	145.4	355.6	683.8	1296.2
16.5	37.3	73.5	146.1	351.7	682.2	1290.7
16.6	37.1	73.7	147.2	352.7	678.4	1289.0
16.7	37.1	73.7	145.3	352.0	682.0	1290.1
16.8	37.2	73.4	144.8	352.6	675.5	1283.4
16.9	37.1	<u>72.5</u>	146.4	348.8	676.4	1281.3
17.0	37.1	73.2	143.9	350.4	671.7	1276.3
17.1	<u>36.9</u>	72.8	144.7	349.1	675.2	1278.7
17.2	36.9	72.8	144.0	347.9	669.1	1270.8
17.3	37.1	72.7	143.7	344.3	666.6	1264.4
17.4	37.1	73.1	<u>142.9</u>	<u>343.6</u>	<u>663.7</u>	<u>1260.3</u>
17.5	37.3	73.0	143.8	346.3	667.1	1267.4
17.6	37.9	74.0	145.4	351.2	669.5	1278.0
17.7	38.8	75.8	149.3	356.5	687.9	1308.3
17.8	40.2	78.7	156.2	369.8	710.8	1355.6
17.9	42.2	83.0	162.6	390.6	747.1	1425.4
18.0	45.2	88.3	173.4	416.4	801.6	1524.9

Table 5.9. Station-keeping costs in cm/s estimated by the target point approach for 2 year mission duration with Type B orbit determination error for refined values of $10^{16} \leq q_1 \leq 10^{18}$.

$log(q_1)$	ΔV_{min} [cm/s]					Sum
	5	10	20	50	100	[cm/s]
16.1	65.0	103.4	188.4	450.7	895.0	1702.5
16.2	65.2	103.1	186.9	450.5	894.4	1700.1
16.3	64.7	102.7	189.0	448.6	892.1	1697.1
16.4	65.1	103.3	188.8	448.3	888.9	1694.4
16.5	64.8	102.8	188.1	448.1	890.8	1694.6
16.6	64.9	103.0	188.8	452.0	887.8	1696.4
16.7	65.2	102.9	186.9	450.4	889.7	1695.0
16.8	65.0	102.2	187.3	446.9	884.8	1686.3
16.9	64.9	102.7	187.8	449.1	886.1	1690.4
17.0	64.5	102.9	187.8	449.5	882.7	1687.4
17.1	64.8	102.1	187.3	446.2	873.9	1674.1
17.2	64.4	101.9	187.2	444.0	874.9	1672.3
17.3	<u>64.3</u>	101.9	<u>184.5</u>	440.5	870.8	1662.0
17.4	64.6	101.7	185.7	442.2	866.4	1660.6
17.5	64.5	<u>101.6</u>	184.7	440.5	866.6	1657.9
17.6	64.3	102.3	185.1	436.4	857.0	1645.0
17.7	64.4	102.2	186.3	<u>436.2</u>	<u>849.0</u>	<u>1638.1</u>
17.8	64.6	103.3	187.3	438.5	856.3	1650.0
17.9	65.6	104.5	188.9	441.8	859.8	1660.7
18.0	67.2	107.6	194.0	451.1	878.5	1698.4

A marginal increase in cost is predicted for $q_1 = 10^{17.4}$ in comparison to the former case. In absolute terms the increase is 0.2 cm/s and relatively this is 0.59%. Similarly, case 2, where ΔV_{min}=100 cm/s for Type A, the lowest maneuver cost of 663.7 cm/s is predicted for $q_1 = 10^{17.4}$. A marginal increase in cost is predicted for $q_1 = 10^{17.3}$ by 2.9 cm/s i.e. 0.44%. Although relative change in case 1 was higher than in case 2, absolute change in case 2 is much larger than in case 1. Minimizing the absolute value is a viable option. To have an absolute decrease in total maneuver cost, it is better to identify a value of q_1 that diminishes larger station-keeping costs, typically for larger ΔV_{min} cases. A simple technique is to compute the sum for all cases against each q_1, that are provided in the last columns in Table 5.8 and Table 5.9. Although the sum has no physical significance, bias is created towards the larger values than the smaller values when performing summation. The q_1 corresponding to the overall smallest sum potentially gives the best performance. The smallest sum in underlined for presentation. The plot between each q_1 value and the corresponding sum is presented in Figure 5.15 and Figure 5.16 for Type A and Type B ODE respectively.
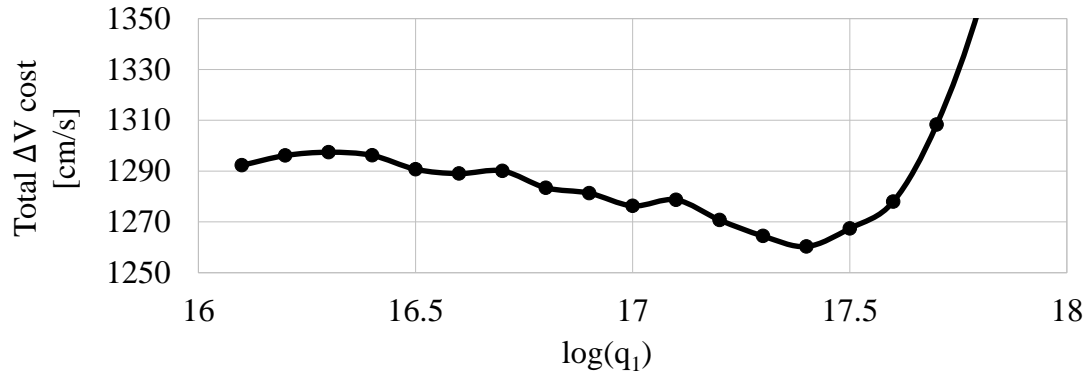
Figure 5.15. Comparison of station-keeping cost estimated for different values of q_1 between 10^{16} and 10^{10} in intervals of $10^{0.1}$ using the target point approach (TPA) for different ΔV_{min} cases and Type A orbit determination error.
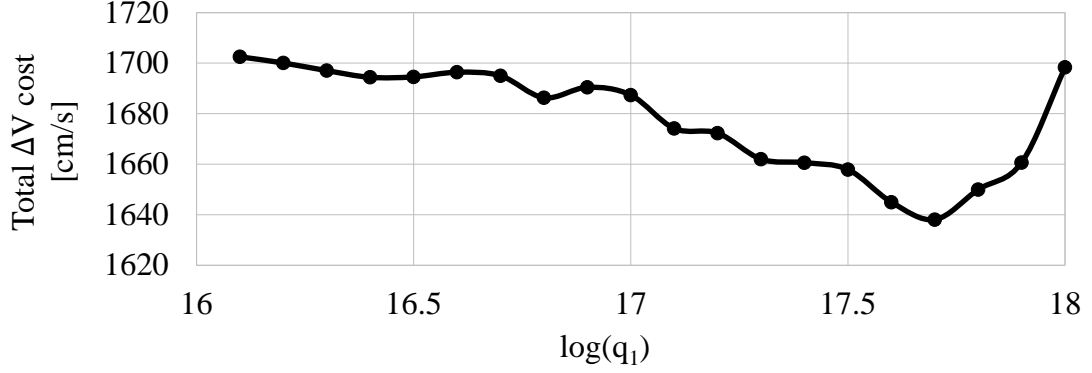
Figure 5.16. Comparison of station-keeping cost estimated for different values of q_1 between 10^{16} and 10^{10} in intervals of $10^{0.1}$ using the target point approach (TPA) for different ΔV_{min} cases and Type B orbit determination error.

Clearly, $q_1 = 10^{17.4}$ provides the best station-keeping cost for Type A ODE while $q_1 = 10^{17.7}$ provides the best station-keeping cost for Type B ODE but it is observed that with increases in the value of q_i, the maneuver magnitude in the corresponding direction is reduced. Very small maneuvers are generally not capable of maintaining spacecraft close to the nominal orbit for a longer duration as it experiences exponential drifting. The value of $q_1 = 10^{17.4}$ for Type A and $q_1 = 10^{17.7}$ for Type B can only be considered if at such values, the spacecraft does not experience large drifting away from nominal trajectory. Otherwise, by the end of the mission duration, the spacecraft would have diverged uncontrollably.

The choice on further refining q_1 is analyzed from the values in Table 5.8 and Table 5.9, where the difference between the costs computed for any two successive q_1 value separated by multiple of $10^{0.1}$ is not larger than 1% except in very few cases. Reducing the step size for more intermediate values therefore, would not necessarily provide any relevant information. Using more computation for finding intermediate values may not be worth. If computational expense is not a concern, performing more Monte

Carlo simulations would be a better choice at each of $10^{16.1}$, $10^{16.2}$, $\cdots$, $10^{17.9}$, $10^{18.0}$ to find more confident values, rather than finding lot of points with poor precision.

5.4.4 Drifting of Spacecraft from the Nominal Path

The cost function in the target point approach is defined, such that it accounts for both the size of maneuver ΔV and the isochronous drift from the nominal trajectory. The weighting matrix Q has considerable but indirect impact on the drift. A smaller value of Q in general, allows the isochronous drift to be the more dominant term of cost function. To reduce the cost function, the algorithm computes a maneuver to minimize the drifting of spacecraft away from the nominal orbit. Alternatively, a large value of Q would effectively compute a low maneuver at the expense of less control on the drift. The spacecraft is thus, highly likely to drift away from the nominal orbit, primarily, because the maneuver computed is minute to be not able to overcome the diverging effect caused due to uncertainties due the orbit determination error.

In the case of x-control maneuver scheme, q_2 and q_3 i.e. the second and the third diagonal elements that controls the maneuver in the y and z-direction are set to be very high that almost no maneuver is computed in y and z-direction. Any errors in the out of plane direction is unlikely to diverge as no perturbing bodies exists along the out of plane direction. Additionally, the station-keeping maneuvers along the x-direction is shown to effectively maintain the spacecraft throughout the mission duration, hence the perturbations along the y-direction at any instant is believed to be correctable using some x-direction maneuver at any later time. The only free variable is q_1, hence the divergence characteristics should depend greatly on q_1. Besides, due to the presence of large gravitational forces acting especially along the x-direction, any untreated errors will cause the spacecraft to diverge. It is evident from the results presented, that q_1 impacts the maneuver being applied, thus, controls the drifting. At larger values of q_1, as the maneuver magnitude is suppressed, the algorithm may

struggle to efficiently overcome the drifting away of spacecraft, therefore, larger q_1 values for station-keeping may be inferior.

For Type A ODE, a low station-keeping cost was detected near values of $q_1 = 10^{17.4}$ but the adoption of $q_1 = 10^{17.4}$ depends greatly on the divergence behavior. Different values of q_1 between 10^{10} and 10^{19} are analyzed to understand the divergence characteristics. The analysis is extended for different ΔV_{min} cases. Same conclusion is valid for Type B ODE. Continuous spacecraft tracking data reveals the deviation characteristics of the spacecraft throughout the mission duration. A 100 Monte Carlo simulation for each value of q_1 is performed and the isochronous deviation for different ΔV_{min} cases for Type A and Type B ODE is plotted as a function of time in Figure 5.17 and Figure 5.18 respectively. Each q_1 is color coded separately for visual assistance. At high values of q_1 the deviations are larger. For few cases, for example, $\Delta V_{min} = 100$ cm/s, $q_1 = 10^{19}$, the deviation exceeds 50000 km that is the terminating drift, hence no converged solutions are obtained. For each q_1, the trend in the deviation are similar. It undergoes an oscillatory behavior that increases with time. The peaks in the plot correspond to the $x - z$ plane crossings where the magnitude of velocity becomes higher in comparison to other regions of the periodic orbit, causing more drift. Besides, for large q_1 values, the deviation is large, but clear depiction of the deviation at the intermediate q_1 values are not distinct from Figure 5.17 and Figure 5.18. To overcome this challenge, the average deviation for each q_1 computed over 100 Monte Carlo simulations at the final time is presented. For better realization, the deviation at the end of mission duration is presented in distinct color gradients in Figure 5.19 and Figure 5.20 for Type A and Type B ODE respectively.

The effectiveness of different q_1 values for station-keeping is portrayed in Figure 5.17 and Figure 5.18 through the mean deviation at the end of the mission duration i.e. 2 years for the two chosen ODE and different ΔV_{min} cases. For all the ΔV_{min} cases, q_1 between 10^{10} and 10^{18} show divergence behavior of almost the same order,
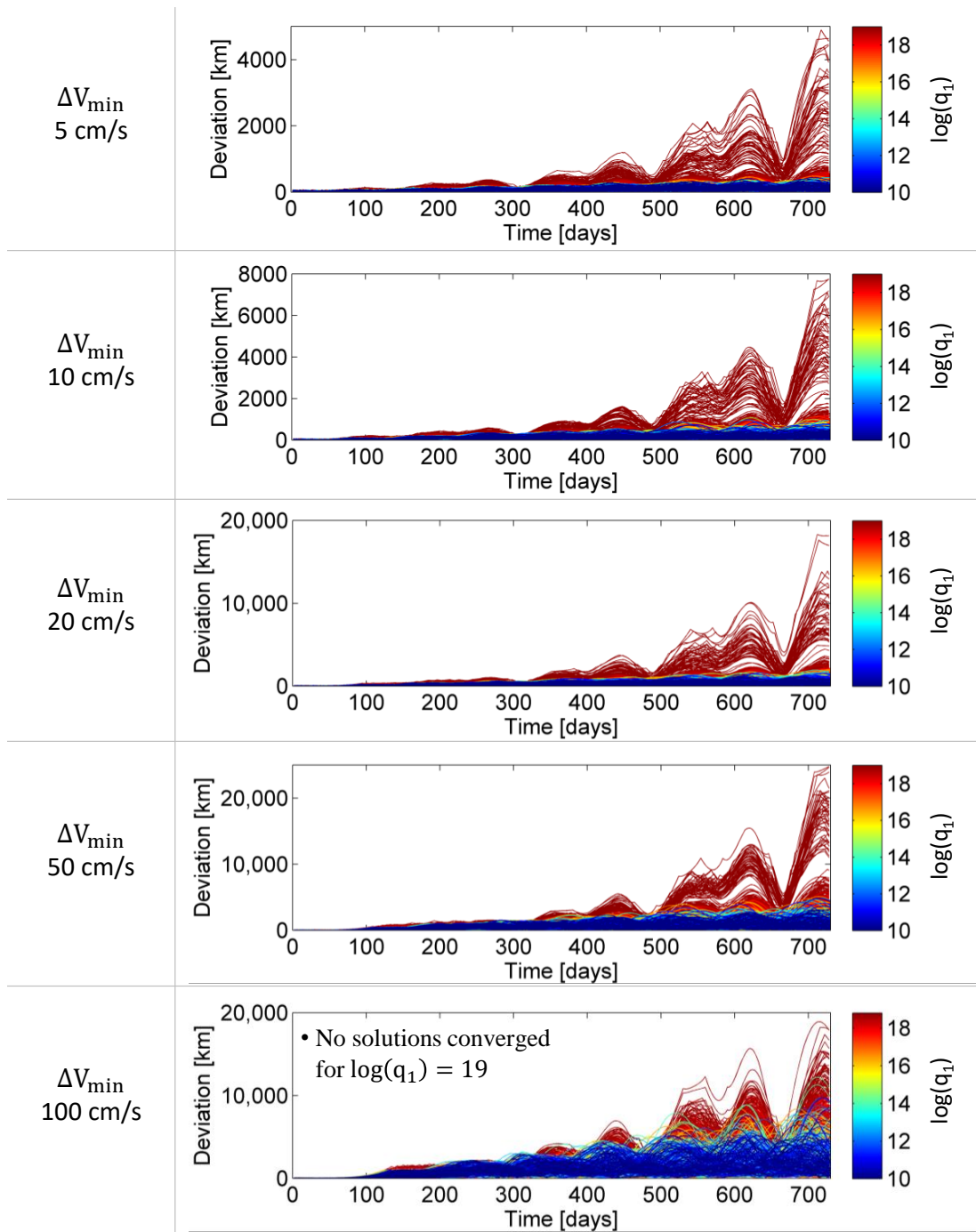
Figure 5.17. Deviation of the spacecraft from the reference orbit for different values of q_1 using the target point approach (TPA) for different ΔV_{min} cases with Type A orbit determination error. Deviation history plotted for 100 independent Monte Carlo iterations.
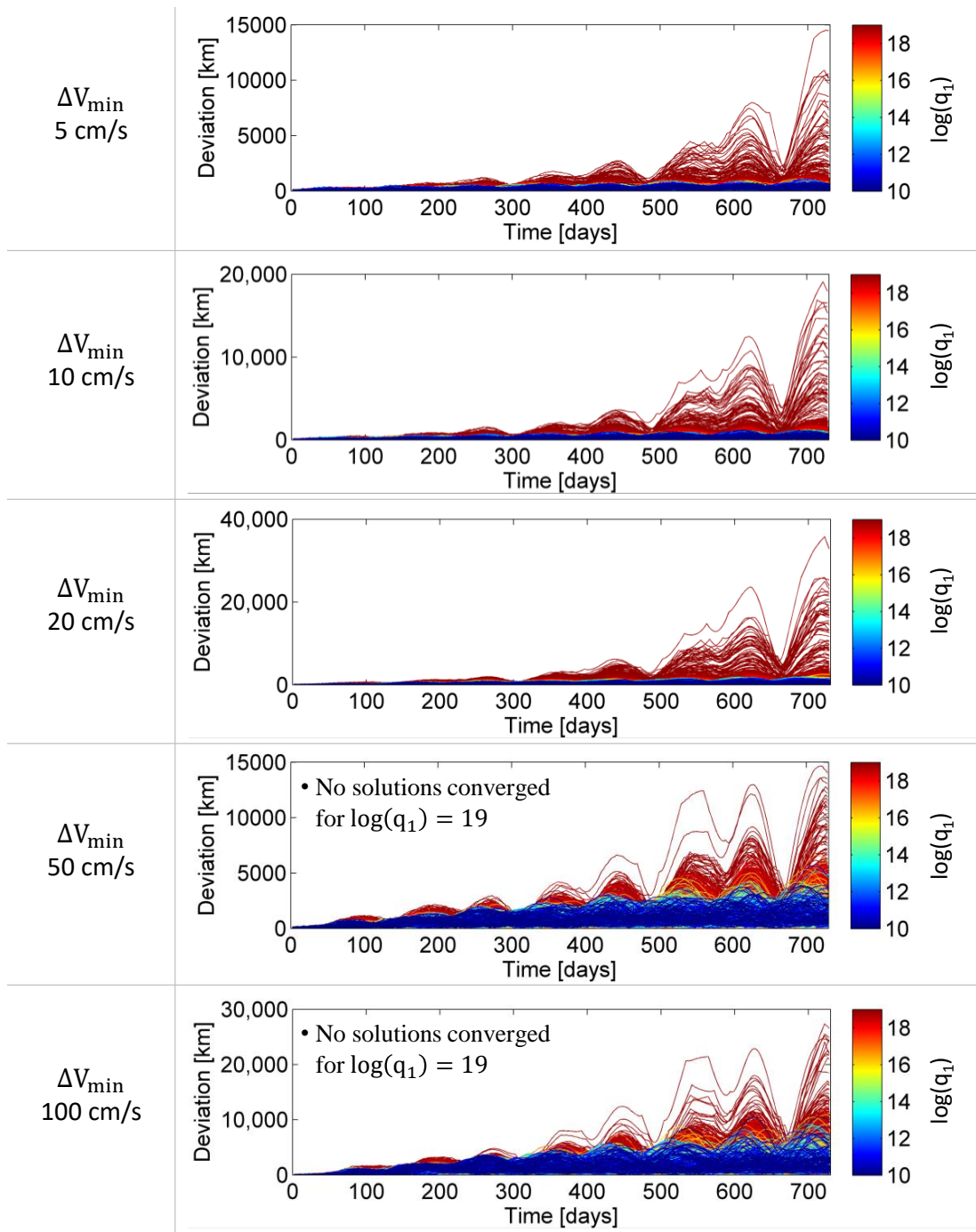
Figure 5.18. Deviation of the spacecraft from the reference orbit for different values of q_1 using the target point approach (TPA) for different ΔV_{min} cases with Type B orbit determination error. Deviation history plotted for 100 independent Monte Carlo iterations.
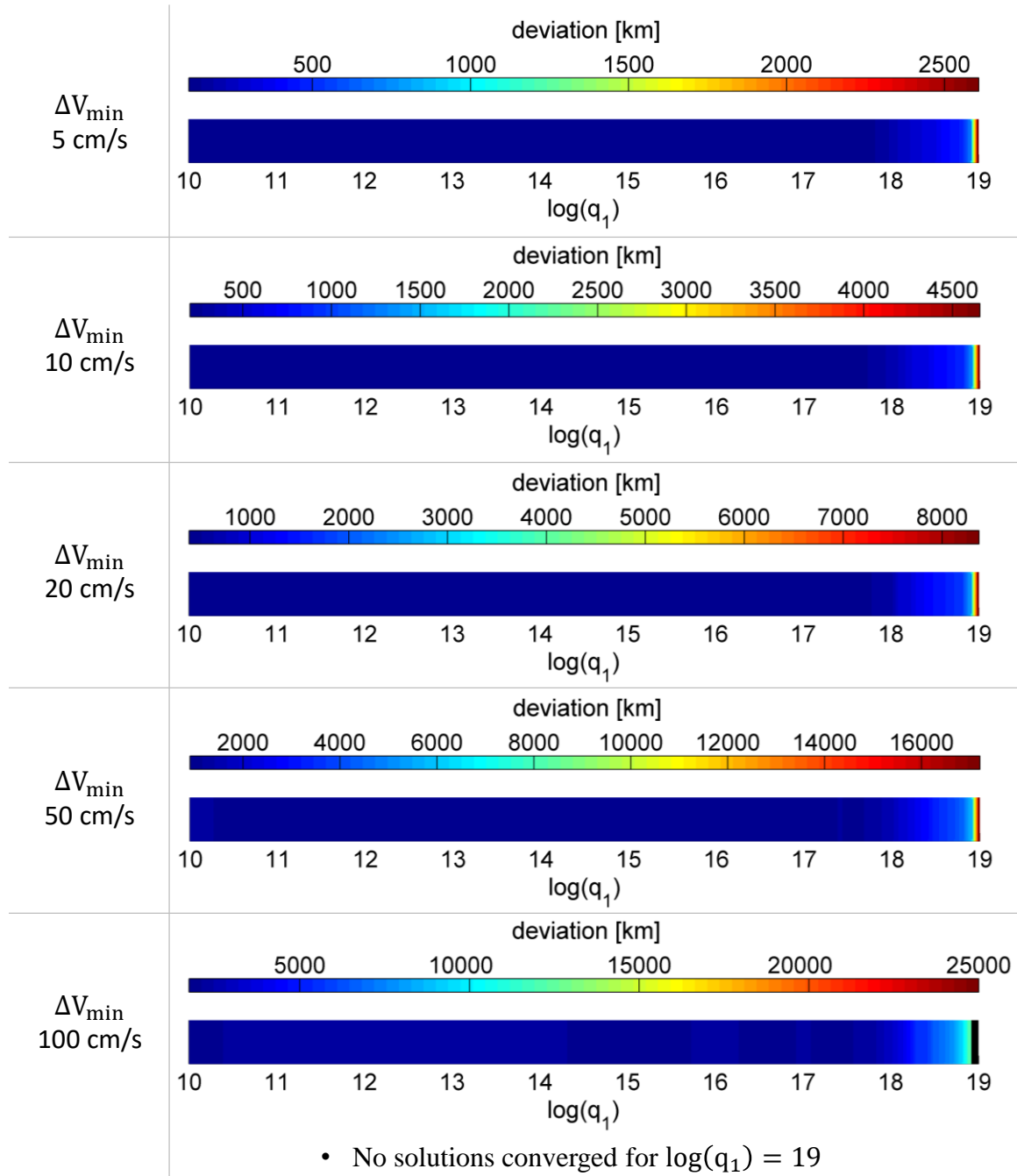
Figure 5.19. Mean deviation at the end of mission duration estimated for different values of q_1 using the target point approach (TPA), for different ΔV_{min} cases and Type A orbit determination error. Mean computed for 100 independent Monte Carlo iterations.
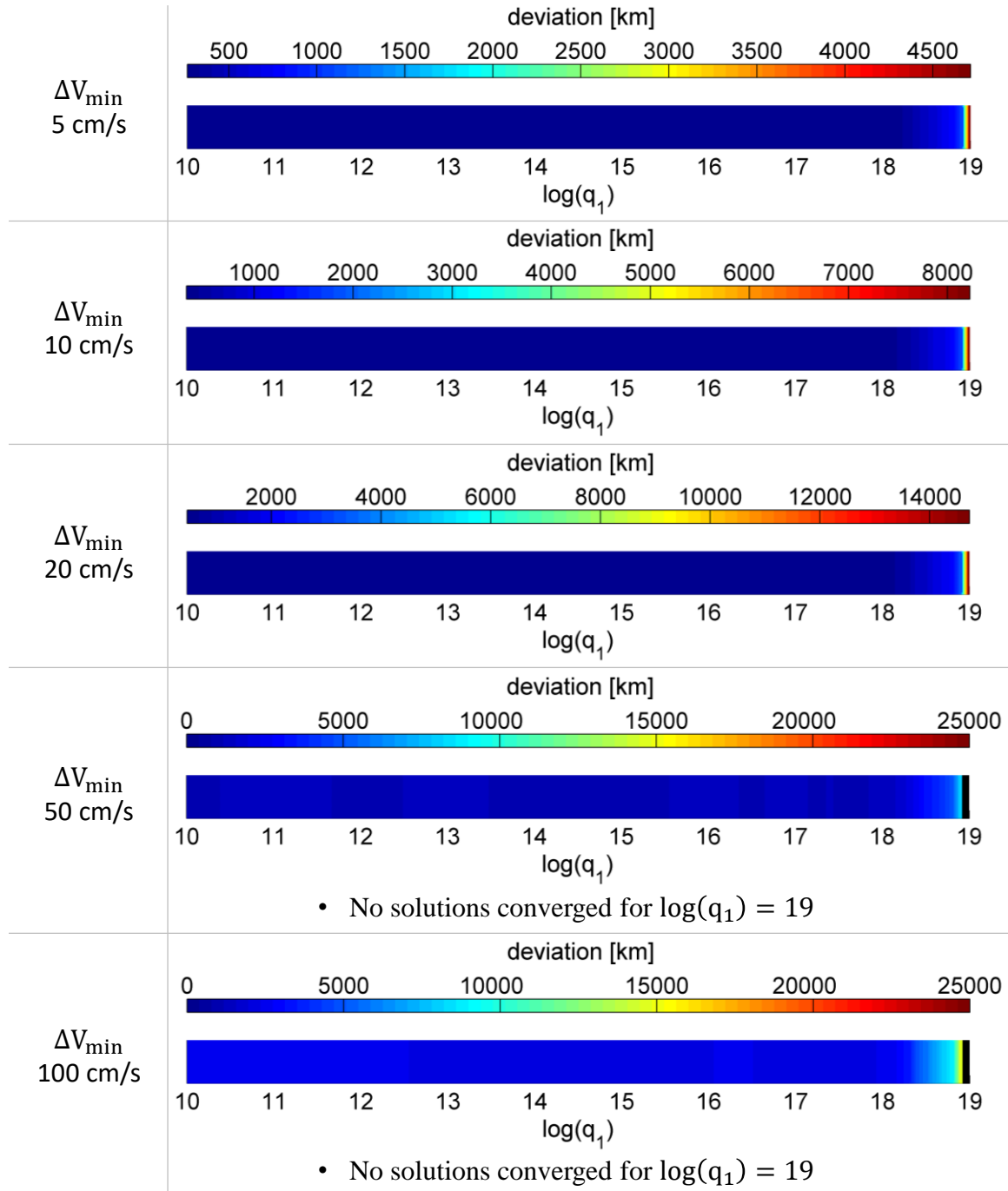
Figure 5.20. Mean deviation at the end of mission duration estimated for different values of q_1 using the target point approach (TPA), for different ΔV_{min} cases and Type B orbit determination error. Mean computed for 100 independent Monte Carlo iterations.

that remains close to the nominal trajectory, while q_1 larger than 10^{18} seems to be inefficient in maintaining the spacecraft near the desired orbit, hence with time the deviation grows rapidly. Since a slow divergence is predicted for $q_1 = 10^{17.4}$ for Type A ODE and $q_1 = 10^{17.7}$ for Type B ODE, that provided the least station-keeping costs, the value of q_1 can be chosen for further enhancements or for final use.

5.4.5   Effect of Weights on Future Position and Velocity Targets

The target point approach for station-keeping is driven by the defined cost function that weighs the magnitude of maneuver and the deviation in position and velocity states at some future time. Based on correlation between TPA and FMA, the future target points are considered to be exactly one period downstream. The weighting matrix Q that directly controls the magnitude of maneuver has been analyzed for both the orbit determination errors chosen for the station-keeping simulation to identify the values that yields in the lowest annual cost. Since the Floquet mode approach weighs is not biased towards position deviation and velocity deviation states, the matrix $\mathbb{R}$ and $\mathbb{R}_V$ that weights future position and velocity targets respectively, were considered to be identity, I. Since $\mathbb{R}$ and $\mathbb{R}_V$ are technically free variables, there is scope to analyze the effect of components of matrices $\mathbb{R}$ and $\mathbb{R}_V$ on the station-keeping costs, by not considering I. Similar to the process adopted for analyzing matrix Q, grid search is performed at each of the maneuver location to identify a certain patterns that can be utilized to further reduce station-keeping costs.

To analyze the weighting matrix $\mathbb{R}$ that accounts for the position deviation at the future time, at every maneuver location, different combinations of $\mathbb{R}$ matrix are

used to compute the maneuver keeping Q and $\mathbb{R}_V$ fixed. Let the positive semidefinite matrix $\mathbb{R}$ be represented as

$$\mathbb{R} = \begin{bmatrix} \tilde{r}_1 & 0 & 0 \\ 0 & \tilde{r}_2 & 0 \\ 0 & 0 & \tilde{r}_3 \end{bmatrix} \tag{5.36}$$

where, $\tilde{r}_1$ weights the position deviation along x-direction, $\tilde{r}_2$ along y-direction and $\tilde{r}_3$ along z-direction. The value of the selected Q matrix is $\text{diag}(10^{17.4}, 10^{25}, 10^{25})$ for Type A ODE and $\text{diag}(10^{17.7}, 10^{25}, 10^{25})$ for Type B ODE, in the dimensional units. Expressed in non-dimensionalized units, Q matrix is $\text{diag}(1.0 \times 10^4, 4.0 \times 10^{11}, 4.0 \times 10^{11})$ for Type A ODE and $\text{diag}(2.0 \times 10^4, 4.0 \times 10^{11}, 4.0 \times 10^{11})$ for Type B ODE. The matrix $\mathbb{R}_V$ is assumed to be I in non dimensional units, while performing the analysis on the effects of matrix $\mathbb{R}$. At every maneuver location, the value of $\mathbb{R}$, that is a non-dimensional unit by itself, is selected as a combination of $\tilde{r}_1$, $\tilde{r}_2$ and $\tilde{r}_3$ that are varied from 10^{-5} to 10^5 and the corresponding maneuver cost is recorded for different ΔV_{min} cases. The four-dimensional array consisting of $\tilde{r}_1$, $\tilde{r}_2$, $\tilde{r}_3$ and ΔV are presented as a three-dimensional space of $\tilde{r}_1$, $\tilde{r}_2$, $\tilde{r}_3$ with the 4th dimension, ΔV color coded for visual assistance. The results are presented in Figure 5.21 for different ΔV_{min} cases. Unlike Figure 5.1 where the effects of Q matrix was analyzed, no specific trend is observable. The chosen range of values of $\tilde{r}_i$ seems to be sufficient to include range of maneuver magnitudes possible but the range of achievable maneuver magnitudes are very narrow in comparison to the range of maneuver magnitudes achieved by varying Q matrix. Due to the lack of any specific pattern in the occurrence of low maneuver magnitude region and the extremely narrow range of maneuver magnitudes achievable, it may not be worth to spend intense computational resources to identify another value of $\mathbb{R}$ that may marginally alter the station-keeping costs predicted using an identity matrix, which is indeed not guaranteed. The use of Monte Carlo process results in uncertainty in the measurement of the mean station-keeping cost. It is not guaranteed that altering the value of matrix $\mathbb{R}$, from identity, will result in station-keeping costs lower than the uncertainty in measurement. Therefore, for this

work the value of $\mathbb{R}$ is allowed to remain as I, however, for other orbits if definite pattern is observable then $\mathbb{R}$ can be analyzed and enhanced.
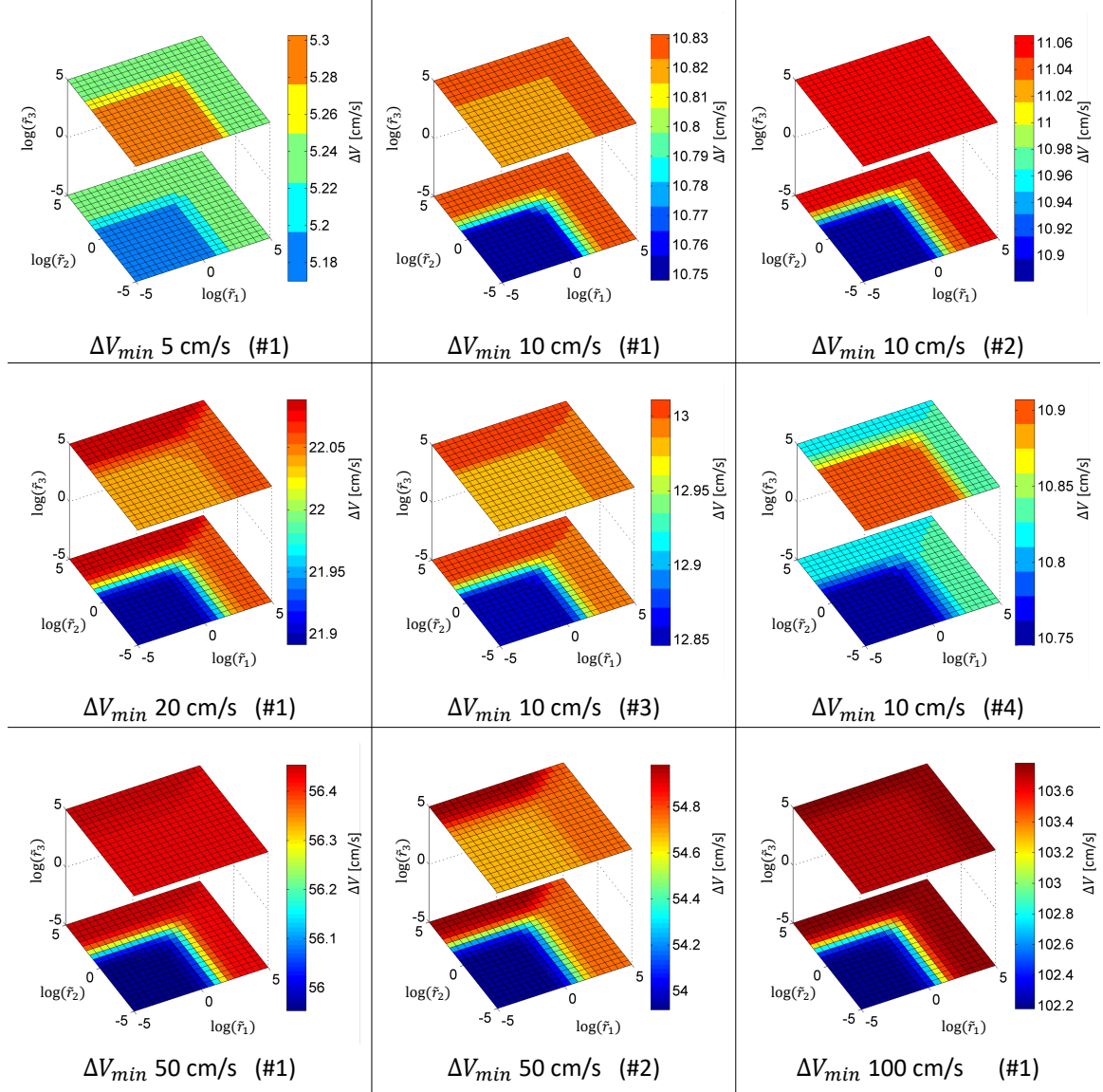
Figure 5.21. Variation in maneuver magnitude for different $\mathbb{R}$ matrix combinations for different ΔV_{min} cases. Each individual plot is for an arbitrary maneuver location. The symbol '#' indicates sequential numbering for a particular ΔV_{min} case.

Similar to analyzing the weighting matrix $\mathbb{R}$, the wighting matrix $\mathbb{R}_V$ that accounts for the velocity deviation at the future time is analyzed. At every maneuver location, different combinations of $\mathbb{R}_V$ matrix are used to compute the maneuver keeping Q and $\mathbb{R}$ fixed. Define the positive semidefinite matrix $\mathbb{R}_V$ as

$$\mathbb{R}_V = \begin{bmatrix} \tilde{r}_{V1} & 0 & 0 \\ 0 & \tilde{r}_{V2} & 0 \\ 0 & 0 & \tilde{r}_{V3} \end{bmatrix} \tag{5.37}$$

where, $\tilde{r}_{V1}$ weights the velocity deviation along x-direction, $\tilde{r}_{V2}$ along y-direction and $\tilde{r}_{V3}$ along z-direction at the future target time. At every maneuver location, the value of $\mathbb{R}_V$, in non-dimensional units, is selected as a combination of $\tilde{r}_{V1}$, $\tilde{r}_{V2}$ and $\tilde{r}_{V3}$ that are varied from 10^{-5} to 10^5 and the corresponding maneuver cost is recorded for different ΔV_{min} cases. Like the case of $\mathbb{R}$, the four-dimensional array consisting of $\tilde{r}_{V1}$, $\tilde{r}_{V2}$, $\tilde{r}_{V3}$ and ΔV are presented as a three-dimensional space of with the 4th dimension, ΔV color coded for visual assistance. The results are presented in Figure 5.22 for different ΔV_{min} cases. Although distinct patterns are visible, they are not very prominent. Low values of $\tilde{r}_{Vi}$ within the domain indicates lower maneuver costs, while larger values seem to increase the maneuver magnitudes. Although the chosen domain for $\tilde{r}_{Vi}$ seems to be sufficient to cover most maneuver magnitudes possible and present the distinct pattern, the range of achievable maneuver magnitude is very narrow in comparison to the range of maneuver magnitudes achieved by varying Q matrix. The selected value of Q already estimates station-keeping costs marginally lower than that estimated using the Floquet mode approach, hence the chance of decreasing orbit maintenance costs significantly lower is very slim. The fact is that the overall cost may or may not change by altering the value of $\mathbb{R}_V$ matrix, that produces marginal change in individual maneuver cost, hence additional computational effort only to have a probability of detecting a marginally smaller station-keeping cost, does not seem appropriate. The value of $\mathbb{R}_V$ is therefore chosen as I for this work. For other cases, if the possible decrease in maneuver magnitude is significant and occurs in

a specific pattern then it may be worth investing additional computational resources to reduce the annual station-keeping cost.
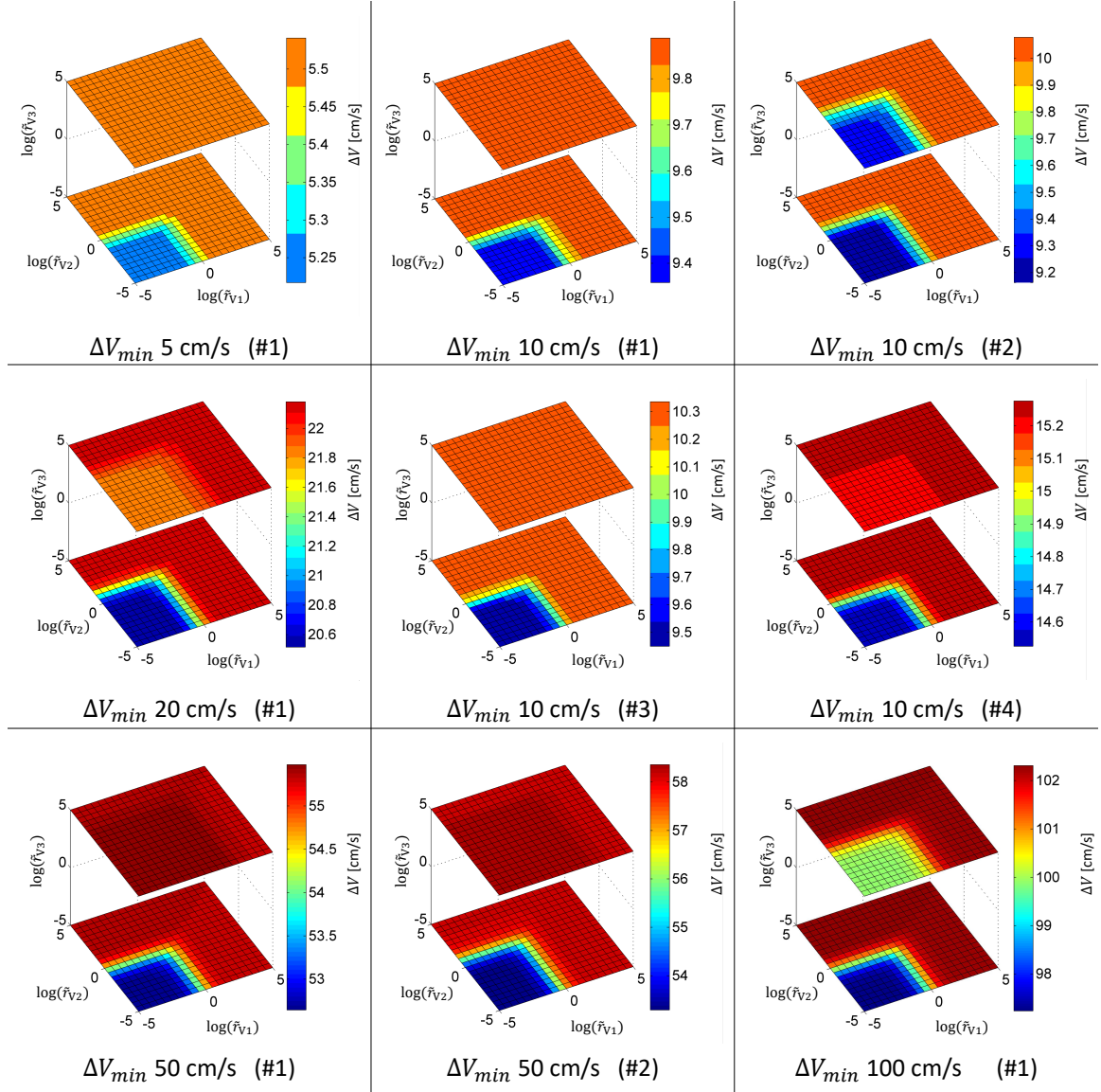
Figure 5.22. Variation in maneuver magnitude for different $\mathbb{R}_V$ matrix combinations for different ΔV_{min} cases. Each individual plot is for an arbitrary maneuver location. The symbol '#' indicates sequential numbering for a particular ΔV_{min} case.

6. CAUCHY GREEN TENSOR STATION-KEEPING STRATEGY

The concept of continuum mechanics deals with the flow of materials as a continuous volume. Cauchy Green tensor is used commonly in the area of continuum mechanics to portray the flow characteristics in different directions. To one's advantage, Cauchy Green tensor can also be used for station-keeping by utilizing the flow characteristics of a reference trajectory. The dynamical flow in the vicinity of a reference or a baseline trajectory depict the imaginary flow of a material volume in a given time duration [49]. The local deformation or the strain generated in the material volume is realized by the Cauchy-Green strain tensor (CGST) or commonly the Cauchy-Green tensor (CGT).

6.1 Cauchy-Green Tensor

The Cauchy Green tensor as well as the state transition matrix yields the dynamical flow characteristics in the vicinity of a reference solution. While the STM relates the variation of each individual states over time, the CGT relates the transformation of perturbation emulated by a material volume over time. The state transition matrix, ϕ, relates the flow in the vicinity of a baseline trajectory by mapping initial perturbation, $\delta \bar{x}_0$, to the final perturbed states, $\delta \bar{x}_f$, as a linear correlation i.e.

$$\delta \bar{x}_f = \phi(t_f, t_0) \delta \bar{x}_0 \tag{6.1}$$

where, t_0 and t_f are initial and final epochs. The CGT, or for mathematically simplicity represented as '$\mathbb{C}$',

$$\mathbb{C}(t_f, t_0) = \phi^T(t_f, t_0) \phi(t_f, t_0) \tag{6.2}$$

defines the deformation as product of transpose of the state transition matrix, ϕ, with itself. Physically, CGT renders the square of magnitude of final deformation to the initial deformation as

$$\begin{aligned} ||\delta\bar{x}_f||^2 = \delta\bar{x}_f^T \delta\bar{x}_f &= \delta\bar{x}_0^T \phi^T(t_f, t_0)\phi(t_f, t_0)\delta\bar{x}_0 \\ &= \delta\bar{x}_0^T \mathbb{C}(t_f, t_0)\delta\bar{x}_0 \end{aligned} \tag{6.3}$$

obtained by squaring equation (6.1). The growth or decay of the quantity $||\delta\bar{x}_f||^2$ describes the sensitivity of the trajectory to initial perturbation, $\delta\bar{x}_0$, however, when the size of an initial perturbation is undefined, the sensitivity information can be directly extracted from CGT. The eigen-decomposition of CGT or the singular value decomposition of STM yields details about direction and magnitude of stretching. Moreover, in a multi-eigenvalue system, the positive definite matrix, CGT, indicates a better behavior for numerical computation than a regular STM [69].

The flow of the perturbation, emulated by a material volume is characterized primarily by magnitude and direction of elongation. The flow of any system can be understood either using the eigendecomposition or singular value decomposition of the corresponding matrices. The eigendecomposition of the CGT, yields eigenvalues λ_i and eigenvectors $\mathbb{V}_i$. For a linear system, the contraction or expansion of the local phase space is given by σ_i in the direction given by $\mathbb{V}_i$. Note that $\sigma_i = \sqrt{\lambda_i}$. The singular values decomposition (SVD) of the STM, reveals the same critical details about the flow in the phase space but with additional direction information. Mathematically, STM is decomposed to matrices, $\mathbb{U}$, Σ and $\mathbb{V}$, such that,

$$\mathbb{U}\Sigma\mathbb{V}^* = \phi \tag{6.4}$$

where, the columns of $\mathbb{U}$ gives the direction of stretching at the final epoch. For a square matrix, ϕ, Σ is a diagonal matrix with the magnitude of stretching along different directions in the ascending order i.e.

$$
\Sigma = \begin{bmatrix} \sigma_1 & & & \\ & \sigma_2 & & \\ & & \ddots & \\ & & & \sigma_n \end{bmatrix}
\tag{6.5}
$$

such that, $\sigma_1 > \sigma_2 > ... > \sigma_n$. The matrix $\mathbb{V}$ provides the principal direction before stretching. The matrices Σ and $\mathbb{V}$ essentially provides the same details acquired using an eigenvalue decomposition, while $\mathbb{U}$ is an additional information captured using singular value decomposition [70]. The matrices $\mathbb{U}$ and $\mathbb{V}$ are orthonormal. The Figure 6.1 reveals how SVD relates the direction of principal axis before and after propagation, as well as the magnitude of contraction or expansion with the example of a two-dimensional system. Consider a unit circle in the phase space near an initial reference which undergoes deformation and evolves into a stretched ellipse. The evolution of this unit circle to an ellipse is a combination of translation and rotation. The matrices $\mathbb{U}$ and $\mathbb{V}$ provides the rotation information while the matrix Σ provides information about translation. The columns of matrix $\mathbb{V}$ represented by $\mathbb{V}_i$ indicates the direction of principal axis on this unit circle which evolves into $\mathbb{U}_i$ (columns of matrix $\mathbb{U}$). The diagonal elements of matrix Σ or σ_i indicates the stretching along corresponding principal directions. The eigenvalue decomposition and the singular value decomposition fundamentally provides the same information except that the later is a more elegant representation of the dynamical flow. Any of these methods can be used to linearly approximate the attainable region in the vicinity of a reference trajectory. The CGT station-keeping strategy uses the same principle.
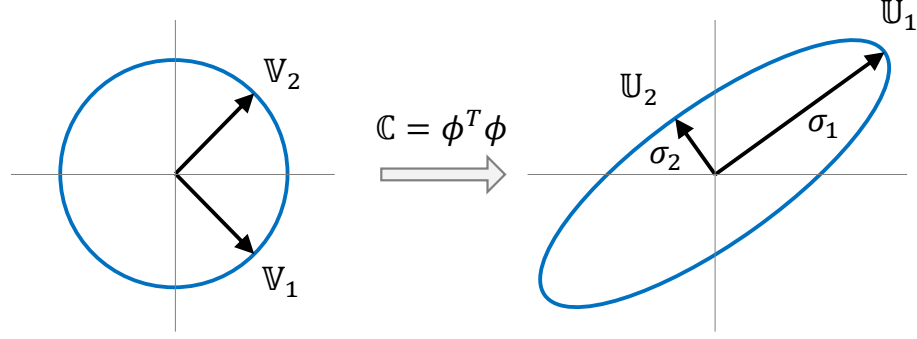
Figure 6.1. Singular value decomposition of a two-dimensional system.

6.2 Cauchy-Green Tensor Station-keeping Strategy

A spacecraft without a maneuver on a libration point orbit tends to deviate from its desired path because of their highly unstable nature and limitations of accurate orbit determination process. A station-keeping technique ensures that maneuvers are executed at regular intervals to maintain the spacecraft in the vicinity of the baseline/nominal trajectory. Ideally, it is expected that the spacecraft meet a target condition $\bar{x}_T$, generally the states of the baseline trajectory, after some horizon time T_h from the current time t_0. Due to perturbations or deviation from the nominal orbit, $\bar{x}_T$ may or may not be achieved, but at-least a solution close to $\bar{x}_T$ is achieved by having the information about the nearest attainable state.

The Cauchy-Green tensor station-keeping strategy uses the geometry of the phase space to compute a corrective maneuver. The CGT approach tracks the evolution of a physical continuum attributed as attainable region, at some epoch time t_f separated by a horizon time T_h i.e. $t_f = t_0 + T_h$, for a set of known finite initial velocity perturbation as demonstrated in Figure 6.2. A point in the attainable region closest to the target condition, $\bar{x}_T$, is chosen to compute the maneuver. A fixed maneuver magnitude, ΔV_M, at the initial time stretches the attainable region to ε at time t_f.

In the phase space, ε is a six-dimensional ellipsoid. Mathematically, the attainable region on the six-dimensional ellipsoid is expressed as,

$$\varepsilon = \left\{ \bar{\mathrm{x}} \mid (\bar{\mathrm{x}} - \bar{c})^T \mathbb{Q}(\bar{\mathrm{x}} - \bar{c}) = 1 \right\} \tag{6.6}$$

where $\bar{c}$ is the center of the ellipsoid while $\mathbb{Q} = \mathbb{U}\mathbb{S}\mathbb{U}^T$ is a symmetric positive semidefinite matrix that gives information of the radius of the ellipsoid in their principal directions. The matrix $\mathbb{U}$ is determined by the singular value decomposition of the state transition matrix while the matrix $\mathbb{S}$,

$$\mathbb{S} = (\Sigma \Delta V_M)^{-2} = \begin{bmatrix} 1/\sigma_1^2 & & & \\ & 1/\sigma_2^2 & & \\ & & \ddots & \\ & & & 1/\sigma_6^2 \end{bmatrix} \Delta V_M^{-2} \tag{6.7}$$

is the inverse square of the radii of the attainable ellipsoid region in all the six dimensions.
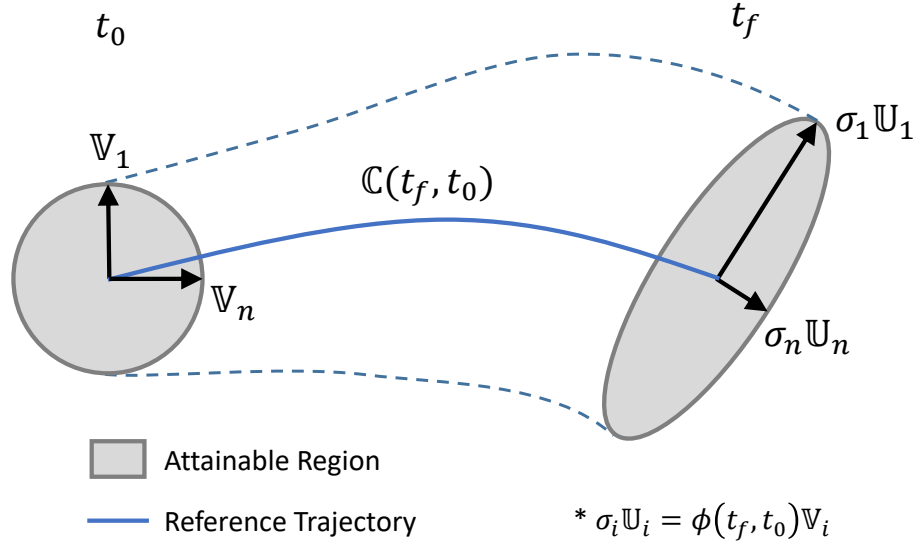
Figure 6.2. Attainable region computed using the Cauchy-Green tensor.

The goal of the CGT station-keeping process is to target position and velocity states along the baseline trajectory at regular intervals to secure the spacecraft path close to the baseline path. Let the point $\bar{x}_T$ be a state on the baseline trajectory that acts as a target condition to compute a maneuver. For a fixed maneuver size ΔV_M, an attainable ellipsoid region ε is computed using the CGT information. It might be challenging to attain the exact states at $\bar{x}_T$, but the point closest to $\bar{x}_T$ on the attainable ellipsoid ε should serve the same purpose, provided that the tolerance is low. The point $\bar{\mathrm{x}}^*$ on this ellipsoid closest to the target state, $\bar{x}_T$, satisfies the following condition,

$$x^* = \underset{\bar{\mathrm{x}} \in \varepsilon}{arg \, min}(\bar{\mathrm{x}} - \bar{x}_T) \tag{6.8}$$

where all possible values of $\bar{\mathrm{x}}$ are the solutions to ε. The computed point $\bar{\mathrm{x}}^*$ is the closest point to the target state $\bar{x}_T$, but it may be overshooting or undershooting the desired target state. Since the aim is to achieve the state that almost exactly reproduces the target state, further refinement to the value of $\bar{\mathrm{x}}^*$ is required.

The geometry of the attainable region is capitalized to compute an increase or decrease in the size of maneuver. Define $^cD^*$ as the distance from the center of the ellipsoid $\bar{c}$, to $\bar{\mathrm{x}}^*$ while $^*D^T$ as the distance from $\bar{\mathrm{x}}^*$ to the target $\bar{x}^T$ and $^cD^T$ is the distance from the center, $\bar{c}$, to target, $\bar{x}^T$ to complete the triangle i.e.

$$^cD^* = \, ^*D^c = ||\bar{\mathrm{x}}^* - \bar{c}|| \tag{6.9}$$

$$^*D^T = \, ^TD^* = ||\bar{\mathrm{x}}^* - \bar{x}_T|| \tag{6.10}$$

$$^cD^T = \, ^TD^c = ||\bar{x}_T - \bar{c}|| \tag{6.11}$$

where each scalar distance $^iD^j = \, ^jD^i$, for $i, j \in \{c, *, T\}$. Once the sides of the triangles are fixed, the relative location of $\bar{c}$, $\bar{\mathrm{x}}^*$ and $\bar{x}^T$ is unique. For reference, the so formed triangle between $\bar{c}$, $\bar{\mathrm{x}}^*$ and $\bar{x}^T$ can be called as *maneuver feedback triangle*, as the geometry of this triangle decides a change in the size of the maneuver. If $^cD^T > \, ^cD^*$ then the size of the maneuver is not sufficient to achieve the target state

and hence an increase in size of maneuver is required. The magnitude of maneuver ΔV_M is increased from the previous value either using the relation

$$\Delta V_M = \Delta V_M + \Delta V_{min} \tag{6.12}$$

where the increment in maneuver magnitude is a step function of size ΔV_{min} or using the relation

$$\Delta V_M = \Delta V_M ({}^c D^T / {}^c D^*) \tag{6.13}$$

that manipulates the dimensions of the maneuver feedback triangle to compute an increase in the size of the maneuver. Similarly, if ${}^c D^T < {}^c D^*$ then the size of the maneuver causes overshooting the target state, hence a decrease in size of maneuver is required. Again equation (6.13) is used to decrease the size of the attainable region in the required proportion. Since the geometry is not linear i.e. $\bar{x}^*$ does not necessarily lie between $\bar{c}$ and $\bar{x}^T$, a single increment or decrement of the maneuver size may not be sufficient to result in achieved closest state $\bar{x}^*$ to almost overlap $\bar{x}^T$, nevertheless the distance ${}^* D^T$ diminishes every iteration. The size of the ellipsoid or the size of the maneuver is refined till the required tolerance level is achieved. The target tolerance can be defined as scalar quantity ϵ_T, such that if ${}^* D^T < \epsilon_T$, it can be assumed that the achievable state $\bar{x}^*$ is almost exactly equal to the desired target $\bar{x}_T$ with tolerance of ϵ_T. Figure 6.3 illustrates the different possible scenarios of maneuver refinement.

Once the final achievable state $\bar{x}^*$ is determined, it is desired to compute the corresponding maneuver. Illustrated in Figure 6.4, each point on the six-dimensional ellipsoid, ε, has a corresponding initial condition represented as a six-dimensional state vector, as a result, $\bar{x}^*$ corresponds to a point, $\bar{x}_i$ at $t = 0$, that would drive the spacecraft to $\bar{x}^*$ at time t_f. In other words, the actual initial state $\bar{x}_0$ at $t = 0$ if continued would reach the final state $\bar{x}_f$ at time t_f. The vector $\bar{x}_f$ is also the center of the ellipsoid represented as $\bar{c}$. In order to reach a different state $\bar{x}^*$ at $t = t_f$, the required condition is $\bar{x}_i$ at $t = t_0$. Since $\bar{x}_f$ (same as $\bar{c}$) is not equal to $\bar{x}^*$; the

(a) Magnitude of maneuver not sufficient. Increase maneuver size.

(b) Excess maneuver. Decrease maneuver size.
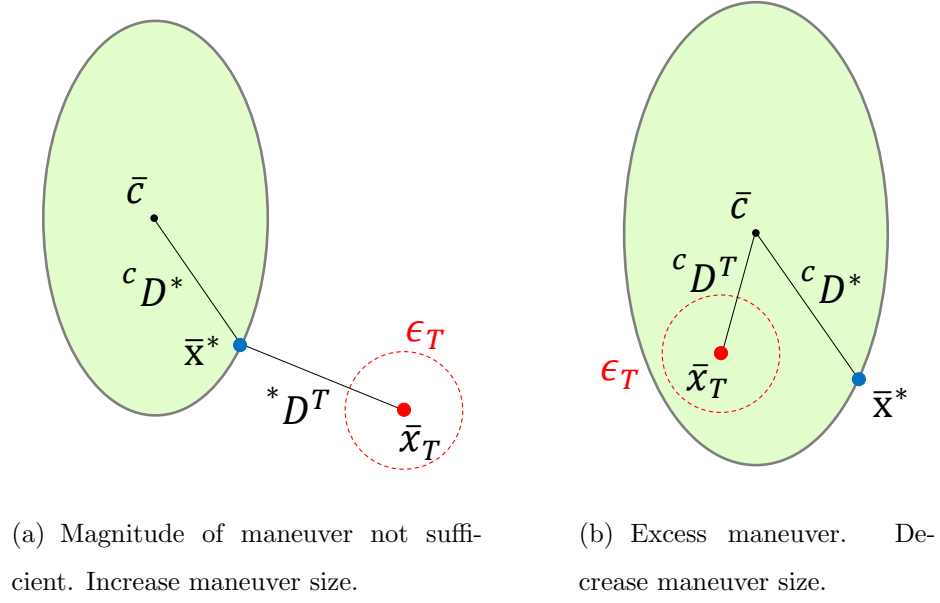
Figure 6.3. Refinement of attainable region produced using CGT.

vectors $\bar{x}_0$ and $\bar{x}_i$ are not the same. The difference between the vector $\bar{x}_i$ and $\bar{x}_0$ is the required initial perturbation vector achieve $\bar{x}^*$.
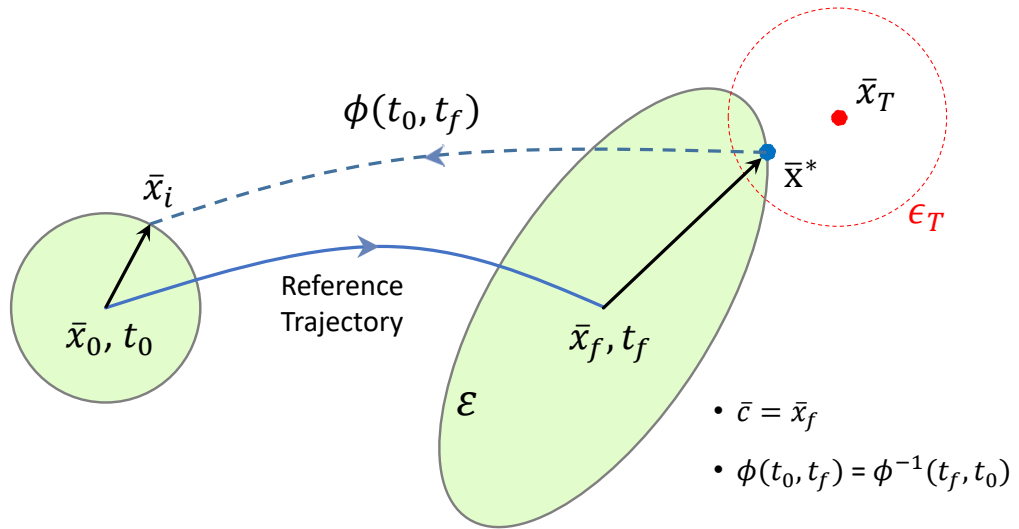
Figure 6.4. Required initial perturbation to achieve state on the attainable region nearest to the target state.

The difference between the state vector $\bar{x}_i$ and $\bar{x}_0$ are both in terms of position and velocity, however, using an impulsive maneuver only the change in velocity states can be achieved. If a perfect solution existed, the corresponding maneuver $\Delta\bar{V}_M$ should satisfy

$$(\bar{x}^* - \bar{c}) = \phi(t_f, t_0) \begin{pmatrix} \bar{0} \\ \Delta\bar{V}_M \end{pmatrix} = \begin{bmatrix} \phi_{rr} & \phi_{rv} \\ \phi_{vr} & \phi_{vv} \end{bmatrix} \begin{pmatrix} \bar{0} \\ \Delta\bar{V}_M \end{pmatrix} \qquad (6.14)$$

$$(\bar{x}^* - \bar{c}) = \begin{bmatrix} \phi_{rv} \\ \phi_{vv} \end{bmatrix} \Delta\bar{V}_M = A\Delta\bar{V}_M \qquad (6.15)$$

where $A = \begin{bmatrix} \phi_{rv} \\ \phi_{vv} \end{bmatrix}$ is a 6×3 matrix. In general, this is an overdetermined system with no perfect solution, therefore, a solution with pure velocity change will have some error. A least squares method [71] produces a possible solution

$$\Delta\bar{V}_M = \left(A^T A\right)^{-1} A^T \left(\bar{x}^* - \bar{c}\right) \qquad (6.16)$$

with the minimal error. Ideally, a position perturbation as well as a velocity perturbation at initial time is required to almost exactly attain the target state. Due to impractical position perturbation, the nearest possible attainable state is achieved by the computed $\Delta\bar{V}_M$. The details of this process is elaborated in Figure 6.5 using two major steps. (1) Firstly, the state $\bar{x}^*$ on ε closest to the target state $\bar{x}_T$ is mapped back to the initial time to determine the actual perturbation required to achieve $\bar{x}^*$, that are in terms of both position and velocity perturbation. (2) Since position perturbation is practically not achievable, the second step determines the best possible alternative in terms of pure velocity perturbation i.e. the maneuver $\Delta\bar{V}_M$ using a least square projection. The computed maneuver, void of any errors, drives the trajectory towards a new achievable state $\bar{x}_f^+$ that is in close vicinity to desired $\bar{x}^*$ or $\bar{x}_T$. Based on the limitation of not achieving the exact target state, regular maneuvers are required to ensure that the spacecraft transits in close vicinity to the reference trajectory. An impulsive maneuver $\Delta\bar{V}_M$ is implemented along with station-keeping execution errors and thus a new initial condition is generated. The new states are propagated and the process is repeated till the end of mission duration.
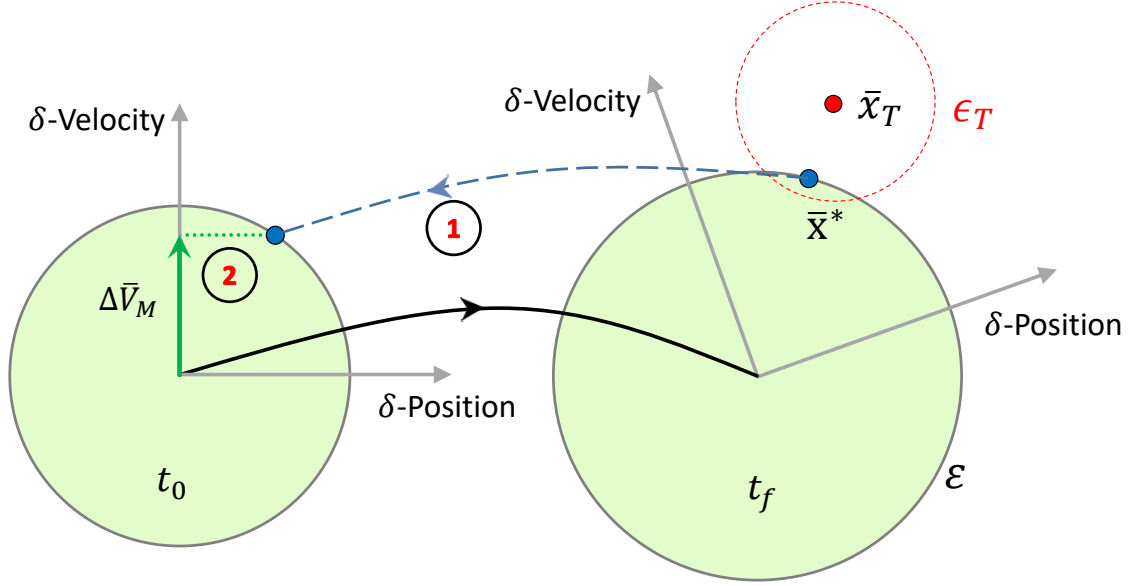
Figure 6.5. CGT station-keeping method; maneuver computation using projection of required perturbation on to the velocity subspace.

Similar to the one noted by Guzzetti et al. [72], Figure 6.6 summarizes the station-keeping process in concise steps. (1) The current state, $\bar{x}_0$, and target state, $\bar{x}_T$, is defined. (2) The current state is propagated for time t_f till it reaches $\bar{x}_f$. (3) Using CGT or STM, for a chosen value of ΔV_M, the attainable region is computed. (4) The point on the attainable region closest to the target state is selected. Further refinements as explained are conducted till the required tolerance is achieved. (5) The point $\bar{x}^*$ that is closest to the target state is mapped back using STM information to find the necessary initial condition required to achieve close proximity to $\bar{x}_T$ at t_f. (6) Corresponding maneuver ΔV_M is procured using least square method.

A linear approximation of the attainable region may be less accurate for a very large ΔV_M. Further, an increase in the horizon time will result in more stretched ε, consequently, modeling the attainable region as a linear approximation may not be reasonable. Additional parameter that can affect the performance of this station-
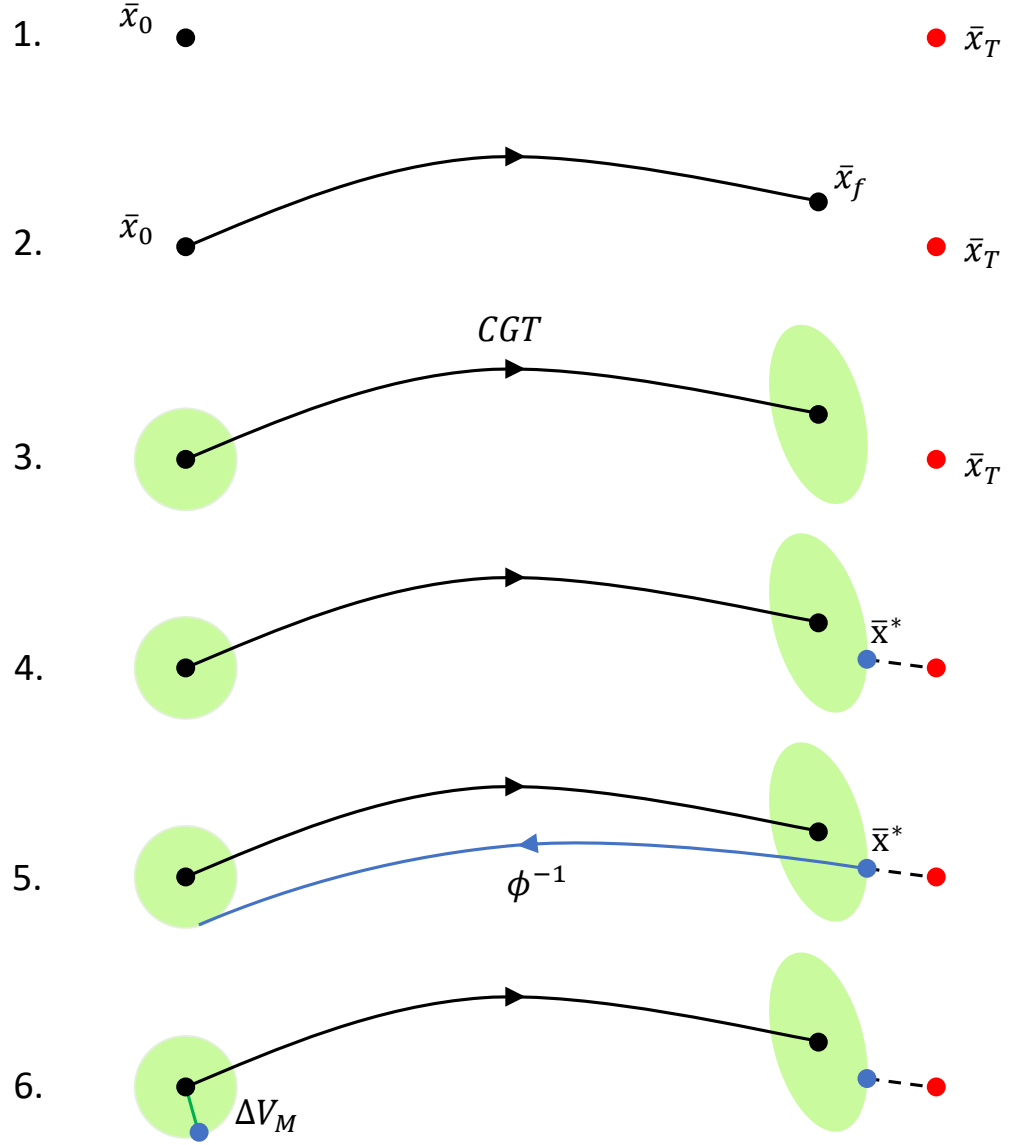
Figure 6.6. CGT station-keeping maneuver computation scheme.

keeping technique is the size of the scalar target tolerance, ϵ_T. Too low value of ϵ_T will enforce the algorithm to compute $\bar{\mathrm{x}}^*$ almost equal to the exact target state $\bar{x}_T$ more accurately, that may be difficult to achieve. Similarly, larger value of ϵ_T may indicate larger separation between $\bar{\mathrm{x}}^*$ and $\bar{x}^T$. It becomes challenging to decide the right size of the target tolerance, ϵ_T. The following sections explores the performance

of CGT station-keeping technique with varying sizes of ΔV_M, different horizon times, T_h, and target tolerance, ϵ_T.

6.3 Effect of Target Tolerance, Horizon Time and Maneuver size

The principle of the Cauchy-Green tensor station-keeping method is to utilize the flow characteristics of the reference trajectory to compute a corrective maneuver, by accessing states on the attainable region at a future time closest to the desired target state. The main hypothesis behind the use of CGT is that the accessible region is computed by linear approximation of flow dynamics near the reference trajectory. The nominal path or the periodic orbits computed either in the CR3BP model or the Ephemeris model are nonlinear, hence, linear approximation may deteriorate over time as well as larger perturbation levels. Essentially, the horizon time and size of maneuver may impact the performance of the CGT method for station-keeping. The CGT method predicts an attainable region which is a six-dimensional ellipsoid at some horizon time downstream. With increase in time, the non linear characteristics become more dominant, therefore the ellipsoid approximation may not hold reliable. The evolution of the attainable region with horizon time is illustrated in Figure 6.7 as red ellipsoids. With increase in horizon time, the bending of the ellipsoid region is apparent, indicating that the linear approximation is deteriorating. Similarly, the increase in the size of the maneuver magnitude is comparable to the flow due to a larger perturbation. The accuracy of the linear approximation of the flow decreases as the perturbation increases, therefore, a larger maneuver size may essentially downgrade the performance of CGT, that is linear estimation of the attainable region. The phenomenon is demonstrated in Figure 6.8 where for a constant horizon time of $1\mathbb{P}$, the attainable region digresses from its ellipsoid shape with increases in the size of maneuver. Another potential challenge is the size of the target tolerance, that is a scalar quantity to judge whether the maneuver feedback triangle requires any additional refinement. Typically a low value of target tolerance will cause more refinement of

the maneuver feedback triangle, increasing the computational expense. Alternatively, a large value of target tolerance may degrade the performance of CGT method for station-keeping and result in larger annual costs. The causes and the impact of the three potential challenges including horizon time, size of maneuver magnitude and size of target tolerance are explored.
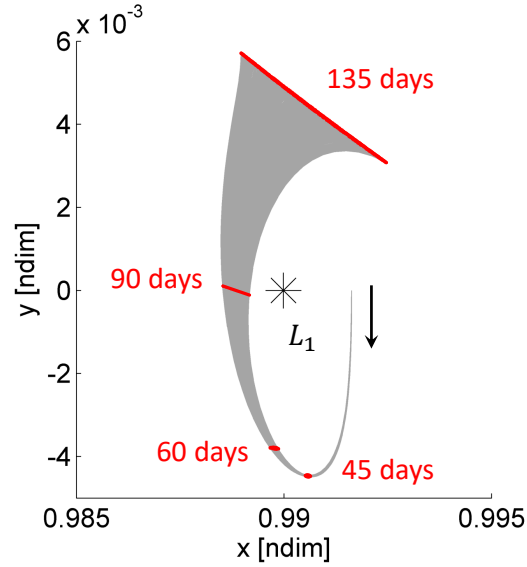
Figure 6.7. Specific example of variation in attainable region for ΔV = 100 cm/s over different horizon time. The attainable region in configuration space is marked as red ellipsoid.

The three potential challenges discussed here i.e. horizon time, size of maneuver magnitude and size of target tolerance are not mutually exclusive hence independent studies may not be profitable. The parameters are inter dependent and hence combinatorial studies are performed. A three-dimensional grid as described in Figure 6.9 provides potential combinations of the three parameters used to explore the performance of the CGT. At a time, one parameter is fixed, and the impact of the remaining two parameters are studied. The combinations are then altered to get a better understanding of the impact of all the three parameters on the station-keeping costs and computational time. For the studies, horizon time of 45, 60 and 90 days
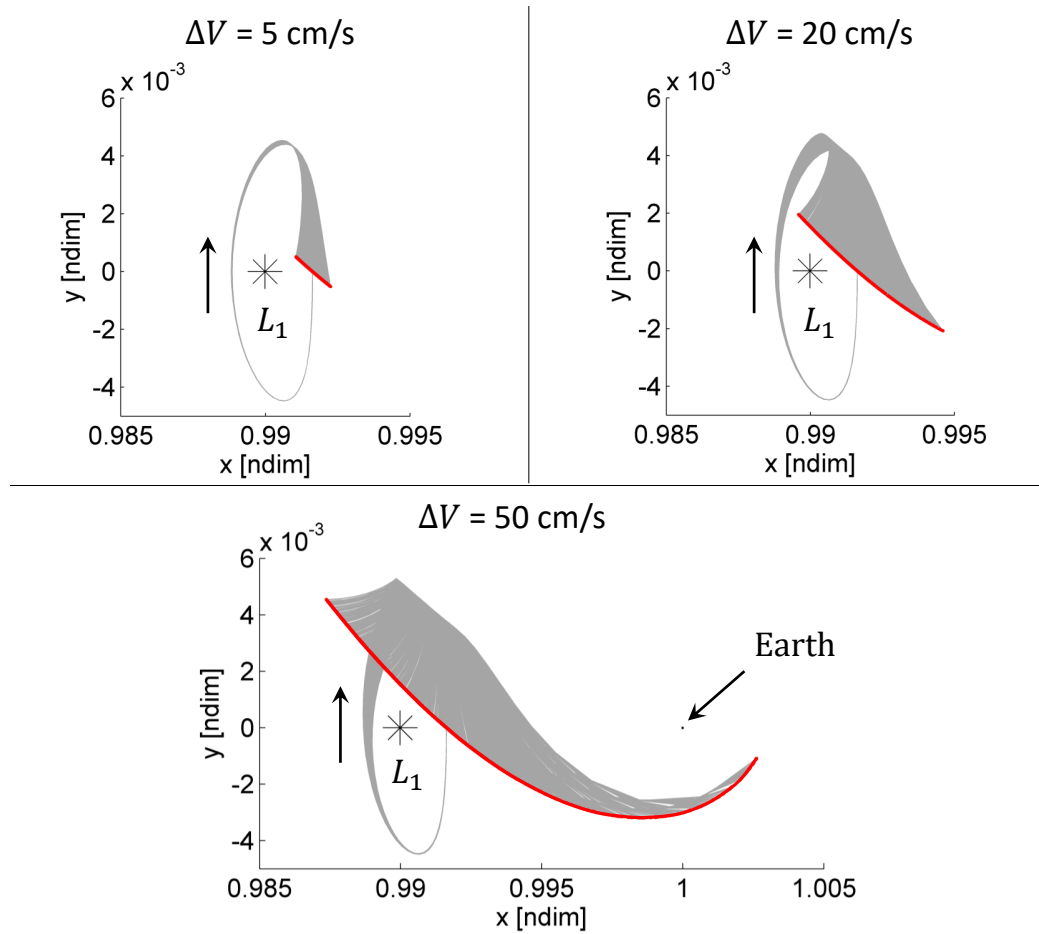
Figure 6.8. Specific example of variation in attainable region for ΔV of size 5 cm/s, 20 cm/s and 50 cm/s over constant horizon time of one period ($1\mathbb{P}$). The attainable region in configuration space is marked as red ellipsoid.

are considered, while the size of the maneuver is controlled by introducing ΔV_{min} constraints of 5, 10, 20, 50 and 100 cm/s. The value of the scalar target tolerance is considered between 10^{-7} and 10^{-3} assuming that the selected range does contain the factual values, which will be assessed later.
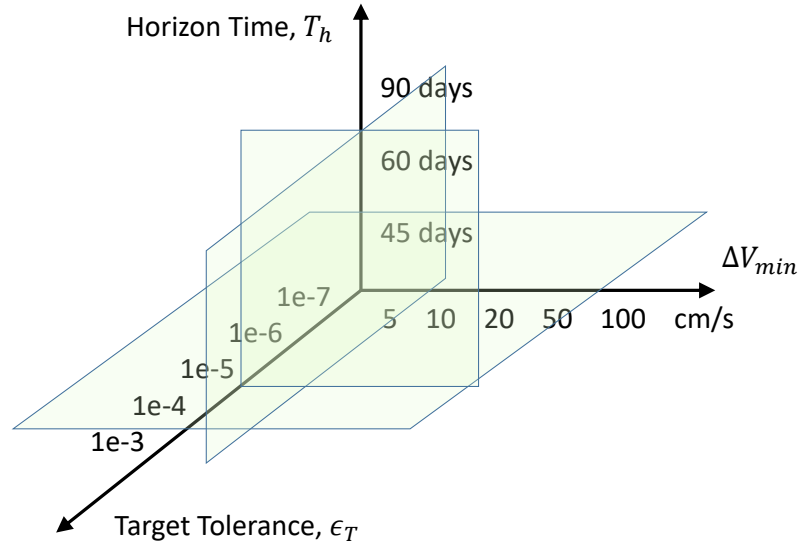
Figure 6.9. Three-dimensional grid for potential combinations of horizon time, size of maneuver and target tolerance to explore performance of CGT station-keeping approach.

6.4   Preliminary Results

6.4.1   Station-keeping Outcomes for various combinations of Horizon Time, T_h, size of Minimum Executable Maneuver, ΔV_{min}, and Target Tolerance, ϵ_T

The horizon time T_h, size of minimum executable maneuver ΔV_{min} and target tolerance ϵ_T are the three important parameters that can influence the performance of the Cauchy-Green tensor station-keeping process, mainly the orbit maintenance costs and the computational expense. A three-dimensional grid as discussed provides potential combinations of the three parameters that are used to simulate a station-keeping scenario. The outcomes including station-keeping costs and computational expense estimated for different combinations of the parameters within the grid provides the impact of these parameters on the CGT method performance. The station-keeping cost estimated for each of the cases are measured in cm/s while the computational

expense is measured as the ratio of the computational resources used compared to a baseline value. The computational expense is inclusive of computational time and number of processors used for Monte Carlo simulation. The baseline value corresponds to the outcome of Type A ODE with horizon time 45 days, $\Delta V_{min} = 10$ cm/s and $\epsilon_T = 10^{-5}$. Computational expense computed for all cases with Type A as well as Type B ODE are compared to this specified baseline value.

A way to analyze the effect of the three parameters, horizon time T_h, size of minimum executable maneuver ΔV_{min} and target tolerance ϵ_T is by maintaining a fixed value of horizon time and varying the size of ΔV_{min} for different values of ϵ_T between 10^{-7} to 10^{-3}. Figure 6.10 and Figure 6.11 provides the variation in station-keeping cost with respect to ϵ_T for fixed values of T_h and different ΔV_{min} case, for Type A and Type B ODE respectively. For both type of ODE, the station-keeping costs for fixed horizon time and ΔV_{min}, almost seem to remain unchanged over different values of ϵ_T. The constant station-keeping cost predicted is the result of the functioning of the algorithm that computes an almost accurate maneuver in the first iteration itself, prior to introduction of the quantity ϵ_T, The computational expense for Type A and Type B ODE for varying ϵ_T with fixed values of T_h and ΔV_{min} case are presented in Figure 6.12 and Figure 6.13 respectively. For smaller values of ϵ_T in the selected range, the computational expense seem to shoot up, especially in the case of higher values of ΔV_{min}. The algorithm performs multiple iterations to compute a state on the attainable region closest to the target state with more accuracy by reforming the maneuver feedback triangle, such that the distance between $\bar{\mathrm{x}}^*$ and $\bar{x}^T$ is within the specified target tolerance. From the trends observed, it can be concluded that very small values of ϵ_T may result in high computational expense without improving the station-keeping costs, while a large value of ϵ_T may result in a poor station-keeping costs especially in sensitive maneuver locations where one iteration of the algorithm may not be sufficient to compute an appropriate maneuver. A better selection of ϵ_T is required for a meaningful station-keeping cost without excess computational load.
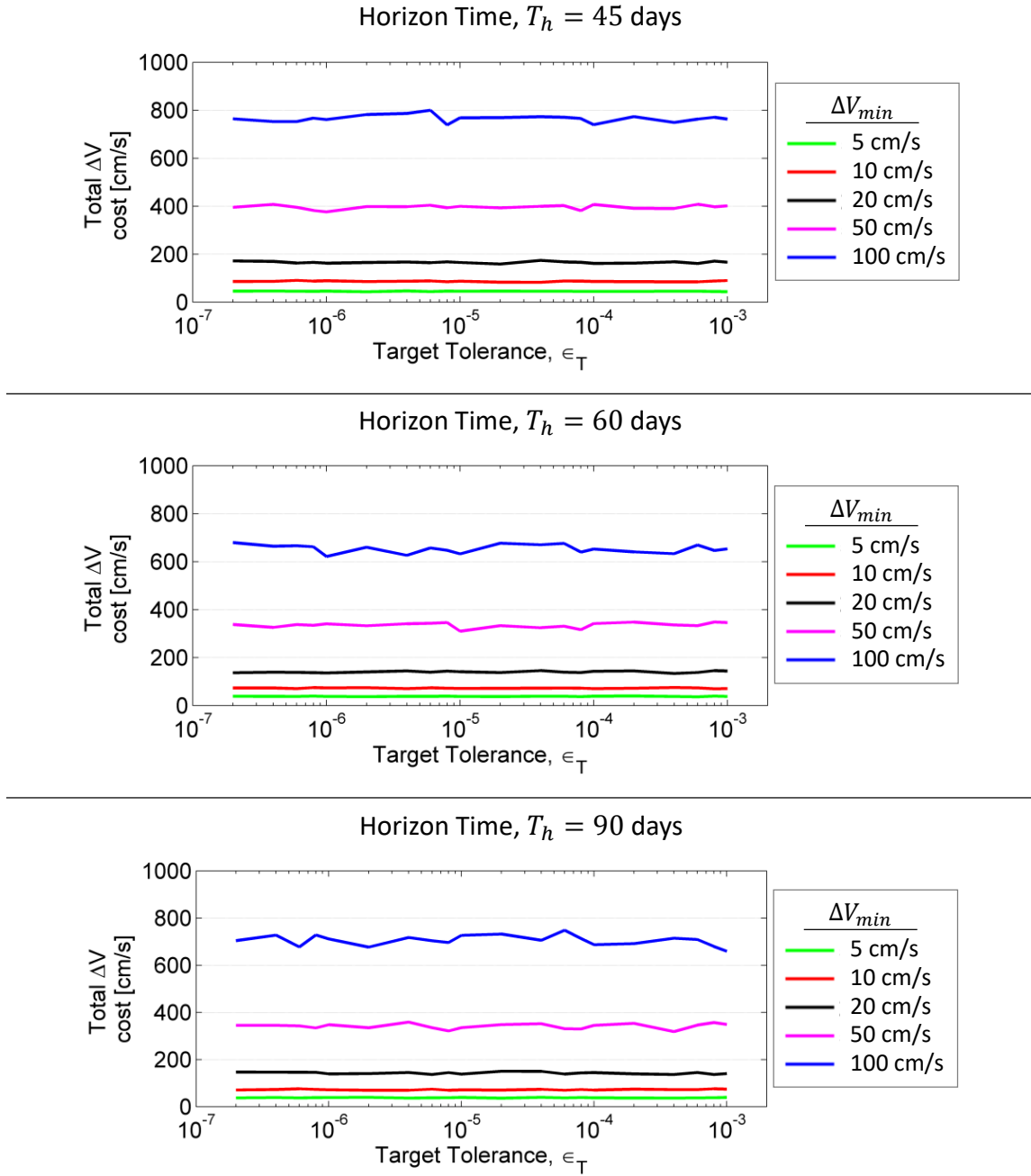
Figure 6.10. Station-keeping costs estimated by the Cauchy-Green tensor approach for 2 year mission duration with Type A orbit determination error. Different horizon times of 45, 60 and 90 days and range of target tolerance between 10^{-7} and 10^{-3} are considered.
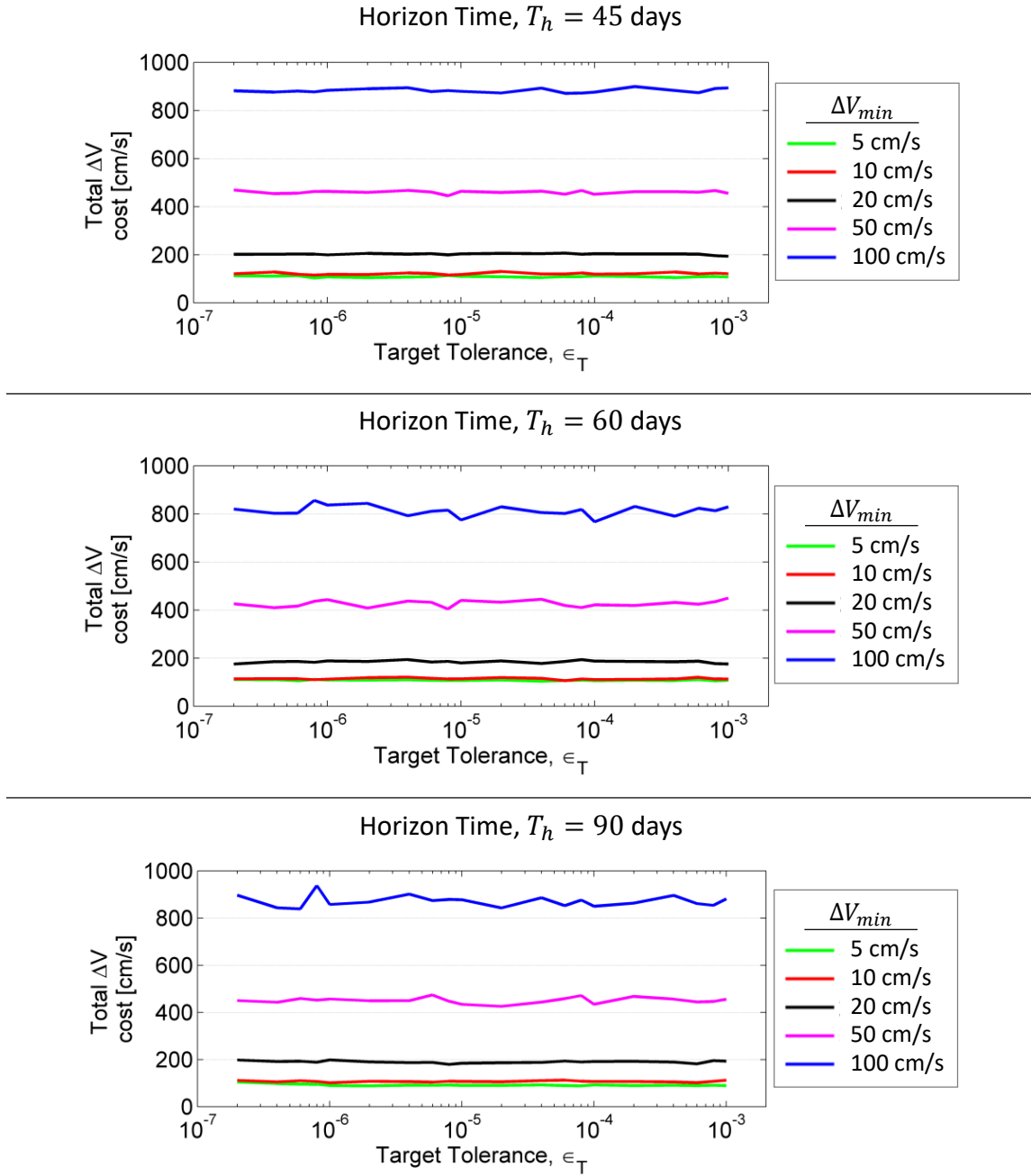
Figure 6.11. Station-keeping costs estimated by the Cauchy-Green tensor approach for 2 year mission duration with Type B orbit determination error. Different horizon times of 45, 60 and 90 days and range of target tolerance between 10^{-7} and 10^{-3} are considered.
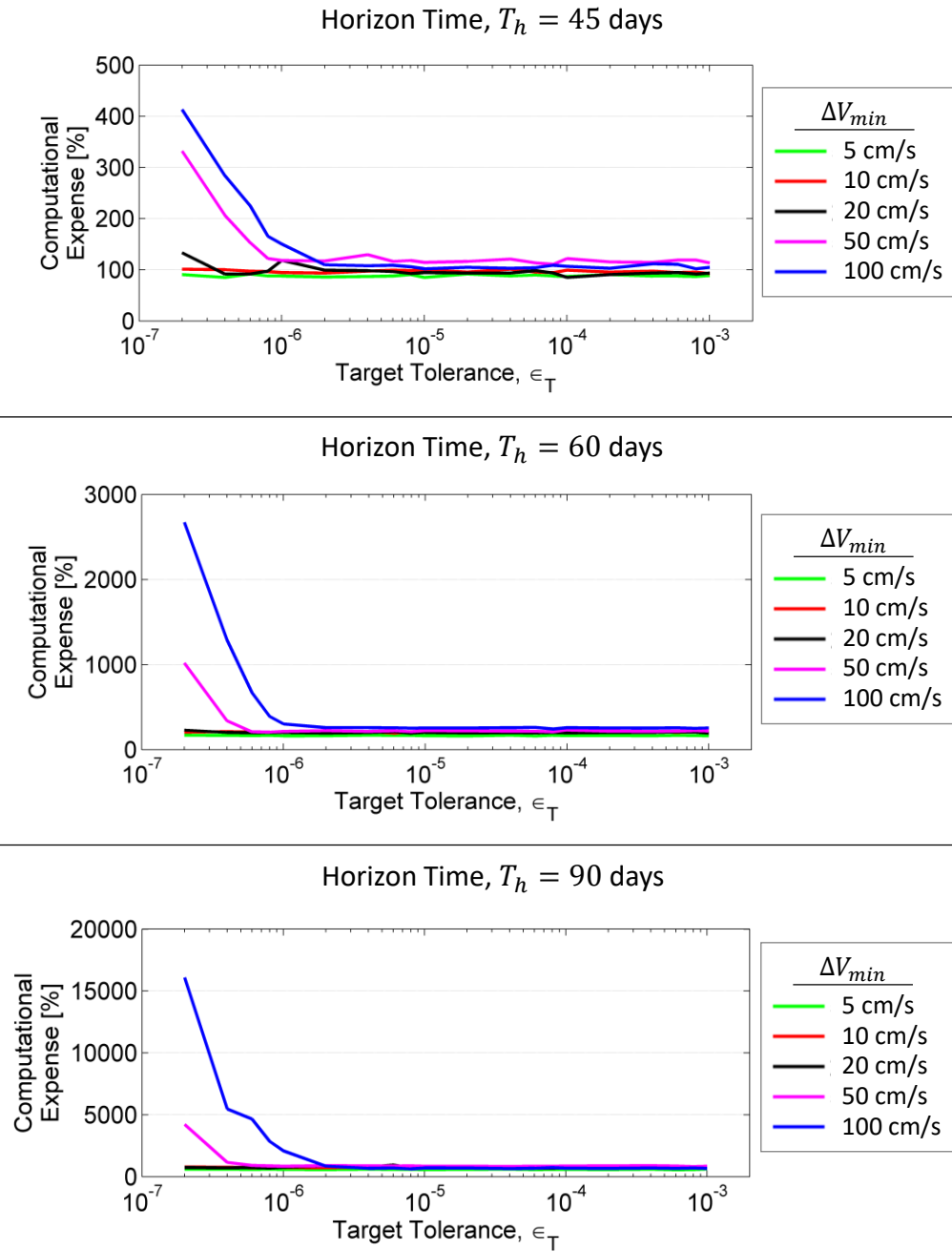
Figure 6.12. Computational expense for station-keeping simulation using the Cauchy-Green tensor approach for 2 year mission duration with Type A ODE, expressed with respect to baseline value. Baseline value is the simulation corresponding to horizon time 45 days, ΔV_{min} = 10 cm/s and $\epsilon_T = 10^{-5}$ for Type A ODE. Different horizon times of 45, 60 and 90 days and range of target tolerance between 10^{-7} and 10^{-3} are considered.
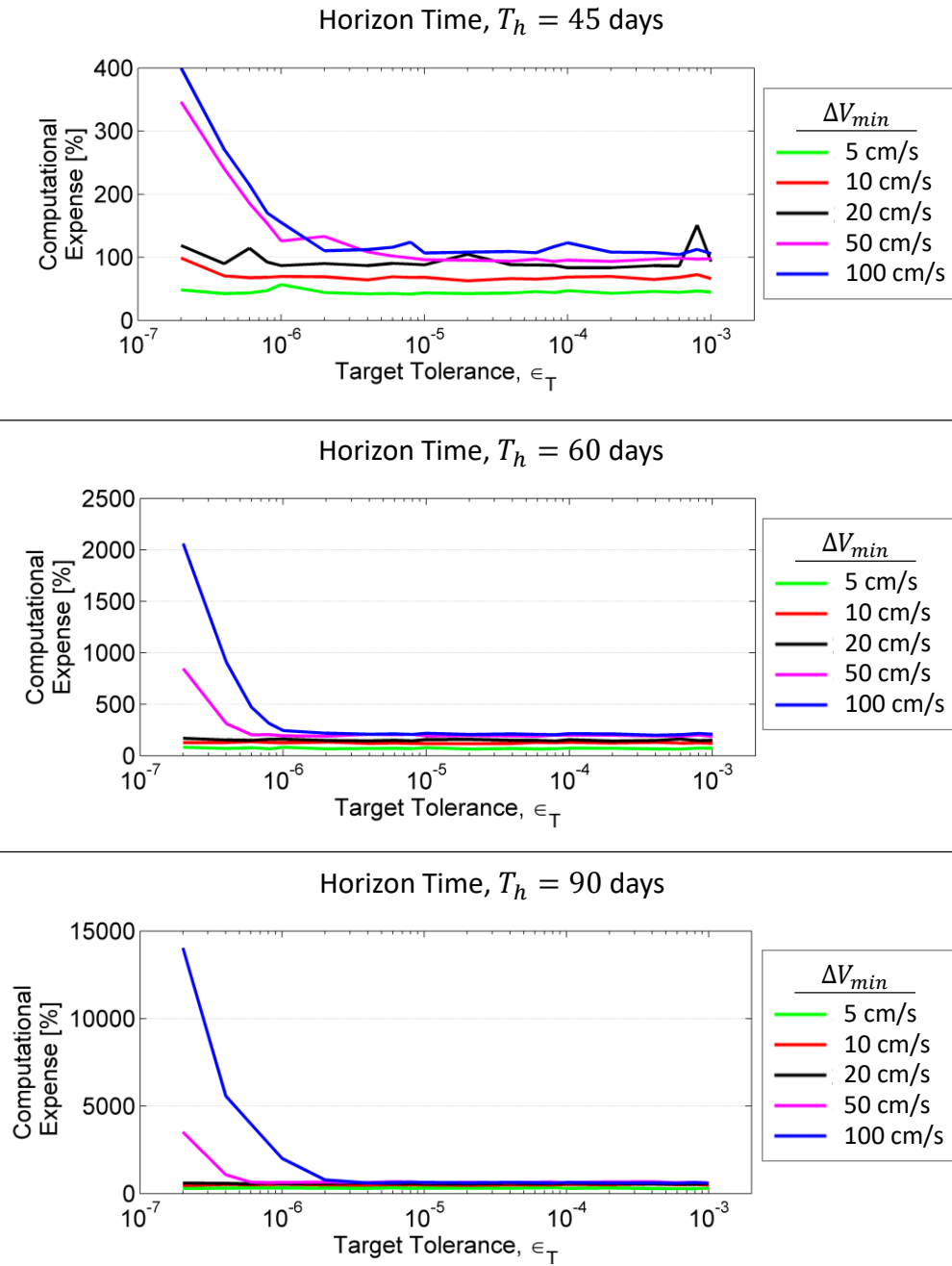
Figure 6.13. Computational expense for station-keeping simulation using the Cauchy-Green tensor approach for 2 year mission duration with Type B ODE, expressed with respect to baseline value. Baseline value is the simulation corresponding to horizon time 45 days, ΔV_{min} = 10 cm/s and $\epsilon_T = 10^{-5}$ for Type A ODE. Different horizon times of 45, 60 and 90 days and range of target tolerance between 10^{-7} and 10^{-3} are considered.

6.4.2   Dynamic selection of Target Tolerance

A station-keeping problem is an attempt to secure the spacecraft near the reference solution for the mission duration. Station-keeping is a stochastic problem, hence locating states of the spacecraft with full accuracy is not possible. There is a limitation to the determination of accurate states of the spacecraft at all times, thereby effort to compute the corrective maneuver with high accuracy is insignificant. The size of the orbit determination error is a potential deciding factor on the value of target tolerance ϵ_T that would deliver the maneuver with the same order of uncertainty as that of the ODE. Desire for more accurate result is meaningless, therefore, it is redundant to invest high computational expenditure for very low values of ϵ_T. To use the ODE information to formulate a relevant ϵ_T, the evolution of the error over time needs to be analyzed. The ODE error is pretended to constitute an error region inclusive of deviation in position and velocity states. The evolution of the flow in the vicinity of a reference trajectory is used to investigate the evolution of the error region and thus develop a way of establishing a value of reasonable ϵ_T.

The Cauchy-Green tensor relates the evolution of the position and velocity deviation described as an error sphere over time to form an error ellipsoid caused by stretching and rotation. Equivalently, the ODE error is also a form of error in both position and velocity and therefore it is assumed that it will also get stretched and rotated as the position and velocity deviation vector. Applying the same linear correlation using cauchy-green tensor, the manner in which the orbit determination error region evolves is determined. As described in Figure 6.14, the region marked in red at initial time represents the region of no significance as a result of orbit determination error. Any value computed smaller than the size of the red circle is not recognizable due to limitations in orbit determination, therefore desiring an accuracy within the size of the red region is not sensible. The boundary of the red region relates to the minimum measurable precision level, therefore the desired value of ϵ_T must be the

measurement corresponding to the outer surface of the red region. The fictitious six-dimensional radius of the red sphere is a relevant scalar quantity that relates to the size of sphere i.e. the size of uncertainty. For a six-dimensional ODE vector, $\delta\bar{x}_{ODE}$, the scalar radius is given as $||\delta\bar{x}_{ODE}||$. Explained by Spreen et al. [73], the rate of separation between two nearby trajectories over a non infinite time interval is predicted by the Finite Time Lyapunov Exponent (FTLE), of which the largest component of the FTLE reflects the most stretching direction. Also labeled as Local Lyapunov Exponent (LLE), the actual separation is given by the square root of the largest eigenvalue of $\phi(t_f, t_0)^T \phi(t_f, t_0)$, where t_0 and t_f are the initial and final epoch. The value predicted by the LLE information is exactly equal to the largest eigenvalue of the Cauchy-Green tensor σ_1. Therefore, the dominant stretching of the no value region indicated by red ellipsoid in Figure 6.14 is in the direction of $\mathbb{U}_1$ with a magnitude of σ_1. The appropriate scalar target tolerance ϵ_T to represent the no value region is given by $\sigma_1 ||\delta\bar{x}_{ODE}||$, such that $||\delta\bar{x}_{ODE}||$ indicates the initial separation while σ_1 is a measure of expansion. The target tolerance ϵ_T is thus represented by a dynamic quantity that takes into consideration the orbit determination error, the horizon time and the location along the orbit that influences the amount of stretching.
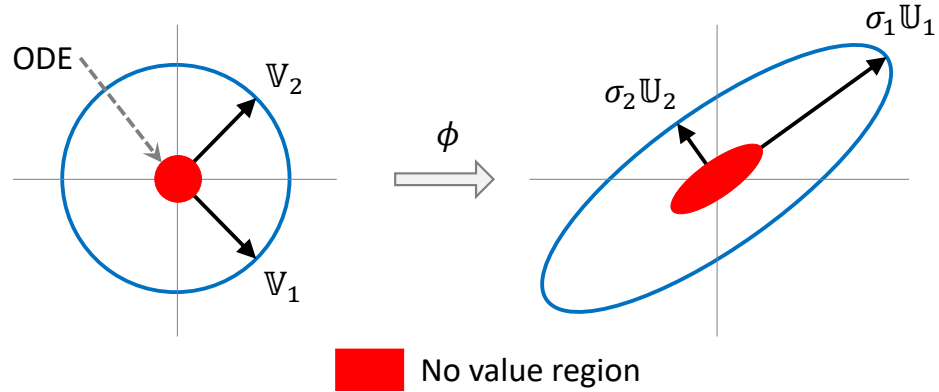
Figure 6.14. Six-dimensional region of no value or non measurable value, resulting from orbit determination error, mapped using a linear state transition matrix.

The dynamic target tolerance ϵ_T is now defined as $\epsilon_T = \sigma_1 ||\delta\bar{x}_{ODE}||$, where σ_1 is a dynamic quantity that depends on the sensitivity of the location along the orbit as well as the horizon time that impacts the amount of stretching. Similar to a LLE surface, an entire spectrum of possible values of σ_1 are generated to identify the corresponding values at different locations along the orbit as well as for different horizon times. The location along the orbit can be represented in terms of the time propagated from a fixed initial location, that is demonstrated in Figure 6.15, where the point on the reference orbit corresponding to $x - z$ plane crossing towards the Sun is considered as the initial fixed location for generating the stretching spectrum. At different locations along the orbit, separated by small time intervals, magnitude of the dominant stretching, σ_1, is computed and recorded for different horizon time between $(0, 1\mathbb{P}]$. The entire data recorded for different combinations of the location and the horizon times are given as a spectrum in Figure 6.16. The colorbar used to represent the spectrum is indicated in natural logarithmic scale to encompass the entire range with proper visualization. Recall that $\sigma_1 = \sigma_{max}$ after singular value decomposition is performed.
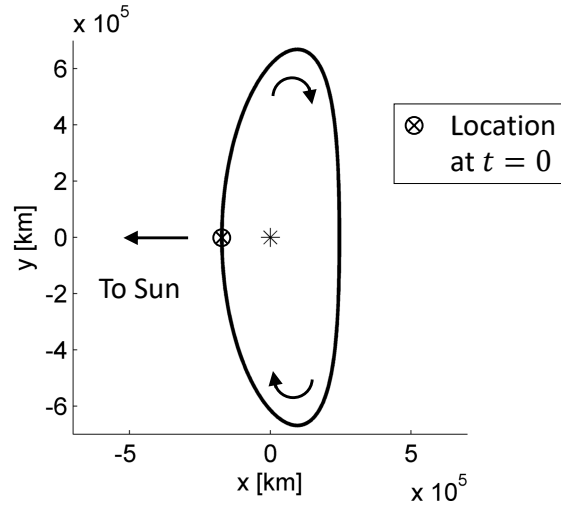
Figure 6.15. Location along the orbit as a measure of elapsed time from the initial fixed location.
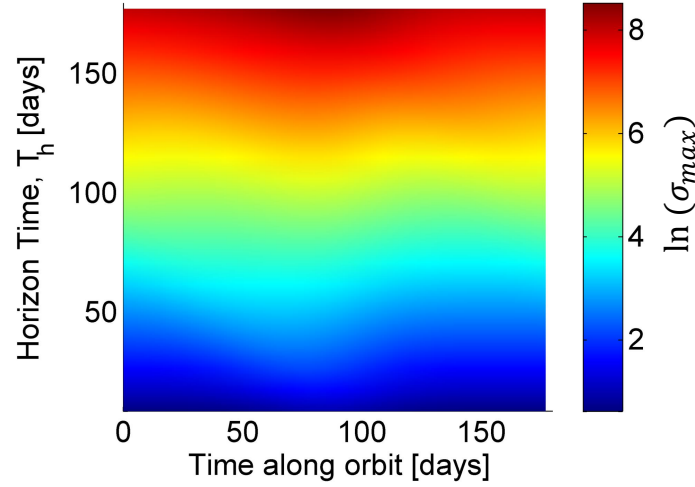
Figure 6.16. Spectrum of magnitude of dominant stretching computed for varying horizon times.

To perform station-keeping, at every maneuver location, depending on the chosen value of horizon time the value of dominant stretching, σ_1, is computed, or retrieved from Figure 6.16. For the three different horizon times 45, 60 and 90 days selected for the station-keeping simulation, the value of dominant stretching are presented in Figure 6.17. Along with the chosen orbit determination error level, the value of target tolerance is predicted as $\epsilon_T = \sigma_1 ||\delta \bar{x}_{ODE}||$. The selected value of target tolerance is a function of the sensitivity at that location and factors in the level of accuracy of measurement. Since the sensitivity at every location along the orbit is different, continuous computation of the magnitude of stretching must be achieved. The eigenvalues of the Cauchy-Green tensor are already known, of which the dominant stretching is the largest eigenvalue of the CGT, therefore, excess computational expenditure is eliminated. The dynamically selected value of target tolerance along with the predefined parameters, horizon time, T_h, and minimum executable maneuver magnitude, ΔV_{min}, are used to estimate the station-keeping outcomes for both Type A and Type B orbit determination errors.
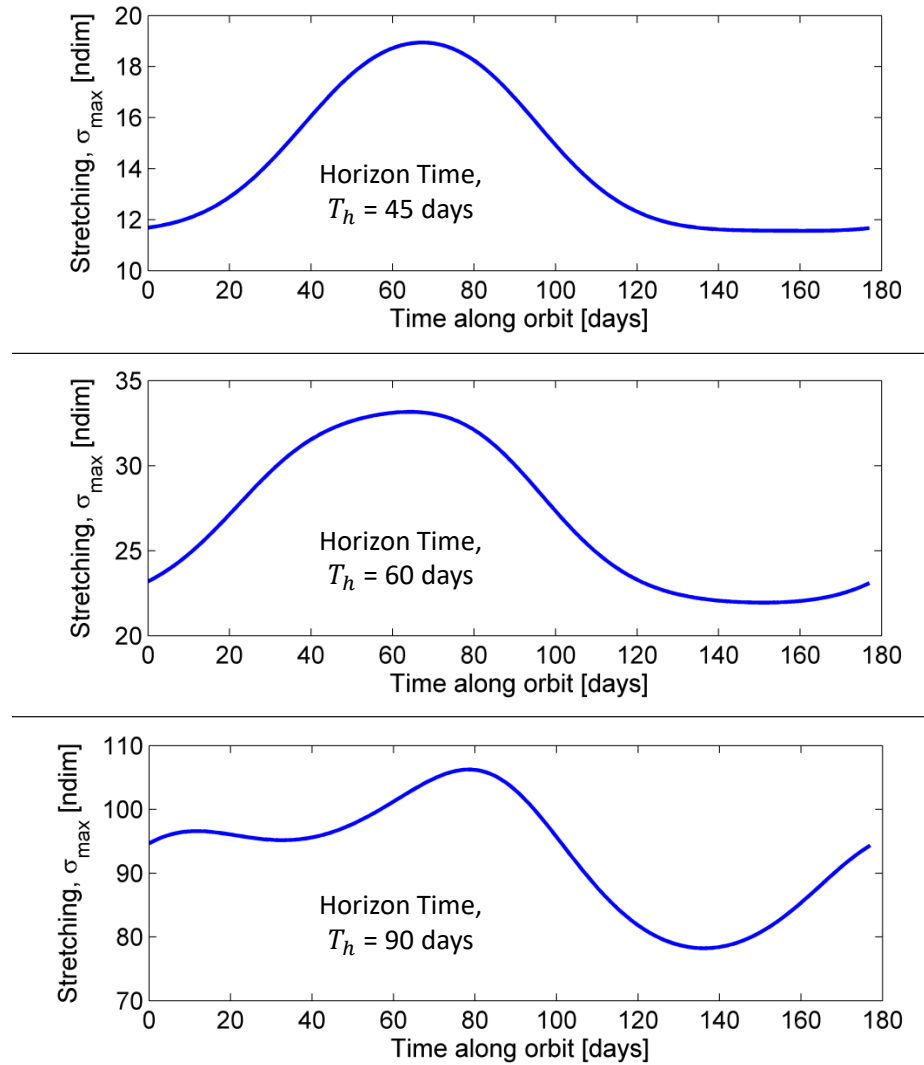
Figure 6.17. Magnitude of dominant stretching along different locations on the chosen reference orbit for horizon time 45, 60 and 90 days.

The station-keeping outcomes, including costs and computational expense as estimated in section 6.4.1 for a range of fixed target tolerance between 10^{-7} and 10^{-3}, in non-dimensional units, are now replaced with dynamical selection of target tolerance to compute the station-keeping outcomes. For both the ODE types, orbit maintenance simulations are performed by 100 Monte Carlo iterations, for horizon time of 45, 60 and 90 days and ΔV_{min} cases of 5, 10, 20, 50 and 100 cm/s. The direction

of corrective maneuvers computed are unconstrained i.e. they are executable in any spatial direction. Unlike the previous section, the target tolerance is selected dynamically. The outcomes for Type A ODE is provided in Table 6.1 while Type B results are in Table 6.2. The station-keeping costs for 2 year mission duration are identical to that predicted using constant values of target tolerance in the range of 10^{-7} and 10^{-3} for both Type A and Type B ODE, however, drastic decrease in computational expense is observed in comparison to low values of ϵ_T chosen before. For Type A ODE with $\Delta V_{min} = 100$ cm/s case, the computational expense for low fixed $\epsilon_T = 2 \times 10^{-7}$ is 413%, 2672% and 16086% for horizon time of 45, 60 and 90 days respectively. Using a dynamical selection of ϵ_T, the same computational expense has decreased to 103%, 206% and 693% for horizon time of 45, 60 and 90 days respectively. Similarly for Type B ODE with $\Delta V_{min} = 100$ cm/s case, the computational expense for low fixed $\epsilon_T = 2 \times 10^{-7}$ is 400%, 2061% and 14032% for horizon time of 45, 60 and 90 days respectively that has reduced to 149%, 300% and 966% respectively, using a dynamical selection of ϵ_T. Moreover, the change in computational expense across different ΔV_{min} cases for a fixed horizon time is minute, except for cases with large ODE and low ΔV_{min} case as the magnitude of ODE becomes significant. A decent level of precision is obtained on 100 Monte Carlo runs, as most relative precision are within 1.52 - 2.72% range. The dynamical selection of the target tolerance, ϵ_T, contributes to better realization of the measurement accuracies and sensitivity of the maneuver location.

The average time between two successive maneuvers is also a crucial component to compare station-keeping outcomes. As expected, the average time between successive maneuvers are less for Type B ODE in comparison with Type A ODE as the size of orbit determination error for Type B is significantly larger than Type A, hence more maneuvers are performed for Type B ODE. Consequently, the station-keeping costs for Type B are higher in contrast to Type A. Moreover, with increase in ΔV_{min} condition, time required by the spacecraft to deviate enough from the reference trajectory to result in a maneuver magnitude of that size also increases, hence larger ΔV_{min}

Table 6.1.   Station-keeping outcomes estimated by the Cauchy-Green tensor approach for 2 year mission duration over 100 Monte Carlo simulations with Type A orbit determination error and three-dimensional/spatial maneuvers.

	T_h [days]	ΔV_{min} [cm/s]				
		5	10	20	50	100
Station-keeping costs [cm/s]	45	46.0	85.5	167.6	401.5	757.5
	60	38.8	72.6	137.5	338.3	648.2
	90	37.6	70.9	144.0	344.6	683.1
Precision [%] (95% confidence or 1.96 σ)	45	1.86	1.87	2.07	2.01	1.84
	60	2.21	1.70	1.92	1.84	2.55
	90	2.23	2.60	2.36	2.45	2.29
Computational expense [%] (wrt baseline)	45	82.61	90.43	91.87	94.77	103.74
	60	155.05	174.69	191.77	205.04	205.94
	90	573.08	639.09	671.35	702.81	693.29
Avg. time b/w successive $\Delta \bar{V}$ [days]	45	81.2	83.6	86.2	90.1	95.1
	60	93.9	99.0	104.1	105.1	110.0
	90	97.0	99.1	99.7	103.3	106.6

case results in larger time span between successive maneuvers. Increasing horizon time from 45 days to 60 days results in marginal increase in average time between successive maneuvers but the change between 60 days to 90 days is neither uniform nor very significant, for both Type A and Type B orbit determination errors. The increase in computational expense across increasing ΔV_{min} cases are also justified with the increase in average time between successive maneuvers. For smaller ΔV_{min} cases, maneuvers are executed frequently. As the algorithm is setup, no maneuvers are computed for 30 days beyond the execution of a corrective maneuver, thereby saving

Table 6.2. Station-keeping outcomes estimated by the Cauchy-Green tensor approach for 2 year mission duration over 100 Monte Carlo simulations with Type B orbit determination error and three-dimensional/spatial maneuvers.

	T_h	ΔV_{min} [cm/s]				
	[days]	5	10	20	50	100
Station-keeping costs [cm/s]	45	106.4	118.9	206.1	462.3	874.0
	60	105.6	115.3	182.3	424.0	837.5
	90	87.9	103.9	188.6	449.0	865.8
Precision [%] (95% confidence or 1.96 σ)	45	2.25	2.50	2.56	2.72	2.51
	60	1.52	2.05	2.47	1.88	2.33
	90	2.02	2.54	2.46	2.41	2.41
Computational expense [%] (wrt baseline)	45	62.01	107.13	126.02	144.27	149.24
	60	108.53	190.55	238.26	282.56	300.46
	90	423.44	703.72	817.92	941.66	966.45
Avg. time b/w successive $\Delta \bar{V}$ [days]	45	40.6	66.9	74.9	81.3	84.1
	60	41.5	68.5	82.7	86.8	87.3
	90	44.8	73.7	79.8	83.7	84.9

computational resources to compute intermediate maneuvers. For larger ΔV_{min} cases, more intermediate maneuvers are computed but not implemented till the ΔV_{min} condition is satisfied. To use average time elapsed between two consecutive maneuvers to compare station-keeping performance with different ODE types is challenging, as it depends on two factors, sensitivity of maneuver locations and the number of maneuver, that have contradicting effects. For larger ODE, it is more likely that the spacecraft deviates from the reference trajectory rapidly on propagating the predefined horizon time downstream, increasing computational efforts for numerical integration.

On the contrary, frequent maneuvers requires less computational resources as a result of reduction in intermediate maneuver computation over 30 days coast/recovery period beyond an executed maneuver. The station-keeping costs and the computational expense are implicitly related to the average time elapsed between successive maneuvers, making it a difficult component to analyze. Apart from the magnitude of the maneuvers and the time span between their occurrence, the direction of the maneuvers also provide details about the behavior of the spacecraft under orbit inaccuracies.

The maneuvers computed using the Floquet mode approach and the target point approach indicated that inclination of most station-keeping maneuvers are towards the rotating x-axis. Such an alignment has serious benefits in mission control as spacecraft orientation need not be altered to perform successive maneuvers, thus preventing any scope of errors. The CGT algorithm is therefore modified to incorporate x-control maneuvers for station-keeping.

6.4.3 x-direction Control Maneuvers using CGT Approach

The orbit chosen for the mission in the vicinity of the Sun-Earth/Moon L_1 libration point has indicated maximum sensitivity towards the rotational x-axis control maneuvers predominantly due to large perturbing gravitational bodies along the rotating x-axis. Within the CR3BP model, as the energy of the spacecraft is increased, the zero velocity curves (ZVCs) evolves, opening the gateway at the L_1 libration point. The least energy access from the vicinity of one primary body to another primary body through the gateway at L_1 is effective only through motion along the rotational x-direction, thus complementing the x-direction sensitivity. The direction of maneuvers at each of the maneuver locations as computed in section 5.4.2, validates the maneuver sensitivity towards x-direction. Fixed direction maneuvers are beneficial for mission operations as it offers a simpler alternative, therefore best if exploited in the direction of highest sensitivity. Besides, the direction of the larger thrusters in

the previous spacecrafts to the orbits near the Sun-Earth L_1 point are aligned fairly close to the rotational x-axis, as per their mission requirements [30, 74, 75].

The Cauchy-Green tensor approach can be considered a versatile station-keeping method only if multiple constraints can be added for station-keeping without significant altercations to the algorithm. To compute a corrective x-control station-keeping maneuver that can secure the spacecraft through the mission duration, the update equation that maps error vector at final time to the initial time is modified. The Cauchy-Green tensor approach computes the closest attainable state on to the target state beyond a predefined horizon time, within the specified target tolerance. The six-dimensional state error vector $(\bar{\mathrm{x}}^* - \bar{c})$ is then mapped back to initial time to identify the necessary corrective maneuver that would drive the spacecraft with minimal error. Recall, $\bar{\mathrm{x}}^*$ is the closest attainable state to the target state at some horizon time downstream while $\bar{c}$ is the state achieved by propagating the initial condition for the same horizon time without any additional perturbation. The pure x-direction maneuver is in fact, a subset of the total maneuvers that could be computed using the CGT method. Equation (6.14) is modified to map error vector $(\bar{\mathrm{x}}^* - \bar{c})$ back to the initial time, with a pure x-control maneuver, $\Delta \bar{V}_M = [\Delta V_x, 0, 0]^T$, as

$$(\bar{\mathrm{x}}^* - \bar{c}) = \phi(t_f, t_0) \begin{pmatrix} \bar{0} \\ \Delta \bar{V}_M \end{pmatrix} = \begin{bmatrix} \phi_{rr} & \phi_{rv} \\ \phi_{vr} & \phi_{vv} \end{bmatrix} \begin{pmatrix} \bar{0} \\ \Delta V_x \\ 0 \\ 0 \end{pmatrix} \qquad (6.17)$$

$$(\bar{\mathrm{x}}^* - \bar{c}) = \begin{bmatrix} \phi_{14} \\ \phi_{24} \\ \phi_{34} \\ \phi_{44} \\ \phi_{54} \\ \phi_{64} \end{bmatrix} \Delta V_x = \underline{A} \Delta V_x \qquad (6.18)$$

where $\underline{A} = [\phi_{14}, \phi_{24}, \phi_{34}, \phi_{44}, \phi_{54}, \phi_{64}]^T$ is the 4th column of the state transition matrix $\phi(t_0 + T_h, t_0)$. Applying least squares method given in equation (6.16) over equation (6.18), the pure x-direction maneuver, ΔV_x, is calculated. The maneuver vector, $\Delta \bar{V}_M$, is therefore $\Delta \bar{V}_M = [\Delta V_x, 0, 0]^T$.

Similar to performing a station-keeping simulation with a spatial maneuvers as the update, the orbit maintenance algorithm is run in the same manner except with x-control maneuvers as updates. Same two ODE cases Type A and Type B are considered with horizon time of 45, 60 and 90 days. Target tolerance is computed dynamically at each step. The station-keeping costs and computational expense for propagating the spacecraft for 2 year mission duration are registered in Table 6.3 and table 6.4 for Type A and Type B ODE respectively.

Station-keeping outcomes for spatial maneuvers as well as x-control maneuvers are compared to analyze the performance of both the maneuver types. The net station-keeping costs are larger for x-control maneuvers irrespective of the orbit determination error levels. A least square method is used to compute the corrective maneuver in the CGT method. Having lesser dimensions to map the deviation vector in the x-control maneuver case, the computed maneuver is unable to correct to its maximum potential, that otherwise is possible through a spatial maneuver. As a result, the x-control maneuver implemented is not as adequate as a spatial maneuver for orbit maintenance, therefore increased station-keeping costs are estimated for x-control maneuver case. The relative precision measured is indicative of the dispersion of individual station-keeping costs predicted for each Monte Carlo simulation. For the x-control maneuver case, the converged precision is of the order of 2.39 - 5.79 % while between 1.52 - 2.72% for spatial maneuvers, indicating that the costs predicted for x-direction maneuvers are more scattered about the computed mean, while individual spatial maneuvers computed are more closer to the mean value. The

Table 6.3. Station-keeping outcomes estimated by the Cauchy-Green tensor approach for 2 year mission duration over 100 Monte Carlo simulations with Type A orbit determination error and x-control maneuvers.

	T_h	ΔV_{min} [cm/s]				
	[days]	5	10	20	50	100
Station-keeping costs [cm/s]	45	49.3	99.3	183.1	421.7	827.6
	60	43.0	93.7	190.1	449.1	834.1
	90	40.1	80.5	158.4	397.0	752.7
Precision [%] (95% confidence or 1.96 σ)	45	2.96	4.64	2.86	4.04	4.05
	60	2.39	3.42	4.61	3.84	4.03
	90	3.29	3.68	3.75	4.17	4.08
Computational expense [%] (wrt baseline)	45	75.34	77.57	82.79	94.28	97.66
	60	156.78	161.71	165.02	165.38	180.19
	90	482.53	526.60	532.95	539.64	574.96
Avg. time b/w successive $\Delta \bar{V}$ [days]	45	78.8	82.1	83.6	92.9	93.3
	60	89.3	91.1	95.3	96.4	101.3
	90	97.7	102.2	103.2	105.4	106.8

computational time seems to have marginally decreased for x-axis maneuvers while no mannerly trend is observed on the variation in the average time between successive maneuvers, for both x-control and spatial maneuver types. The arbitrary change in the average time between successive maneuver can be due to contradicting effects. Since projection of deviation vector on to the available subspaces are the basis of maneuver computation, it would take larger time for x-control maneuver magnitude to reach ΔV_{min} constrain than for a spatial maneuver where components along all the three dimensions increase, consequently the average time between successive ma-

Table 6.4. Station-keeping outcomes estimated by the Cauchy-Green tensor approach for 2 year mission duration over 100 Monte Carlo simulations with Type B orbit determination error and x-control maneuvers.

	T_h	ΔV_{min} [cm/s]				
	[days]	5	10	20	50	100
Station-keeping costs [cm/s]	45	117.9	156.9	236.1	552.7	1118.8
	60	109.3	115.8	225.7	494.5	1004.9
	90	70.6	108.8	192.0	469.0	955.2
Precision [%] (95% confidence or 1.96 σ)	45	5.79	4.63	4.10	4.32	5.42
	60	5.24	3.27	3.58	2.93	3.80
	90	3.22	2.52	2.39	3.85	3.58
Computational expense [%] (wrt baseline)	45	52.04	59.69	68.82	77.83	86.22
	60	90.35	129.95	134.85	159.96	171.21
	90	348.00	397.00	430.31	471.54	492.42
Avg. time b/w successive $\Delta \bar{V}$ [days]	45	45.4	56.9	70.3	72.5	76.3
	60	47.3	69.1	73.7	79.7	81.4
	90	63.3	74.9	81.3	85.8	86.0

neuvers should be larger for x-control maneuver case. On the contrary, x-direction maneuvers are not superior than spatial maneuvers in orbit maintenance due to errors in least square computation when mapping to lesser dimensions, hence the spacecraft would deviate rapidly away from the reference orbit, causing frequent maneuvers. For any case, the average time between two consecutive maneuvers are a combination of the two parameters discussed, that are contrary, hence a common trend is not available from the recorded data. Although, in general, for the orbit chosen for mission design, x-control maneuver still acts as a superior choice for orbit maintenance. Al-

most all the Monte Carlo simulations were successful, complementing the ability to of x-control maneuvers to secure the spacecraft throughout the mission duration.

Sources from literature also complement the benefits and ability of x-control maneuvers for station-keeping for libration point missions in the Sun-Earth/Moon L_1 orbits. Rohrbaugh and Schiff [29] while their investigation on station-keeping for Microwave Anisotropy Probe mission reported that x-control maneuvers are as efficient as unconstrained spatial maneuvers. Anderson et al. [76] indicated large sensitivities along the line joining the primaries through their investigation using local Lyapunov exponents, that is evident as overcoming deviations along the x-direction seems to be an effective way of maintaining the orbit. As mentioned by Roberts [74] for SOHO mission and Williams et al. [30] for Genesis spacecraft, the requirements for SOHO and Genesis spacecrafts were to point towards the direction of the Sun throughout their mission duration to satisfy their objectives of studying the Sun, requiring maneuvers to be along the Sun-spacecraft line, that is almost $\pm 0.25^o$ from the rotating x-axis. The study of x-control maneuvers for these missions have shown great potential.

The Cauchy-Green tensor approach is a flexible station-keeping technique that can compute maneuvers with added constraint other than just spatial maneuvers. The ability to perform maneuvers constrained in rotational x-direction is an illustration of added constraint in maneuver computation. Overall, CGT approach identifies to be a convenient method for station-keeping but the formulation of the CGT algorithm for maneuver computation is sophisticated. The reliability of the sophisticated maneuver computation is therefore reviewed with a more simpler differential correction process for maneuver computation, to gain confidence in the maneuvers generated.

6.4.4   Maneuvers using Differential Correction Process

A differential correction process using a linear state transition matrix is the most straightforward way of computing any corrections in the Ephemeris or CR3BP system. In general, the differential corrections are applied to under-determined system or system with a unique solution, so that output of the differential correction method can be used to update the initial condition to attain the final state. A corrective maneuver can be calculated by targeting position states at a future time and getting a perfect solution, however, station-keeping using a CGT approach targets both position and velocity state at some horizon time downstream. To mimic the CGT approach, a differential correction process is applied to target both position and velocity states at the end of some predefined horizon time. Since the corrections are possible only in the velocity states but the target conditions are combination of both position and velocity states, the system is over-determined. A differential correction can be performed using direct STM but with least squares technique. The update will not perfectly drive to the desired target states as the solution obtained is only a least square solution to an over-determined system, but drives close to the target state with some error. The maneuvers computed using the STM in a very uncomplicated manner is compared with the maneuvers computed using CGT approach to gain confidence in the CGT solution.

At every maneuver location, the maneuver is computed using the CGT method as well as the differential correction method with a direct STM and compared. The comparison process is extended to different combinations of ΔV_{min} cases, horizon time, ODE and direction of maneuvers. Figure 6.18 and Figure 6.19 are two of the many cases, for comparing the maneuver size, computed using the CGT approach and the differential correction process. Figure 6.18 demonstrates the comparison made for Type B ODE with horizon time of 45 days and ΔV_{min} of 10 cm/s while Figure 6.19 describes the resemblance for Type B ODE with horizon time of 90 days and

ΔV_{min} of 100 cm/s. The maneuvers computed, not necessarily implemented, at each maneuver location depends only on the deviation from the reference orbit at current time and the target states at some predefined horizon time downstream. The value is independent of the orbit determination error. In both Figure 6.18 and Figure 6.19, Subfigure 'a' indicates the maneuvers computed using CGT approach at each maneuver location for the mission duration of 2 years, over 10 Monte Carlo iterations, while Subfigure 'b' describes the maneuver magnitude computed using a differential correction process with a direct linear STM, at the same maneuver location. The dotted lines marked in Subfigure 'a' and 'b' indicates the ΔV_{min} value chosen for the specific case. Subfigure 'c' presents the difference between the maneuver magnitudes computed using CGT approach vs direct STM, at a fixed maneuver location with the same target condition. Subfigure 'd' is a histogram depicting the distribution of the points presented in Subfigure 'c' with very small bin size. Subfigures 'a', 'b' and 'c' are plotted 10 Monte Carlo simulations while Subfigure 'd' is estimated for 100 Monte Carlo simulations. Based on the plots, it is apparent that the maneuver magnitudes computed using CGT approach and the differential correction process with a direct STM are comparable. Subfigure 'd' in both Figure 6.18 and Figure 6.19 provide histogram which resembles a Gaussian distribution centered about zero. More than 99.5% of the points recorded in the histogram are within 10% of the ΔV_{min} values that is almost equivalent to 3σ limits. Alternatively, the 1σ limit corresponds to about 3.33% of the chosen ΔV_{min} value, indicating the closeness in values computed using the sophisticated CGT approach and the direct differential correction process.

In general, the Subfigure 'a' and 'b' of Figure 6.19 appears to have a more orderly behavior in terms of maneuver computation spaced equally at tracking interval of 2 days as opposed to Figure 6.18 that appears to be scattered. The primary reason for this is the size of the orbit determination error levels in comparison to the actual size of the maneuver. Figure 6.19 corresponds to case with ΔV_{min} of 100 cm/s contrary to Figure 6.18 with ΔV_{min} of 10 cm/s. As a result the effect of the orbit determination

a. Maneuvers computed using CGT approach

b. Maneuvers computed using direct STM

c. Difference between maneuvers computed using CGT vs STM

d. Distribution of points in 'c'
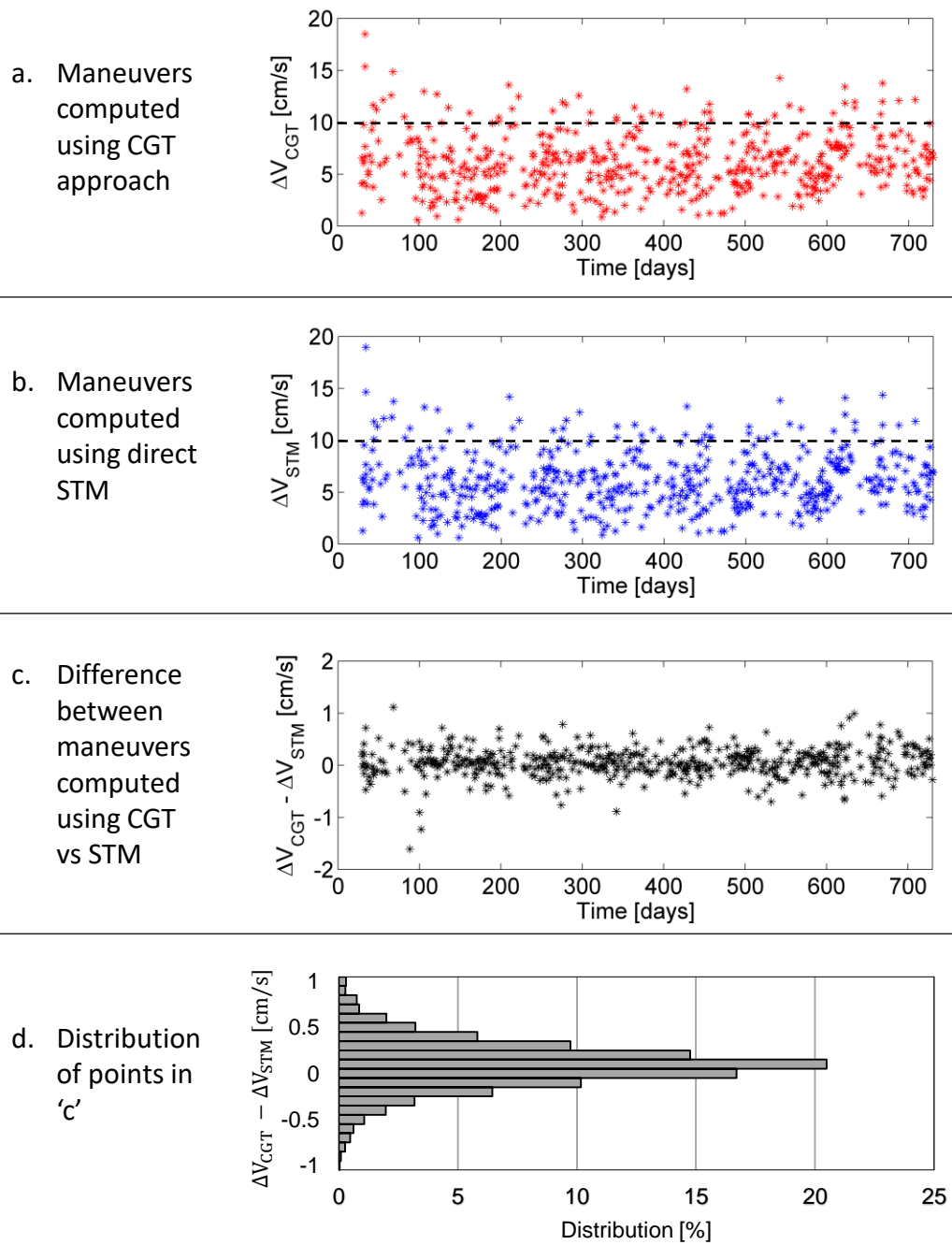
Figure 6.18. Comparison of maneuver magnitudes computed using CGT approach and differential correction process using direct STM, for Type B ODE with horizon time 45 days and ΔV_{min} of 10 cm/s, computed for 10 Monte Carlo simulations.
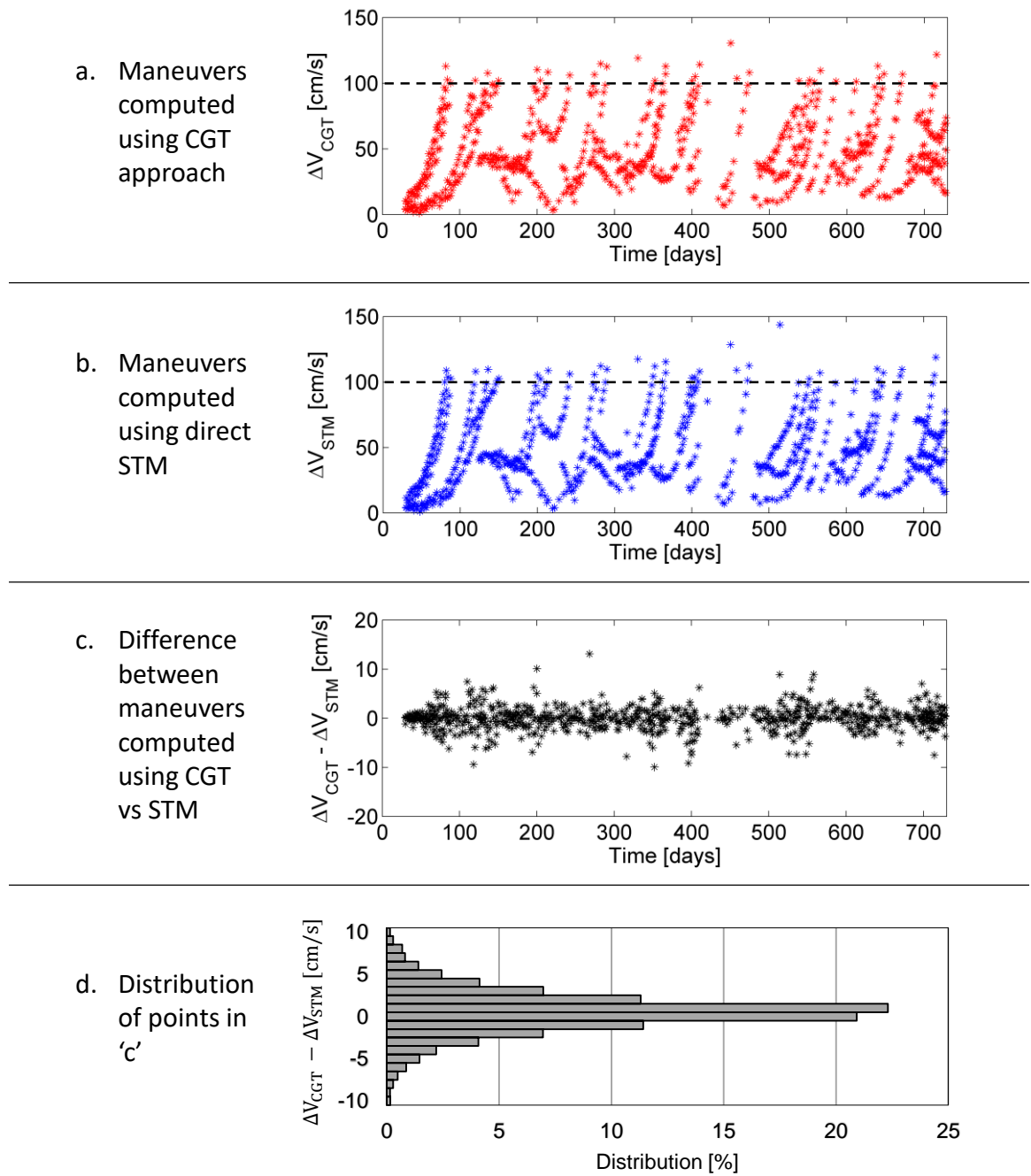
Figure 6.19. Comparison of maneuver magnitudes computed using CGT approach and differential correction process using direct STM, for Type B ODE with horizon time 90 days and ΔV_{min} of 100 cm/s, computed for 10 Monte Carlo simulations.

errors in more apparent for lower values of ΔV_{min}. With increase in ΔV_{min} values, the effect of ODE in velocity estimation diminishes.

The Cauchy-Green tensor approach appears to be a versatile method like the Floquet mode and the target point approach for station-keeping in libration point orbits in the Sun-Earth/Moon system, with the capability to tune the direction of the maneuvers without significant modifications like the previous methods. The ability to adjust parameters with the measurement inaccuracies is advantageous. The application of the CGT method for station-keeping in the Sun-Earth/Moon libration point orbits, as studied for the Aditya-1 mission, indicate great potential for more such missions applications.

7. OBSERVATIONS AND RESULTS

There are many orbit maintenance strategies for Sun-Earth/Moon libration point orbits and have been used successfully in the past. This research mainly investigates the target point, the Floquet mode and the Cauchy-Green tensor approach for station-keeping. Few outcomes like the net station-keeping costs and the maneuver locations are worth examining. The aim of this research is not to find advantages or disadvantages of any method but to extend the capabilities of its functioning, by probing the effects of different parameters that potentially influences the overall costs or the computational expenditure or both.

7.1 Station-keeping Costs

The most common parameter for comparison between different station-keeping strategies is the cost. The comparison made on the costs are just to analyze different strategies for orbit maintenance and not to decide if one strategy is superior than the other. To be consistent in the comparison, x-control maneuvers are selected for the target point, the Floquet mode and the Cauchy-Green tensor approach for station-keeping. The algorithms and the steps involved in maneuver computation are essentially different across different strategies adopted, hence it is not sensible to make a direct comparison on their supremacy and control on overall costs. The spatial maneuvers computed using the Floquet mode approach are solutions to an under-determined system, hence infinitely many solutions exists. A possible spatial maneuver is just one out of infinite solutions available, generally identified using a minimum norm solution. Any two additional constraints can be added to convert the under-determined system to a system with unique solution. Restricting any maneuver component along the y and z-direction is equivalent to adding two constraints.

The unique solution of this system is the x-control maneuver, generated using the Floquet mode approach. The maneuver generation using the target point approach depends on the magnitude of weights along different directions. As discussed, a low weight allows unrestricted maneuver component along that particular direction and vice versa. Since the range of weighting matrices that were selected at majority of th maneuver locations indicated dominance along the x-axis, any maneuver along the y and z-directions were restricted on purpose. The x-control maneuver computed is the unique solution to the governing equation. The Cauchy-Green tensor approach uses a totally different approach. The method tries to compute a maneuver that targets an attainable position and velocity states nearest to the desired state. Unlike the previous method, the governing equation in a CGT method is always over-constrained, no solutions exists, therefore a least squares method is adopted to calculate a maneuver that minimizes the error. A detailed summary of the station-keeping costs for the three approaches are provided in Table 7.1 for both Type A and Type B orbit determination errors. The target point approach and the Floquet mode approach targets one time period downstream while the CGT approach uses different horizon times indicated as $< T_h >$ in the table. The station-keeping costs within the CGT method decreases with increase in horizon time, which is expected as more time is available to make the correction. Although the CGT approach yields a marginally larger station-keeping costs, the CGT approach offers a great initial set of values that can be further tuned using other strategies. Overall the maneuver magnitudes between different strategies are almost of the same order of magnitude.

7.2   Maneuver Locations

The distribution of the maneuver locations complements the sensitivity along the halo orbit chosen for the mission. In a CR3BP model, the chosen periodic orbit has a stability index of 866.98, that is highly unstable. Perturbations along such an unstable orbit tends to diverge rapidly. Additionally, the local stretching characteristics

Table 7.1. Station-keeping cost in cm/s estimated by the target point, the Floquet mode and the Cauchy-Green tensor approach for 2 year mission duration over 100 Monte Carlo simulations with x-control maneuvers.

		TPA	FMA	CGT $< 45 >$	CGT $< 60 >$	CGT $< 90 >$
Orbit injection & tracking error (1σ)		Type A [1.5, 2.5, 15] km & [1, 1, 3] mm/s				
Maneuver execution error (1σ)		2.5% of planned maneuver magnitude in each direction				
ΔV_{min} [cm/s]	5	37.1	37.2	49.3	43.0	40.1
	10	73.0	74.1	99.3	93.7	80.5
	20	142.9	146.2	183.1	190.1	158.4
	50	343.6	355.5	421.7	449.1	397.0
	100	663.7	685.5	827.6	834.1	752.7
Remarks		$q_1 = 10^{17.4}$	-	Horizon time $< T_h >$ in days		
Orbit injection & tracking error (1σ)		Type B [3, 30, 30] km & [15, 15, 30] mm/s				
Maneuver execution error (1σ)		5% of planned maneuver magnitude in each direction				
ΔV_{min} [cm/s]	5	64.4	65.4	117.9	109.3	70.6
	10	102.2	102.8	156.9	115.8	108.8
	20	186.3	188.8	236.1	225.7	192.0
	50	436.2	454.5	552.7	494.5	469.0
	100	849.0	893.5	1118.8	1004.9	955.2
Remarks		$q_1 = 10^{17.7}$	-	Horizon time $< T_h >$ in days		

along the halo orbit as portrayed in Figure 6.16 shows a smooth transition and indicates no selective region of higher sensitivity. Although region on the halo orbit that is closer to the Earth has marginally more tendency to diverge, it is not significantly larger than the other regions. The almost similar stretching characteristics is primarily because of the location of the chosen halo orbit. The chosen orbit is significantly far from any gravitational body hence all regions experience the gravitational field of almost the same order of magnitude. At any point along the orbit, as horizon time increases, the gradient seems to increase almost linearly in the logarithmic scale, that is reflective of exponential divergence that causes the deviation to increase rapidly. Consequently, an early maneuver is regarded. No region seems to provide any significant benefits than the other, hence a maneuver is likely in all regions along halo orbit.

To study the specifics of the distribution of the maneuver locations along the halo orbit, the maneuver location is defined with respect to the Lagrange point L_1 in terms of the in-plane angle, ψ as shown in Figure 7.1. The in-plane angle, ψ, is defined in sync with the conventional coordinate system with angles increasing in the anticlockwise direction. A histogram is plotted that indicates the distribution of maneuver locations along the halo orbit, in terms of angle ψ, over two-year mission duration. The exercise is performed for the target point, the Floquet mode and the Cauchy-green tensor approach and plotted in Figure 7.2 and Figure 7.3 for Type A and Type B orbit determination errors respectively. Since x-control maneuvers are more preferable for the chosen mission scenarios, the histograms are plotted for x-control maneuvers. Different practically feasible ΔV_{min} of 5, 10, 20, 50 and 100 cm/s cases are considered within each control strategy.

Maneuver data obtained for the three different station-keeping strategies are consistent with the argument that for such an unstable orbit as chosen, maneuvers are likely at all locations. More specifically, the distribution is however not uniform throughout the orbit. For both, low and high orbit determination errors as in Type
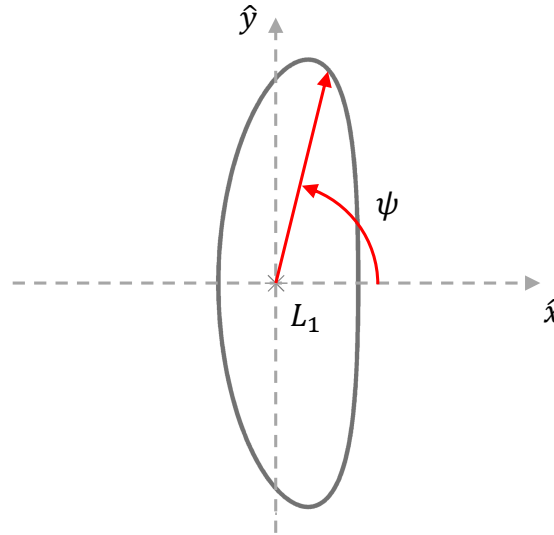
Figure 7.1. In-plane angle at the maneuver location measured with respect to positive x-axis centered about L_1.

A and type B respectively, more maneuvers happen close to the region where the angle subtended is $\pm 80^o$. The region is close to the extreme y coordinates that occurs at $\pm 81.35^o$. The reason for this selective dominance is primarily due to the spacecraft velocity characteristics in this region. Figure 7.4 provides the relation between velocity magnitude and the in-plane angle ψ subtended at different locations along the halo orbit. Clearly, close to the extreme y positions, there is a considerable drop in the velocity magnitude thus allowing a larger time for the spacecraft to coast in the region, thus providing sufficient time for orbit estimation. As soon as the divergence is detected a maneuver is applied. As y position is close to zero near the line joining the primaries, the magnitude of velocity is high, therefore very less time is spent hovering near this region, resulting in lesser time for orbit estimation and lower number of maneuvers in this region. The plot on the relation between in-plane angle and the time along the orbit represented in Figure 7.5 also justifies the distribution of the maneuver locations. Recall, the time along the orbit is defined as in Figure 6.15. Close to the extreme y positions the rate of change in angle vs time is gradual, therefore more orbit estimation happens at angles close to extreme y positions. A
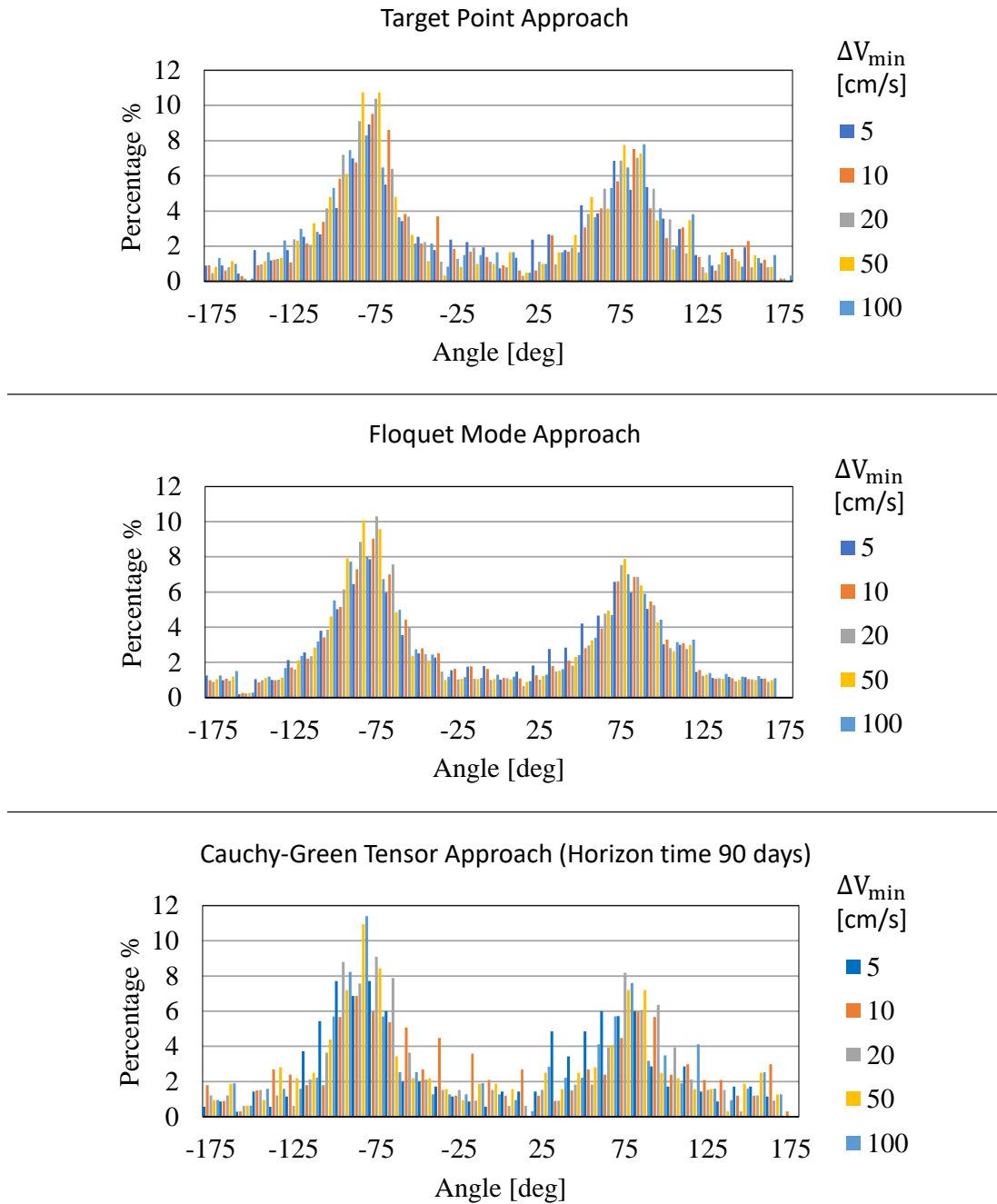
Figure 7.2. Distribution of maneuver locations with respect to the Lagrange points L_1 computed for Type A ODE. Measurements are taken in terms of the in-plane angle ψ.
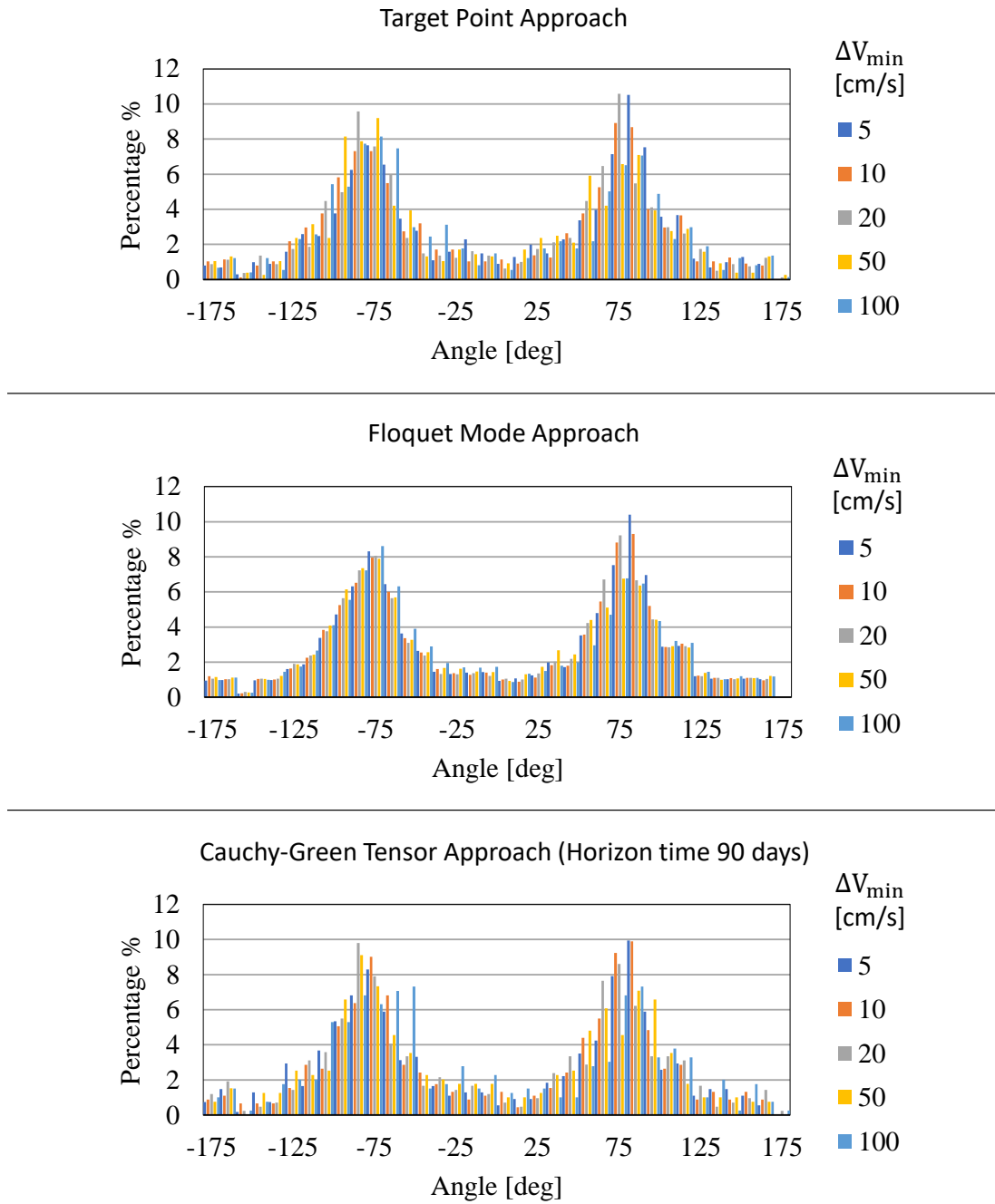
Figure 7.3. Distribution of maneuver locations with respect to the Lagrange points L_1 computed for Type B ODE. Measurements are taken in terms of the in-plane angle ψ.

maneuver is executed immediately as divergence is detected. At y values close to the line joining the primaries, the rate of change in angle is abrupt, reducing the number orbit estimation data, lowering the chance of detecting a maneuver.
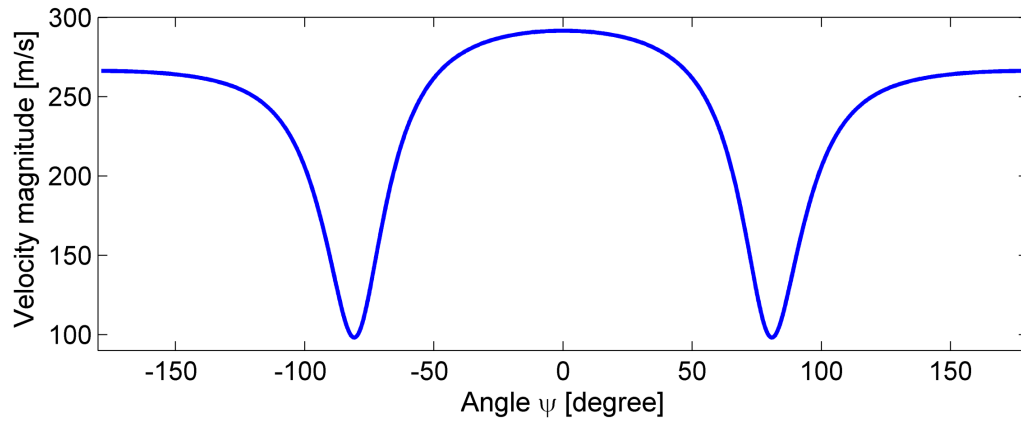
Figure 7.4. Variation in velocity magnitude along the chosen halo orbit. Location along the orbit is represented in terms of angle ψ.
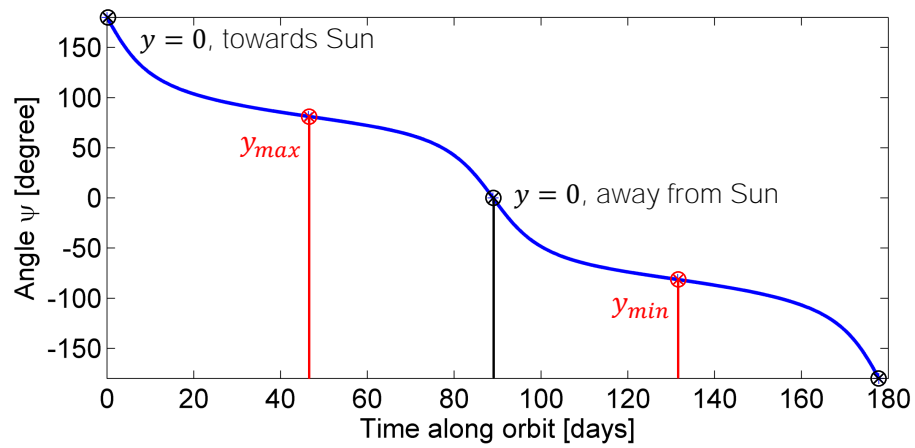
Figure 7.5. Variation of inplane angle, ψ, as a function of time.

7.3   Survey of Libration Point Orbit Station-keeping Studies

For confidence and completeness of the work, it is crucial to examine the station-keeping outcomes for similar missions in the past. The orbit maintenance costs serves as the common baseline for the survey. The challenges in comparing the data is that different missions have different reference orbit, different equipment for orbit determination and different thruster types and capacity. Despite such inconsistencies, it is assumed that the values for similar mission types must results in the same order of magnitude, if not precise. Further the station-keeping costs are assumed to be linear function of time and therefore scaled to 2-year mission duration.

The station-keeping cost is generated by performing Monte Carlo trials and computing the mean. The standard deviation of the distribution is attributed to the confidence in the computed mean. The costs mentioned in few literature sources without any details about their distribution or the sample size, are assumed to correspond to the computed mean rather than a particular outcome of one Monte Carlo trial. Further comparison on confidence interval cannot be performed due to insufficiency in the statistical data.

Despite certain inaccuracies, the most appropriate way of exploring orbit maintenance outcomes for the previous Sun-Earth/Moon L_1 libration point orbits is using the station-keeping cost comparison. The station-keeping survey is detailed in Table 7.2. The table corresponds to previous station-keeping (SK) results available from different literature sources, that have been cited. All the costs are scaled to 2-year mission duration. Different values of orbit determination and tracking errors that have been used for different missions are documented. Few mission use additional Solar Reflectivity (SR) uncertainty while other have not considered such errors. Additional parameters important to analyze the data are provided in the 'Remarks' column, provided that those details are mentioned in the literature source. Not all

range of costs are comparable as they are solutions to different ΔV_{min} conditions.

Table 7.2.: Survey of station-keeping costs for the Sun-Earth/Moon L_1 halo orbits.

Source	Tracking errors (1σ) [km] [mm/s]	Maneuver execution error (1σ)	2-year SK cost [m/s]	Remarks
Howell & Pernicka [24, 25]	[1.5, 2.5, 15] [1, 1, 3]	2.5%	0.33 - 4.02	ΔV_{min} : 0.05 - 0.5 m/s $\Delta t_{min} = 30$ days
			0.77 - 3.61	ΔV_{min} : 0.05 - 0.5 m/s $\Delta t_{min} = 60$ days
Howell & Gordon [40, 41]	[1.46, 2.64, 4.81] [1.40, 1.85, 2.49]	10%	0.76 - 0.87	SR uncertainty = 13% $\Delta t_{min} = 60$ days
			0.92 - 1.23	SR uncertainty = 13% $\Delta t_{min} = 80$ days
Gomez et.al [44]	[1.5, 2.5, 15] [1, 1, 3]	2.5%	0.4	20 cm/s/year SR uncertainty = 2.5%
Gomez et.al [26]	[3, 30, 30] [15, 15, 30]	10%	13.3	$\Delta V_{min} = 1.5$ m/s $\Delta t_{min} = 60$ days Tracking int. : 3 days
Simo et al. [47]	[1.7, 2.2, 5.5] [1.4, 1.4, 2.4]	2.5%	0.35 - 0.4	0.7 - 0.8 m/s for 4 years SR uncertainty = 5%
Howell & Keeter [42, 43]	[3, 30, 30] [15, 15, 30]	2.5%	0.34 - 18.8	Δt_{min} : 30 - 90 days
ISEE-3 [21, 77]			15	Actual mission data

Table 7.2.: *continued*

WIND [2, 53]			2.0	Actual mission data
ACE [2, 53]			2.0	Actual mission data
SOHO [53, 74]			4.8	Actual mission data
This work (x-axis control)	[1.5, 2.5, 15] [1, 1, 3]	2.5%	0.37 - 8.27	ΔV_{min} : 0.05 - 1.0 m/s $\Delta t_{min} = 30$ days Tracking int. : 2 days
	[3, 30, 30] [15, 15, 30]	5%	0.64 - 11.18	ΔV_{min} : 0.05 - 1.0 m/s $\Delta t_{min} = 30$ days Tracking int. : 2 days

There seems to a broad variance in the station-keeping costs estimated for a spacecraft in the Sun-Earth/Moon L_1 halo type orbits. The wide range costs is attributed to the difference in the orbit determination error levels used for simulating the mission scenarios and the dissimilarity in the algorithm chosen to perform the orbit maintenance. Nevertheless, the station-keeping costs computed in this work for x-control maneuvers using the target point, the Floquet mode and the Cauchy-Green tensor approach are in the same order of magnitude. For the type A ODE, the station-keeping costs estimated in this work is almost equal to the values predicted in by Howell and Pernicka [24, 25] that uses the same ODE level. Similarly, for Type B ODE, the station-keeping costs estimated in this work fall in the range of values obtained by other researchers that used the similar uncertainty levels. The work presents a range of station-keeping costs considering a wide range of ΔV_{min} and ODE

values. The actual costs for a mission depends on the capacity of the engine and the measurement accuracy of the equipment in use. It is expected that the values estimated for the real mission will be in the range of costs computed in this work. Further, no claim has been made on the optimality of the solutions.

8. SUMMARY AND RECOMMENDATIONS

8.1 Summary

The goal of this work is to explore different station-keeping strategies such as the target point, the Floquet mode and the Cauchy-Green tensor approach. Effort has been put to make parameter selections information based rather than human choice based selection. The intent is not to find advantages or disadvantages of one method over the other rather to explore and enhance the parameter selection within each strategy. The issues are administered in an progressive manner.

The first chapter summarizes the different questions that this research work focuses. The background studies and the development of the circular restricted three body problem are addressed. A detailed description of previous missions to the Sun-Earth/Moon L_1 libration point orbits and various orbit maintenance strategies are provided.

In the second chapter, the different system models that are used throughout this work are discussed. The equations of motion in the circular restricted three body problem are derived and equilibrium solutions are calculated. To study the behavior of a spacecraft in the vicinity of an equilibrium solution, linearized solutions are formulated. The solutions in a circular restricted model is an approximation of the behavior of the spacecraft under the influence of two main primary bodies, however there will be perturbations due to elliptic orbit and presence of other gravitational bodies and forces. In order to simulate a real life scenario, the behavior of the spacecraft must be analyzed in the presence of multiple forces that significantly affects the motion of the spacecraft hence, the higher fidelity ephemeris model is described with

a new set of equations of motion. It is desirable to analyze the the motion of the spacecraft in the inertial coordinate frame as well as the rotational frame fixed with the primaries, therefore a coordinate transformation matrix is developed.

Chapter three is an outline of the tools used in the circular restricted three body model as well as the ephemeris model to target certain boundary conditions. A state transition matrix is developed that maps the evolution of some initial perturbation to a final time in the linear sense, derived upon an arbitrary reference solution. An explanation of the differential correction process that predicts linear modification to attain some final condition is illustrated. To solve boundary value problems in a more complex regime, a robust multiple shooting technique, that is a cumulative sin-gle shooting differential correction problem, is elaborated.

The outline of an orbit maintenance operation is detailed in chapter four. The selection of a nominal orbit in the CR3BP and transformation into the ephemeris model is discussed. The station-keeping problem is stochastic in nature due to in-accuracies in measurements. For simulation, the inaccuracies are purposefully incor-porated to mimic a real mission scenario. The overall orbit maintenance algorithm is discussed, and parameters like minimum executable maneuver ΔV_{min}, minimum time between maneuvers Δt_{min}, drift from the reference orbit $\underline{d}$, that influence the station-keeping performance are introduced. Background on Monte Carlo process to evaluate a stochastic problem like station-keeping is provided.

In chapter five, functioning of the target point and the Floquet mode approach are elaborated. The qualitative information available from the Floquet mode ap-proach are leveraged to identify the right range of values of the weighting matrices in the target point approach that can mimic the Floquet mode results as well as decrease the station-keeping costs. The range of weights substantiates the dominance of maneuvers along the rotational x-axis at majority of the locations, indicative of

pure x-control maneuver that would be sufficient for orbit maintenance. The drifting pattern is observed for a range of weights to determine if the spacecraft will deviate uncontrollably by the end of the mission duration.

An application of the recently developed method for station-keeping using the Cauchy-Green tensor approach in the Sun-Earth/Moon system is analyzed in chapter six. The approach is tested in the Sun-Earth/Moon system for the first time and shows promising results. The effects of target tolerance, size of executable maneuver and horizon time on station-keeping costs and computational expense are analyzed. Smaller target tolerance increased the computational expense while station-keeping costs remained almost the same for the range of target tolerance selected for the analysis. The flow in the vicinity of a reference trajectory and the size of the orbit determination error is used to define a dynamic value of target tolerance that is selected based on dynamical information available rather than heuristics. The feasibility of x-direction control maneuvers for the selected orbit is investigated using the CGT approach. Similar to the spatial maneuvers, the x-direction control maneuvers were successful in maintaining the spacecraft near the reference orbit for the mission duration except for a marginal increase in annual orbit maintenance costs. Finally, the maneuvers computed using sophisticated approach like CGT is seen to be of the same order as that predicted with the simple differential correction tool, thus presenting confidence in the CGT results.

The common basis for comparing multiple orbit maintenance strategies is the station-keeping costs, therefore the values obtained using the target point, the Floquet mode and the Cauchy-Green tensor approach are compared for the purpose of understanding the functioning of different approaches rather to identify if any method is superior to another. The details are presented in chapter seven. It was identified that more maneuvers are likely at extreme y positions due to the smaller velocities f the spacecraft in those regions allowing larger duration for orbit estimation. Lastly,

a summary of station-keeping costs from different literature sources are documented to compare the order of magnitude of the values obtained in this research and gain confidence. The station-keeping costs for some of the previous missions are in the range of costs computed in this work.

8.2   Recommendations for Future Work

The application of the target point, the Floquet mode and the Cauchy-Green tensor approach for station-keeping in the Sun-Earth/Moon system looks promising. The analysis was done in the higher fidelity model with gravitational forces of the Sun, the Earth and the Moon only. For more specific case, additional gravitational forces can be incorporated. For a mission that uses solar sail, solar radiation pressure and its effects on the motion of the spacecraft can be incorporated for the station-keeping problem. Similarly, application of continuous controller and/or low thrust propulsion system are potential options for future work. Specific to the Cauchy-Green tensor approach, that was tested in the Sun-Earth/Moon system for the first time, orbit maintenance simulations were initially performed for spatial maneuvers. Addition of two more constraints i.e. restriction of y and z direction components, resulted in x-control maneuvers. Modification of constraints types to generate different kinds of maneuver than just x-control maneuver is worth investigating, specific example for that is maneuvers along the Sun-spacecraft line, that may be beneficial for certain missions. The nominal orbit chosen for the mission was an unstable southern halo orbit in the Sun-Earth/Moon L_1 region. Other orbits such as Lissajous, Lyapunov, quasi-periodic orbits etc. are worth inspecting. Moreover, orbits in the vicinity of L_2 region and orbits around the primary bodies are also candidates for future missions hence station-keeping analysis might be valuable.

The continued interests in libration point missions will keep orbit maintenance a popular topic of research. The three approaches for station-keeping have their own

advantages, simplicity and robustness of the target point approach, the qualitative information provided by the Floquet mode approach and the knowledge about the local stretching given by the Cauchy-Green tensor approach. The success of future libration point missions relies on the enhancement of these station-keeping approaches.

REFERENCES

REFERENCES

[1] Robert W Farquhar, Daniel P Muhonen, Charles R Newman, and Howard S . Heubergerg. Trajectories and orbital maneuvers for the first libration-point satellite. *Journal of Guidance, Control, and Dynamics*, 3(6):549–554, 1980.

[2] Craig E Roberts. Long term missions at the Sun-Earth Libration Point L1: ACE, SOHO, and WIND. In *AAS/AIAA Astrodynamics Specialist Conference, Girdwood, Alaska*, 2011.

[3] Daniel B Reisenfeld, Roger C Wiens, Bruce L Barraclough, John T Steinberg, Marcia Neugebauer, Jim Raines, and Thomas H Zurbuchen. Solar wind conditions and composition during the genesis mission as measured by in situ spacecraft. *Space Science Reviews*, 175(1-4):125–164, 2013.

[4] Indian Space Research Organisation (ISRO). *Aditya - L1 First Indian mission to study the Sun*, 2017 (accessed August 19, 2017).

[5] National Aeronautics and Space Administration (NASA). *The James Webb Space Telescope*, 2017 (accessed August 19, 2017).

[6] Johannes Kepler, Max Caspar, Walther von Dyck, and Franz Hammer. *Astronomia nova*. CH Beck'sche Verlagsbuchhandlung, 1937.

[7] Johannes Kepler. *Epitome of Copernican Astronomy and harmonies of the World*. Prometheus Books, 1995.

[8] Sir Isaac et al. Philosophiae naturalis principia mathematica. 1977.

[9] C Edward Sandifer. *The early mathematics of Leonhard Euler*, volume 1. MAA, 2007.

[10] Joseph Louis Lagrange. *Theory of analytic functions: containing the principles of differential computation, taking into account any considerations of 'Infinitely small, vanouissan, boundaries and fluxions, and reactions to the algebraic analysis of the quantities finished*. Ve. Courcier, 1813.

[11] Carl Gustav Jakob Jacobi. *Vorlesungen über dynamik*. G. Reimer, 1866.

[12] Henri Poincaré. *New methods of celestial mechanics*, volume 13. Springer Science & Business Media, 1992.

[13] Victor Szebehely. Theory of orbits. the restricted problem of three bodies. *New York: Academic Press,— c1967*, 1967.

[14] Robert W. Farquhar. *The control and use of libration-point satellites*. PhD Dissertation, Department of Aeronautics and Astronautics, Stanford University, 1968.

[15] Robert W Farquhar and Ahmed A Kamel. Quasi-periodic orbits about the translunar libration point. *Celestial Mechanics*, 7(4):458–473, 1973.

[16] David L Richardson. Halo orbit formulation for the ISEE-3 mission. *Journal of Guidance and Control*, 3(6):543–548, 1980.

[17] Kathleen Connor Howell. Three-dimensional, periodic, halo orbits. *Celestial Mechanics*, 32(1):53–71, 1984.

[18] KC Howell and HJ Pernicka. Numerical determination of lissajous trajectories in the restricted three-body problem. *Celestial Mechanics*, 41(1-4):107–124, 1987.

[19] Pranav Nath and RV Ramanan. Precise halo orbit design and optimal transfer to halo orbits from earth using differential evolution. *Advances in Space Research*, 57(1):202–217, 2016.

[20] David N Spergel, Licia Verde, Hiranya V Peiris, E Komatsu, MR Nolta, CL Bennett, M Halpern, G Hinshaw, N Jarosik, A Kogut, M. Limon, S.S. Meyer, L. Page, G.S. Tucker, J.L. Weiland, E. Wollack, and E.L. Wright. First-year Wilkinson Microwave Anisotropy Probe (WMAP) observations: determination of cosmological parameters. *The Astrophysical Journal Supplement Series*, 148(1):175, 2003.

[21] Robert Farquhar, Daniel Muhonen, and Leonard C Church. Trajectories and orbital maneuvers for the ISEE-3/ICE comet mission. In *AISS/AAS Astrodynamics Conference, Seattle, Washington*, 1984.

[22] H Heuberger. Halo orbit station keeping for International Sun-Earth Explorer-C/ISEE-C. In *AIAA/AAS Astrodynamics Specialist Conference, Jackson Hole, Wyoming*, 1977.

[23] JA Erickson and AB Glass. Implementation of ISEE-3 trajectory control. In *Paper No. AAS 79-128, AIAA/AAS Astrodynamics Specialist Conference, Provincetown, Massachusetts*, 1979.

[24] KC Howell and HJ Pernicka. Stationkeeping method for libration point trajectories. *Journal of Guidance Control and Dynamics*, 16:151–151, 1993.

[25] Henry John Pernicka. *The Numerical Determination of Nominal Libration Point Trajectories and Development of a Station-Keeping Strategy*. PhD Dissertation, School of Aeronautics and Astronautics, Purdue University, 1990.

[26] Gerard Gómez, Jaume Llibre, Regina Martínez, and Carles Simó. *Dynamics and Mission Design Near Libration Points: Volume I: Fundamentals: The Case of Collinear Libration Points*, volume 2. World Scientific, 2001.

[27] J Rodriguez-Canabal and M Hechler. Orbital aspects of the SOHO mission design. In *Orbital Mechanics and Mission Design, Proceedings of the AAS/NASA International Symposium, Greenbelt, Maryland*, pages 347–357, 1989.

[28] P. Sharer, H. Franz, and D. Folta. WIND Trajectory Design and Control. In *Paper No. MS95/032, CNES International Symposium on Space Dynamics, Toulouse, France*, 1995.

[29] Dave Rohrbaugh and Conrad Schiff. Stationkeeping approach for the Microwave Anisotropy Probe (MAP). In *Paper No. AIAA-2002-4429, AIAA/AAS Astrodynamics Specialist Conference, Monterey, California*, 2002.

[30] Kenneth Williams, R Wilson, M Lo, K Howell, and B Barden. Genesis halo orbit station keeping design. In *International Symposium: Space Flight Dynamics, Biarritz, France*, 2000.

[31] L Janes and M Beckman. Stationkeeping maneuvers for the James Webb Space Telescope. In *Goddard Flight Mechanics Symposium*. Goddard Space Flight Center Greenbelt, MD, 2005.

[32] John V Breakwell, Ahmed A Kamel, and Martin J Ratner. Station-keeping for a translunar communication station. *Celestial Mechanics*, 10(3):357–373, 1974.

[33] JV Breakwell. Investigation of halo satellite orbit control. 1973.

[34] G Colombo. The stabilization of an artificial satellite at the inferior conjunction point of the Earth-Moon system. *Smithsonian Contributions to Astrophysics*, 6:213, 1963.

[35] Edward A Euler and EY Yu. Optimal station-keeping at collinear points. *Journal of Spacecraft and Rockets*, 8(5):513–516, 1971.

[36] David Folta, Mark Woodard, and Daniel Cosgrove. Stationkeeping of the first earth-moon libration orbiters: The ARTEMIS mission. In *Paper No. AAS 11-515, AAAS/AIAA Astrodynamics Specialist Conference, Girdwood, Alaska, United States*, 2011.

[37] David Folta, TA Pavlak, KC Howell, MA Woodard, and DW Woodfork. Stationkeeping of Lissajous trajectories in the Earth-Moon system with applications to ARTEMIS. In *20th AAS/AIAA Space Flight Mechanics Meeting, San Diego, California*, pages 10–113, 2010.

[38] David C Folta, Thomas A Pavlak, Amanda F Haapala, Kathleen C Howell, and Mark A Woodard. Earth–Moon libration point orbit stationkeeping: theory, modeling, and operations. *Acta Astronautica*, 94(1):421–433, 2014.

[39] T Pavlak and Kathleen C Howell. Strategy for long-term libration point orbit stationkeeping in the Earth-Moon system. In *Paper No. 11-516, Proceedings of the AAS/AIAA Astrodynamics Specialist Conference, AAS Paper*, 2011.

[40] KC Howell and SC Gordon. Orbit determination error analysis and a stationkeeping strategy for Sun-Earth L1 libration point orbits. *Journal of the Astronautical Sciences*, 42:207–228, 1994.

[41] Steven Craig Gordon. *Orbit Determination Error Analysis and Station-Keeping for Libration Point Trajectories*. PhD Dissertation, School of Aeronautics and Astronautics, Purdue University, 1991.

[42] Timothy M. Keeter. *Station-Keeping Strategies for Libration Point Orbits: Target Point and Floquet Mode Approaches*. M.S. Thesis, School of Aeronautics and Astronautics, Purdue University, 1994.

[43] KC Howell and TM Keeter. Station-keeping strategies for libration point orbits-target point and Floquet mode approaches. *Spaceflight mechanics*, pages 1377–1396, 1995.

[44] G Gómez, J Llibre, R Martinez, and C Simó. Station keeping of libration point orbits. *Final Report: ESOC Contract 5648/83/D/JS (SC)*, 1985.

[45] Gerard Gómez, KC Howell, J Masdemont, and Carles Simó. Station-keeping strategies for translunar libration point orbits. *Advances in Astronautical Sciences*, 99(Pt 2):949–967, 1998.

[46] C Simó, G Gómez, J Llibre, and R Martínez. Station keeping of a quasiperiodic halo orbit using invariant manifolds. In *Proceed. 2nd Internat. Symp. on spacecraft flight dynamics, Darmstadt*, pages 65–70, 1986.

[47] C Simó, G Gómez, J Llibre, R Martinez, and J Rodriguez. On the optimal station keeping control of halo orbits. *Acta Astronautica*, 15(6):391–397, 1987.

[48] YunHe Meng, YueDong Zhang, and JinHai Dai. Floquet-based design and control approach to spacecraft formation flying in libration point orbits. *Science China Technological Sciences*, 54(3):758–766, 2011.

[49] Davide Guzzetti, Emily M Zimovan, Kathleen C Howell, and Diane C Davis. Stationkeeping analysis for spacecraft in lunar near rectilinear halo orbits. In *Paper No. 17-395, AAS/AIAA Spaceflight Mechanics Meeting, San Antonio, Texas*, 2017.

[50] Mehrdad Ghorbani and Nima Assadian. Optimal station-keeping near Earth–Moon collinear libration points using continuous and impulsive maneuvers. *Advances in Space Research*, 52(12):2067–2079, 2013.

[51] KC Howell and BT Barden. Trajectory design and stationkeeping for multiple spacecraft in formation near the Sun-Earth L1 point. In *IAF 50th International Astronautical Congress*, pages 4–8, 1999.

[52] Jing Lü, Qishao Lu, and Qi Wang. A station-keeping strategy for collinear libration point orbits. *Theoretical and Applied Mechanics Letters*, 1(3):033002, 2011.

[53] Maksim Shirobokov, Sergey Trofimov, and Mikhail Ovchinnikov. Survey of station-keeping techniques for libration point orbits. *Journal of Guidance, Control, and Dynamics*, 2017.

[54] Gerhard Beutler. *Methods of Celestial Mechanics: Volume I: Physical, Mathematical, and Numerical Principles*. Springer Science & Business Media, 2004.

[55] George T Gillies. The newtonian gravitational constant: recent measurements and related studies. *Reports on Progress in Physics*, 60(2):151, 1997.

[56] Jayme M. Howsman. *Investigation of Transfer Trajectories to Periodic Horseshoe Orbits*. M.S. Thesis, School of Aeronautics and Astronautics, Purdue University, 2011.

[57] Robert Pritchett. *Numerical Methods for Low-Thrust Trajectory Optimization*. M.S. Thesis, School of Aeronautics and Astronautics, Purdue University, 2016.

[58] Alexandre G. Van Anderlecht. *Tadpole orbits in the L4/L5 region: Construction and links to other families of Periodic Orbits*. M.S. Thesis, School of Aeronautics and Astronautics, Purdue University, 2016.

[59] Victor S Ryaben'kii and Semyon V Tsynkov. *A theoretical introduction to numerical analysis*. CRC Press, 2006.

[60] John V Breakwell and John V Brown. The halo family of 3-dimensional periodic orbits in the Earth-Moon restricted 3-body problem. *Celestial mechanics and dynamical astronomy*, 20(4):389–404, 1979.

[61] Earth Observation Portal. *Aditya-L1 Solar Coronagraph Mission*, 2017 (accessed November 28, 2017).

[62] Jason S. Nuss. *The Use of Solar Sails in the Circular Restricted Problem of Three Bodies*. M.S. Thesis, School of Aeronautics and Astronautics, Purdue University, 1998.

[63] Allan I. S. McInnes. *Strategies for Solar Sail Mission Design in the Circular Restricted Three-Body Problem*. M.S. Thesis, School of Aeronautics and Astronautics, Purdue University, 2000.

[64] Julia Lea Bell. *The Impact of Solar Radiation Pressure on Sun-Earth L1 Libration Point Orbits*. M.S. Thesis, School of Aeronautics and Astronautics, Purdue University, 1991.

[65] Thomas A. Pavlak. *Mission Design Applications in the Earth-Moon System: Transfer Trajectories and Stationkeeping*. M.S. Thesis, School of Aeronautics and Astronautics, Purdue University, 2010.

[66] K Muralidharan. *Six sigma for organizational excellence: A statistical approach*. Springer, 2015.

[67] NP Dwivedi. Deterministic optimal maneuver strategy for multi-target missions. *Journal of Optimization Theory and Applications*, 17(1):133–153, 1975.

[68] Kiarash Tajdaran. *Incorporation of Mission Design Constraints in Floquet Mode and Hamiltonian Structure-Preserving Orbital Maintenance Strategies for Libration Point Orbits*. M.S. Thesis, School of Aeronautics and Astronautics, Purdue University, 2015.

[69] Robert J Vanderbei. Symmetric quasidefinite matrices. *SIAM Journal on Optimization*, 5(1):100–113, 1995.

[70] Michael E Wall, Andreas Rechtsteiner, and Luis M Rocha. Singular value decomposition and principal component analysis. In *A practical approach to microarray data analysis*, pages 91–109. Springer, 2003.

[71] Carl D Meyer. *Matrix analysis and applied linear algebra*, volume 2. SIAM, 2000.

[72] Davide Guzzetti and Kathleen Howell. *Final Report*. Grant No. NNX13AK60, 2016.

[73] Christopher Spreen, Kathleen Howell, and Belinda Marchand. Node placement capability for spacecraft trajectory targeting in an ephemeris model. In *Paper No. AAAS 15-638, AIAA/AAS Astrodynamics Specialist Conference, Vail, Colorado*, 2015.

[74] Craig E Roberts. The SOHO mission L1 halo orbit recovery from the attitude control anomalies of 1998. In *Proceedings of the Conference on Libration Point Orbits and Applications*, 2002.

[75] David W Dunham and Craig E Roberts. Stationkeeping techniques for libration-point satellites. *The Journal of the Astronautical Sciences*, 49(1):127–144, 2001.

[76] Rodney L Anderson, Martin W Lo, and George H Born. Application of local lyapunov exponents to maneuver design and navigation in the three-body problem. In *Paper No. AAS 03-569, AIAA/AAS Astrodynamics Specialist Conference, Big Sky, Montana*, 2003.

[77] L Efron, J Ellis, DK Yeomans, PW Chodas, and RI Premkumar. ISEE-3/ICE navigation analysis. In *Paper No. AIAA-84-1981, AIAA/AAS Astrodynamics Specialist Conference, Seattle, Washington*, 1984.